2022, March
Graduate School of Natural Science and Technology
(Doctoral Course)
Okayama University

Detailed analyses of multi-functional carbon materials toward high-performance supercapacitor electrodes

高性能電気二重層キャパシタ電極材料開発に向けた
多機能性炭素材料の詳細な分析

学籍番号: 51430755

提出者: 梅澤 成之

DECLARATION

The material presented in this thesis is the outcome of my research under the supervision of Professor Yasuhiko HAYASHI at Okayama University. It has not been previously submitted, in part or whole, to any university or institution for any degree or other qualification.

Signed:

Name: Shigeyuki Umezawa

Date: 17 February 2022

提出年月日: 2022 年 2 月 17 日

指導教員: 林 靖彦 教授

Abstract

This doctoral thesis aims at investigating multi-functional carbons, such as porous carbons and hetero-atoms-doped carbons, for supercapacitor (SC) electrodes.

Chapter 1 gives an overview of porous carbons for SC electrodes. The author summarizes the history of typical syntheses of porous carbon materials and heteroatom-doped carbons in the first part. The second part presents the importance of developing SC electrode materials in terms of environmental and energy concerns.

Chapter 2 discusses the electrochemical properties of SC electrodes experimentally and analytically to promote a better understanding. First, the author examined the electrochemical properties of SCs using three kinds of commercial porous carbon materials. Thereafter, the author introduced simulation models to analyze and evaluate experimental data. The findings contribute to the discussion in the subsequent chapter.

Chapter 3 reports nitrogen (N)-doped porous carbons prepared by the direct carbonization of imine-based covalent organic frameworks (ICOFs). The obtained carbon particle size was successfully controlled depending on the synthetic conditions. Interestingly, the particle size was observed to affect the specific surface area (S_{BET}) of the resultant carbons. The electrochemical properties of carbonized ICOFs (CICOFs) were examined to confirm the pseudo-capacitive effect induced by N-doping.

Chapter 4 reports the unique acid-free process of producing template porous carbons using boron oxides (B_2O_3). B_2O_3 dissolves well in water compared to other metal oxides. B_2O_3-templating carbon was prepared by carbonization of Boron (B)-based COFs (COF-5) at 1000 °C. Subsequently, porous carbon was obtained by removing B_2O_3 through the gentle water treatment. Further, the obtained porous carbon was found to be a B-doped material. The electrochemical properties of COF-5 derived carbons were examined in detail.

Chapter 5 discusses the mechanism underlying pore generation during carbonization by

employing zinc-based metal-organic frameworks (ZMOFs) as a carbon precursor. The carbonization of ZMOFs generates zinc oxides (ZnO) on the carbon below 800 °C. Above 800 °C, carbons reduced ZnO to gaseous Zn. The Zn sublimation provided pores on the carbons, resulting in up to 2700 m^2 g^{-1}. Most interestingly, the in situ-dynamic techniques revealed that the pore generation mechanism was closely related to either the Zn/C ratio or the O/C ratio, depending on the calcination temperature.

Chapter 6 verifies the feasibility of SCs based on ZMOF-derived carbons. To the best of the author's knowledge, most of the work on SCs employed aqueous solutions as electrolytes in evaluating electrochemical performance. However, in most cases, non-aqueous solutions have been commonly used for the commercial SC cells, as they withstand a wider voltage window than aqueous solutions. Thus, the electrochemical performance with an aqueous solution (H_2SO_4) was fundamentally evaluated at first through the three-electrode system. Then, the symmetrical SC cells with non-aqueous solutions (tetraethylammonium tetrafluoroborate ($TEABF_4$) in propylene carbonate (PC)) were assembled to evaluate the feasibility of the electrode materials under study.

Contents

1 Introduction

1.1 Progress in porous carbons

1.1.1 Background

Excessive industrialization and human activities have generated greenhouse gases and recent climate changes. Mass production has generated some pollutants like volatile organic compounds (VOC), carbon dioxide (CO_2), and sulfur dioxide (SO_2), which have damaged the atmosphere and threatened human health. Chemical or industrial compounds have polluted the existing water sources, worsening matters. Thus, environmental and energy issues have become non-negligible concerns for the past few decades. Researchers from different scientific fields have been trying to overcome these severe issues.

Porous carbons are expected to cast a light upon the issues mentioned above, as they can be used as gas/contaminants absorbers, water purifiers, fuel cell (FC) catalysts for oxygen reduction reaction (ORR), and electrode materials in lithium-ion batteries (LIBs) and supercapacitors (SCs) [1.1–1.5], owing to their high surface area (Figure 1.1). The above applications could provide some environmental contributions. Furthermore, porous carbons have excellent thermal, chemical, and electrochemical stabilities and good electrical conductivity. Thus, significant attention has been paid to porous carbons so far.

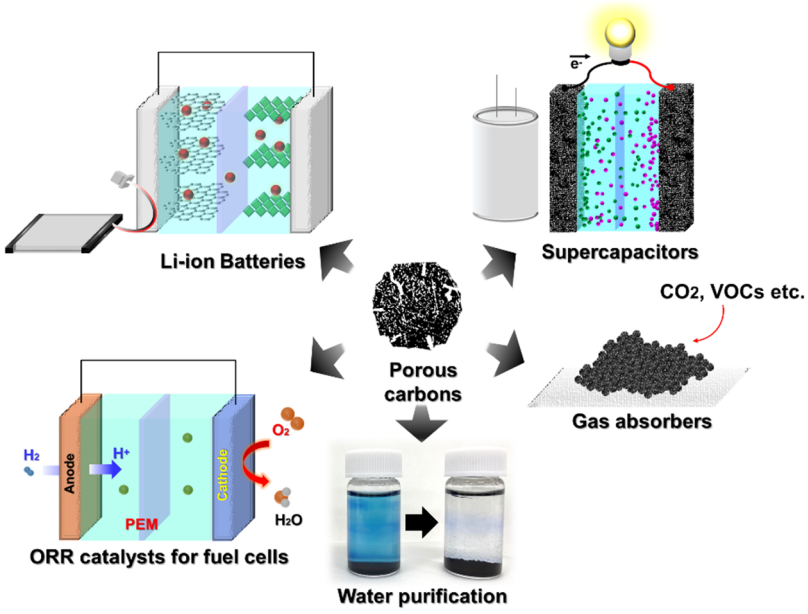

Figure 1.1 Schematic of the application of porous carbons.

1.1.2 Activated carbons

Activated carbon has been commonly used as absorbents and SCs electrode materials, which have extremely small pores for electrolyte ions to access smoothly. These tiny pores are called micropores (~2 nm) and mesopores (2–50 nm), defined by IUPAC. Activated carbons are produced by carbonizing biomass materials, followed by the activation process roughly classified into physical and chemical activation [1.6], as shown in Figure 1.2.

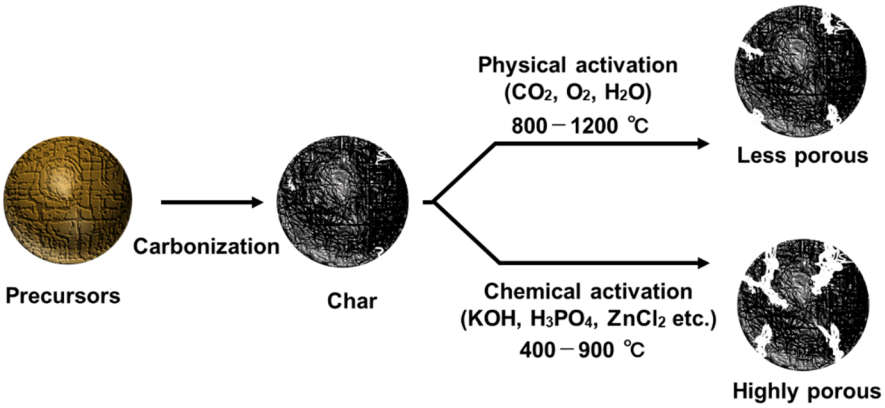

Figure 1.2 Schematic of the preparation of activated carbons.

Physical activation involves the carbonization process (pyrolysis) under inert gas atmosphere and the subsequent activation at 800–1200 °C under oxidizing agents, such as water (H_2O)-steam, CO_2, and oxygen (O_2) to produce micro-mesopores. The O_2 activation process can be considered more economical due to the endothermic reaction than the other activations in terms of energy efficiency. However, this method suffers from pore control and unstable yield due to intensive combustion by O_2 oxidation. In the activation processes, active edge sites of carbon atoms react with active agents like H_2O, CO_2, and O_2 to gaseous carbon monoxide (CO) or CO_2, as expressed in the following equation [1.7].

$$2C + O_2 = 2CO, \qquad \Delta H = -221 \ \text{kJ mol}^{-1} \tag{1.1}$$

$$2CO + O_2 = 2CO_2, \qquad \Delta H = -556 \ \text{kJ mol}^{-1} \tag{1.2}$$

$$C + H_2O = CO + H_2, \qquad \Delta H = 117 \ \text{kJ mol}^{-1} \tag{1.3}$$

$$C + CO_2 = 2CO, \qquad \Delta H = 159 \ \text{kJ mol}^{-1} \tag{1.4}$$

$$CO + H_2O = CO_2 + H_2, \qquad \Delta H = 41 \ \text{kJ mol}^{-1} \tag{1.5}$$

Physical activation requires a long activation time and high energy consumption. Thus, these issues were improved through chemical activation. It requires some chemical agents such as, potassium hydroxide (KOH) [1.8], sodium hydroxide (NaOH) [1.9], calcium chloride ($CaCl_2$) [1.10], potassium carbonate (K_2CO_3) [1.11], phosphoric acid (H_3PO_4) [1.12], sulfuric acid (H_2SO_4) [1.13], and zinc chloride ($ZnCl_2$) [1.14]. The carbon precursor is prepared by first saturating the raw material in oxidizing and highly dehydrated chemicals and heating at a temperature ranging from 400 to 900 °C to provide high porosity. Subsequently, the resultant carbon is washed repeatedly to recover pure activated carbons. Chemical activation achieves a higher surface area of up to 4200 $m^2\ g^{-1}$ [1.15] and higher yields than physical activation. Among several chemical agents, KOH is the most common activating agent. KOH's activation processes are roughly divided into the following equations [1.7, 1.8].

$$6KOH + 2C = 2K + 3H_2 + 2K_2CO_3 \tag{1.6}$$

$$K_2CO_3 + C = K_2O + 2CO \tag{1.7}$$

$$K_2CO_3 = K_2O + CO_2 \tag{1.8}$$

$$C + CO_2 = 2CO \tag{1.9}$$

$$2K + CO_2 = K_2O + CO \tag{1.10}$$

KOH oxidizes carbons at 400 °C, generating metallic K, H_2, and K_2O_3, followed by the reaction between C and K_2CO_3 above 700 °C. In addition to the chemical etching by KOH and K_2O_3, the resultant gases like CO, CO_2, and H_2 can act as activating agents. Further, the intercalation of the metallic K into the carbon matrix can successfully provide many micropores. However, chemical activations require repeated water treatment to remove the remaining chemical agents from the resulting carbons. The first water treatment generated wastewater, requiring a secondary treatment process.

1.1.3 Templated carbons

To realize the precise pore control, templates for synthesizing porous carbons have been developed to substitute for the traditional activation method [1.16, 1.17]. The method is roughly divided into hard-template and soft-template methods, as shown in Figure 1.3. Silica materials [1.18], zeolite [1.19–1.22], or metal oxides (ZnO, MgO, and $CaCO_3$) [1.14, 1.23, 1.24], and a surfactant, polymer, and biopolymer have been employed as hard-templating and soft-templating agents, respectively. In these methods, carbon precursors are incorporated into the pores of the templating agents (hard-template method) or coassembled with templating agents (soft-template method). Subsequently, carbon precursors with templating agents are carbonized, followed by the acid treatment to remove templating agents and obtain porous carbons. Consequently, the template methods enable the resulting pore size or pore structure to be tunable to some extent.

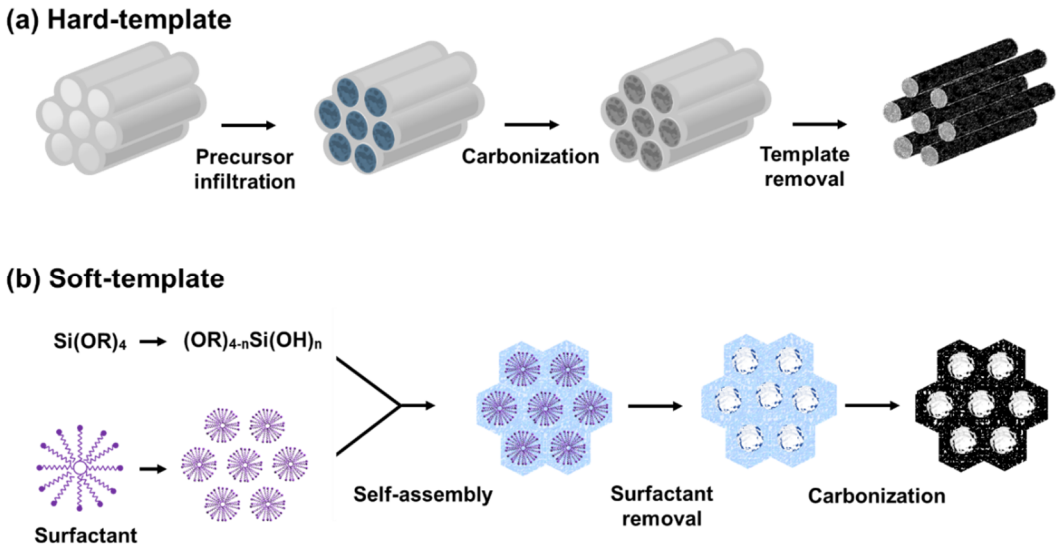

Figure 1.3 Schematic of the synthesis of mesoporous carbons through (a) hard-template method and (b) soft-template method.

However, in these traditional templates, the use of corrosive products, such as hydrofluoric acid (HF) or hydrochloric acid (HCl), is unavoidable to remove the templates from the resulting carbons. For this reason, an additional water treatment process is required to dilute the resultant hazardous wastewater. To this end, the author developed the facile processes of producing porous carbons from metal oxides template carbons in chapter 4 and 5.

1.1.4 Metal-organic frameworks (MOFs)-derived carbons

Many researchers have employed metal-organic frameworks (MOFs) as carbon precursors for porous carbons [1.25]. MOFs are composed of metal ions/clusters and organic ligands, forming one-, two-, or three-dimensional porous crystalline materials [1.26]. Direct carbonization of MOFs provides multi-functional carbons, such as highly porous carbons, heteroatom-doped carbons, and metal/carbon composites, as shown in Figure 1.4 [1.25]. Considerable combinations of metal ions and organic ligands can provide such versatile carbon materials. Particle size can be controlled by adjusting several synthetic conditions, such as PH, temperatures, concentration, and reaction rate [1.27]. Furthermore, heating conditions also affect the properties of the resulting carbons. Therefore, carbon nanoparticles can be intentionally designed depending on synthetic and heating conditions. Yamauchi et al. reported unique MOFs-derived carbon nanoparticles, which indicated good electrochemical performance [1.28, 1.29].

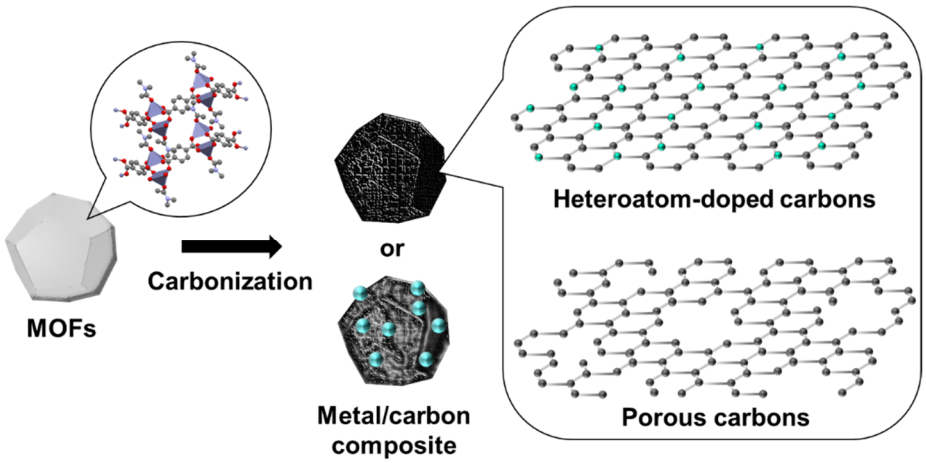

Figure 1.4 Schematic of the synthetic route for multi-functional carbons. The above unit cell structure of MOF ([Zn(BDC)(DMA)]) was taken from the literature [1.30].

1.1.5 Covalent-organic frameworks (COFs)-derived carbons

Covalent organic frameworks (COFs) have been employed as carbon precursors [1.31, 1.32]. COFs have emerged as a new class of porous materials, constructed from organic building units to form a two- dimensional (2D) or three-dimensional (3D) polymer network with a

precise porous structure based on covalent bonds [1.33–1.37] (Figure 1.5). Conventional polymerizations are based on irreversible reactions, which form covalent bonds [1.38]. Meanwhile, COFs have attracted considerable attention owing to their reversible reaction system, which allows linked organic polymers to repeat their reunion/separation reversibly until they form a stable structure, resulting in high porosity and crystallinity. The COFs' covalent bonds enable high electrochemical durability and high resistance to acids or bases compared to the coordination bonds of MOFs [1.37]. COFs introduce new redox functional groups [1.37]. Notably, as is the case in MOFs, direct carbonization of COFs provides heteroatom-doped carbons because COF structures contain various atoms, such as boron, nitrogen, and oxygen, in addition to carbon [1.39–1.44]. Further, graphitized carbons can be produced through the carbonization of COFs with π–conjugated structures [1.37, 1.45]. Umezawa et al. reported boron (B)-doped porous carbons derived from a B-based COF (COF-5) [1.32]. The obtained carbon materials exhibited a higher charge density than the other commercial activated carbons. More detail can be found in chapter 4.

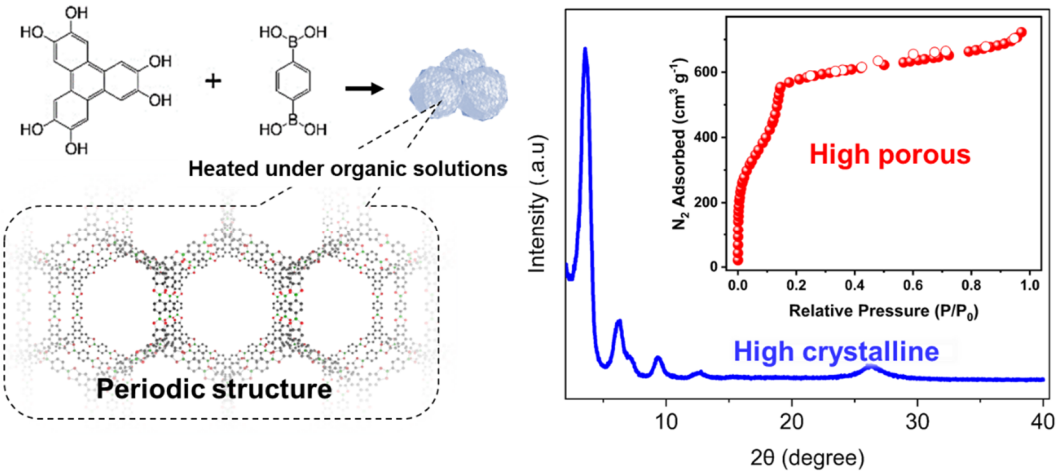

Figure 1.5 Schematic of the synthesis of COF-5 and their PXRD pattern and nitrogen adsorption/desorption isotherm.

1.2 Porous carbon materials for supercapacitor electrodes

1.2.1 Background

As mentioned above, anthropogenic activities have caused massive environmental pollution and consumption of fossil fuels, which are responsible for recent climate changes. Even in this challenging time, human beings cannot avoid consuming energy resources to maintain the minimum living standards. The development of energy storage such as secondary batteries has successfully reduced the frequency of consuming fossil fuels. However, the vital issues still have not been improved solely through the development of energy storage; more use of alternative energy resources is required than ever before. Thus, there has been a substantial demand for technological advancement in renewable energy systems, such as solar, tidal, geothermal, and wind energy [1.46]. Many scientists and engineers from different scientific fields have intensely tackled these issues. Particularly among many scientific fields, renewable energy resources are expected to give some solutions toward the non-use of fossil fuels. The use of renewable energy resources has faced fluctuation issues; power supplies from renewable energy largely depend on the climate. Therefore, SCs have been paid attention to by many researchers for their high-power density, which enables to level out such high-powered power supplies efficiently.

1.2.2 Supercapacitors

SCs can provide an extremely high power density (~10 kW kg^{-1}) than that of batteries such as LIBs (~300W kg^{-1}) [1.47]. This is attributed to the charging/discharging mechanism in SCs, which physically absorb/desorb electrolyte ions onto/from the porous electrode surface (see Figure 1.6), leading to a non-faradic current without any chemical reaction (faradic process). The adsorption of electrolyte ions induces an electric double-layer (EDL) capacitor between the electrode surface and electrolyte ions [1.48], as shown in Figure 1.6. SC electrode materials require high porosity on their surface to accumulate many electrolyte ions for high capacity. Thus, various kinds of porous carbons have been proposed as SC electrode materials, as mentioned in the previous section [1.48]. Besides, SCs achieve long

cycling durability (>500,000 cycles) compared with LIBs (about 1000 cycles) [1.49], as they do not involve any chemical reactions in charging/discharging. Due to their excellent properties such as high power density and long cycle durability, SCs are expected to level out the power supplies from wind energy and be used as energy storage devices for the energy regenerating system. However, SCs have suffered from limited energy density (~10 Wh kg^{-1}), which is lower than that of batteries (~200 Wh kg^{-1} for LIBs) [1.47].

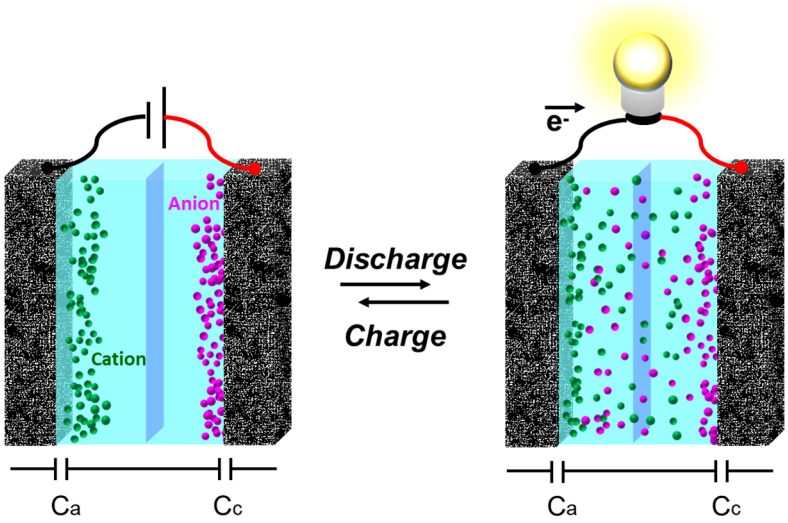

Figure 1.6 Schematic illustration of the storage mechanism of the electric double-layer capacitor

The energy density (E, Wh kg^{-1}) is determined by the following equation [1.47, 1.50]:

$$E = \frac{1}{2}CV^2 \tag{1.11}$$

$$\frac{1}{C} = \frac{1}{C_a} + \frac{1}{C_c} \tag{1.12}$$

where C and V represent the specific EDL capacitance and the voltage window, respectively. C_a and C_c represent the EDL capacitance based on the adsorption of the anions and cations,

respectively. To increase the energy density, higher capacitance and wider voltage windows are required, according to the above equation (1.11). The specific capacitance on a single electrode is determined by the following equation [1.47]:

$$C = \varepsilon_r \varepsilon_0 \frac{S}{d} \tag{1.13}$$

where, ε_r, ε_0, S, and d represent relative permittivity, vacuum permittivity, electrode surface area available to electrolyte ions, and EDL effective thickness, respectively.

Among these parameters, increasing S has been a common method to enhance the specific capacitance. However, this method has limitations. An extremely high surface area is composed of many tiny pores. The electrode materials with smaller pores could hamper electrolyte ions' smooth access. In contrast, the electrode materials having larger pores ease the transportation of electrolyte ions, leading to high power density. However, larger pores decrease the surface area available to electrolyte ions. Therefore, the relationship between pores and ions in their size determines the suitable surface area for high capacitance. The electrochemical performance of three kinds of porous carbons, YP50F (coconut shell origin, physical activation with H_2O-steam, Kuraray Chemical Co. Ltd., Osaka, Amagasaki, Japan) and MSP20 (phenol resin origin, chemical activation with KOH, Kansai Coke and Chemicals, Japan), and CNovel (MJ (4)030-00, MgO-templated carbons, TOYO TANSO Co. Ltd., Osaka, Japan), were evaluated to investigate the relationship between pore size and the specific capacitance. More details can be found in chapter 2.

Many researchers have proposed pseudo-capacitors to achieve a significantly higher capacitance (~2200 F g^{-1}) than EDL capacitance [1.51]. Pseudo-capacitances are based on three different mechanisms: (a) faradic redox reaction, (b) electrosorption, or (c) intercalation processes on electrode surfaces, as shown in Figure 1.7. A few transitional metal oxides, conducting polymers, and heteroatom-doped carbon materials are promising

candidates for pseudo-capacitive electrode materials. Most pseudo-capacitive behaviors occur within the narrow potential windows (~100–130 mV) [1.52]. Therefore, ruthenium oxides (RuO_2) or manganese oxides (MnO_2) were traditionally used as pseudo-capacitive electrode materials, as Ru or Mn can exhibit the multiple valence state changes during charging/discharging, which can induce pseudo-capacitive behavior in a wider voltage window. However, pseudo-capacitor electrodes suffer from poor power density and cycle durability compared with normal SCs. Improvements in the disadvantages have been earnestly desired.

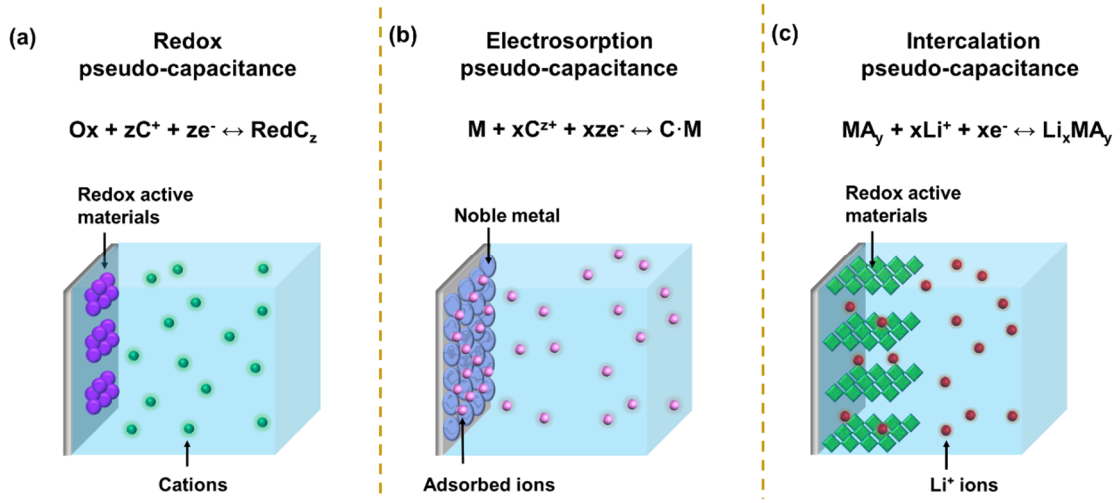

Figure 1.7 Schematic illustration of pseudo-capacitive charge storage based on (a) redox reactions, (b) electrosorption, and (c) intercalations.

Heteroatom-doped carbons and conducting polymers can exhibit pseudo-capacitive effects because they act as an electron acceptor or donor and attract anions or cations toward the electrode surface. To realize this, Umezawa et al. attempted to synthesize porous carbons with high charge density by introducing boron atoms (B) in the carbons. They gave detailed analyses of B-doped carbons in chapter 4. Apart from EDL capacitors and pseudo-capacitors, hybrid-capacitors have been studied. The hybrid capacitor comprises an EDL capacitive electrode at one end and a battery electrode at the other end. This doctoral thesis does not deal with the hybrid capacitor.

In addition to the EDL capacitance (C), a wider voltage window can also increase energy density (E) according to the equation (1.11). V is determined by the withstand voltage of electrolytes, solvents in electrolyte solutions, or electrode materials. The modification of carbon surfaces or electrolyte solutions attained a wider voltage window [1.53]. V depends on the oxidizability or reducibility of electrolyte solutions or electrode materials and the work function [1.54]. In most works, SC performances have been evaluated using aqueous electrolytes such as H_2SO_4, KOH, and NaCl. Aqueous solutions suffer from a narrow voltage window as they are electrolyzed at ~1.23 V, based on the electrochemical theory. However, non-aqueous solutions attain a higher voltage window of ~2.7 V, leading to higher energy density than aqueous solutions. However, to the best of the author's knowledge, most works on SC electrode materials have employed aqueous solutions rather than non-aqueous solutions. One conceivable reason for this is that it is easier to evaluate the electrochemical performance using aqueous solutions than non-aqueous solutions, which do not allow even a lower oxygen concentration in assembling SCs. Besides, in the case of aqueous solutions, redox reactions are likely to be induced depending on the used electrode materials, resulting in high specific capacitance. However, non-aqueous solutions have been commonly used for commercial SCs to apply for high-voltage operations. Thus, the electrochemical performance should be fundamentally evaluated at first through the three-electrode system with aqueous solutions. Then, the symmetrical SC cell should be assembled using non-aqueous solutions to confirm the feasibility of the electrode materials under study.

1.3 Objective of the study

This study aims to prepare multi-functional carbons for supercapacitor (SC) electrodes. The thesis is divided into six chapters as follows:

Chapter 1 summarizes the history of multi-functional carbons and SCs.

Chapter 2 discusses the electrochemical properties of SC electrodes experimentally and analytically to promote a better understanding. In the first part, the author evaluated the electrochemical properties of SCs based on the three kinds of commercial porous carbon materials; YP50F, MSP20, and CNovel, which are prepared by physical activation, chemical activation, and templating method, respectively. The relationship between the pore size and the electrochemical performance was investigated. Both aqueous and non-aqueous solutions were used to elaborately analyze the difference between the two kinds of electrolytes in the electrochemical properties. In the second part, the author introduced simulation models to analyze and evaluate experimental data. These findings contribute to the subsequent discussion.

Chapter 3 reveals that direct carbonization of COF-derived carbons results in multi-functional carbon materials. The author verifies that carbon particle size can be controlled depending on the synthetic conditions, which could determine the morphology of the resultant carbons. ICOFs were employed as carbon precursors. Interestingly, the particle size was found to affect the S_{BET} of the resultant carbons. Besides, nitrogen-doped carbons were successfully prepared by carbonization of the ICOFs (CICOFs). Finally, electrochemical properties were investigated using CICOFs as SC electrode materials.

Chapter 4 reports the unique acid-free process of producing template porous carbons. Several syntheses of porous carbon materials have suffered from individual disadvantages, as mentioned in 1.1. Templated methods are fascinating processes for pore control. However, most of these methods require corrosive products, such as HF or HCl. Therefore, the author attempted to develop a unique acid-free process of producing template porous carbons using B_2O_3 [1, 32]. B_2O_3 is dissolved well in water compared to the other metal oxides. B_2O_3-templating carbon was prepared by carbonization of B-based carbon source at 1000 °C.

Subsequently, porous carbon was obtained by removing B_2O_3. Furthermore, the obtained porous carbon was found to be B-doped material. The author provides detailed analyses of the obtained carbons in this chapter.

Chapter 5 reports zinc (Zn)-activating carbons and the Zn dynamic behavior during carbonization. Direct carbonization of ZMOFs can result in highly porous carbons because Zn sublimes at high temperatures (above 900 °C). This procedure is a single calcination step for highly porous carbon materials. Thus, it is essential to clarify the mechanism underlying pore generation. Umezawa et al. revealed that the pore generation mechanism was closely related to either the precursors' Zn/C or O/C ratio, depending on the calcination temperature [1.55].

Chapter 6 describes the electrochemical properties of high porous carbons based on Z MOFs. First, the electrochemical properties were fundamentally evaluated using an aqueous solution (H_2SO_4) according to the results obtained in chapter 2. Second, the electrochemical performance was investigated using a non-aqueous solution ($TEABF_4$) to confirm whether SC cells based on electrodes using ZMOFs-derived carbons are feasible. Here except for the basic electrochemical properties, such as specific capacitances, electrical conductivity, and rate performances, cycling, and thermal durability were elaborately investigated.

1.4 References

[1.1] K. Xia, Q. Gao, W. Li, X. Guo, J. Jiang, J. Hu, "Hierarchical porous carbons with controlled micropores and mesopores for supercapacitor electrode materials." Carbon **46**, 1718–1726 (2008).

[1.2] H. Liu, X. Liu, W. Li, X. Guo, Y. Wang, G. Wang, D. Zhao, "Porous carbon composites for next generation rechargeable lithium batteries." Adv. Energy Mater. **7**, 1700283 (2017).

[1.3] B. Xu, H. Zhang, H. Mei, D. Sun, "Recent progress in metal–organic framework-based supercapacitor electrode materials." Coord. Chem. Rev. **420**, 213438 (2020).

[1.4 Z. Yang, H. Nie, X. Chen, X. Chen, S. Huang, "Recent progress in doped carbon nanomaterials as effective cathode catalysts for fuel cell oxygen reduction reaction." J. Power Sources. **236**, 238–249 (2013).

[1.5] R. Gusain, N. Kumar, S. S. Ray, "Recent advances in carbon nanomaterial-based adsorbents for water purification." Cood.Chem. Rev. **405**, 213111 (2020).

[1.6] Z. Heidarinejad, M.H. Dehghani, M. Heidari, G. Javedan, I. Ali, M. Sillanpaa, "Methods for preparation and activation of activated carbon: a review." Environ. Chem. Lett. **18**, 393–415 (2020).

[1.7] X.-L. Zhou, H. Zhang, L.-M. Shao, F. Lu, P.-J. He, "Preparation and application of hierarchical porous carbon materials from waste and biomass: A review." Waste Biomass Valorization. **12**, 1699–1724 (2021).

[1.8] J. Wang, S. Kaskel, "KOH activation of carbon-based materials for energy storage." J. Mater. Chem. **22**, 23710 (2012).

[1.9] M. A. Islam, M. J. Ahmed, W. A. Khanday, M. Asif, B. H. Hameed, "Mesoporous activated carbon prepared from NaOH activation of rattan (Lacosperma secundiflorum) hydrochar for methylene blue removal." Ecotoxicol. Environ. Saf. **138**, 279–285 (2017).

[1.10] G. Yuan, K. Guan, H. Hu, B. Lei, Y. Xiao, H. Dong, Y. Liang, Y. Liu, M. Zheng, "Calucium-chloride-assisted approach toward green and sustainable synthesis of hierarchical porous carbon microspheres for high-performance supercapacitive energy storage." J. Colloid Interface Sci. **582**, 159–166 (2021).

[1.11] M.-J. Kim, S. W. Choi, H. Kim, S. Mun, K. B. Lee, “Simple Synthesis of spent coffee ground-based microporous carbons using K_2O_3 as an activation agent and their application to CO_2 capture.” Chem. Eng. J. **397**, 125404 (2020).

[1.12] D. N. K. P. Negra, T. G. T. Nindhia, I. W. Surata, F. Hidajat, M. Sucipta, “Textural characteristics of activated carbons derived from tabah bamboo manufactured by using H_3PO_4 chemical activation.” Mater. Today. **22**, 148–155 (2020).

[1.13] A. H. Jawad, R. Razuan, J. N. Appaturi, L. D. Wilson, “Adsorption and mechanism study for methyklene blue dye removal with carbonized watermelon (Citrullus lanatus) rind prepared via one-step liquid phase H_2SO_4 activation.” Surf. Interfaces. **16**, 76–84 (2019).

[1.14] L. Qin, Z. Xiao, S. Zhai, S. wang, H. Wang, G. Wang, W. Cai, Z. Li, Q. An, “Alginate-derived porous carbon obtained by nano-ZnO hard template-induced ZnCl2-activation method for enhanced electrochemical performance.” J. Electrochem. Soc. **167**, 040505 (2020).

[1.15] A. S. Jalilov, Y. Li, J. Tian, J. M. Tour, “Ultra-high surface area activated porous asphalt for CO_2 capture through competitive adsorption at high pressures.” Adv. Energy Mater. **7**, 1600963 (2017).

[1.16] L. Xie, Z. Jin, Z. Dai, Y. Chang, X. Jiang, H. Wang, “Porous carbons synthesized by templating approach from fluid precursors and their applications in environment and energy storage: A review.” Carbon. **170**, 100–118 (2020).

[1.17] N. Diez, M. Sevilla, A. B. Fuertes, “Synthesis strategies of template porous carbons beyond the silica nanocasting technique.” Carbon. **178**, 451–476 (2021).

[1.18] M. Elma, E. L. A. Rampun, A. Rahma, Z. L. Assyaifi, A, Sumardi, A. E. Lestari, G. S. Saputro, M. R. Bilad, A. Darmawan, “Carbon template strategies of mesoporous silica applied for water desalination: A review.” J. Water. Process. Eng. **38**, 101520 (2020).

[1.19] T. Kyotani, Z. Ma, A. Tomita, “Template synthesis of novel porous carbons using various types of zeolites.” Carbon. **41,** 1451–1459 (2003).

[1.20] P. Boonyoung, T. Kasukabe, Y. Hoshikawa, Á. Berenguer-Murcia, D. Cazorla-Amorós, B. Boekfa, H. Nishihara, T. Kyotani, K. Nueangnoraj, “A simple ‘nano-templating’ method using zeolite Y toward the formation of carbon schwarzites.”Front. Mater. **6,** 1–9 (2019).

[1.21] N.P. Stadie, S. Wang, K.V. Kravchyk, M.V. Kovalenko, “Zeolite-templated carbon as an ordered microporous electrode for aluminum batteries.” ACS Nano. **11,** 1911–1919 (2017).

[1.22] R.J. Dubey, T. Colijn, M. Aebli, E.E. Hanson, R. Widmer, K.V. Kravchyk, M.V. Kovalenko, N.P. Stadie, “Zeolite-templated carbon as a stable, high power magnesium-ion cathode material.” A.C.S. Appl. Mater. Interfaces **11**, 39902–39909 (2019).

[1.23] A. Kamiyama, K. Kubota, D. Igarashi, Y. Youn, Y. Tateyama, H. Ando, K. Gotoh, S. Komaba, “MgO-template synthesis of extremely high capacity hard carbon for Na-ion battery.” Angew. Chem. Int. Ed. **60**, 5114–5120 (2021).

[1.24] Y. Yang, Y. Yan, B. Ren, C. Fan, Y. Liu, Q. Deng, L. Zhong, C. You, Y. Xu, R. Yang, “Modified nano-$CaCO_3$ hard template method for hierarchical porous carbon powder with enhanced electrochemical performance in lithium-sulfur battery.” Adv Powder Technol. **32**, 3574–3584 (2021).

[1.25] L. Wang, Y. Han, X. Feng, J. Zhou, P. Qi, B. Wang, “Metal-organic frameworks for energy storage: Batteries and supercapacitors.” Coord. Chem. Rev. **307**, 361–381 (2016).

[1.26] A. Schoedel, Z. Ji, O. M. Yaghi, “The role of metal-organic frameworks in a carbon-neutral energy cycle.” Nat. Energy **1**, 16034 (2016).

[1.27] N. Stock, S. Biswas, “Synthesis of metal-organic frameworks (MOFs): Routes to various MOF topologies, and composites” Chem. Rev. **112**, 993 (2012).

[1.28] N. L. Torad, M. Hu, Y. Kamachi, K. Takai, M. Imura, M. Naito, Y. Yamauchi, “Facile synthesis of nanoporous carbons with controlled particle sizes by direct carbonization of monodispersed ZIF-8 crystals.”Chem. Commun. **49**, 2521 (2013).

[1.29] R. R. Salunkhe, C. Young, J. Tang, T. Takei, Y. Ide, N. Kobayashi, Y. Yamauchi, “A high-performance supercapacitor cell based on ZIF-8-derived nanoporous carbon using an organic electrolyte.” Chem. Commun. **26**, (2016).

[1.30] F.-K. Wang, S.-Y. Yang, R.-B. Huang, L.-S. Zheng, S. R. Batten “Control of the topologies and packing modes of three 2D coordination polymers through variation of the solvent ratio of a binary solvent mixture.” Cryst. Eng. Comm. **10**, 1211 (2008).

[1.31] X. Zhang, G. Zhu, M. Wang, J. Li, T. Lu, L. Pan, “Covalent-organic frameworks derived N-doped porous carbon materials as anode for superior long-life cycling lithium and sodium ion

batteries.” Carbon. **116**, 686–694 (2017).

[1.32] S. Umezawa, T. Douura, Y. Yoshikawa, Y. Takashima, M. Yoneda, K. Gotoh, V. Stolojan, S. R. P. Silva, Y. Hayashi, D. Tanaka, “Supercapacitor electrode with high charge density based on boron-doped carbon derived from covalent organic frameworks.” Carbon. **184**, 418–425 (2021).

[1.33] A.P. Côté, A.I. Benin, N.W. Ockwig, M. O’Keeffe, A.J. Matzger, O.M. Yaghi, Porous, crystalline, covalent organic frameworks, Science **310**, 1166–1170 (2005).

[1.34] N. Zhang, A. Ishag, Y. Li, H. Wang, H. Guo, P. Mei, Q. Meng, Y. Sun, Recent investigations and progress in environmental remediation by using covalent organic framework-based adsorption method: A review, J. Cleaner Prod. **277**, 123360 (2020).

[1.35] X. Li, C. Yang, B. Sun, S. Cai, Z. Chen, Y. Lv, J. Zhang, Y. Liu, Expeditious synthesis of covalent organic frameworks: A review, J. Mater. Chem. A **8**, 16045–16060 (2020).

[1.36] H.L. Qian, C.X. Yang, W.L. Wang, C. Yang, X.P. Yan, Advances in covalent organic frameworks in separation science, J. Chromatogr. A **1542**, 1–18 (2018).

[1.37] J. Kim, J.H. Kim, K. Ariga, Redox-active polymers for energy storage Nanoarchitectonics, Joule. **4**, 739–768 (2017).

[1.38] F. Haase, B. V. Lotsh, Solving the COF trilemma: towards crystalline, stable and functional covalent organic frameworks, Chem. Soc. Rev. **49**, 8469–8500 (2020).

[1.39] X. Zhang, G. Zhu, M. Wang, J. Li, T. Lu, L. Pan, Covalent-organic-frameworks derived N-doped porous carbon materials as anode for superior long-life cycling lithium and sodium ion batteries, Carbon **116**, 686–694 (2017).

[1.40] Y.-B. Huang, P. Pachfule, J.-K. Sun, Q. Xu, From covalent–organic frameworks to hierarchically porous B-doped carbons: A molten-salt approach, J. Mater. Chem. A **4**, 4273–4279 (2016).

[1.41] Y. Li, X. Xu, S. Hou, J. Ma, T. Lu, J. Wang, Y. Yao, L. Pan, Facile dual doping strategy via carbonization of covalent organic frameworks to prepare hierarchically porous carbon spheres for membrane capacitive deionization, Chem. Commun. **54**, 14009–14012 (2018).

[1.42] C. Young, R. R. Salunkhe, J. Tang, C.-C. Hu, M. Shahabuddin, E. Yanmaz, M. S. A. Hossain, J. H. Kim, Y. Yamauchi, Zeolitic imidazolate framework (XIF-8) derived nanoporous

carbon: the effect of carbonization temperature on the supercapacitor performance in an aqueous electrolyte, Phys. Chem. Chem. Phys **18**, 29308–29315 (2016).

[1.43] P. Liang, C. Zhang, H. Hun, S. Liu, M. Tabe, S. Wang, Photocatalysis of C, N-doped ZnO derived from ZIF-8 for dye degradation and water oxidation, RSC Adv. **6**, 95903–95909 (2016).

[1.44] J. Zou, P. Liu, L. Huang, Q. Zhang, T. Lan, S. Zeng, X. Zeng, L. Yu, S. Liu, H. Wu, W. Tu, Y. Yao, Ultrahigh-content nitrogen-decorated nanoporous carbon derived from metal organic frameworks and its application in supercapacitors, Electrochim. Acta. **271**, 599–608 (2018).

[1.45] F. Xu, D. Wu, R. Fu, B. Wei, Design and preparation of porous carbons from conjugated polymer precursors, Mater. Today. **10**, 629–656 (2017).

[1.46] M. S. Nazir, Z. M. Ali, M. Bilal, H. M. Sohai, H. M. N. Iqbal, "Environmental impacts and risk factors of renewable energy paradigm-a review." Environ. Sci. Pollut. Res. **27**, 33516–33526 (2020).

[1.47] V. Aravindan, J. Gnanaraj, Y.-S. Lee, S. Madhavi, "Insertion-type electrodes for nanaqueous Li-ion capacitors." Chem. Rev. **114**, 11619–11635 (2014).

[1.48] Y. Wamg, L. Zhang, H. Hou, W. Xu, G. Duan, S. He, K. Liu, S. Jiang, "Recent progress in carbon-based materials for supercapacitor electrodes: a review." J. Mater. Sci. **56**, 173–200 (2021).

[1.49] W. Raza, F. Ali, N. Raza, Y. Luo, K.-H. Kim, J. Yang, S. Kumar, A. Mehmood, E. E. Kwon, "Recent advancements in supercapacitor technology." Nano Energy. **52**, 441–473 (2018).

[1.50] L. Liu, Y. Yu, C. Yan, K. Li, Z. Zheng, "Wearable energy-dense and power-dense supercapacitor yarn enabled by scalable graphene-metallic textile composite electrodes." Nat. Commun. **6**, 7260 (2015).

[1.51] P.Forouzandeh, V. Kumaravel, S. C. Pillai, "Electrode materials for supercapacitors: A Review advances." Catalysts. **10**, 969 (2020).

[1.52] K. Fic, E. Frackowiak, F. Beguin, "Unusual energy enhancement in carbon-based electrochemical capacitors." J. Mater. Chem. **22**, 24213 (2012).

[1.53] W. Ye, H. Wang, J. Ning, Y. Zhong, "New types of hybrid electrolytes for supercapacitors." J. Mater. Chem. **57**, 219–232 (2021).

[1.54] J.-C. Liu, Z.-H. Huang, T.-Y. Ma, “Aqueous supercapacitor with ultrahigh voltage window beyond 2.0 Volt.” JSmall Struct. **1**, 2000020 (2020).

[1.55] S. Umezawa, T. Douura, K. Yoshikawa, D. Tanaka, V. Stolojan, S. R. P. Silva, M. Yoneda, K. Gotoh, Y. Hayashi, “Zinc-based metal-organic frameworks for high-performance supercapacitor electrodes: Mechanism underlying pore generation. Energy Environ. Mater. **1**, 2000020 (2021).

2 Fundamental evaluation of porous carbons and their electrochemical performance

2.1 Introduction

In this chapter, the electrochemical properties of SC electrodes were discussed both experimentally and analytically for a greater understanding of SCs.

To the best of the author's knowledge, most fundamental works on SC electrodes employ aqueous solutions in evaluating electrochemical properties [2.1–2.3], instead of using non-aqueous solutions. According to the electrochemical theory, aqueous solutions are known to decompose electrochemically within 1.23 V [2.4]. Meanwhile, non-aqueous solutions can withstand a wider voltage window (~3 V) than aqueous solutions [2.5]. Consequently, most commercial SCs employ non-aqueous solutions to achieve higher energy density, which is proportional to the voltage squared. The ionic conductivity, ion size, and withstanding voltage of electrolytic solutions could affect the electrochemical properties of SC electrodes. The author evaluated the electrochemical performance of three kinds of commercial porous carbons fundamentally by using a three-electrode system under an aqueous solution. Thereafter, symmetrical SC cells with non-aqueous electrolytes were assembled to examine the difference between aqueous and non-aqueous solutions in their electrochemical properties.

To obtain more detailed information on the experimental results, galvanostatic charge/discharge (GCD) and electrochemical impedance spectroscopy (EIS) curves were simulated by introducing the equivalent circuit model based on an SC cell or a porous electrode material. Through the results, the author attempted to explain the relationship between the simulated waveforms and electrochemical parameters, such as ionic conductivity, pore size, capacitance, leak current, and contact resistance, providing critical information on the experimental data.

2.2 Experimental

2.2.1 Fabrication of electrodes (for aqueous electrolytic cells)

The three kinds of porous carbon, YP50F (coconut shell origin, physical activation with steam, Kuraray Chemical Co. Ltd., Japan), MSP20 (phenol resin origin, chemical activation with KOH; Kansai Coke and Chemicals, Japan), and CNovel (MJ (4)030–00, MgO-templated carbons, TOYO TANSO, Co., Ltd., Osaka, Japan) were selected as active materials for evaluating porous carbons and SC electrode materials [2.6, 2.7]. The active material (30 mg of YP50F, MSP20, or CNovel), a conductive additive (DENKA BLACK, Denka Co. Ltd., Japan) (3.75 mg), and a poly (tetrafluoroethylene) (PTFE) binder (6-J, Chemours-Mitsui Fluoroproducts Co. Ltd., Japan) (3.75 mg) were mixed at a mass ratio of 8:1:1 and kneaded with an agate mortar and pestle until a sheet material was formed (Figure 2.1(a), (b)). Disks of 13 mm diameter were prepared by molding and compressing (60 MPa) the sheet material in a powder-compressed tablet machine (Shimadzu Corporation, Japan) (Figure 2.1(c),(d)). The working electrode was obtained by attaching the disk to a titanium (Ti) mesh current collector, which was not dissolved in H_2SO_4 (Figure 2.1(e)). The mass of the active material in each electrode disk was 37.5 mg. Although mass loading increases the total resistance of the SC electrodes, it is required for avoiding mass error and evaluating the exact capacitance.

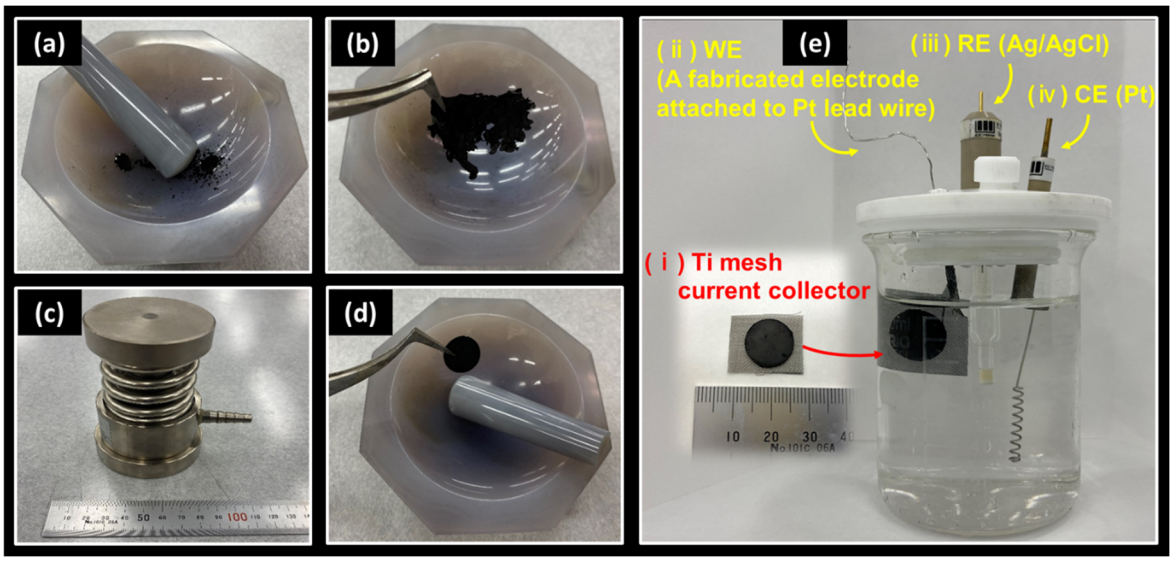

Figure 2.1 Photographs of (a) the active material, carbon black, and PTFE with a mass ratio of 8:1:1 mixed using an agate pestle; (b) Sheet material obtained by kneading in the agate mortar; (c) tableting machine used in this work; (d) obtained electrode material formed into a 13-mm disk. The mixed powder of active material, carbon black, and PTFE was kneaded with a pestle in a mortar for several minutes (a), forming a sheet-like composite material (b). Subsequently, the sheet material was cut into small pieces and transferred to the tableting machine (c) where it was compressed at 10 MPa, forming the 13-mm-diameter disk composite material (d). (e) Photograph showing the active material attached to a Ti mesh current collector, the working electrode (WE), the reference electrode (RE, Ag/AgCl), and the counter electrode (CE, Pt).

2.2.2 Fabrication of electrodes (for supercapacitor cells with non-aqueous electrolytes)

SC cells were prepared from electrode films of YP50F, MSP20, or CNovel. The films were deliberately thin to reduce the resistance, which increases with film thickness. An active material, carbon black (DENKA BLACK, Denka Company Limited, Japan), and a poly vinylidene difluoride (PVDF) binder (W#9300, Kureha Corporation, Japan) were mixed at a mass ratio of 8:1:1. The mixture was stirred in N-methyl-2-pyrrolidone (NMP; Nacalai Tesque, Inc.) for 10 min. The obtained slurry was pasted onto an etched aluminum foil and evacuated at 150 °C for 24 h to remove NMP from the carbon.

2.2.3. Material characterization

The morphology of each sample was characterized by scanning electron microscopy (SEM) (JSM-6010LA, JEOL Ltd., Japan) at an accelerating voltage of 15 kV (SE mode) and by transmission electron microscopy (TEM) (JEM-2100F, JEOL Ltd., Japan) at an accelerating voltage of 200 kV. In preparation for SEM, the powdery sample was set onto a carbon tape on an Al sample holder (10 mm (φ) × 10 mm (H)). For TEM, the sample dispersed in ethanol was poured onto a holey carbon film supported on 3 mm Cu grids, then dried at 80 °C for 1 h. The crystallinities of the resulting products were confirmed in a powder X-ray diffraction (PXRD) analysis (Smart Lab SE, Rigaku, Japan) with Cu $K\alpha_1$ (λ = 0.154 nm) radiation at a scan rate of 10° min^{-1}. The graphitization degree was investigated by Raman spectroscopy (Raman, NRS-4500NMDS, JASCO, Japan) with a 532-nm excitation laser calibrated on Si. The intensity and exposure time were 2 mW and 300 s, respectively.

Nitrogen adsorption/desorption (BEL-SORP min, Microtrac-BEL, Japan) isotherms were acquired at 77 K for the S_{BET} measurement, average pore size distribution (PSD), and information on the pore structure of each sample. Prior to the measurements, the samples were degasified by heating at 300 °C for 24 h in a vacuum. The S_{BET} of each sample was estimated from the isotherms using the BET method (P/P_0 = 0.05–0.10). The S_{meso} was estimated using the Barrett–Joyner–Halenda (BJH) method. The total pore (V_{total}), micropore (~2 nm) (V_{micro}), and mesopore (2–50 nm) (V_{meso}) volumes were calculated using the BET, MicroPore analysis method (MP), and BJH methods, respectively. The PSD was calculated using the non-local density functional theory (NLDFT).

2.2.4 Electrochemical measurements (for aqueous electrolytic cells)

The electrochemical properties of the SC electrodes based on porous carbons were measured in a three-electrode system (with reference, counter, and working electrodes of Ag/AgCl, platinum, and a porous carbon, respectively). The electrolyte solution was 1.0 M H_2SO_4 (Nacalai Tesque Inc., Japan). Prior to the measurement, the H_2SO_4 in the electrolytic cell was bubbled with N_2 gas for 30 min to remove the dissolved oxygen. Cyclic voltammetry (CV), EIS, and GCD tests were performed on a VSP-300 system (BioLogic, France). CV tests were performed in the potential window 0.2–0.8 V at 1 mV s^{-1}. EIS measurements were conducted at 0 V and a sinusoidal 5.0 mV signal over 1.0 mHz to 1.0 MHz frequency range. The equivalent circuit model was applied to the experimental EIS curves of the electrolytic cell, resulting in the calculated EIS curves. The solution resistance (R_1), contact resistance (R_2), and diffusion resistance (R_{d3}) were separated from the total cell resistance to fit the calculated curves into the experimental ones. GCD tests were performed within a 0–0.8 V potential window at several current densities (50, 100, 200, 250, 500, 1000, 2000, and 5000 mA g^{-1}). From the GCD curves, the specific capacitance was determined as

$$C_{\mathrm{g(three)}} = (I \times \Delta t)/(m \times \Delta V) \tag{2.1}$$

where $C_{\mathrm{g(three)}}$ and m are the gravimetric capacitance (F g^{-1}) and mass of the active material (g), respectively, on a single electrode, I is the discharge current (A), Δt is the discharge time (s), and ΔV is the potential window of the discharge voltage (V) [2.8–2.10]. The positive and negative electrodes were separately estimated based on the following formula [2.11]:

$$C_{+} = (I \times \Delta t_{+})/(m \times \Delta V_{+}) \tag{2.2}$$

$$C_{-} = (I \times \Delta t_{-})/(m \times \Delta V_{-}) \tag{2.3}$$

where C_+ and C_- are the positive and negative capacitances induced by the adsorption of the cations and the desorption of the anions, respectively. $\Delta t_+/\Delta V_+$ and $\Delta t_-/\Delta V_-$ denote the discharge time (s)/the potential window of the adsorption of the cations and desorption of the anions, respectively. All electrochemical tests were conducted at 25 °C, and the temperature was maintained in an incubator.

2.2.5 Electrochemical measurements (of supercapacitor cells)

The fabricated electrode was roll-pressed and punched to adjust its dimensions to that of the test cell (HS Flat Cell, Hohsen Corporation, Japan). The electrochemical test cell comprised two symmetrical electrodes divided by a cellulose separator (TF40-50, Nippon Kodoshi Corporation, Japan). The electrolyte was a 1.0 M solution of tetraethylammonium tetrafluoroborate ($TEABF_4$) in propylene carbonate (PC) (LIPASTE-P/EAF 1N, Tomiyama Pure Chemical Industries Ltd., Japan). The test cell was assembled in an argon-filled glove box under oxygen at an extremely low concentration, and the moisture was maintained below 1 ppm to prevent oxygen and moisture contamination.

The electrochemical performance was evaluated in GCD tests conducted in a symmetric two-electrode system on a VSP-300 system. The cell capacitance (F g^{-1}) was determined as

$$C_{g(two)} = (I \times \Delta t)/(m \times \Delta V) \tag{2.4}$$

where $C_{g(two)}$ is the gravimetric cell capacitance (F g^{-1}), m is the mass of the active material (g) on both positive and negative electrodes, and the other variables are as defined above. In the GCD tests, the cell voltage window was 0–2.5 V, and the current density was varied (40, 50, 100, 200, 500, 1000, 2000, 5000, and 10000 mA g^{-1}). All electrochemical tests were conducted at 25 °C, and the temperature was maintained in an incubator.

The electrochemical performances of the three carbons (YP50F, MSP20, and CNovel) were determined from Ragone plots. The energy (Wh kg^{-1}) and power density (W kg^{-1}) were respectively calculated as [2.12]

$$E = (1/2) \times (C_{g(two)} \times 1000) \times (\Delta V^2)/3600 \quad (2.5)$$

$$P = (E/\Delta t) \times 3600 \quad (2.6)$$

and $C_{g(three)}$ was computed as [2.13]

$$C_{g(three)} = 4 \times C_{g(two)} \quad (2.7)$$

The volumetric specific capacitance (F cm^{-3}) was calculated as

$$C_{U(three)} = (I \times \Delta t)/(U \times \Delta V) \quad (2.8)$$

where $C_{U(three)}$ and U are the volumetric specific capacitance (F cm^{-3}) and the volume of the electrode material (cm^3), respectively, on a single electrode. $C_{U(three)}$ was computed as

$$C_{U(three)} = 4 \times C_{U(two)} \quad (2.9)$$

The electrode bulk density (ρ, g cm^{-3}) was calculated as

$$\rho = M/U \quad (2.10)$$

where M and U are the mass of the electrode material (g) and the volume of the electrode material (cm^3), respectively on a single electrode.

2.3 Experimental results and discussion

Figure 2.3 (a), (b), and (c) show the SEM images of YP50F, MSP20, and CNovel particles, respectively. YP50F and MSP20 particles had similar morphology, whereas CNovel particles were aggregates. Figure 2.4 (a), (b), and (c) show the TEM images of YP50F, MSP20, and CNovel, respectively. Amorphous structures can be observed in all three carbon samples. Interestingly, CNovel formed circular structures in nanoscale. In producing CNovel, pores were produced by removing MgO particles from MgO-templated carbons with an acid treatment [2.7]. Consequently, pores can be considered to form such circular structures. Unlike CNovel, rough surfaces can be observed in YP50F and MSP20.

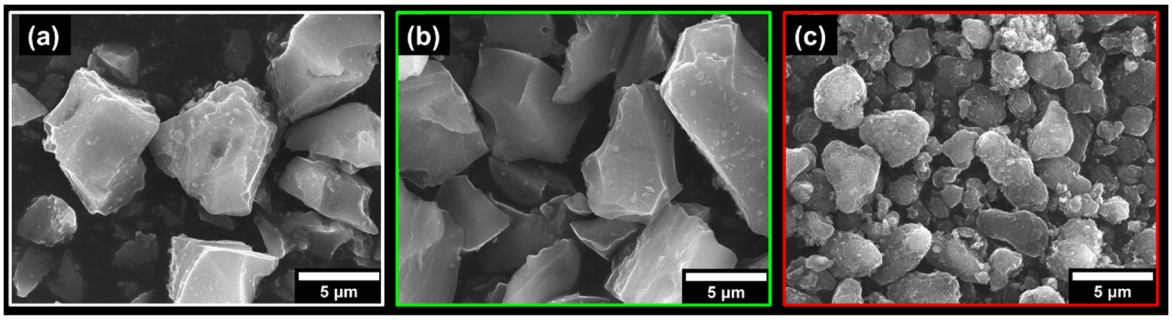

Figure 2.3 SEM images of (a) YP50F, (b) MSP20, and (c) CNovel.

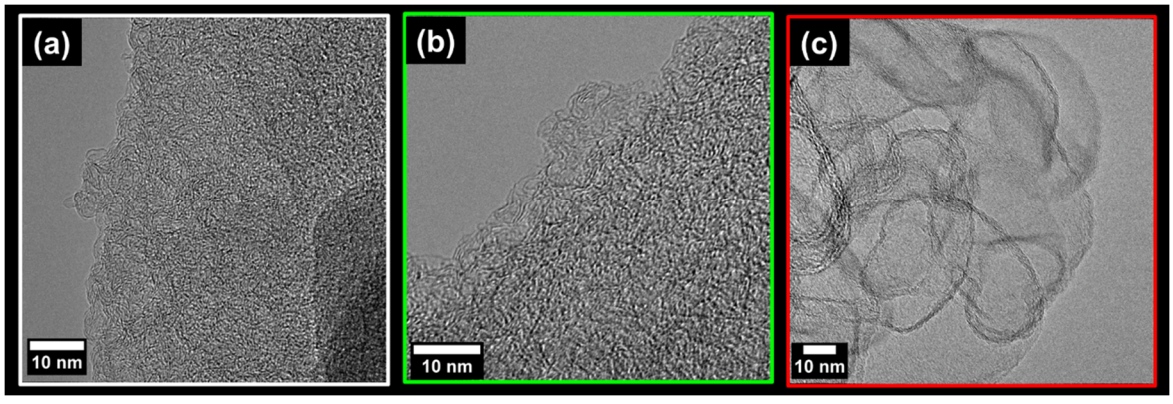

Figure 2.4 TEM images of (a) YP50F, (b) MSP20, and (c) CNovel.

These results agree with the pore characteristics of the three samples. CNovel has a much larger mesopore volume than YP50F and MSP20, as shown in Figure 2.5 and Table 2.1. Figure 2.5 (b) indicates that micropores are rich in YP50F and MSP20 compared to CNovel. Notably, KOH activation tends to provide many micropores, as discussed in chapter 1.1.2.

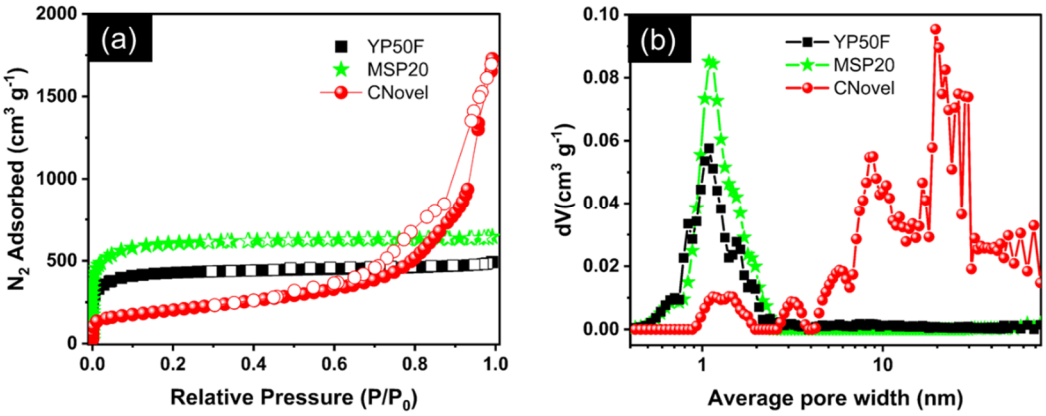

Figure 2.5 (a) Nitrogen adsorption/desorption (solid/empty symbols, respectively) isotherms and (b) Average pore size distributions (average pore width on the semi-logarithmic scale) of YP50F (black), MSP20 (fluorescent green), and CNovel (red) showing that CNovel has remarkable mesopore volumes compared to YP50F and MSP20.

Table 2.1 Pore characteristics of YP50F, MSP20, and CNovel

Sample	S_{BET} * ($m^2\ g^{-1}$)	S_{meso} *** ($m^2\ g^{-1}$)	V_{total} * ($cm^3\ g^{-1}$)	V_{micro} ** ($cm^3\ g^{-1}$)	V_{meso} *** ($cm^3\ g^{-1}$)	Average pore width ****(nm)
YP50F	1600	133	0.76	0.70	0.15	1.09
MSP20	2266	148	1.00	1.02	0.12	1.09
CNovel	709	674	2.59	-	2.54	19.6

*S_{BET} and V_{total} were calculated based on the Brunauer–Emmett–Teller (BET) method.
**V_{micro} was calculated using the MicroPore analysis (MP) method.
***S_{meso} and V_{meso} were calculated based on the Barrett–Joyner–Halenda (BJH) method.
**** Average pore widths were computed using the non-local density functional theory (NLDFT).

The Raman spectra of three carbon samples (Figure 2.6 (a)) provide the degree of carbon graphitization. The intensity ratios of the D (1350 cm^{-1}) and G (1590 cm^{-1}) bands (I_G/I_D) of three carbon samples were 0.93 (YP50F), 1.00 (MSP20), and 1.01 (CNovel), showing that all three carbons formed amorphous structures, as can be confirmed from the results of PXRD (Figure 2.6 (b)). The spectrum of all three samples contain a peak corresponding to the 2D band (2600–2800 cm^{-1}), which characterizes a few graphene layers [2.14].

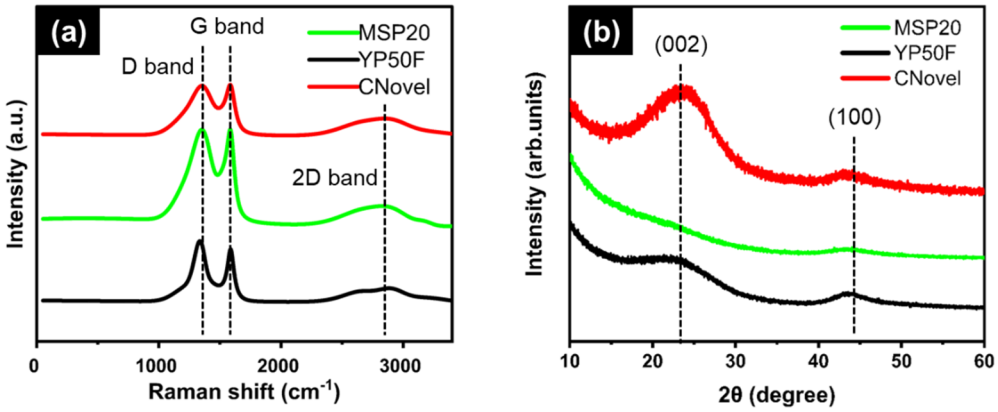

Figure2.6 Raman spectra and powder X-ray diffraction patterns of YP50F (black), MSP20 (fluorescent green), and CNovel (red), confirming the purity of the three samples and their amorphous structures.

Electrochemical properties of YP50F, MSP20, and CNovel were evaluated using aqueous electrolytes (1.0 M H_2SO_4). Figure 2.7 (a) and (b) show the GCD (at 50 mA g^{-1}) and CV (at 1 mVs^{-1}) curves of YP50F, MSP20, and CNovel, respectively, indicating typical capacitive behavior. Based on the GCD curves, the specific capacitances (F g^{-1}) of YP50F, MSP20, and CNovel were calculated to be 222, 307, and 144 F g^{-1}, respectively (Table 2.2). The result shows that the gravimetric specific capacitance is proportional to S_{BET} to some degrees. Additionally, no prominent peak was observed in the CV curves in all three samples. Thus, pseudo-capacitive effects can be ignored in the case of the three samples. Figure 2.7 (c) shows the specific capacitance at several current densities (50–5000 mA g^{-1}), confirming that CNovel maintains higher capacitance retention at high current densities than YP50F

and MSP20. This can be explained by many CNovel mesopores, which allows electrolytic ions to access the pores. The Nyquist plots of all three samples exhibit vertical lines in the low-frequency region, confirming their ideal capacitive behavior;[2.15] their frequency range was 1.0 mHz to 1.0 MHz (Figure 2.7 (d)). All three spectra contain two semicircles, which can be divided into a smaller and larger one in the high-frequency region, and indicating that resistances were introduced by the inter-particle gaps, the particle/current collector interfaces, and charge transfer [2.16]. An equivalent circuit model (Figure 2.7 (e)) was used to separate the individual resistances, such as the solution resistance (R_1), the contact resistance owing to particle gaps or the particle/current collector interface (R_2), and the diffusion resistance (R_3), from the total cell resistance. M_3 indicates the restricted linear diffusion model [2.17]. R_1, R_2, and R_3 were not different for the three carbon-based cells, whereas CNovel's diffusion time t_{d3} was much smaller than that of YP50F and MSP20, as shown in Figure 2.7 (f) and Table 2.2. This is due to abundant mesopores in CNovel, which enable electrolytic ions to smoothly access the pores deeply. On the other hand, the volumetric specific capacitance (F cm^{-3}) of CNovel was extremely smaller than that of other activated carbons (YP50F and MSP20), as shown in Table2.3. This is owing to the large mesopore volume of CNovel, leading to the lower electrode bulk density (Table 2.3).

Table 2.2 Calculated values of the resistance, capacitance, and diffusion time by fitting the equivalent circuit model to the experimental EIS data.

Sample	R_1 (Ohm)	C_2 (F)	R_2 (Ohm)	R_{d3} (Ohm)	t_{d3} (s)
YP50F	0.584	0.042	0.204	5.15	16.4
MSP20	0.444	0.004	0.279	3.97	18.7
CNovel	0.400	0.005	0.217	2.69	6.85

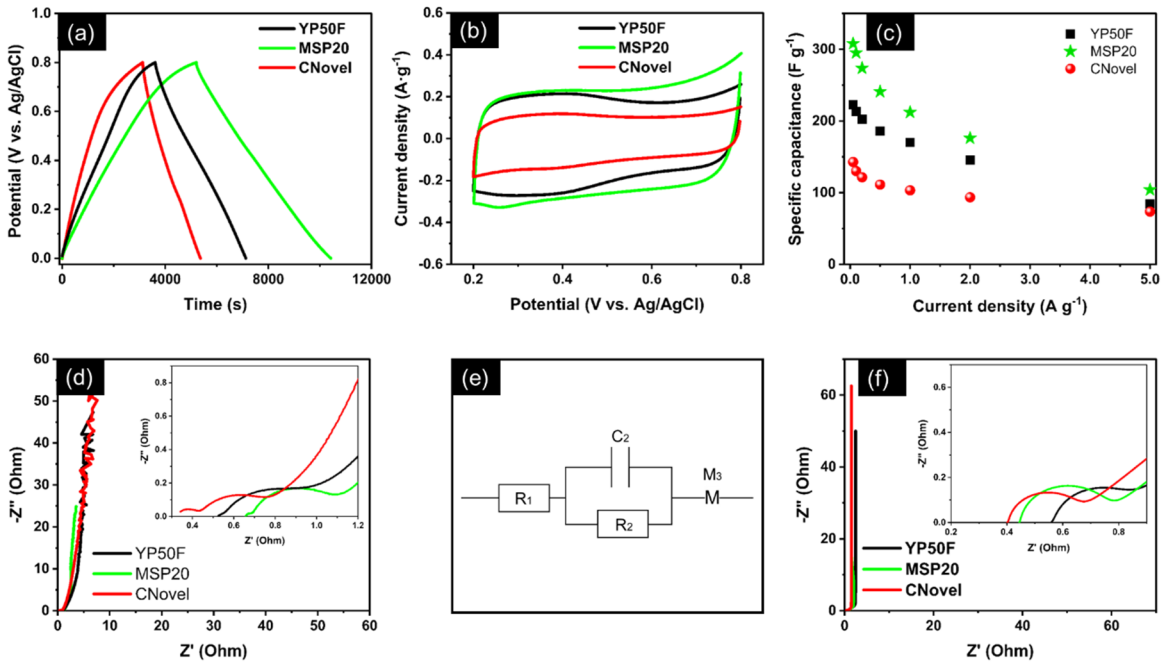

Figure 2.7 (a) GCD curves of YP50F, MSP20, and CNovel in 1-M H_2SO_4 solution at a current density of 50 mA g^{-1}, confirming their capacitive behavior. (b) CV curves of YP50F, MSP20, and CNovel in 1-M H_2SO_4 solution at 1 mV s^{-1}, showing a nearly rectangular shape. (c) Specific capacitances of YP50F (black), MSP20 (fluorescent green), and CNovel (red) in 1-M H_2SO_4 solution versus current density (50–5000 mA g^{-1}) showing that CNovel exhibits a good capacitance rate among the three samples. (d) Nyquist plots of YP50F (black), MSP20 (fluorescent green), and CNovel (red) at 0 V and 5.0 mV amplitude, with frequencies ranging from 1.0 mHz to 1.0 MHz (e) An equivalent circuit model applied to the experimental EIS curves. (f) The fitting curves of YP50F (black), MSP20 (fluorescent green), and CNovel (red).

Table 2.3 S_{BET}, volumetric specific capacitance (F cm^{-3}) under H_2SO_4 electrolytic solution, gravimetric specific capacitance (F g^{-1}) under H_2SO_4 electrolytic solution, electrode thickness (μm), and electrode bulk density (g cm^{-3}) of YP50F, MSP20, and CNovel.

Sample	S_{BET} (m^2 g^{-1})	Volumetric capacitance (F cm^{-3}) @50 / 250 / 1000 mAg^{-1}	Gravimetric capacitance (F g^{-1}) @50 / 250 / 1000 mAg^{-1}	Electrode thickness (μm)	Bulk density (electrode) (g cm^{-3})
YP50F	1600	122 / 107 / 93	222 / 197 / 170	413	0.68
MSP20	2266	149 / 129 / 103	307 / 267 / 212	449	0.60
CNovel	709	42 / 35 / 30	144 / 119 / 103	769	0.36

Figure 2.8 shows the open circuit potential (OCP) of YP50F, MSP20, and CNovel. The OCP of YP50F, MSP20, and CNovel was estimated to be 0.3, 0.29, and 0.38 V, respectively. Interestingly, CNovel's OCP indicates 0.38 V (vs. Ag/AgCl), higher than that of YP50F and MSP20. Higher OCP might be related to the mesopore volume. A similar tendency can be confirmed for CZMOF2, the material discussed in chapter 6. However, the rationale for this cannot be explained. For more detailed characterization, the electrochemical properties of the active material as the positive and negative electrodes were individually discussed. CV was conducted at a moderately low sweep rate of 1 mV s^{-1} to exactly analyze each electrochemical property of the anions and cations. Figure 2.9 (a), (b), and (c) show the two cyclic voltammograms separated based on their YP50F, MSP20, and CNovel electrodes' OCP, respectively. In all three samples, the current densities at the positive/negative electrode through the adsorption/desorption of the anions were similar to those of the cations. The positive and negative capacitance was estimated separately based on the galvanostatic discharge curves (Figure 2.9 (d)–(f) and Table 2.4). In all three samples, the capacitance by desorption of the anions (C_a) was smaller than that by the adsorption of cation (C_c), as shown in Table 2.4. Notably in CNovel, C_a was much smaller than C_c. The estimated diameters of solvated H^+ and SO_4^{2-} were 0.56 and 0.76 nm, respectively [2.18]. It was observed that the relationship between the anions (SO_4^{2-}) and pore size in CNovel is significantly different from that in YP50F and MSP20. This suggests that the specific capacitance could also be determined by the average pore size or porous structures.

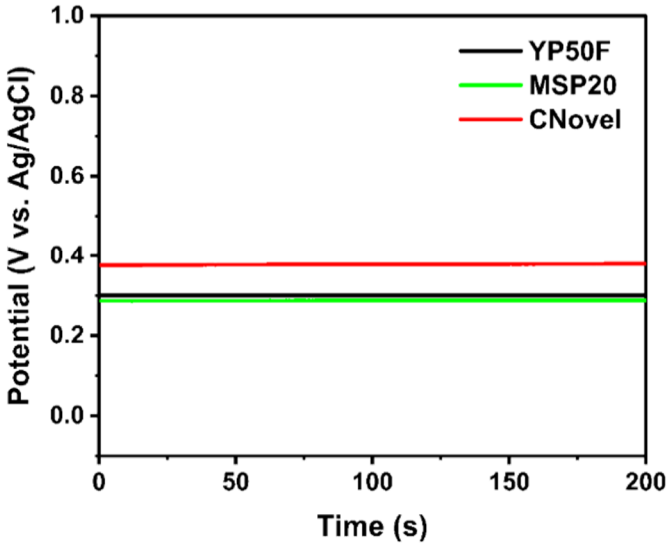

Figure 2.8 Open circuit potential of the YP50F, MSP20, and CNovel electrode materials vs. Ag/AgCl in 1.0 M H_2SO_4.

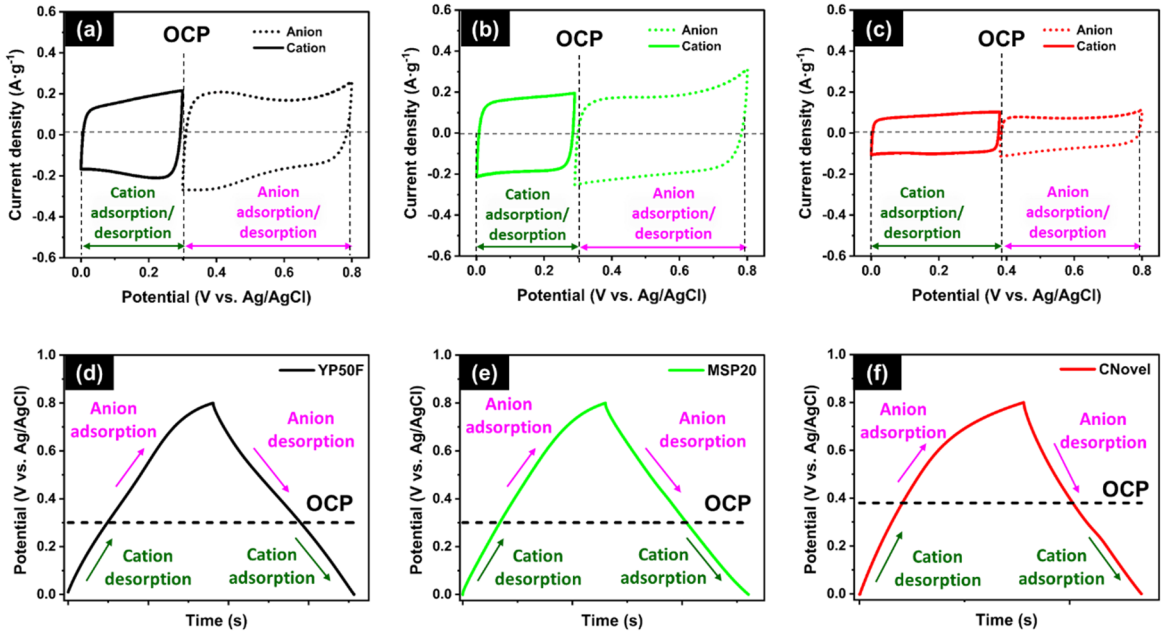

Figure 2.9 Electrochemical properties of the anions and cations, and the performance of the positive and negative electrodes of YP50F, MSP20, and CNovel in aqueous electrolytes (1.0 M H_2SO_4): Cyclic voltammograms of (a) YP50F, (b) MSP20, and (c) CNovel. GCD curves of (d) YP50F, (e) MSP20, and (f) CNovel.

Table 2.4 Specific capacitance by adsorption of the cation (C_a) and desorption of the cations (C_c)

Sample	C_a / F g^{-1}	C_c / F g^{-1}
YP50F	222	234
MSP20	306	365
CNovel	109	172

The electrochemical performance of the three carbons was evaluated in the symmetrical electrode cell under a non-aqueous solution ($TEABF_4$ in PC). Figure 2.10 (a) and (b) show the GCD curves of the three samples measured at 50 mA g^{-1} and each sample's capacitance retention calculated from the GCD curves as functions of current density (50–10000 mA g^{-1}). CNovel exhibited an outstanding rate performance at high current densities compared with the other carbons owing to its large quantity of mesopores (Table 2.1 and 2.5). Based on the GCD curves, the specific capacitance at 50 mA g^{-1} of YP50F, MSP20, and CNovel are calculated to be 23.2, 38.9, and 12.9 F g^{-1}, respectively. According to equation (2.7), the specific capacitance (F g^{-1}) on a single YP50F, MSP20, and CNovel electrode is computed as 92.8, 155.6, and 51.6 F g^{-1}, respectively. In all the three carbon samples, the electrode bulk density of the pellet electrode was almost the same as that of the slurry electrode, as shown in Table 2.6. Figure 2.10 (c) shows that the specific capacitance estimated under $TEABF_4$ has a linear relation with S_{BET} as with that under H_2SO_4. The proportional coefficients of the approximately linear lines are calculated as 0.1038 and 0.0657 for H_2SO_4 and $TEABF_4$, respectively. The result suggests that porous carbons with a high S_{BET} can enhance the capacitance when using H_2SO_4 rather than $TEABF_4$. Note that the linear relationship cannot be applied to porous samples with narrower pore sizes. As shown in Table 2.7, the specific capacitances of the three samples estimated under H_2SO_4 are higher than those under $TEABF_4$. This is attributed to the difference between H_2SO_4 and $TEABF_4$ in the electrolytic ion size. The estimated diameters of solvated H^+ and SO_4^{2-} were 0.56 and 0.76 nm, respectively,[2.18] whereas those of TEA^+ and BF_4^- were reported as 1.36 and 1.40 nm, respectively.[2.18] Therefore, suitable relationship between ion size and pore size could increase the specific capacitance.

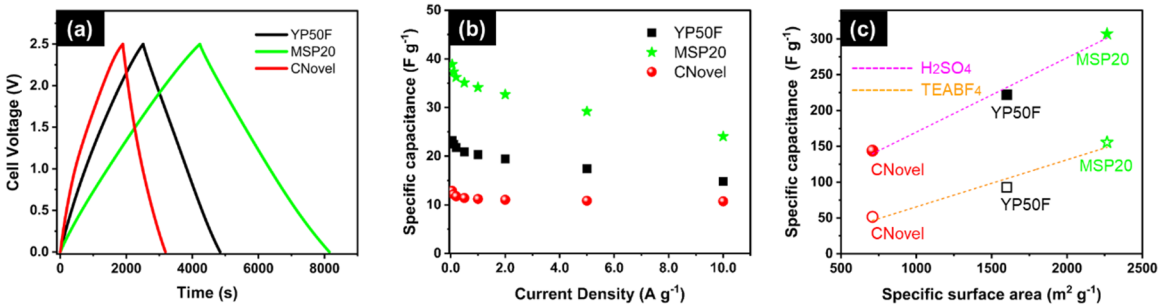

Figure 2.10 (a) GCD curves of YP50F (black), MSP20 (fluorescent green), and CNovel (red) in 1-M $TEABF_4$ in PC at a current density of 50 mA g^{-1}. (b) Capacitance retentions of YP50F (black), MSP20 (fluorescent green), and CNovel (red) in 1-M $TEABF_4$ in PC versus current density (50–10000 mA g^{-1}), showing that CNovel exhibited the highest capacitance retention among the three samples. (c) Specific capacitance based on H_2SO_4 or $TEABF_4$ vs. S_{BET}

Table 2.5 Capacitance retentions of YP50F, MSP20, and CNovel under $TEABF_4$

Sample	Capacitance retention (%)		
	At 500 mA^{-1}	At 1 A g^{-1}	At 10 A g^{-1}
YP50F	90.0	87.4	63.8
MSP20	90.3	87.8	61.9
CNovel	88.4	86.9	83.1

Table 2.6 Electrode bulk density of YP50F, MSP20, and CNovel

Sample	Pellet electrode (g cm^{-3})	Slurry electrode (g cm^{-3})
YP50F	0.68	0.70
MSP20	0.60	0.58
CNOvel	0.36	0.30

Table 2.7 Specific capacitance on a single electrode of YP50F, MSP20, and CNovel

Sample	S_{BET} * (m^2 g^{-1})	Specific capacitance under H_2SO_4 (Fg^{-1}) at 50 mA g^{-1}	Specific capacitance under $TEABF_4$ (Fg^{-1}) at 50 mA g^{-1}
YP50F	1600	222	92.8
MSP20	2266	307	155.6
CNovel	709	144	51.6

As shown in the Ragone plots of the three samples (Figure 2.11), the energy density (Wh kg^{-1}) was higher in $TEABF_4$/PC than in H_2SO_4 because the withstanding voltage was higher in the non-aqueous electrolyte $TEABF_4$/PC than in the aqueous H_2SO_4. The conductivity is reportedly lowered in non-aqueous solutions because the solvated anions and cations are larger and the viscosity is higher than in aqueous solutions.[2.19] In this test, the energy densities of the three samples were lower in H_2SO_4 than in $TEABF_4$ at high power densities (over 5 kW kg^{-1}). This result can be explained by the greater thickness (and hence resistance) of the pellet electrode than the thin film electrode (~800 μm vs. ~50 μm) (Figure 2.12).

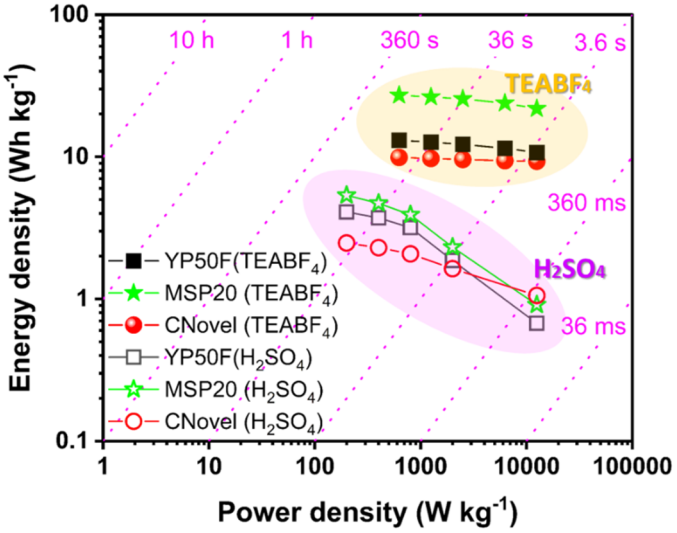

Figure 2.11 Ragone plots of the supercapacitors based on YP50F (black solid symbols), MSP20 (fluorescent green solid symbols), and CNovel (red solid symbols) with $TEABF_4$/PC showing higher energy densities than those based on YP50F (black empty symbols), MSP20 (fluorescent green empty symbols), and CNovel (red empty symbols) with H_2SO_4.

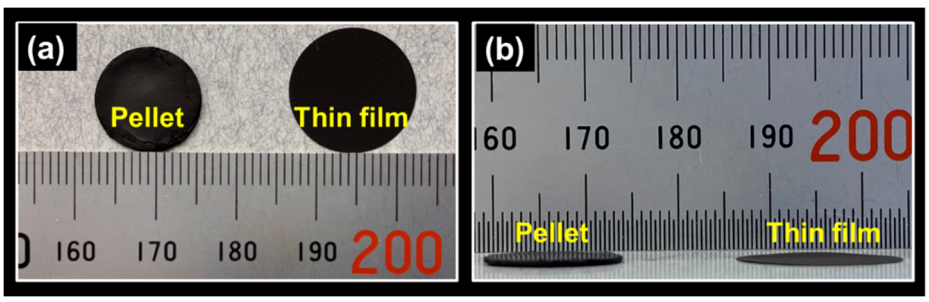

Figure 2.12 Images of the (a) upper views and (b) side views of the pellet (left image) and thin film (right image). Note that the pellet electrode is thicker than the thin film electrode.

2.4 Analytical results and discussion

2.4.1 Analytical method to obtain GCD curves

The following differential equation (2.11) was formularized based on the equivalent circuit model of an SC cell during charging (Figure 2.13).

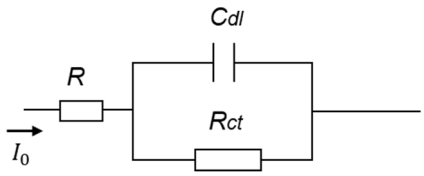

Figure 2.13 Equivalent circuit model of an SC cell

$$\frac{dV}{R_{ct}I_0 - V_C} = \frac{dt}{R_{ct}C_{dl}} \tag{2.11}$$

where C_{dl}, R, R_{ct}, and I_0 are the capacitance, total resistance derived from a material, charge transfer resistance derived from redox reactions, and constant current used in a GCD test, respectively. V_C is the voltage induced to a capacitor (C_{dl}). By solving the equation, the charging voltage was defined as a time function, as follows:

$$V_C = R_{ct}I_0\left(1 - \exp\left(-\frac{1}{R_{ct}C_{dl}}t\right)\right) \tag{2.12}$$

Therefore, the charging voltage induced to an entire SC cell (V) was determined as follows:

$$V = R_{ct}I_0\left(1 - \exp\left(-\frac{1}{R_{ct}C_{dl}}t\right)\right) + I_0R \tag{2.13}$$

In discharging, by substituting I_0 for–I_0 in equation (2.11), the following differential

equation was obtained.

$$\frac{dV}{R_{ct}I_0 + V_C} = -\frac{dt}{R_{ct}C_{dl}} \tag{2.14}$$

Similarly, by solving the equation, the discharging voltage was obtained as a time function as follows:

$$V_C = \left(E_0 + I_0(R_{ct} - R)\right)\exp\left(-\frac{1}{R_{ct}C_{dl}}t\right) - R_{ct}I_0 \tag{2.15}$$

where (E_0–V_C) is the voltage induced to resistance (R) at the start of the discharge. Therefore, the discharging voltage induced to an entire SC cell (V) was determined as follows:

$$V = \left(E_0 + I_0(R_{ct} - R)\right)\exp\left(-\frac{1}{R_{ct}C_{dl}}t\right) - R_{ct}I_0 - RI_0 \tag{2.16}$$

Here, denoting the time of full charge as t_0, the above equation can be rewritten as follows:

$$V = \left(E_0 + I_0(R_{ct} - R)\right)\exp\left(-\frac{1}{R_{ct}C_{dl}}(t - t_0)\right) - R_{ct}I_0 - RI_0 \tag{2.17}$$

2.4.2 Analytical method to obtain Nyquist plots

To analyze the resistive components individually, the transmission-line (TML) model was introduced, as shown in Figure 2.14 (a) and (b). Then, the complex impedance was obtained as follows (eq. 2.18) [2.17, 2.20. 2.21].

$$Z = \sqrt{Z_A Z_B}\,coth L\sqrt{\frac{Z_A}{Z_B}} \tag{2.18}$$

$$Z_A = r_{ion} \tag{2.19}$$

$$Z_B = r_{pore} + \frac{1}{j\omega C_{dl}} \tag{2.20}$$

where L, r_{ion}, r_{pore}, C_{dl}, ω, and j are the thickness of an electrode (cm), ionic resistance (Ω cm), pore resistance (Ω cm^3), double-layer capacitance (F cm^{-3}), angular frequency (rad s^{-1}), and imaginary unit, respectively. Shiroma and Ioroi [2.21] added the term of the charge transfer resistance derived from inter-particle gaps (Z_C) to the equation (2.18) (Figure 2.14 (c)), giving the following equation (2.21)–(2.23).

$$Z = \frac{Z_A Z_C}{Z_A + Z_C}\cdot L + \frac{\sqrt{Z_B}}{\sqrt[3]{Z_A + Z_C}}\cdot\frac{(Z_A^2 + Z_C^2)cosh\beta + 2Z_A Z_C}{sinh\beta} \tag{2.21}$$

$$\beta = L\cdot\sqrt{\frac{Z_A + Z_C}{Z_B}} \tag{2.22}$$

$$Z_C = \frac{R_e}{1 + \omega j C_{gb} R_e} \tag{2.23}$$

where R_e and C_{gb} are the charge transfer resistance (Ω cm) and a grain-boundary resistance, respectively. Additionally, the author considered the resistance corresponding to the leak current, R_{ct} (Ω cm^3), as shown in Figure 2.14 (d) and rewrote Z_B as follows;

$$\frac{1}{Z_B} = \frac{1}{r_{pore} + \frac{1}{j\omega C_{dl}}} + \frac{1}{R_{ct}} \quad \leftrightarrow \quad Z_B = \frac{R_{ct}(1 + r_{pore}C_{dl}\omega j)}{1 + \left(R_{ct} + r_{pore}\right)C_{dl}\omega j} \tag{2.24}$$

Finally, the author obtained the following complex impedance for the subsequent discussion.

$$Z = \frac{Z_A Z_C}{Z_A + Z_C} \cdot L + \frac{\sqrt{Z_B}}{\sqrt[3]{Z_A + Z_C}} \cdot \frac{(Z_A^2 + Z_C^2)cosh\beta + 2Z_A Z_C}{sinh\beta} \tag{2.25}$$

$$Z_A = r_{ion} \tag{2.26}$$

$$Z_B = \frac{R_{ct}(1 + r_{pore}C_{dl}\omega j)}{1 + \left(R_{ct} + r_{pore}\right)C_{dl}\omega j} \tag{2.27}$$

$$Z_C = \frac{R_e}{1 + \omega j C_{gb} R_e} \tag{2.28}$$

$$\beta = L \cdot \sqrt{\frac{Z_A + Z_C}{Z_B}} \tag{2.29}$$

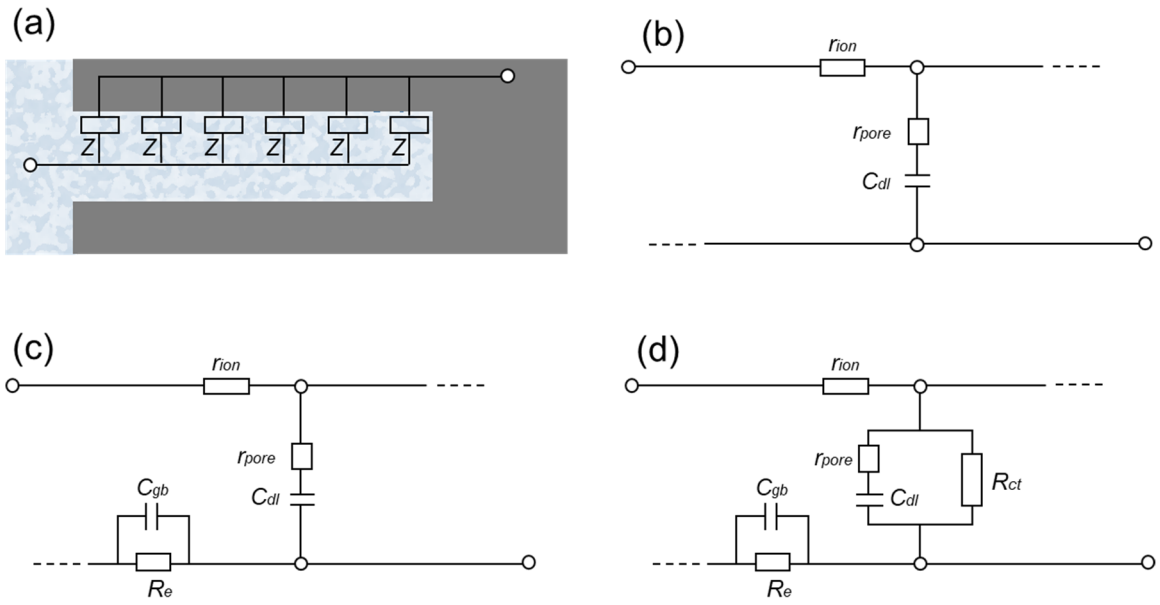

Figure 2.14 (a) A single cylindrical pore and the corresponding TML model. (b) The basic TML model proposed by De Levie [2.22]. (c) TML model proposed by Shiroma and Ioroi [2.21]. (d) TML model proposed by the author.

2.4.3 Analytical GCD curves

Figure 2.15 shows a simulated GCD curve based on the equation (2.13 and 2.17) and an experimental GCD curve of the YP50F electrode with $TEABF_4$. The used parameters and actual data are shown in Table 2.8. The simulated GCD curve formed a theoretical capacitive curve. Based on the analytical data listed in Table 2.8, the waveform of simulated curves can be used in the later discussion to reveal their relationship with the parameters, such as the current (I_0), capacitance (C_{dl}), total resistance (R) derived from a material, and charge transfer resistance (R_{ct}).

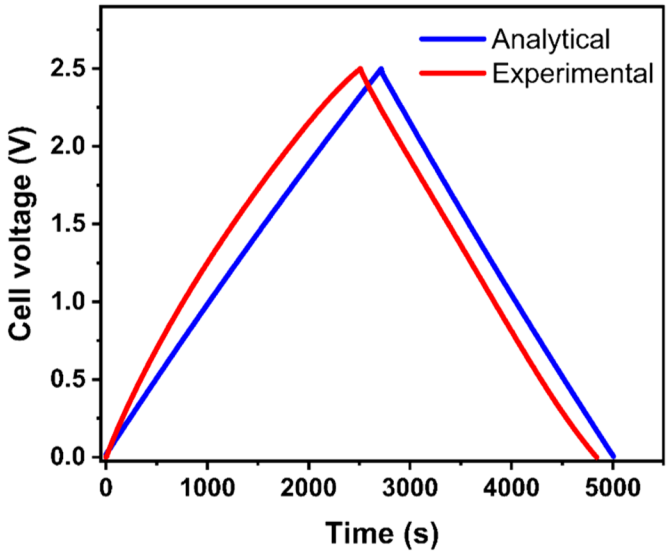

Figure 2.15 An experimental GCD curve (red) and a simulated GCD curve (blue)

Table 2.8 Parameters used in simulating the GCD curve and actual data of YP50F with $TEABF_4$

	I_0 (mA)	C_{dl} (F)	R_{ct} (Ω)	R (Ω)
Analytical	1.5	1.5	10000	10
Actual (YP50F)	1.5	1.28	-	-

Figure 2.16 (a) shows the simulated GCD curves of the three models with different I_0. Table 2.9 indicates the parameters used for the calculation. It was observed that the charging/discharging time decreases with increasing I_0. For small I_0 (model 4), charging and discharging curves deviated from ideal linear capacitive waveform in the higher and lower cell voltage, respectively. Further, in model 5, with an extremely small I_0, the cell voltage does not attain the maximum voltage (2.5 V). Probably, in this case, a leak current cannot be ignored. The calculation is expected to be applicable to the result of the same sample's GCD test under different current densities.

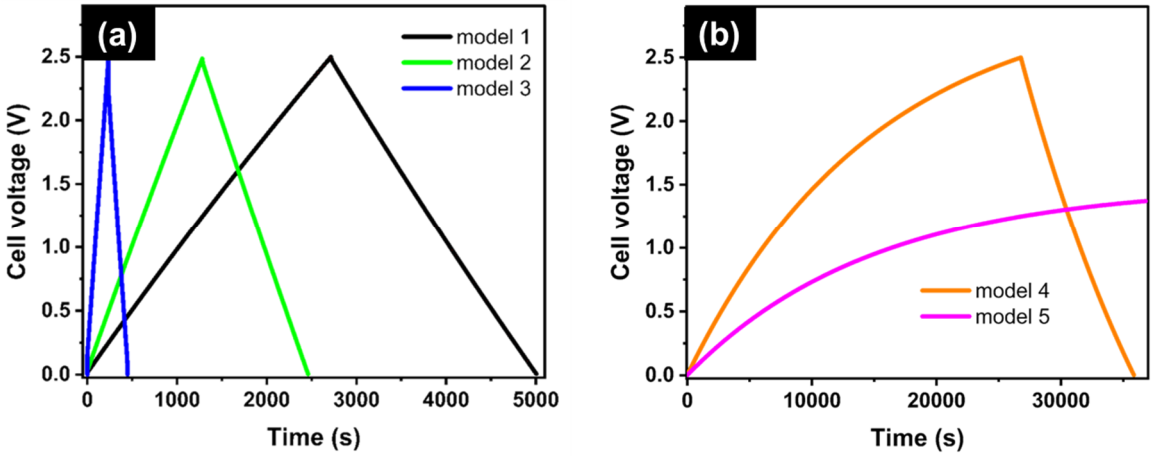

Figure 2.16 Simulated GCD curves of the three models with different I_0

Table 2.9 Parameters used in simulating the GCD curves in Figure 2.16

	I_0 (mA)	C_{dl} (F)	R_{ct} (Ω)	R (Ω)
Model 1	1.5	1.5	10000	10
Model 2	15	1.5	10000	10
Model 3	30	1.5	10000	10
Model 4	0.3	1.5	10000	10
Model 5	0.15	1.5	10000	10

Figure 2.17 shows the simulated GCD curves of the three models with different C_{dl}. Table 2.10 indicates the parameters used for the calculation. The charging/discharging time increases with increasing C_{dl}. These results agree well with the experimental data (Figure 2.10 (a)).

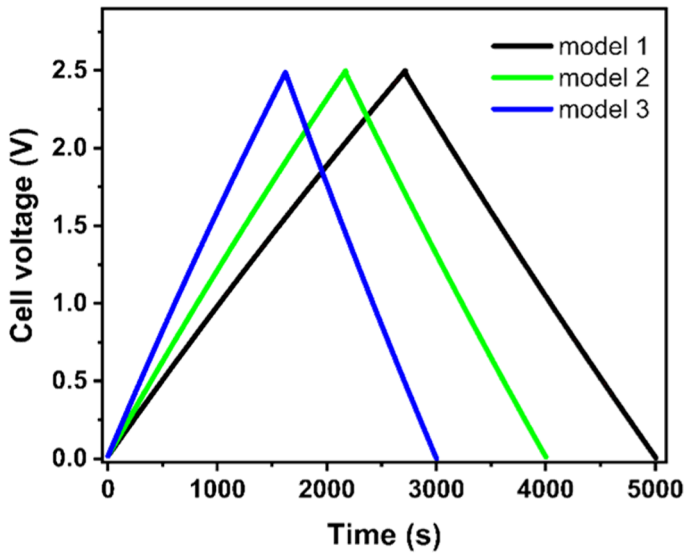

Figure 2.17 Simulated GCD curves of the three models with different C_{dl}

Table 2.10 Parameters used in simulating the GCD curves in Figure 2.17

	I_0 (mA)	C_{dl} (F)	R_{ct} (Ω)	R (Ω)
Model 1	1.5	1.5	10000	10
Model 2	1.5	1.2	10000	10
Model 3	1.5	0.9	10000	10

Figure 2.18 shows the simulated GCD curves of the three models with different R_{ct}. Table 2.11 indicates the parameters used for the calculation. It can be observed that the R_{ct} affected the slope of the charging curves at a higher cell voltage. A smaller R_{ct} means that leak current flows in an SC cell. Especially in model 3, the voltage does not attain its maximum (2.5 V). To the best of the author's knowledge, the deviated GCD curves can be seen in several studies on SC electrodes with aqueous electrolytes [2.3]. Here, the leak current can be considered to flow along with redox reactions.

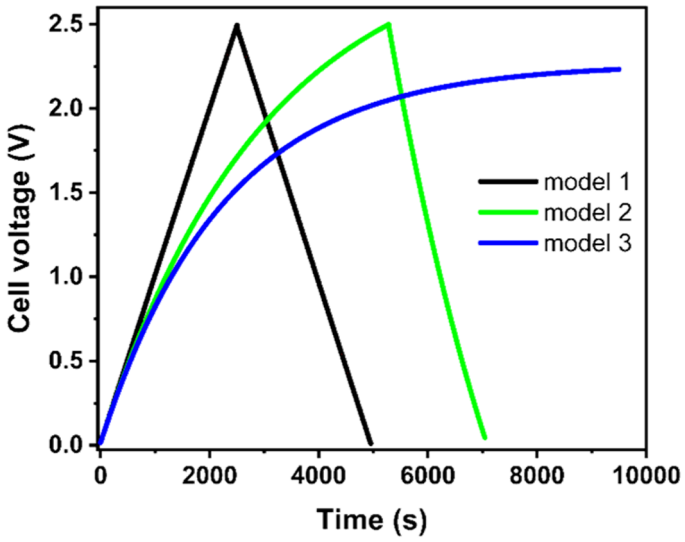

Figure 2.18 Simulated GCD curves of the three models with different R_{ct}

Table 2.11 Parameters used in simulating the GCD curves in Figure 2.18

	I_0 (mA)	C_{dl} (F)	R_{ct} (Ω)	R (Ω)
Model 1	15	1.5	10000	10
Model 2	15	1.5	2000	10
Model 3	15	1.5	1500	10

Figure 2.19 shows the simulated GCD curves of the three models with different *R*. Table 2.12 indicates the parameters used for the calculation. IR drop can be observed in models 2 and 3. Notably, the three models' waveforms show liner charging/discharging curves unlike those simulated by changing R_{ct}.

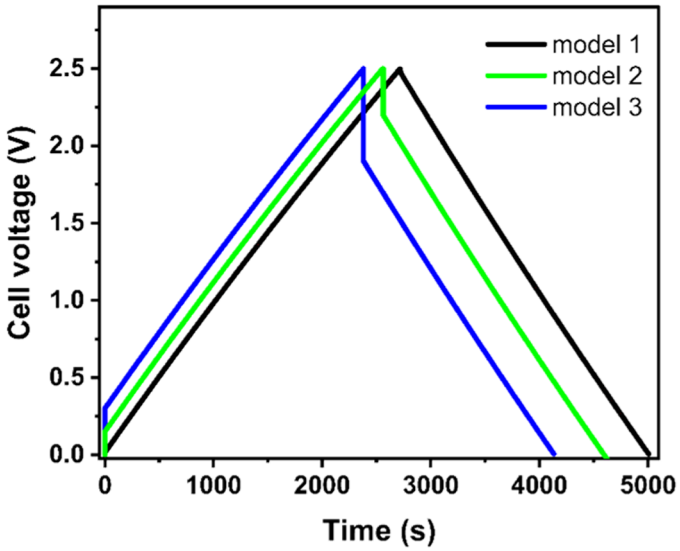

Figure 2.19 Simulated GCD curves of the three models with different *R*

Table 2.12 Parameters used in simulating the GCD curves in Figure 2.19

	I_0 (mA)	C_{dl} (F)	R_{ct} (Ω)	R (Ω)
Model 1	15	1.5	10000	10
Model 2	15	1.5	10000	100
Model 3	15	1.5	10000	200

2.4.4 Analytical EIS spectra

A simulated Nyquist plot ranging from 10 mHz to 1.0 MHz is shown in Figure 2.20 as a reference model. The inset shows the enlarged Nyquist plot in the high-frequency region. Based on the reference model, the spectrum was examined in the subsequent discussion to clarify their relationship with the parameters, such as r_{ion}, r_{pore}, R_{ct}, R_e, C_{dl}, C_{gb}, and L. The parameters used for the calculation are listed below (Table 2.13).

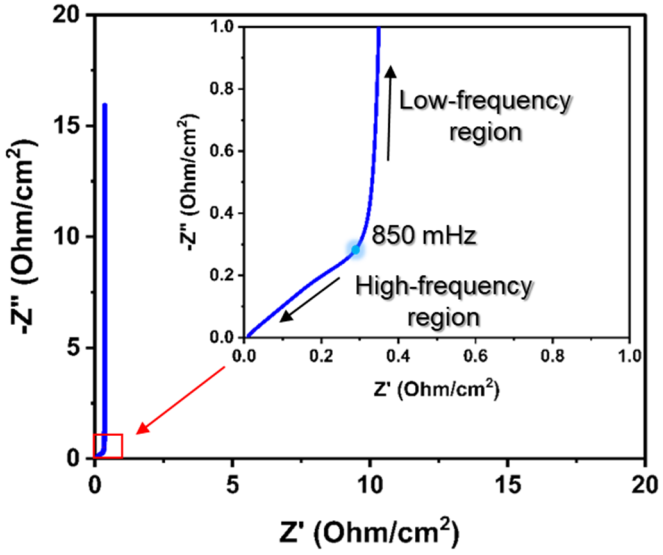

Figure 2.20 Simulated Nyquist plot of the reference model.

Table 2.13 Parameters used in simulating the Nyquist plot in Figure 2.20

r_{ion} (Ω cm)	r_{pore} (Ω cm^3)	R_{ct} (Ω cm^3)	R_e (Ω cm)	C_{dl} (F/cm^3)	C_{gb} (F/cm)	L (cm)
100	1.0×10^{-6}	10000	10	100	0.1	0.01

The simulated Nyquist plots of the three models with different *L* are shown in Figure 2.21. The parameters used for the calculation are listed in Table 2.14. It was observed that the length of the diagonal line in the low-frequency region increased with increasing *L*. These results show that the ions take time to diffuse into porous electrode materials. The results and discussion are expected to apply to the experimental Nyquist plots with different thicknesses of porous electrode materials.

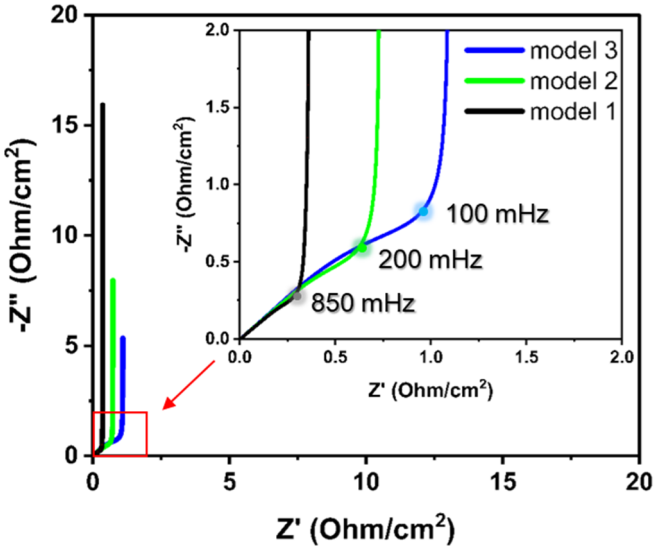

Figure 2.21 Simulated Nyquist plot of the three models with different *L*.

Table 2.14 Parameters used in simulating the Nyquist plot in Figure 2.21

	r_{ion} (Ω cm)	r_{pore} (Ω cm^3)	R_{ct} (Ω cm^3)	R_e (Ω cm)	C_{dl} (F/cm^3)	C_{gb} (F/cm)	L (cm)
Model 1	100	1.0×10^{-6}	10000	10	100	0.1	0.01
Model 2	100	1.0×10^{-6}	10000	10	100	0.1	0.02
Model 3	100	1.0×10^{-6}	10000	10	100	0.1	0.03

The simulated Nyquist plots of the three models with different r_{pore} are shown in Figure 2.22. The parameters used for the calculation are listed in Table 2.15. It was observed that the point of the horizontal axis (Z') crosses shifted in the positive direction of Z' with increasing r_{pore}. The results and discussion are expected to apply to the experimental Nyquist plots of porous electrode materials with different pore sizes.

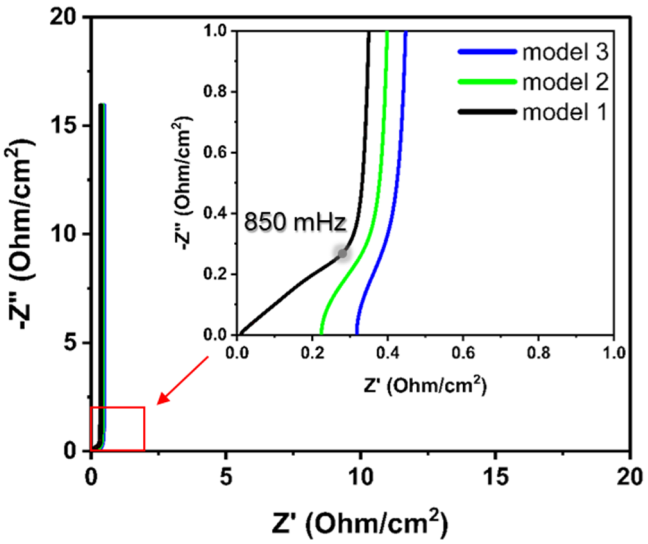

Figure 2.22 Simulated Nyquist plot of the three models with different r_{pore}.

Table 2.15 Parameters used in simulating the Nyquist plot in Figure 2.22

	r_{ion} (Ω cm)	r_{pore} (Ω cm^3)	R_{ct} (Ω cm^3)	R_e (Ω cm)	C_{dl} (F/cm^3)	C_{gb} (F/cm)	L (cm)
Model 1	100	1.0×10^{-6}	10000	10	100	0.1	0.01
Model 2	100	5.0×10^{-4}	10000	10	100	0.1	0.01
Model 3	100	1.0×10^{-3}	10000	10	100	0.1	0.01

The simulated Nyquist plots of the three models with different r_{ion} are shown in Figure 2.23. The parameters used for the calculation are listed in Table 2.16. As with the simulated Nyquist plots with different L, the length of the linear line in the low-frequency region increased as r_{ion} increased. This means that lower ionic conductivity increased the diffusion time for electrolytic ions access into pores. The results and discussion are expected to apply to the experimental data with different electrolyte solutions.

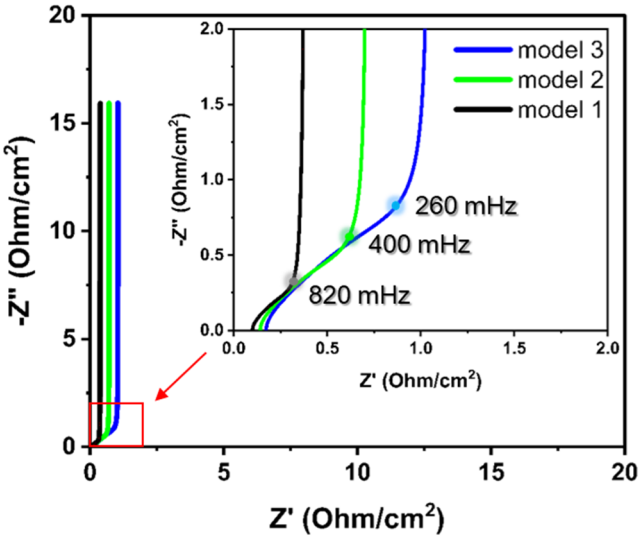

Figure 2.23 Simulated Nyquist plot of the three models with different r_{ion}.

Table 2.16 Parameters used in simulating the Nyquist plot in Figure 2.23

	r_{ion} (Ω cm)	r_{pore} (Ω cm^3)	R_{ct} (Ω cm^3)	R_e (Ω cm)	C_{dl} (F/cm^3)	C_{gb} (F/cm)	L (cm)
Model 1	100	1.0×10^{-4}	10000	10	100	0.1	0.01
Model 2	200	1.0×10^{-4}	10000	10	100	0.1	0.01
Model 3	300	1.0×10^{-4}	10000	10	100	0.1	0.01

The simulated Nyquist plots of the three models with different C_{dl} were shown in Figure 2.24 (a) – (c). The parameters used for the calculation are listed in Table 2.17. As discussed above, the effect of a leak current in an SC cell can be ignored in extremely high R_{ct}. In this case, the equation (2.24) can be rewritten as follows:

$$\lim_{R_{ct}\to\infty}(Z_B) = \frac{(1 + r_{pore}C_{dl}\omega j)}{C_{dl}\omega j} \tag{2.30}$$

Further, electrolytic ions can smoothly access deep into pores in the low-frequency region than in the high-frequency region. This is because electrolytic ions can follow the lower frequency. In this case, r_{pore} can be approximated to 0. That is, Z_B can be given as follows;

$$\lim_{(R_{ct},\ r_{pore})\ \to\ (\infty,0)}(Z_B) = \frac{1}{C_{dl}\omega j} \tag{2.31}$$

The equation indicates the impedance of the normal capacitance in the alternating-current circuit theory. The complex impedance is composed only of the imaginary part. Based on this, the length of the line in the low-frequency area get shorter with increasing C_{dl}

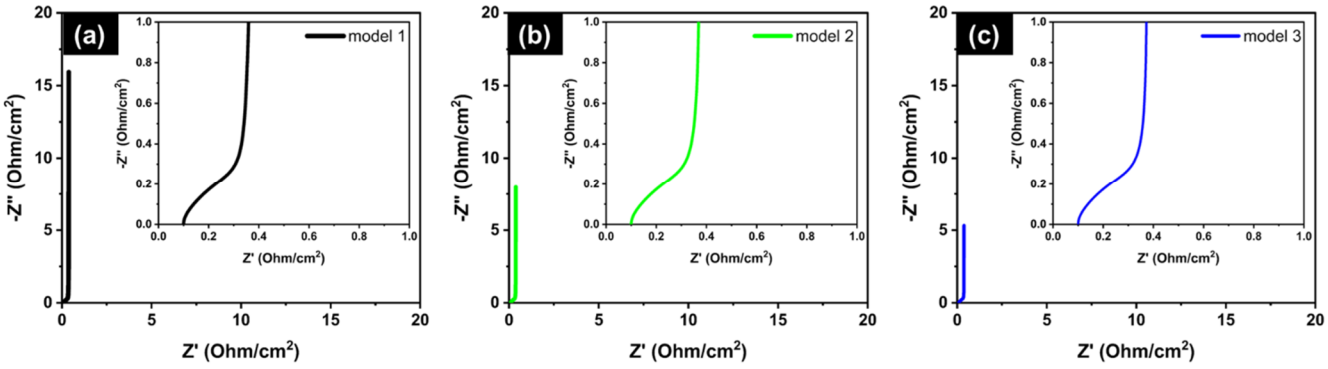

Figure 2.24 Simulated Nyquist plot of (a) model1, (b) model2, and (c) model3.

Table 2.17 Parameters used in simulating the Nyquist plot in Figure 2.24

	r_{ion} (Ω cm)	r_{pore} (Ω cm^3)	R_{ct} (Ω cm^3)	R_e (Ω cm)	C_{dl} (F/cm^3)	C_{gb} (F/cm)	L (cm)
Model 1	100	1.0×10^{-4}	10000	10	100	0.1	0.01
Model 2	100	1.0×10^{-4}	10000	10	200	0.1	0.01
Model 3	100	1.0×10^{-4}	10000	10	300	0.1	0.01

The simulated Nyquist plots of the three models with different R_{ct} are shown in Figure 2.25. The parameters used for the calculation are listed in Table 2.18. Unlike the other parameters, the Nyquist plot was observed to lean in the direction of the Z' axis as R_{ct} decreases. In this case, a leak current flows or redox reactions occur in an SC cell. The deviated curves such as models 1 and 2 can be criteria to confirm whether a leak current flows or redox reactions occur in an SC cell.

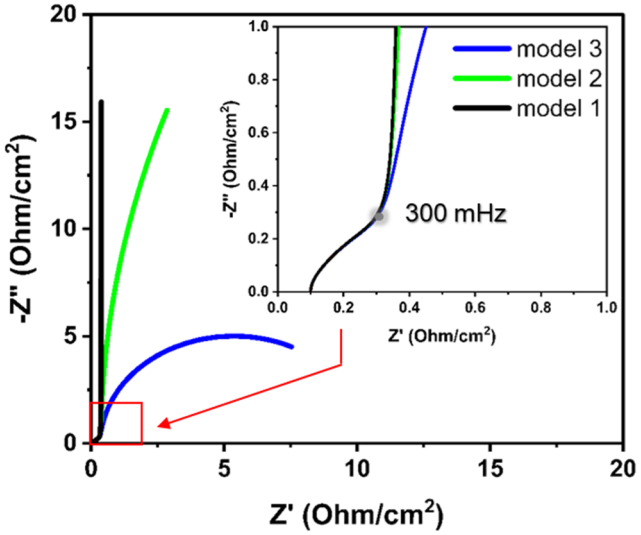

Figure 2.25 Simulated Nyquist plot of the three models with different R_{ct}.

Table 2.18 Parameters used in simulating the Nyquist plot in Figure 2.25

	r_{ion} (Ω cm)	r_{pore} (Ω cm^3)	R_{ct} (Ω cm^3)	R_e (Ω cm)	C_{dl} (F/cm^3)	C_{gb} (F/cm)	L (cm)
Model 1	100	1.0×10^{-4}	10000	10	100	0.1	0.01
Model 2	100	1.0×10^{-4}	1	10	100	0.1	0.01
Model 3	100	1.0×10^{-4}	0.1	10	100	0.1	0.01

The simulated Nyquist plots of the three models with different C_{gb} are shown in Figure 2.26. The parameters used for the calculation are listed in Table 2.19. It was observed that the small semicircle appeared as the C_{gb} decreased. The results and discussion are expected to apply to those with different particle sizes or morphologies.

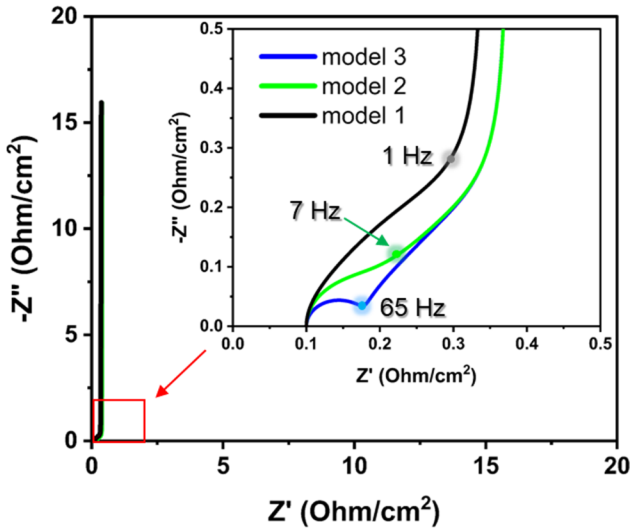

Figure 2.26 Simulated Nyquist plot of the three models with different C_{gb}.

Table 2.19 Parameters used in simulating the Nyquist plot in Figure 2.26

	r_{ion} (Ω cm)	r_{pore} (Ω cm^3)	R_{ct} (Ω cm^3)	R_e (Ω cm)	C_{dl} (F/cm^3)	C_{gb} (F/cm)	L (cm)
Model 1	100	1.0×10^{-4}	10000	10	100	1	0.01
Model 2	100	1.0×10^{-4}	10000	10	100	0.001	0.01
Model 3	100	1.0×10^{-4}	10000	10	100	0.0001	0.01

The simulated Nyquist plots of the three models with different R_e are shown in Figure 2.27. The parameters used for the calculation are listed in Table 2.20. The size of the semicircle in the Nyquist plot was observed to increase with increasing R_e. As in the previous discussion, the results are expected to apply to those with different particle sizes or morphologies.

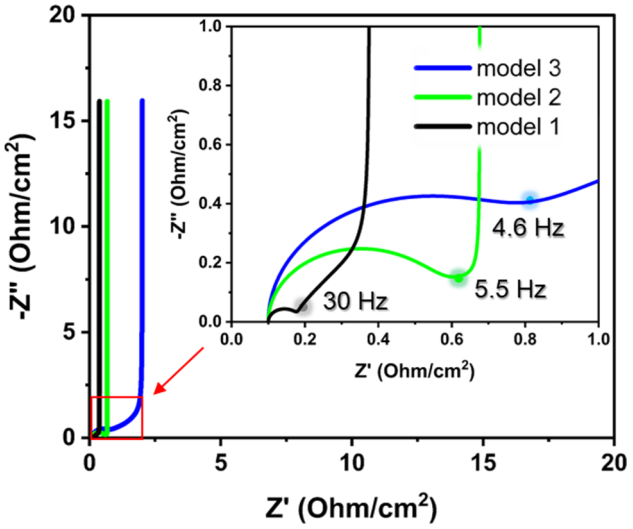

Figure 2.27 Simulated Nyquist plot of the three models with different R_e.

Table 2.20 Parameters used in simulating the Nyquist plot in Figure 2.27

	r_{ion} (Ω cm)	r_{pore} (Ω cm³)	R_{ct} (Ω cm³)	R_e (Ω cm)	C_{dl} (F/cm³)	C_{gb} (F/cm)	L (cm)
Model 1	100	1.0×10^{-4}	10000	10	100	0.0001	0.01
Model 2	100	1.0×10^{-4}	10000	100	100	0.0001	0.01
Model 3	100	1.0×10^{-4}	10000	500	100	0.0001	0.01

Here, the impedance term owing to particle/current collector interface (Z_D) was introduced to the proposed equivalent circuit model (Figure 2.14(d)).

$$Z_D = \frac{R_i}{1 + C_i R_i \omega j} \tag{2.32}$$

where *Ri* and *Ci* are the resistance and capacitance due to particle/current collector interface, respectively. Finally, the following equation was obtained:

$$Z = \frac{Z_A Z_C}{Z_A + Z_C} \cdot L + \frac{\sqrt{Z_B}}{\sqrt[3]{Z_A + Z_C}} \cdot \frac{(Z_A^2 + Z_C^2)cosh\beta + 2Z_A Z_C}{sinh\beta} + Z_D \qquad (2.33)$$

Nyquist plots of the three models with different R_i are shown in Figure 2.28. The parameters used for the calculation were listed in Table 2.21. The size of the semicircle increased with increasing R_i.

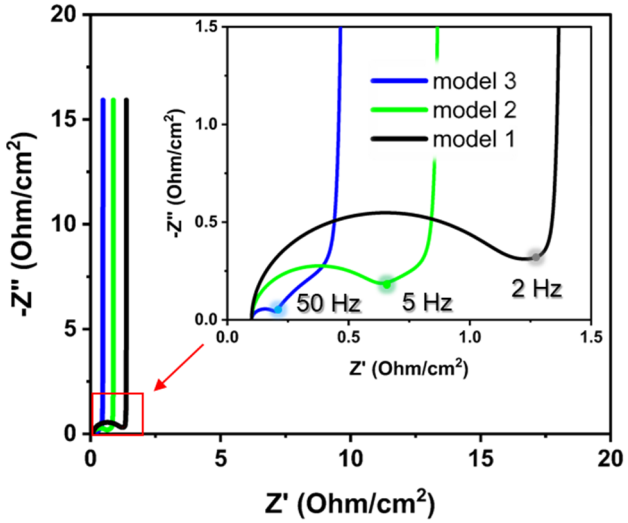

Figure 2.28 Simulated Nyquist plot of the three models with different R_i

Table 2.21 Parameters used in simulating the Nyquist plot in Figure 2.28

	r_{ion} (Ω cm)	r_{pore} (Ω cm³)	R_{ct} (Ω cm³)	R_e (Ω cm)	C_{dl} (F/cm³)	C_{gb} (F/cm)	L (cm)	R_i (Ω/cm²)	C_i (Fcm²)
Model 1	100	1.0×10^{-4}	10000	10	100	0.0001	0.01	1	0.01
Model 2	100	1.0×10^{-4}	10000	100	100	0.0001	0.01	0.5	0.01
Model 3	100	1.0×10^{-4}	10000	500	100	0.0001	0.01	0.1	0.01

Based on these results, the simulated GCD curves and the Nyquist plots were confirmed to contain essential information on the resistance and capacitance components. The relationship between resistance and capacitance components in a SC cell decided the GCD waveform. Further, the Nyquist plots could be used to separate the individual resistance and capacitance components from the experimental ones. However, in most cases, it is difficult to exactly separate the individual components only by observing a spectrum in a Nyquist plot. Therefore, an effective method is to fit a conceivable equivalent circuit model to an experimental Nyquist plot to separate resistance and capacitance components individually.

2.5 Conclusion

Three kinds of porous carbons were characterized in terms of carbon, porous, and electrochemical properties. The fundamental analyses of electrochemical properties successfully provided more detailed information on the relationship between the specific capacitance and pore size. Mesoporous carbons exhibited higher capacitance retention at high currents. The specific capacitance was observed to be proportional to the S_{BET} of porous carbons when using H_2SO_4 or $TEABF_4$. Furthermore, the capacitance was notably enhanced using H_2SO_4 compared with $TEABF_4$. Importantly, the energy density of the three carbons with $TEABF_4$ was confirmed to be higher than those with H_2SO_4. This is simply because non-aqueous electrolytes offer a wider voltage window. Based on these results, the author employs both aqueous and non-aqueous solutions properly according to the kinds of electrode materials in the latter discussion (chapter 3–6).

This chapter discussed the electrode bulk density, giving the key information on the electrode materials. Importantly, mesoporous carbons with a relatively larger pore such as CNovel exhibited a high rate performance of SCs electrode material under both aqueous and non-aqueous electrolytes. On the other hand, such a mesoporous carbon was confirmed to suffer from the lower volumetric capacitance (F cm^{-3}). The results contributed to the subsequent chapter.

Analytical GCD and EIS curves revealed conceivable resistance and capacitance components behind an SC cell. By changing parameters, such as r_{ion}, r_{pore}, R_{ct}, R_e, C_{dl}, C_{gb}, R_i, C_i, and L, the author successfully clarified their relationship with the curves in Nyquist plots. The findings could contribute to the subsequent results and discussion.

2.6 References

[2.1] L. Wang, Y. Han, X. Feng, J. Zhou, P. Qi, B. Wang, "Metal-organic frameworks for energy storage: Batteries and supercapacitors." Coord. Chem. Rev. **307**, 361–381 (2016).

[2.2] B. Xu, H. Zhang, H. Mei, D. Sun, "Recent progress in metal-organic framework-based supercapacitor electrode materials." Coord. Chem. Rev. **420**, 213438 (2020).

[2.3] S. Saini, P. Chand, A. Joshi, "Biomass derived carbon for supercapacitor applications: Review." J. Energy Storage. **39**, 102646 (2021).

[2.4] F. Wan, J. Zhu, S. Huang, Z. Niu, "High voltage electrolytes for aqueous energy storage devices." Batteries Supercaps. **3**, 323–330 (2020).

[2.5] S. Ishimoto, Y. Asakawa, M. Shinya and K. Naoi,. *Soc.*, "Degradation Responses of Activated-Carbon-Based EDLCs for Higher Voltage Operation and Their Factors." J. Electrochem. **156**, A563–A571 (2009).

[2.6] H. M. Lee, K. H. An, S. J. Park and B. J. Kim, "Mesopore-rich activated carbons for electrical double-layer capacitors by optimal activation condition." *Nanomaterials*, **9**, 608 (2019).

[2.7] Y. Kado, Y. Soneda, "Capacitor performance of MgO-templated carbons synthesized using hydrothermally treated MgO particles", *Microporous Mesoporous Mater*. **310**, 110646 (2021).

[2.8] R. Ramachandran, C. Zhao, D. Luo, K. Wang and F. Wang, "Morphology-dependent electrochemical properties of cobalt-based metal organic frameworks for supercapacitor electrode materials." *Electrochim. Acta*, **267**, 170−180 (2018).

[2.9] C. Young, R. R. Salunkhe, J. Tang, C. C. Hu, M. Shahabuddin, E. Yanmaz, M. S. Hossain, J. H. Kim and Y. Yamauchi, "Zeolitic imidazolate framework (ZIF-8) derived nanoporous carbon: the effect of carbonization temperature on the supercapacitor performance in an aqueous electrolyte." *Phys. Chem. Chem. Phys.*, **18**, 29308–29315 (2016).

[2.10] N. L. Torad, R. R. Salunkhe, Y. Li, H. Hamoudi, M. Imura, Y. Sakka, C. C. Hu and Y. Yamauchi, "Electric double-layer capacitors based on highly graphitized nanoporous carbons derived from ZIF-67." *Chem. Eur. J.*, **20**, 7895–7900 (2014).

[2.11] D. Hulicova-JuracovaJ, M. Seredych, Y. Jin, G. Qing Lu, T. J. Bandosz, "Specific anion

and cation capacitance in porous carbon blacks." *Carbon*, **48**, 1767−1778 (2010).

[2.12] C. Young, R. R. Salunkhe, J. Tang, C. C. Hu, M. Shahabuddin, E. Yanmaz, M. S. Hossain, J. H. Kim and Y. Yamauchi, "Zeolitic imidazolate framework (ZIF-8) derived nanoporous carbon: the effect of carbonization temperature on the supercapacitor performance in an aqueous electrolyte." *Phys. Chem. Chem. Phys.*, **18**, 29308–29315 (2016).

[2.13] D. Qu, H. Shi, "Studies of activated carbons used in double-layer capacitors." *J. Power Sources*, **74**, 99−107 (1998).

[2.14] L. M. Malard, M. A. Pimenta, G. Dresselhaus and M. S. Dresselhaus, "Raman spectroscopy in graphene." *Phys. Rep.*, **473**, 51–87 (2009).

[2.15] C. Lei, N. Amini, F. Markoulidis, P. Wilson, S. Tennison and C. Lekakou, "Activated carbon from phenolic resin with controlled mesoporosity for an electric double-layer capacitor (EDLC)." *J. Mater. Chem. A*, **1** (2013).

[2.16] C. Lei, F. Markoulidis, Z. Ashitaka and C. Lekakou, "Reduction of porous carbon/Al contact resistance for an electric double-layer capacitor (EDLC)." *Electrochim. Acta*, **92**, 183–187.

[2.17] L. M. D. Silva, R. Cesar, C. M. R. Moreira, J. H. M. Santos, L. G. D. Souza, B. M. Pires, R. Vicentini, W. Nunes, and H. Zanin, "Reviewing the fundamentals of supercapacitors and the difficulties involving the analysis of the electrochemical findings obtained for porous electrode materials." *Energy Stor. Mater*., **27**, 555–590 (2020).

[2.18] L. Pilon, H. Wang and A. d'Entremont, "Recent advances in continuum modeling of interfacial and transport phenomena in electric double layer capacitors." *J. Electrochem. Soc.*, **162**, A5158–A5178 (2015).

[2.19] E. Frackowiak, "Carbon materials for supercapacitor application." *Phys. Chem. Chem. Phys.*, **9**, 1774–1785 (2007).

[2.20] M. Itagaki, Y. Hatada, I. Shitanda, K. Watanabe, "Complex impedance spectra of porous electrode with fractal structure." *Electrochim. Acta*, **55**, 6255–6262 (2010).

[2.21] Z. Siroma, T. Ioroi, "expected electrochemical impedance responses of porous electrodes based on theoretical solutions of transmission-line models." *Electrochemistry.* **83**, 425–433 (2015).

[2.22] S. Fletcher, V.J. Black, I. Kirkpatrick, "A universal equivalent circuit for carbonbased

Supercapacitors.” *J. Solid State Electrochem*. **18**, 1377–1387 (2014).

3 Nitrogen-doped porous carbons derived from imine-based covalent-organic frameworks

3.1 Introduction

Multi-functional carbon materials, such as highly porous carbons, heteroatom-doped carbons, and metal/carbon composites, can be prepared by direct carbonization of MOFs or COFs, as mentioned in chapter 1[3.1–3.3]. MOFs or COFs-derived carbons have several important properties, such as unique morphologies, high S_{BET}, heteroatom-doping effects, and good conductivity. The synthetic conditions of MOFs or COFs could determine the particle morphology, pore characteristics, electrochemical, and thermal properties of the resultant carbons. Many highly porous carbons have been prepared via the carbonization of MOFs or COFs [3.4, 3.5]. Among MOF or COF-derived carbons, heteroatom-doped carbons have been proposed as promising SC electrode materials, where B-doped carbons exhibit good electrochemical performance [2.3]. Besides, N-doped carbons show high-performance SC electrodes. Pyridinic N and pyrrolic N from N-doped carbons play an important role in the pseudo-capacitive effect under acid solutions (H_2SO_4), according to equations (3.1) and (3.2) [3.6, 3.7].

$$> C = NH \; + \; 2e^- \; + 2H^+ \; \leftrightarrow \; > CH - NH_2 \tag{3.1}$$

$$> C - NHOH \; + \; 2e^- \; + 2H^+ \; \leftrightarrow \; > C - NH_2 + H_2O \tag{3.2}$$

Furthermore, the presence of N atoms incorporated into graphene or in the carbon matrix can enhance electron negativity, leading to good electrical conductivity between electrolytes and N-containing functional groups [3.8, 3.9]. To confirm these properties, the author synthesized the ICOFs, showing that their direct carbonization can produce N-doped porous carbons. Finally, electrochemical properties were examined using CICOFs.

3.2 Experimental procedures

3.2.1 Preparation of ICOFs and CICOFs

Two types of ICOFs (COFA and ICOFB) were prepared to provide two particles of different sizes. ICOFA/ICOFB were obtained by heating the mixture of 1,4-phenylenediamine (PDA) (Tokyo Chemical Industry Co. Ltd., Japan) and 2-hydroxy-1,3,5-benzentricarbaldehyde (HBTCA) (Tokyo Chemical Industry Co. Ltd., Japan) under the solution of 1,4-dioxane (Nacalai Tesque Inc., Japan) and acetic acid (Nacalai Tesque Inc., Japan) at 120 °C for 72 h to obtain the red-colored powders. Thereafter, the as-prepared ICOFs were calcined at 600 °C, 800 °C, and 1000 °C for 1 h under 200 mL min^{-1} nitrogen flow to obtain the three carbon samples. Note that the calcined ICOFs were referred to as CICOFs. The schematic route from the PDA and HBTCA to the ICOFs and CICOFs is shown in Figure 3.1.

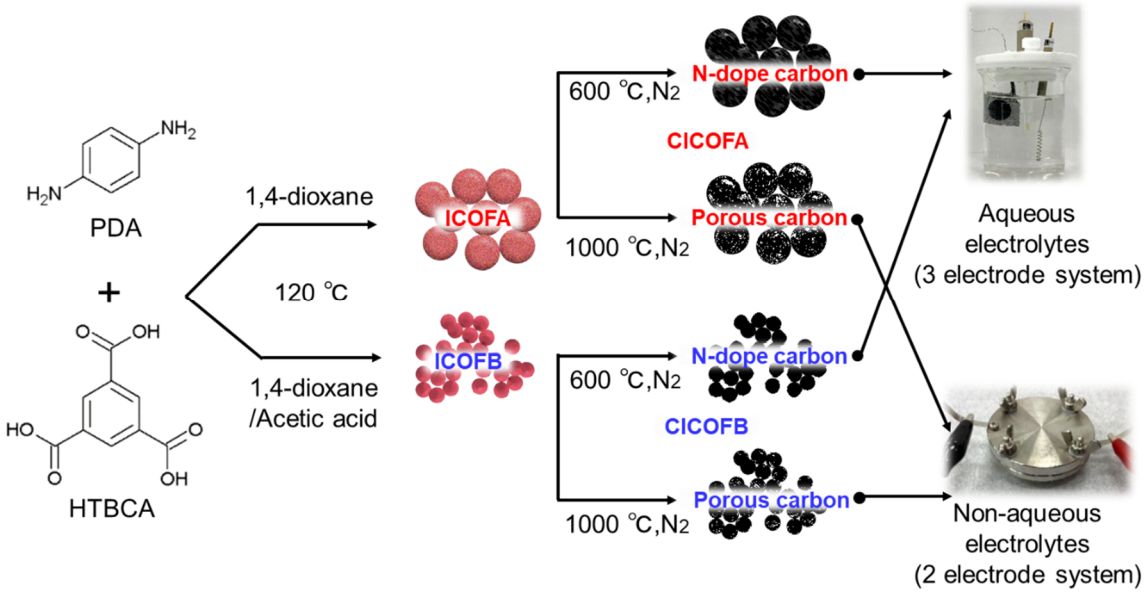

Figure 3.1 The schematic route from the PDA and HTBCA to the ICOFs and CICOFs.

3.2.2 Material characterization

The morphology of each sample was characterized using SEM (JSM-6010LA, JEOL Ltd., Japan) at an accelerating voltage of 15 kV (SE mode) and using TEM (JEM-2100F, JEOL Ltd., Japan) at an accelerating voltage of 200 kV. In the SEM preparation, the powdery sample was set onto a carbon tape on an Al sample holder (10 mm (φ) × 10 mm (H)). For TEM, the sample dispersed in ethanol was poured onto a holey carbon film supported on 3 mm Cu grids, then dried at 80 °C for 1 h. The resulting products' crystallinity was confirmed in a PXRD analysis (Smart Lab SE, Rigaku, Japan) with Cu $K\alpha_1$ (λ = 0.154 nm) radiation at 10° min^{-1} scan rate. The samples' surface functionalities and mass ratio were examined by X-ray photoelectron (XP) spectroscopy (XPS) (ESCA5700, ULVAC-PHI Inc., Japan) with Mg $K\alpha_1$ radiation at a 15 kV accelerating voltage.

The phase-change temperature of each sample was determined by thermogravimetry (TG) and differential thermal analysis (DTA) (DTG-60, Shimadzu Corporation, Japan), which was performed at 10 °C min^{-1} under a 200 mL min^{-1} nitrogen flow. In the TG–DTA preparation, ~5 mg of the powdery sample was placed in the Pt holder. Nitrogen adsorption/desorption (BEL-SORP min, Microtrac-BEL, Japan) isotherms were acquired at 77 K for the S_{BET} measurement, average PSD, and information on each sample's pore structure. Before the measurements, the samples were degasified by heating at 300 °C for 24 h in a vacuum. The S_{BET} of each sample was estimated from the isotherms using the BET method (P/P_0 = 0.05–0.10). The S_{meso} was estimated using the BJH method. The total pore (V_{total}), micropore (~2 nm) (V_{micro}), and mesopore (2–50 nm) (V_{meso}) volumes were calculated using the BET, MP, and BJH methods, respectively. The PSD was calculated using the NLDFT.

3.2.3 Fabrication of electrode materials (for aqueous electrolytic cells)

The active material (30 mg of CICOFA or CICOFB), a conductive additive (DENKA BLACK, Denka Co. Ltd., Japan) (3.75 mg), and a poly (tetrafluoroethylene) (PTFE) binder (6-J, Chemours-Mitsui Fluoroproducts Co. Ltd., Japan) (3.75 mg) were mixed at 8:1:1 mass ratio and kneaded with an agate mortar and pestle until a sheet material was formed. Disks of 13 mm diameter were prepared by molding and compressing (60 MPa) the sheet material in a powder-compressed tablet machine (Shimadzu Corporation, Japan) (see Figure 2.1).

3.2.4 Fabrication of electrodes (for supercapacitor cells with non-aqueous electrolytes)

SC cells were prepared from electrode films of the CICOFs. The films were deliberately thin to reduce the resistance, which increases with film thickness. An active material (CICOFA or CICOFB), carbon black (DENKA BLACK, Denka Company Limited, Japan), and a PVDF binder (W#9300, Kureha Corporation, Japan) were mixed at a mass ratio of 8:1:1. The mixture was stirred in NMP (Nacalai Tesque Inc., Japan) for 10 min. The obtained slurry was pasted onto an etched aluminum foil and was evacuated at 150 °C for 24 h to remove NMP from the carbon. The two activated carbons YP50F (coconut shell origin, physical activation with steam, Kuraray Chemical Co. Ltd., Japan), and MSP20 (phenol resin origin, chemical activation with KOH; Kansai Coke and Chemicals, Japan), and CNovel (MJ (4)030–00, MgO-templated carbons, TOYO TANSO, Co., Ltd., Osaka, Japan) were used as the reference electrodes in SC cells with non-aqueous electrolytes.

3.2.5 Electrochemical measurements (for aqueous electrolytic cells)

The working electrode was prepared by attaching the obtained disk-shaped electrode material to a titanium (Ti) mesh current collector, which was not dissolved in H_2SO_4 (see Figure 2.1). The electrochemical properties of the CICOFs were compared with those of the reference activated carbons, namely, YP50F, MSP20, and CNovel used for the production of porous carbons and SC electrode materials [3.10, 3.11]. The same fabrication process was applied to YP50F, MSP20 and CNovel. The mass of the active material in each electrode

disk was 37.5 mg. Although mass loading increases the SC electrodes' total resistance, it is required for avoiding mass error and evaluating the exact capacitance.

The electrochemical properties of the SC electrodes based on CICOFs were measured in a three-electrode system (with reference, counter, and working electrodes of Ag/AgCl, platinum, and a porous carbon, respectively). The electrolyte solution was 1.0 M H_2SO_4 (Nacalai Tesque Inc., Japan). Before measurement, the H_2SO_4 in the electrolytic cell was bubbled with N_2 gas for 30 min to remove the dissolved oxygen. CV, EIS, and GCD tests were performed on a VSP-300 system (BioLogic, France). CV tests were carried out in 0.2–0.8 V potential window at several sweep rates (1, 5, and 10 mV s^{-1}).

EIS measurements were conducted at 0 V and a sinusoidal 5.0 mV signal over 1.0 mHz to 1.0 MHz frequency range. GCD tests were performed within 0–0.8 V potential window at several current densities (50, 100, 200, 250, 500, 1000, 2000, and 5000 mA g^{-1}). From the GCD curves, the specific capacitance, C_g (F g^{-1}) [3.12] and double-layer capacitance, C_S (μF cm^{-2}) [3.12, 3.13] were calculated as follows:

$$C_{g(three)} = (I \times \Delta t)/(m \times \Delta V) \tag{3.3}$$

$$C_{S(three)} = C_{g(three)}/S_{BET} \tag{3.4}$$

where $C_{g(three)}$ and m are the gravimetric capacitance (F g^{-1}) and mass of the active material (g), respectively, on a single electrode, I is the discharge current (A), Δt is the discharge time (s), and ΔV is the potential window of the discharge voltage (V). All electrochemical tests were conducted at 25 °C, and the temperature was maintained in an incubator.

3.2.6 Electrochemical measurements (for supercapacitor cells with non-aqueous electrolytes)

The fabricated electrode was attached to an etched Al foil to adjust its dimensions to that of the test cell (HS Flat Cell, Hohsen Corporation, Japan). The electrochemical test cell comprised two symmetrical electrodes divided by a cellulose separator (TF40-50, Nippon Kodoshi Corporation, Japan). The electrolyte was a 1.0 M solution of $TEABF_4$ in PC

(LIPASTE-P/EAF 1N, Tomiyama Pure Chemical Industries Ltd., Japan). The test cell was assembled in an argon-filled glove box under oxygen at extremely low concentration, and the moisture was maintained below 1 ppm to prevent oxygen and moisture contamination.

The electrochemical performance was evaluated using a symmetric two-electrode system via GCD, EIS, and CV experiments, performed on a VSP3000 system (Biologic Science instruments). The CV was conducted in −2.0–2.0 V cell voltage range at 10 mV s^{-1}. GCD tests were conducted in 0–2.5 V cell voltage range at different current densities (40, 100, 500, 1000, 2000, and 5000 mA g^{-1}). The cell capacitance (F g^{-1}) was determined as

$$C_{\mathrm{g(two)}} = (I \times \Delta t)/(m \times \Delta V) \tag{3.5}$$

where $C_{\mathrm{g(two)}}$ is the gravimetric cell capacitance (F g^{-1}), m is the mass of the active material (g) on the amount of both positive and negative electrodes, and the other variables are as defined above. EIS measurements were conducted at 0 V and a sinusoidal 5.0 mV signal over the frequency range 10 mHz to 1.0 MHz. The equivalent circuit model was applied to the experimental EIS curves, resulting in the calculated EIS curves. The solution resistance (R_1), contact resistance (R_2), and diffusion resistance (R_{d3}) were separated from the total cell resistance to fit the calculated curves into the experimental ones. All electrochemical tests were conducted at 25 °C, and the temperature was maintained in an incubator.

The volumetric specific capacitance (F cm^{-3}) was calculated as

$$C_{\mathrm{U(three)}} = (I \times \Delta t)/(U \times \Delta V) \tag{3.6}$$

where $C_{\mathrm{U(three)}}$ and U are the volumetric specific capacitance (F cm^{-3}) and the volume of the electrode material (cm^3), respectively, on a single electrode.

The electrode bulk density (ρ, g cm^{-3}) was calculated as

$$\rho = M/U \tag{3.7}$$

where M and U are the mass of the electrode material (g) and the volume of the electrode material (cm^3), respectively on a single electrode.

3.3 Results and discussion

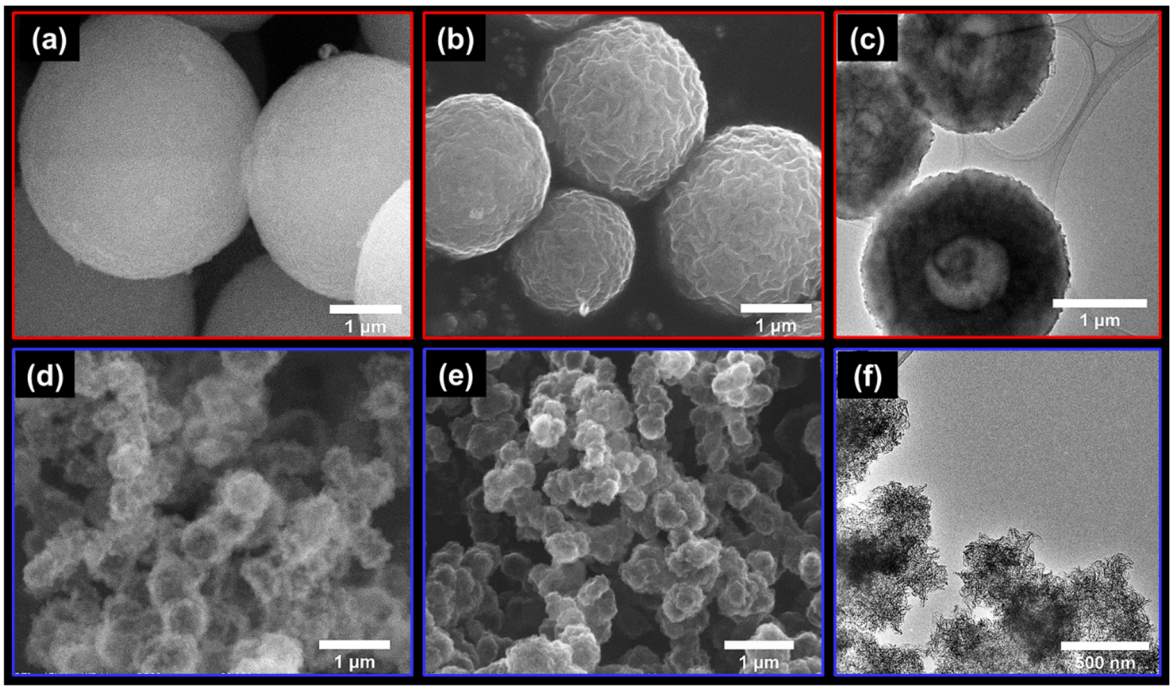

Figure 3.2 SEM images of (a) ICOFA, (b) CICOFA (1000 °C), (d) ICOFB, and (e) CICOFB (1000 °C), confirming that the particle with different sizes can be successfully prepared. TEM images of (c) CICOFA and (f) CICOFB.

The particle size was found to be successfully controlled by the above synthetic procedures, as can be seen in the SEM images of the ICOF particles (Figure 3.2 (a), (d)). The ICOFA particle size is larger than that of ICOFB. In ICOFB, acetic acid serves as a catalyst [3.14], promoting a faster reaction rate. Generally, a fast reaction rate can produce many small crystallites, resulting in small particle sizes. Figure 3.2 (b) and (e) show the SEM images of CICOFA and CICOFB, which were calcined at 1000 °C, respectively. It can be observed that the resultant carbon particle size is similar to that of the precursors. Interestingly, the two CICOF TEM images indicate a unique morphology (Figure 3.2 (c) and (f)). CICOFA particles formed spherical shell structures, whereas CICOFB particles formed numerous

spikes on their surfaces.

Figure 3.3 (a) shows the PXRD patterns for the ICOFs and CICOFs which were calcined at 1000 °C, indicating that the COF crystalline frameworks collapsed after carbonization. The ICOFs TG curves indicate that ICOFs decomposed approximately at 400 °C (Figure 3.3 (b)). Figure 3.3 (c), (d) show the nitrogen adsorption/desorption isotherms of the ICOFs and CICOFs which were calcined at 600 and 1000 °C. Based on the results, S_{BET} of ICOFA, ICOFB, CICOFA (1000 °C), and CICOFB (1000 °C) calculated to be 990, 1766, 499, and 1155 $m^2 g^{-1}$, respectively, as shown in Table 3.1. ICOFB has a larger S_{BET} than ICOFA, as small-sized particles have a larger geometrical surface area than large-sized ones. In both ICOFs, S_{BET} decreased after carbonization, suggesting that the ICOFs crystalline frameworks broke into amorphous carbons during carbonization. Figure 3.3 (e), (f) show the PSD of ICOFs and CICOFs. Interestingly, it was observed that the average pore size shifted toward a narrower pore size after carbonization in both ICOFs. This suggests that the ICOFs pores may have shrunk during carbonization, resulting in narrower pore size.

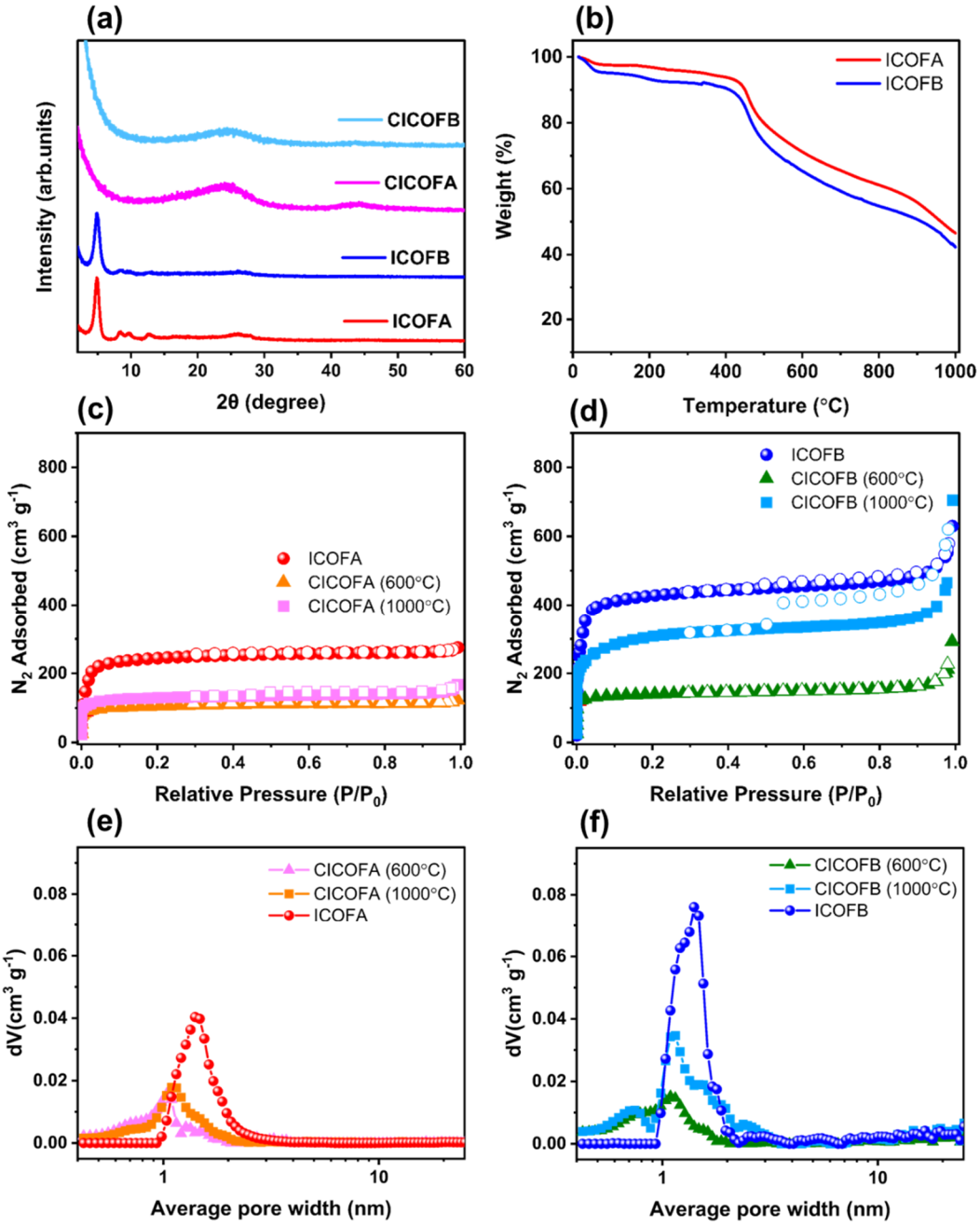

Figure 3.3 (a) PXRD patterns of ICOFs and CICOFs (1000 °C), (b) TG curves of ICOFA and ICOFB. Nitrogen isotherms (c) ICOFA and CICOFAs (600 and 1000 °C) and those of (d) ICOFB and CICOFBs (600 and 1000 °C). Average pore size distributions of (e) ICOFA and CICOFAs (600 and 1000 °C) and those of (f) ICOFB and CICOFBs (600 and 1000 °C).

Table 3.1 Pore characteristics of ICOFs, CICOFs, YP50F, and MSP20

Sample	S_{BET} ($m^2\ g^{-1}$)	S_{meso} ($m^2\ g^{-1}$)	V_{total} ($cm^3\ g^{-1}$)	V_{micro} ($cm^3\ g^{-1}$)	V_{meso} ($cm^3\ g^{-1}$)
ICOFA	990	77	0.42	0.41	0.08
ICOFB	1766	155	0.96	0.69	0.36
CICOFA (600 °C)	406	38	0.19	0.18	0.04
CICOFB (600 °C)	545	52	0.44	0.22	0.24
CICOFA (1000 °C)	499	41	0.26	0.22	0.07
CICOFB (1000 °C)	1155	176	1.03	0.49	0.63
YP50F	1600	133	0.76	0.70	0.15
MSP20	2266	148	1.00	1.02	0.12
CNovel	709	674	2.59	-	2.54

As shown in Figure 3.4 (a)–(f), the XP spectra of CICOFs confirmed that the direct carbonization of ICOFs could obtain N-doped carbons. Both CICOFA and CICOFB, which were prepared by carbonizing the two kinds of ICOFs at 600 °C and 800 °C, have two or three peaks (~398.4, ~400.6, and ~403 eV), showing the presence of pyridinic N, graphitic (quaternary) N, and oxidized N, respectively [3.2, 3.15] (Figure 3.5). Meanwhile, these peaks were not observed in the spectra of both CICOFB prepared by carbonizing ICOFB at 1000 °C. The content of nitrogen atoms was observed to diminish with increasing temperatures, as shown in Table 3.2. This is probably because gases such as NO_2, NH_3, and N_2 evolved as temperature increased to 1000 °C.

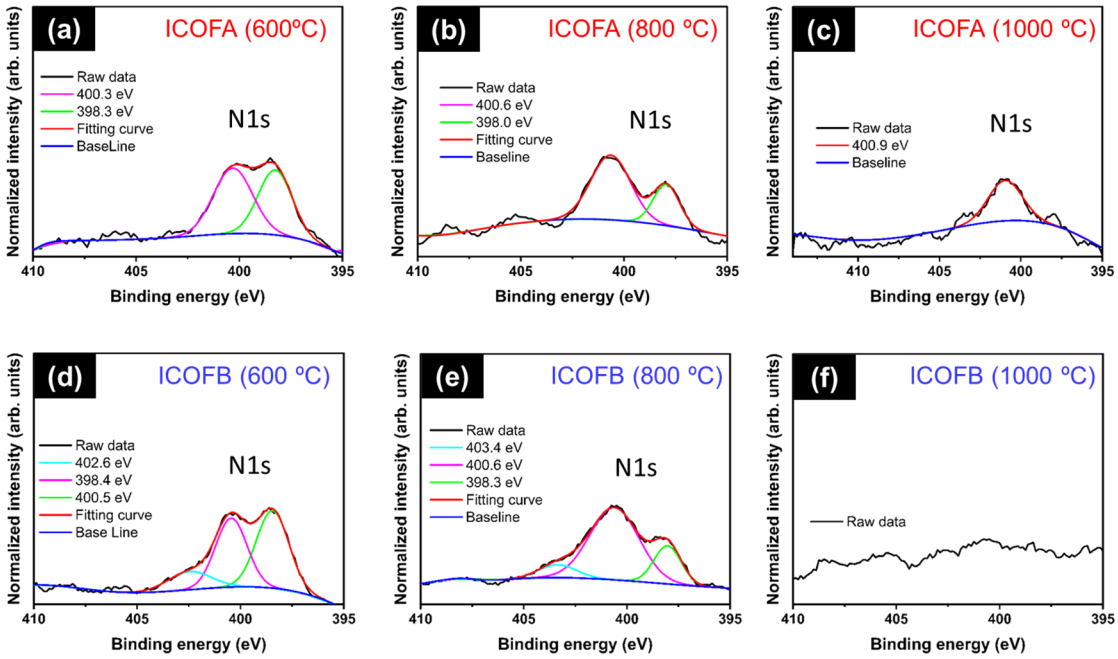

Figure 3.4 XP N1s spectra of CICOFA/CICOFB, which were prepared by carbonizing ICOFA/ICOFB at (a)/(d) 600, (b)/(e) 800, and (c)/(f) 1000 °C, respectively.

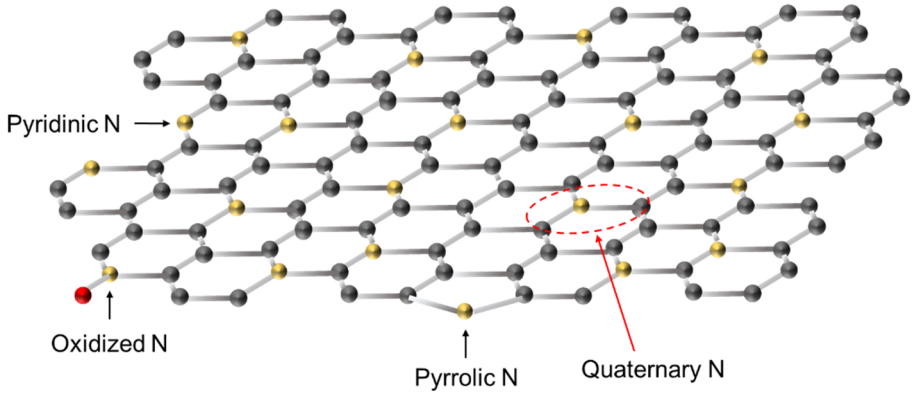

Figure 3.5 Conceivable bonding configurations for nitrogen atoms in CICOFs

Table 3.2 Molar ratios of C, O, and N atoms in CICOFs samples from XPS

Sample	Temperatures / °C	at % (XPS)		
		C	N	O
CICOFA	600	83.06	2.84	14.10
	800	85.51	2.95	11.54
	1000	89.89	2.30	7.81
CICOFB	600	80.72	3.04	16.24
	800	87.85	2.96	9.18
	1000	80.35	0.54	19.11

The electrochemical properties of CICOFs were evaluated fundamentally using the three-electrode system with an aqueous electrolyte (1.0 M H_2SO_4). As shown in Table 3.2, CICOFs, prepared by carbonizing ICOFs at 600 °C, hold approximately 3% of N atoms, the highest content among samples calcined at 600–1000 °C. Thus, the CICOFs calcined at 600 °C were employed to confirm whether the N-doping effect induces the pseudo-capacitance. The CICOFA and CICOFB GCD curves indicate distorted curves (Figure 3.6(a),(b)), which might be attributable to the pseudo-capacitive effect[3.16]. These results agree well with those calculated with redox reactions in chapter 2 (Figure 2.18). Figure 3.6 (c) and (d) show the CV curves of CICOFA and CICOFB, respectively, suggesting lower electrical conductivity in both samples. Based on the GCD curves, C_g of CICOFA and CICOFB at a current density of 50 mA g^{-1} are calculated to be 150.3 and 84.8 F g^{-1}, respectively. According to equations (3.3) and (3.4), C_s of CICOFA and CICOFB at the same current density are calculated to be 37.4 and 15.5 μF cm^{-2}, respectively. As shown in Table 3.3, CICOFA achieved an outstanding high charge density (37.4 μF cm^{-2}), compared with the three commercial porous carbons (YP50F, MSP20, and CNovel). This might be attributed to the pseudo-capacitive effect because the S_{BET} of CICOFs is relatively lower than that of other porous carbons. As discussed above, both CICOFs (calcined at 600 °C) indicate the presence of pyridinic N, which can induce the pseudo-capacitive effect [3.6, 3.7]. C_g and C_s of CICOFB are much lower than those of CICOFA. Figure 3.6 (e) shows the Nyquist plots of CICOFs, confirming that the spectra were similar to those simulated with different R_{ct}, as discussed in chapter 2 (Figure 2.25). The inset of Figure 3.6 (e) shows the enlarged Nyquist plots of CICOF samples, where semicircles can be observed in the high-frequency region. The corresponding semicircles reveal the presence of resistive and capacitive elements in parallel in the electrolytic cell based on the CICOFs. In these cases, the contact resistance between inter-particle gaps could be responsible for the semicircles. These results agree well with those calculated with inter-particle gaps in chapter 2 (Figure 2.26). Based on the SEM images of CICOFs particles (Figure 3.2), CICOFB particles are observed to be smaller than the CICOFA. This suggests that CICOFA's particle gaps might

be larger than those of CICOFB, leading to lower electrical conductivity. Furthermore, in the low-frequency region, a part of a large-sized semicircle can be observed in the Nyquist plot of CICOFB. Thus, CICOFB has much lower electrical conductivity than CICOFA. This can be confirmed from the capacitance retention results, as shown in Figure 3.6 (f). This can be explained by the lower bulk density (the larger thickness) of the CICOFB electrode compared with CICOFA, as shown in Table 3.3. Although the filling factor of the particle was geometrically the same ($\simeq 52.3\%$ (calculated from $(\pi/6)\times 100)$) regardless of the particle size (Figure 3.7), the actual bulk density of large-sized particles tends to be larger than that of small-sized particles. Smaller-sized particles aggregate with each other. This may result in much more voids and cause the larger thickness of the electrode.

Figure 3.8 shows 10000 cycling GCD curves of CICOFA and CICOFB electrodes, which were conducted at 1.0 A g^{-1}. Interestingly, the capacitance retention of CICOFA reached 134 % at 10000 cycles. This may be attributed to electrochemical activation [3.17].

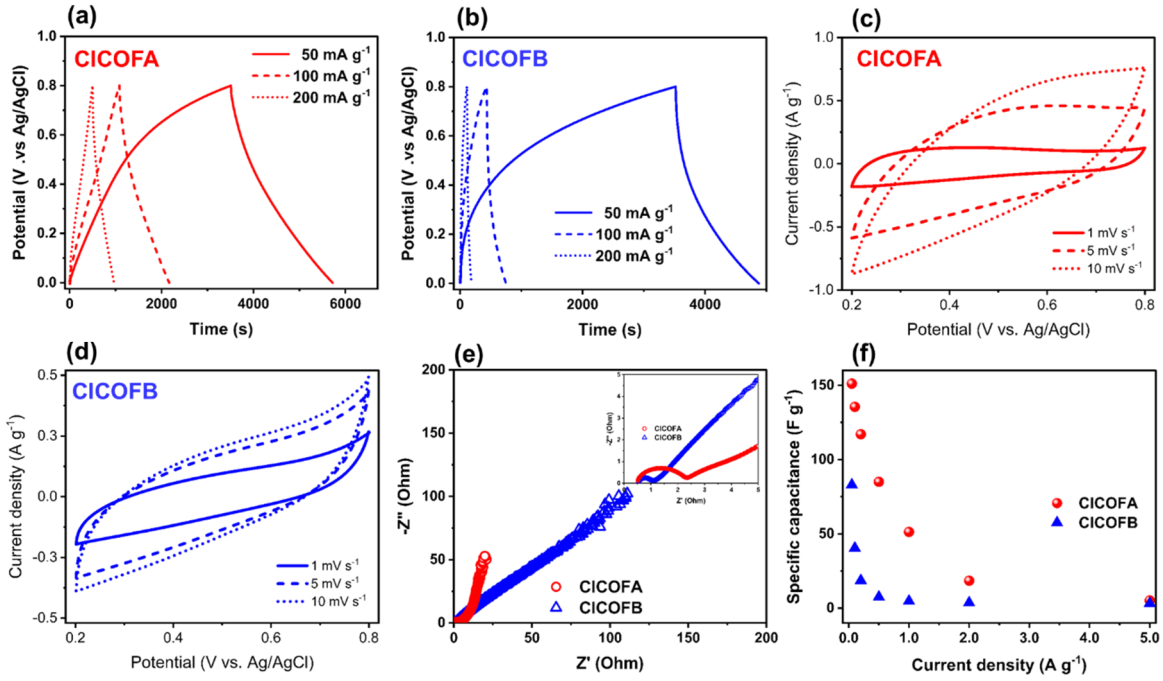

Figure 3.6 GCD/CV curves of (a)/(c) CICOFA and (b)/(d) CICOFB in 1 M H_2SO_4 solution at several current densities/sweep rates, confirming their capacitive behavior. (e) Nyquist plots of CICOFA (red, empty symbols) and CICOFB (blue, empty symbols) at 0 V and at an amplitude of 5.0 mV and frequencies ranging from 1.0 mHz to 1.0 MHz. (f) Specific capacitances of CICOFA (red), CICOFB (blue) in 1 M H_2SO_4 solution versus current density (50–5000 mA g^{-1})

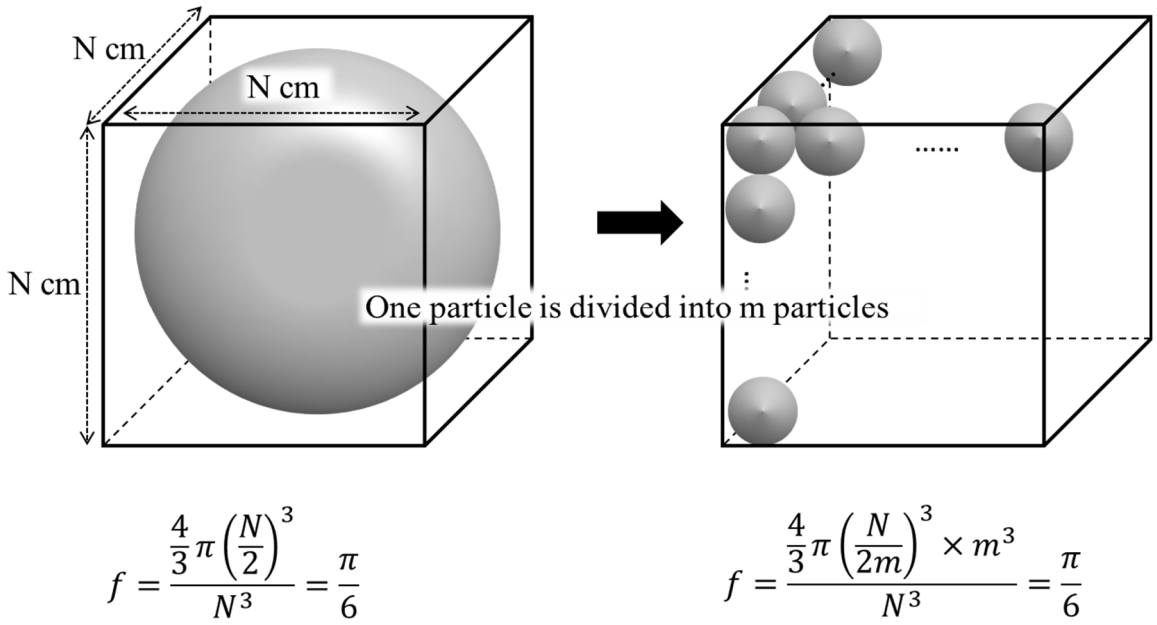

$$f = \frac{\frac{4}{3}\pi\left(\frac{N}{2}\right)^3}{N^3} = \frac{\pi}{6}$$

$$f = \frac{\frac{4}{3}\pi\left(\frac{N}{2m}\right)^3 \times m^3}{N^3} = \frac{\pi}{6}$$

Figure 3.7 Geometrical model of the filling factor when comparing small particles with large ones

Table 3.3 Pore characteristics, electrode bulk density (g cm^{-3}), and capacitances (C_g, C_U, and C_s) of CICOFs, YP50F, MSP20, and CNovel, showing the higher charge density (μF cm^{-2}) of CICOFA

Sample	S_{BET} (m^2 g^{-1})	Total pore volume (cm^3 g^{-1})	Bulk density (electrode) (g cm^{-3})	C_g (F g^{-1})	C_U (F cm^{-3})	C_S (μF cm^{-2})
CICOFA	406	0.19	0.90	152	112	37.4
CICOFB	545	0.44	0.68	85	46	15.6
YP50F	1600	0.79	0.68	222	122	13.9
MSP20	2318	1.00	0.60	307	149	13.5
CNovel	709	2.59	0.36	144	42	20.3

The C_g, C_U, and C_s of all the samples were determined at a current density of 50 mA g^{-1}.

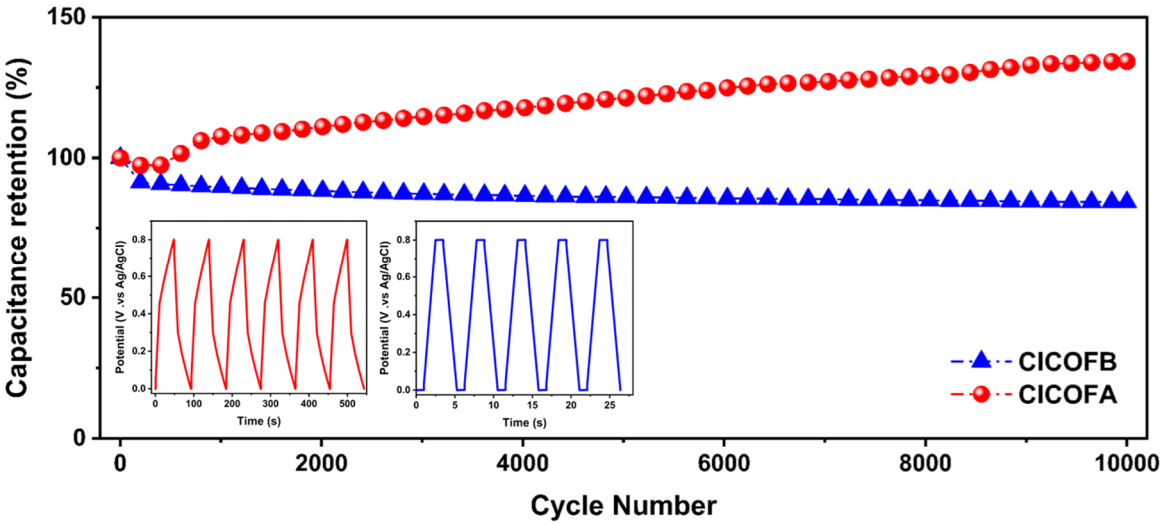

Figure 3.8 Cycling durability of CICOFA (red) and CICOFB (blue) over 10000 GCD cycles in 1M H_2SO_4 solution. Insets are typical GCD curves representing capacitive behavior.

The electrochemical properties based on CICOFs with non-aqueous electrolytes ($TEABF_4$ in 1.0 M PC) were briefly examined to confirm if the capacitive behavior differs from that with aqueous electrolytes. The samples prepared by carbonizing ICOFs at 1000 °C were employed as their S_{BET} values were largest among samples calcined at 600–1000 °C, as can be seen in Figure 3.3 and Table 3.1. Figure 3.9 (a) shows GCD curves of CICOFs indicating ideal capacitive behavior. Based on the GCD curves, the specific capacitance at 40 mA g^{-1} current density for CICOFA and CICOFB was calculated as 8.2 and 17.6 F g^{-1}, respectively. In both CICOFs-based capacitors, the ideal capacitive rectangular CV curves are observed in Figure 3.9 (b), showing that a pure EDL mainly induced the capacitance without pseudo-capacitive effects. Therefore, the specific capacitance of the two CICOFs in the (8.2 and 17.6 F g^{-1}) can be determined by the S_{BET} of the two samples (499 and 1155 m^2 g^{-1}). Figure 3.9 (c) shows CICOFs' capacitance retention at several current densities (40, 100, 500, 1000, 2000, and 5000 mA g^{-1}). CICOFB has better electrical conductivity than CICOFA. This agrees well with the EIS results. The Nyquist plots of both samples exhibited vertical lines in the low-frequency region, confirming their ideal capacitive behavior,[3.18] and their frequency range was 1.0 mHz to 1.0 MHz (Figure 3.9 (d)). In the high-frequency region, semicircles were observed in both curves, indicating that resistances were introduced by the

inter-particle gaps, the particle/current collector interfaces, and charge transfer.[3.19] The total resistance of the CICOFA electrolytic cell was higher than that of CICOFB. To provide a conceivable explanation for the difference, an equivalent circuit model (inset of Figure 3.9 (d)) was employed to separate the individual resistances, such as the solution resistance (R_1), contact resistance owing to particle gaps (R_2), and diffusion resistance (R_3), from the total cell resistance. M_3 indicates the restricted linear diffusion model [3.20]. R_1 was not so different between the two CICOF cells, whereas CICOFA's R_2 was much higher than that of CICOFB. This can be explained by the SEM images of both CICOFs, as can be seen in Figure 3.2 (b), (e). The CICOFA-based electrode material may have voids between particles, as the particles were large-sized spherical ones, resulting in the contact resistance. R_{d3} of CICOFA was much higher than that of CICOFB, as shown in Table 3.4. This is attributed to the particle gaps of the CICOFA-based electrode. However, CICOFB's diffusion time (t_{d3}) is much longer than CICOFA due to CICOFB's higher S_{BET} than CICOFA.

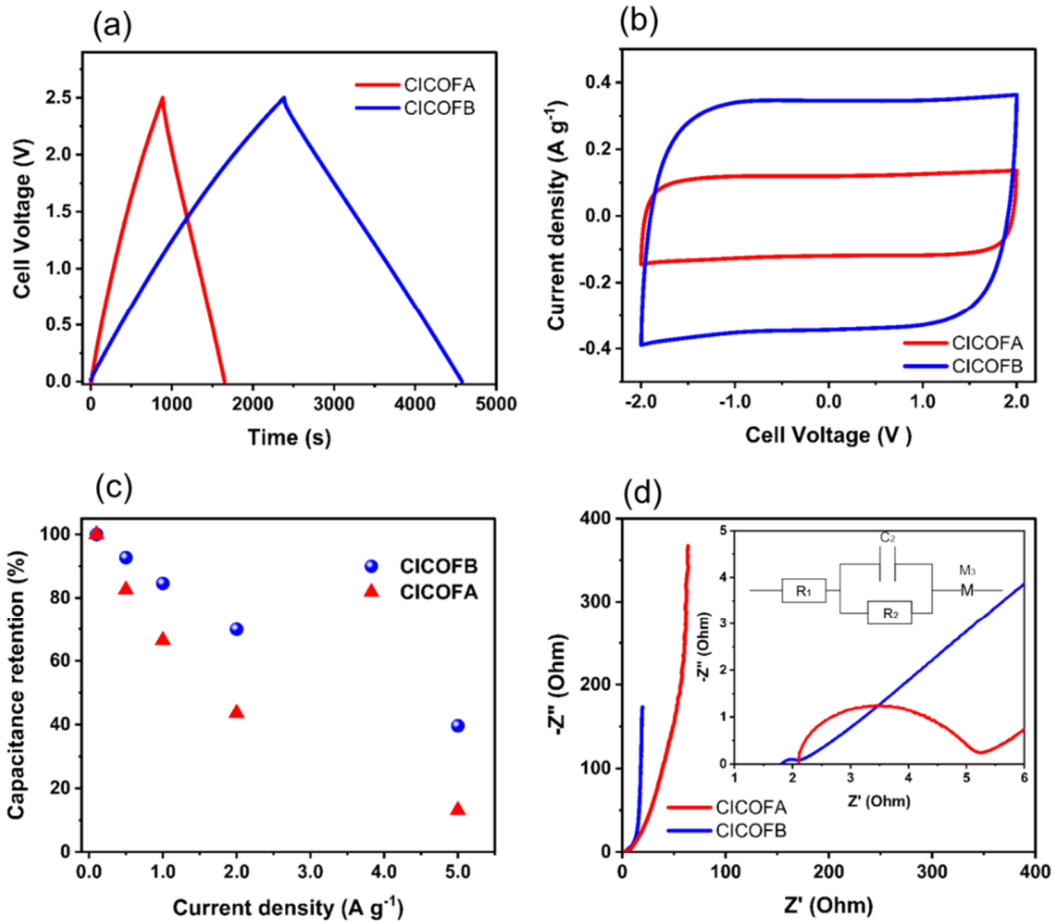

Figure 3.9 (a) GCD curves of the CICOFs in $TEABF_4$ solution at 40 mA g^{-1}, confirming their capacitive behavior. (b) CV curves of CICOFs in $TEABF_4$ solution at 10 mV s^{-1}, confirming their ideal capacitive rectangular curves. (c) Specific capacitances of CICOFs in $TEABF_4$ solution versus current density (50–5000 mA g^{-1}) (d) Nyquist plots of CICOFs at 0 V and at an amplitude of 5.0 mV and frequencies ranging from 1.0 mHZ to 10 MHz.

Table 3.4 Calculated values of the resistance, capacitance, and diffusion time by fitting the equivalent circuit model to the experimental EIS data.

Sample	R_1 (Ohm)	C_2 (μF)	R_2 (Ohm)	R_{d3} (Ohm)	t_{d3} (s)
CICOFA	2.16	0.633	2.705	71.66	16.73
CICOFB	1.84	26	0.296	32.13	28.18

3.4 Conclusion

Direct carbonization of ICOFs successfully produced multi-functional carbons, such as porous, nitrogen-doped, and core shell-structured carbons. Particle size was observed to be successfully controlled by adjusting synthetic conditions, which could determine the pore characteristics of the resulting carbons. Furthermore, N-doped CICOFA achieved higher charge density (37.4 μFcm^{-2}) than other porous carbons, owing to the N-doping effect. These results confirm that the direct carbonization of COFs produces various properties and that they will become a promising carbon precursor for multi-functional carbon materials. B-doped porous carbons, obtained from boron-based COFs, are discussed in the next chapter.

3.5 References

[3.1] L. Wang, Y. Han, X. Feng, J. Zhou, P. Qi, B. Wang, "Metal-organic frameworks for energy storage: Batteries and supercapacitors." Coord. Chem. Rev. **307**, 361–381 (2016).

[3.2] X. Zhang, G. Zhu, M. Wang, J. Li, T. Lu, L. Pan, "Covalent-organic frameworks derived N-doped porous carbon materials as anode for superior long-life cycling lithium and sodium ion batteries." Carbon. **116**, 686–694 (2017).

[3.3] S. Umezawa, T. Douura, Y. Yoshikawa, Y. Takashima, M. Yoneda, K. Gotoh, V. Stolojan, S. R. P. Silva, Y. Hayashi, D. Tanaka, "Supercapacitor electrode with high charge density based on boron-doped carbon derived from covalent organic frameworks." Carbon **184**, 418–425 (2021).

[3.4] V. Shrivastav, S. Sundriyal, P. Goel, H. Kaur, S. K. Tuteja, K. Vikrant, K.-H. Kim, U. K. Tiwari, A. Deep, "Metal-organic frameworks (MOFs) and their composites as electrodes for lithium battery applications: Novel means for alternative energy strage." Coord. Chem. Rev. **393**, 48–78 (2019).

[3.5] Y. Li, X. Xu, S. Hou, J. Ma, T. Lu, J. Wang, Y. Yao, L. Pan, "Facile dual doping strategy via carbonization of covalent organic frameworks to prepare hierarchically porous carbon spheres for membrane capacitive deionization." Chem. Commun. **54**, 14009–14012 (2018).

[3.6] F. Beguin, K. Szostak, G. Lota, E. Frackowiak, "A self-supporting electrode for supercapacitors prepared by one-step pyrolysis of carbon nanotube/polyacrylonitrile blends." Adv. Mater. **17**, 2380–2384 (2005).

[3.7] H. Chen, J. Chen, D. Chen, H. Wei, P. Liu, W. Wei, H. Lin, S. Han, "Nitrogen-and oxygen-rich dual-decorated carbon materials with porosity for high-performance supercapacitor." J. Mater. Sci. **54**, 5625–5640 (2019).

[3.8] V. Selvamani, R. Ravikumar, V. Suryanarayanan, D. Velayutham, S. Gopukumar, "Garlic peel derived high capacity hierarchical N-doped porous carbon anode for sodium/lithium ion cell." Electrochem. Acta. **190**, 337–345 (2016).

[3.9] S. Zhong, C. Zhang, D. Cao, "Zeolitic imidasolate framework-derived nitrogen-doped porous carbons as high performance supercapacitor electrode materials"Carbon. **85**, 51–59 (2015).

[3.10] H. M. Lee, K. H. An, S. J. Park and B. J. Kim, "Mesopore-rich activated carbons for

electrical double-layer capacitors by optimal activation condition." *Nanomaterials*, **9**, 608 (2019).

[3.11] Y. Kado, Y. Soneda, "Capacitor performance of MgO-templated carbons synthesized using hydrothermally treated MgO particles," Microporous Mesoporous Mater. **310**, 110646 (2021).

[3.12] L. Ling, M. Qing-Han, "Electrochemical properties of mesoporous carbon aerogel electrodes for electric double layer capacitors." J. Mater. Sci. **40**, 4105–4107 (2005).

[3.13] S. Shiraishi, M. Kibe, T. Yokoyama, H. Kurihara, N. Patel, A. Oya, Y. Kaburagi, Y. Hishiyama, "Electric double layer capacitance of multi-walled carbon nanotubes and B-doping effect." Appl. Phys. **A 82**, 585–591 (2005).

[3.14] C. Wu, X. Wang, T. Zhu, P. Li, S. Xia, "Covalent organic frameworks embedded membrane via acetic-acid-catalyzed interfacial polymerization for dyes separation: Enhanced permeability and selectivity." Chemosphere. **261**, 1–10 (2020).

[3.15] J. Zhou, J. Lian, L. Hou, J. Zhang, H. Gou, M. Xia, Y. Zhao, T. A. Strobel, L. Tao, F. Gao, "Ultrahigh volumetric capacitance and cyclic stability of fluorine and nitrogen co-doped carbon microspheres." Nat. Commun. **6**, 8503 (2015).

[3.16] Y. Jiang, J. Liu, "Definitions of pseudocapacitive materials: A brief review." Energy Environ. Mater. **0**, 1–8 (2019).

[3.17] B. H. Ka and S. M. Oh, "Electrochemical Activation of Expanded Graphite Electrode for Electrochemical Capacitor." J. Electrochem. Soc., **155**, A685–A692 (2008).

[3.18] C. Lei, N. Amini, F. Markoulidis, P. Wilson, S. Tennison and C. Lekakou, "Activated carbon from phenolic resin with controlled mesoporosity for electric double-layer capacitor (EDLC)."J. Mater. Chem. A, **1**, (2013).

[3.19] C. Lei, F. Markoulidis, Z. Ashitaka and C. Lekakou, "Reduction of porous carbon/Al contact resitance for an electric double-layer capacitor (EDLC)." Electrochim. Acta. **92**, 183–187, (2013).

[3.20] L. M. D. Silva, R. Cesar, C. M. R. Moreira, J. H. M. Santos, L. G. D. Souza, B. M. Pires, R. Vicentini, W. Nunes, and H. Zanin, "Reviewing the fundamentals of supercapacitors and the difficulties involving the analysis of the electrochemical findings obtained for porous electrode materials."Energy Stor. Mater. **27**, 555–590, (2020).

4 Facil synthesis of producing boron-doped porous carbons for supercapacitor electrodes with high charge density

4.1 Introduction

Porous carbon materials have attracted considerable attention owing to their high S_{BET}, good conductivity, and chemical and thermal stabilities, and they are promising for several practical applications. They can be employed as gas adsorbers, catalysts for the ORR in FCs, and electrode materials in LIBs and SCs [4.1–4.4]. Among the various methods for preparing porous carbons, the templated growth of carbon is particularly interesting. This method allows control over the pore size, morphology, and heteroatom configuration in the carbon matrix with a simple choice of a suitable template, such as a zeolite [4.5–4.8], a metal-oxide [4.9–4.12], or a MOF [4.13–4.15]. Several template removal procedures for producing pores in carbon material, however, still involve the use of dangerous acids like HF or HC. As a result, simplistic processes for fabricating template carbons have been extensively investigated to date.

In this study, the author developed a simple method for fabricating porous carbon by the calcination of COFs. COFs are a new class of porous materials made up of organic building blocks that are used to create a two-dimensional (2D) or three-dimensional (3D) polymer network with a precise porosity structure based on covalent bonds [4.16–4.20]. The covalent bonds of COFs can lead to high electrochemical durability and high resistance to acids or bases as compared to those of the coordination bonds of MOFs [4.20]. COFs have been reported to be suitable for introducing new redox functional groups, unlike MOFs [4.20]. Direct carbonization of COFs, such as MOFs, results in heteroatom-doped carbons because COF structures contain a variety of elements in addition to carbon, such as boron, nitrogen, and oxygen[4.21–4.26]. Further, graphitized carbon materials can be obtained via the carbonization of COFs with π–conjugated structures [4.20, 4.27]. The author created porous carbon in this study by carbonizing a boron-based COF with the theoretical formula $C_9H_4BO_2$ directly (referred to as COF-5) [4.16]. The resulting crude carbon could be washed with water, instead of a strong

acid, to remove the byproduct, B_2O_3. The technique of making porous carbon from COF-5 is depicted in Figure 4.1. COF-5 was first synthesized, then calcined at 1000 °C under nitrogen flow in this manner. Subsequently, the resultant carbon (referred to as CCOF-5) was washed with water to remove B_2O_3 and recover the boron-doped porous carbon (WCCOF-5). Finally, the author tested the electrochemical characteristics of the boron-doped carbon produced in an organic electrolyte, confirming its potential for application as an electrode material for SCs.

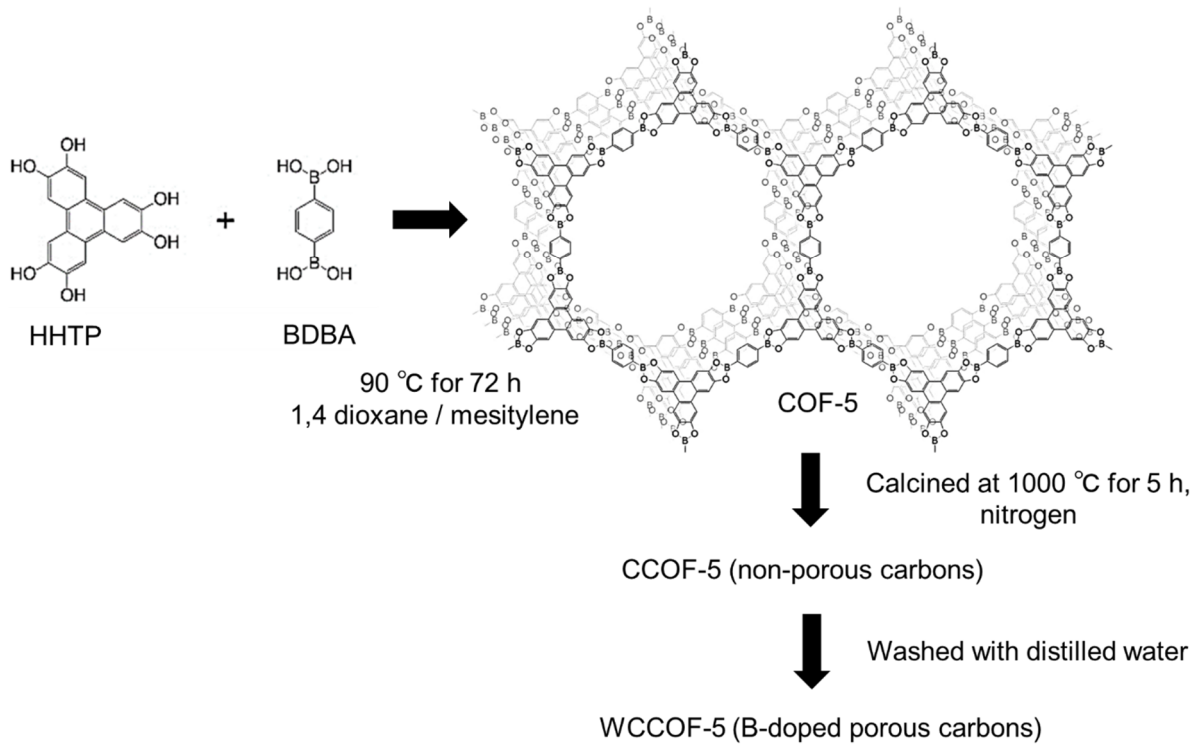

Figure 4.1. Schematic illustration of the preparation of COF-5, CCOF-5, and WCCOF-5.

4.2 Experimental procedures

4.2.1 Synthetic procedure

COF-5 particles were synthesized according to a previously reported procedure [[4.16] with slight modification. Briefly, 1,4-phenylenediboronic acid (BDBA; Tokyo Chemical Industry CO., Ltd., Tokyo, Japan), 2,3,6,7,10,11-hexahydroxytriphenylene hydrate (HHTP; Tokyo Chemical Industry CO., Ltd., Tokyo, Japan), and a mixed solution of 1,4-dioxane (Nacalai Tesque, Inc.) and mesitylene (Nacalai Tesque, Inc.) were added to a 100-mL beaker. To avoid contamination with oxygen and water, the mixture was sonicated for 30 min to obtain a homogenous suspension, and then transferred to a sealed 50-mL Teflon-lined autoclave under argon. The autoclave was heated to 90 °C and held there for 72 h. After that, the precipitate was transferred to a 1-L beaker and steeped for several days in 500 mL anhydrous acetone (5, 7, or 9 days). COF-5 was recovered as a gray powder after drying at 120 °C under vacuum for 12 hours.

4.2.2 Heating conditions

The COF-5 powder was placed in a ceramic boat and the boat was transferred to a furnace tube. It was then heated to 1000 °C, at a rate of 10 °C min^{-1}, under a nitrogen flow (flow rate: 200 mL min^{-1}). Under the same conditions, the temperature was kept constant at 1000 °C for 5 h. The sample was then allowed to cool to ambient temperature (18–25 °C). CCOF-5 is the name given to the resulting carbon.

4.2.3 Washing conditions

The CCOF-5 powder was suspended in 100-mL of distilled water in a beaker; the resulting mixture was sonicated in an ultrasonic bath for 30 min, and then left undisturbed for 24 h. Next, the supernatant was removed, and the precipitate was heated at 120 °C for 24 h to collect the product (WCCOF-5).

4.2.4 Preparation of electrode films

Before preparing the electrode films, the carbon material was washed with distilled water (WCCOF-5) and then pulverized into nanoparticles (referred to as PCCOF-5) by ball milling in water, using zirconium balls of two diameters: 0.5 and 1 mm. Then, the mixture of the zirconium balls and washed carbon was transferred to a zirconium pot, and distilled water was added to it. For 12 h, the pot was covered with a lid and spun at 400 rpm. The supernatant was then removed, and the final product was formed by heating the precipitate for 24 hours at 120 °C.

An electrode slurry was prepared by mixing the active material (PCCOF-5), carbon black (DENKA BLACK, Denka Company Limited), and a PVDF binder (W#9300, KUREHA CORPORATION) at a mass ratio of 8:1:1. The mixture was stirred in NMP (Nacalai Tesque, Inc.) for 10 minutes. To extract NMP from the carbon material, the resulting slurry was pasted onto an etched aluminum foil and vacuum-dried at 150 °C for 24 h. Two common types of activated carbon, YP50F (coconut shell origin, physical activation with steam, Kuraray Chemical Co., Ltd., Osaka, Amagasaki, Japan) and MSP20 (phenol resin origin, chemical activation with KOH, Kansai Coke and Chemicals, Japan), were used as reference materials for the porous carbon and SC electrodes, using the same procedure[4.28].

4.2.5 Material characterization

The morphology of each sample was characterized using SEM (JSM-6010LA, JEOL Ltd.) at 15-kV accelerating voltage, and TEM (JEM-2100F, JOEL Ltd.) at 200-kV accelerating voltage. The crystallinity of the resulting products was confirmed using PXRD (RINT-Ultima+ diffractometer, Rigaku) using Cu $K\alpha$ (λ = 0.154 nm) radiation. The degree of graphitization was evaluated using Raman spectroscopy (Raman, NRS-4500NMDS, JASCO) using a 532-nm excitation laser. The phase-change temperature of each sample was determined by TG–DTA (DTG-60, Shimadzu Corporation, Japan), which was performed at 10 °C min^{-1} under a 200 mL min^{-1} nitrogen flow. In the TG–DTA preparation, ~5 mg of the powdery sample was placed in the Pt holder. The surface functionalities of the samples were

examined by XPS (ESCA5700, ULVAC-PHI Inc., Japan) with Mg Kα$_1$ radiation at a 15 kV accelerating voltage. At 77 K, nitrogen adsorption/desorption isotherm measurements (BELSORP min, Microtrac-BEL) were taken to determine S_{BET} and PSD, as well as other pore structure parameters. The S_{BET} of the samples were estimated from the isotherms using the BET method (P/P_0 = 0.05–0.10). The isotherm types were determined based on the IUPAC definitions. S_{meso} was estimated using the BJH method. The total pore volume (V_{total}) and mesopore volume (V_{meso}) were calculated based on the BET and BJH methods, respectively. The NLDFT was used to calculate PSD. XPS was used to analyze the surface functionalities of the samples (JSP-9010MC, JEOL).

4.2.6 Electrochemical measurements

The fabricated electrode was roll-pressed and punched to adjust its dimensions to those of the test cell (HS Flat Cell, Hohsen Corp., Japan). The electrochemical test cell consisted of two symmetrical electrodes separated by a cellulose separator (TF40-50, NIPPON KODOSHI CORPORATION, Japan). A 1.0-M solution of $TEABF_4$ in PC (LIPASTE-P/EAF 1N, Tomiyama Pure Chemical Industries, Ltd., Japan) was used as the electrolyte. To avoid contamination from air and moisture, the test cell was built in an argon-filled glove box with a very low oxygen concentration and moisture kept below 1 ppm.

The electrochemical performance was evaluated using a symmetric two-electrode system via GCD tests, EIS, and CV, which were performed on a VSP3000 system (Biologic Science instruments). The specific capacitance, $C_{g(two)}$ (F g^{-1}) [4.29] and double-layer capacitance, $C_{S(three)}$ (μF cm^{-2}) [4.29, 4.30] were calculated as follows:

$$C_{g(two)} = (I \times \Delta t)/(m \times \Delta V) \quad (4.1)$$

$$C_{S(three)} = C_{g(two)}/S_{BET} \quad (4.2)$$

$$C_{g(three)} = 4 \times C_{g(two)} \quad (4.3)$$

where m is the mass (g) of the active material on a single electrode, I is the discharge current (A), Δt is the discharge time (s), and ΔV is the potential window of the discharge voltage (V). The volumetric specific capacitance (F cm^{-3}) was calculated as

$$C_{\mathrm{U(three)}} = (I \times \Delta t)/(U \times \Delta V) \tag{4.4}$$

where $C_{\mathrm{U(three)}}$ and U are the volumetric specific capacitance (F cm^{-3}) and the volume of the electrode material (cm^3), respectively, on a single electrode. $C_{\mathrm{U(three)}}$ was computed as

$$C_{\mathrm{U(three)}} = 4 \times \mathrm{C_{U(two)}} \tag{4.5}$$

The electrode bulk density (ρ, g cm^{-3}) was calculated as

$$\rho = M/U \tag{4.6}$$

where M and U are the mass of the electrode material (g) and the volume of the electrode material (cm^3), respectively on a single electrode.

CV was conducted in the cell voltage range of 0–2.5 V at different sweep rates (10, 20, 30, 40, and 50 mV s^{-1}). EIS was conducted at 0 V using a 5.0-mV sinusoidal signal over the frequency ranging from 100 mHz to 1.0 MHz. GCD tests were conducted in the cell voltage range of 0–2.5 V at different current densities (40, 50, 100, 200, 500, 1000, 2000, 5000, and 10000 mA g^{-1}). All these electrochemical tests were conducted at 25 °C, and the temperature was maintained using an incubator.

4.3 Results and discussion

COF-5 was synthesized through a solvothermal method, as reported elsewhere [4.16]. To begin, the surface area of COF-5 was increased by optimizing the synthesis conditions. A mixture of BDBA and HHTP in a solution of 1,4-dioxane and mesitylene was heated at 90 °C for 3 days, as illustrated in Figure 4.1. The precipitate obtained was subsequently soaked in acetone for several days (5–9 days) to remove impurities or HTTP remaining within the pores [4.16], and the resulting sample was dried at 120 °C under vacuum for 12 h. The COF-5 samples were divided into three groups based on how long they were exposed to acetone following synthesis (5, 7, or 9 days). The PXRD patterns of the three samples are shown in Figure 4.2(a), and they are very similar to those previously reported for COF-5[4.16]. Figure 4.2(b) shows the nitrogen adsorption/desorption isotherms of the three COF-5 samples treated for different times (5, 7, or 9 days); two sharp increments that correspond to the two PSD peaks are observed [4.16] (see Figure 4.2(c)). The treatment time affected the surface area of the sample. The sample soaked in acetone for 5 days showed an S_{BET} of ≈1392 $m^2 g^{-1}$, whereas that soaked for 7 days showed an S_{BET} of ≈1728 $m^2 g^{-1}$, comparable to that obtained in a previous study (1590 $m^2 g^{-1}$) [4.16]. Inadequate treatment leads to COF-5 with a reduced S_{BET}, as previously observed [4.16], due to guest molecules such as HTTP or other contaminants trapped inside the pores. The S_{BET} of the sample soaked in acetone for 9 days, on the other hand, fell to ≈1392 $m^2 g^{-1}$. The colorless supernatant turned brown after 9 days of treatment, showing that COF-5 was hydrolyzed to its precursors (HTTP and BDBA) by the minimal quantity of water present in acetone when soaked for an extended period of time [4.31]. Therefore, the samples treated for 5 or 7 days were selected for further studies.

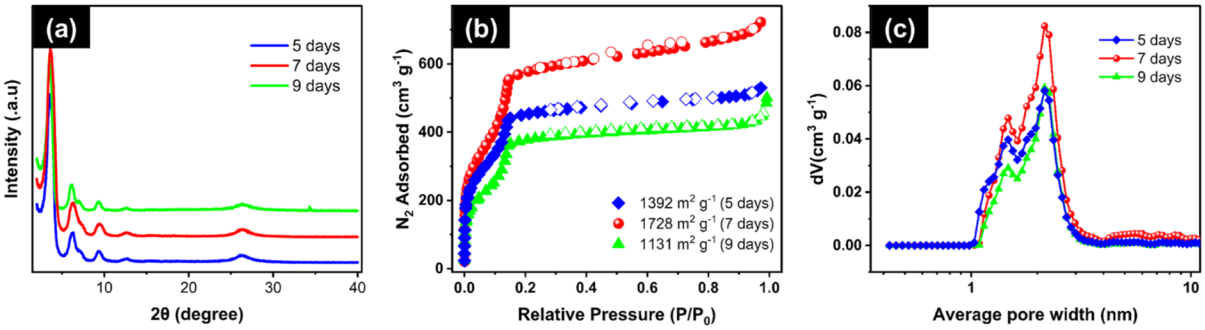

Figure 4.2 (a) Powder X-ray diffraction patterns, (b) nitrogen adsorption/desorption (solid/empty symbols) isotherms, and (c) Average pore size distributions of the three COF-5 samples (the average pore width is shown on a semilogarithmic scale).

The thermal stability of COF-5 was assessed via TG measurements. The TG curve of COF-5 indicates that its thermal decomposition occurs at ~600 °C (Figure 4.3). Its good thermal stability stems from the higher B–O bond energy (516 kJ mol^{-1}) than that of C–C (345 kJ mol^{-1}), and the formation of B_2O_3, which fixes oxygen and reduces carbon loss during thermal decomposition [4.32]. As a consequence, COF-5 was calcined at 1000 °C in the presence of nitrogen, and the resulting carbon (CCOF-5) was washed with water to remove B_2O_3 and recover the boron-doped porous carbon (WCCOF-5).

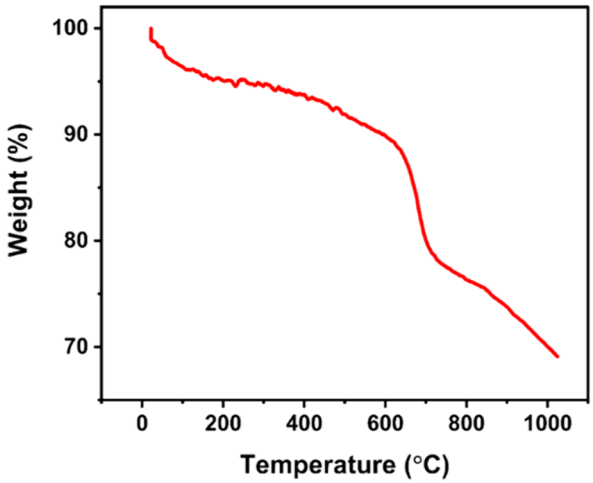

Figure 4.3 Thermogravimetric curve of COF-5

Figure 4.4(a), (b), and (c) show the SEM images of COF-5, CCOF-5, and WCCOF-5, respectively. The SEM image of COF-5 shows crystalline nanorod aggregates.

Furthermore, the particle size of CCOF-5 and WCCOF-5 did not change considerably following carbonization and water washing.

CCOF-5 nanoparticles were discovered to be somewhat larger than WCCOF-5 nanoparticles, which could be due to the presence of B_2O_3 in their structure. The TEM images of WCCOF-5 in Figure 4.4(d) and (e) indicate some degree of graphitization; several ordered layers are observed, consistent with the 002 reflections of graphite. This may be attributed to the distance between adjacent layers in COF-5 (3.46 Å, d_{001} interlayer spacing) [4.16], which is similar to that of graphite layers (3.35 Å, d_{002} interlayer spacing). Figure 4.4(f) shows the Raman spectra of CCOF-5 and WCCOF-5, which provided some information on the crystallinity of the carbon materials. The intensity ratios of the D band (1350 cm^{-1}) to G (1590 cm^{-1}) band (I_G/I_D) of both the samples were similar at 0.99 (CCOF-5) and 0.98 (WCCOF-5). Further, the Raman spectra of both the samples showed a peak corresponding to the 2D band (2600–2800 cm^{-1}), indicating several layers of graphene with a short-range order [4.33].

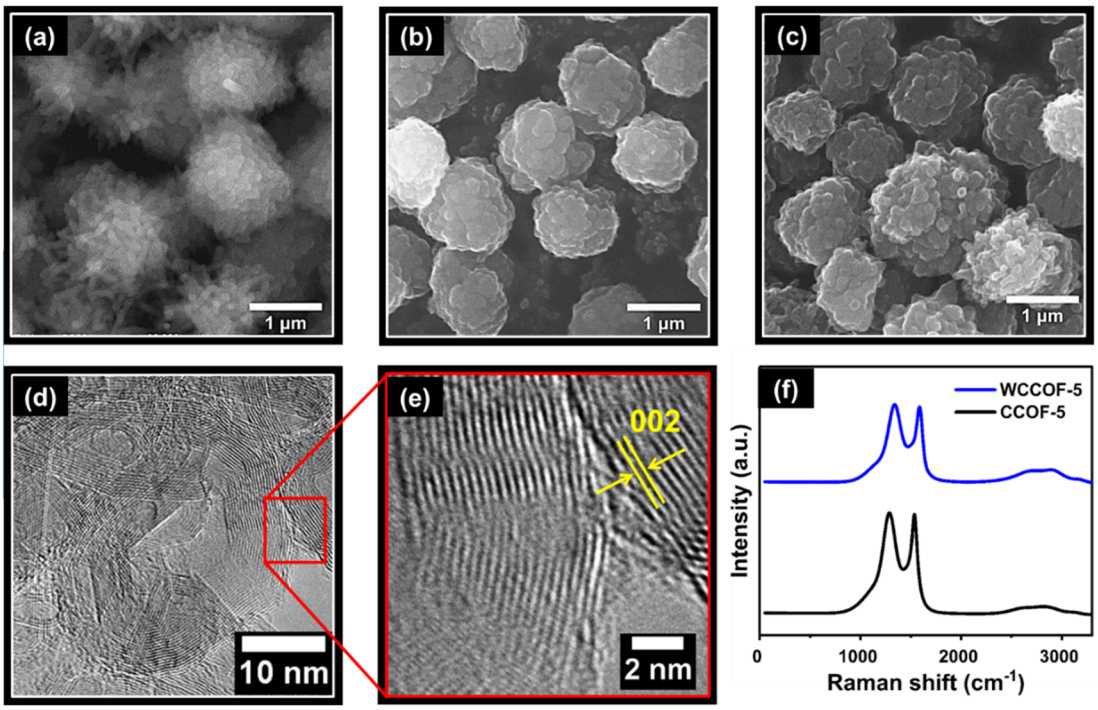

Figure 4.4 SEM images of (a) COF-5, (b) CCOF-5, and (c) WCCOF-5. (d) TEM image of WCCOF-5 and (e) an enlarged TEM image of the portion enclosed by a square in (d). (f) Raman spectra of CCOF-5 and WCCOF-5.

Figure 4.5(a) and (b) show the nitrogen adsorption/desorption isotherms and PSDs, respectively, of COF-5, CCOF-5, and WCCOF-5. The pore properties of these samples are shown in Table 4.1. As demonstrated in Figure 4.5(a), (b), and (c), the structure of CCOF-5 differs dramatically from that of COF-5. CCOF-5 has a type-II isotherm (Figure 4.5(a), (d)), which is typical of non-microporous materials[4.34]. Two possible reasons for this drastic decrease in the S_{BET} of CCOF-5 are (i) pore shrinkage during carbonization and (ii) the reaction of certain boron atoms with oxygen to form B_2O_3 clusters, leading to the blockage of the pore openings. The S_{BET} of WCCOF-5, which was produced from non-porous CCOF-5, increased to 774 $m^2\ g^{-1}$, indicating that pores were formed when CCOF-5 was washed with distilled water. Further, the average pore width of WCCOF-5 was found to be smaller than that of COF-5, as shown in Figure 4.5(b).

Table 4.1 Specific surface area (S_{BET}) of COF-5, CCOF-5, and WCCOF-5 according to the acetone treatment time, confirming the increased surface area after B_2O_3 removal from CCOF-5

Sample	Treatment time (days)	S_{BET} (COF-5) ($m^2\ g^{-1}$)	S_{BET} (CCOF-5) ($m^2\ g^{-1}$)	S_{BET} (WCCOF-5) ($m^2\ g^{-1}$)
1	5	1081	15	774
2	5	1359	77	709
3	5	1392	84	533
4	7	1658	95	550
5	7	1728	26	525

The size of the B_2O_3 nanocrystals in CCOF-5 can be determined to a certain degree of accuracy using the Debye–Scherrer equation shown below [4.35]:

$$D = (\mathrm{K}\lambda)/\beta cos\theta \quad (4.7),$$

where D is the crystallite size, K is a form factor (Scherrer constant), β is the full-width at half maximum (FWHM), and θ is the diffraction angle. In this study, β values were estimated as 1.1 and 0.6 for the two peaks observed at 2θ of 15.2° and 28.2°, respectively. λ is 0.154 nm. K is a form factor (0.3–0.9) that depends on the method employed to determine the thickness of the crystal. Using these values, D was found to be in the range of 2.5–7.5 nm and 4.4–13.2 nm, respectively. The PSD of the three WCCOF-5 samples (Figure 4.5 (e)), which had mesopores with pore sizes ranging from 2 to 10 nm, is within the range of the B_2O_3 nanocrystal sizes predicted using the Scherrer equation. After the water treatment, B_2O_3 nanocrystals may have been removed, leaving mesopores (2–10 nm) in the carbon (WCCOF-5). These results are further supported by the PXRD patterns of CCOF-5 and WCCOF-5 (Figure 4.5(c)). Some peaks in the PXRD pattern of CCOF-5 agree with those of the commercial B_2O_3 powder (Figure 4.5(f)). In the PXRD pattern of WCCOF-5, however, there are no peaks attributed to B_2O_3, showing that B_2O_3 was eliminated from

CCOF-5 after washing with distilled water, resulting in a porous carbon structure. Boron atoms in carbon frameworks have been reported to evaporate upon heating up to 1100 °C [4.22]. However, residual boron oxides (B_xO_y) were discovered in CCOF-5, which could not be eliminated by calcination under the author's experimental conditions. At temperatures below 1000 °C, boron is known to be more reactive to oxygen than carbon, according to the Ellingham diagram[4.36, 4.37]. Thus, in this study, the boron atoms, located at the edge of the carbon frameworks, may have readily reacted with a small number of oxygen atoms during or after carbonization.

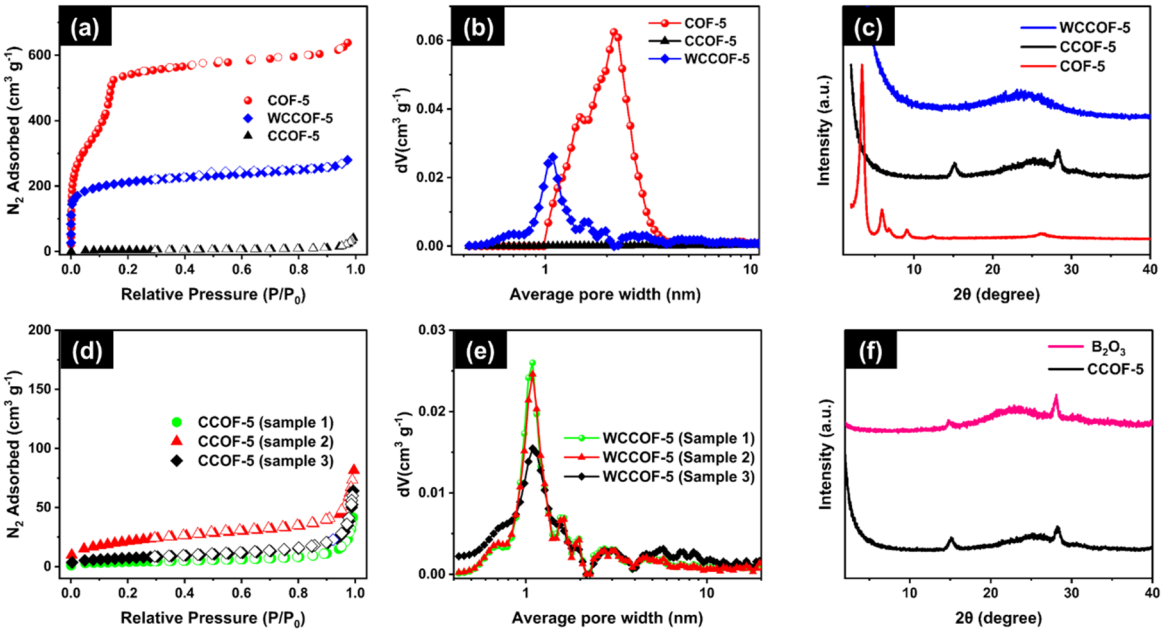

Figure 4.5 (a) Nitrogen adsorption/desorption (filled/empty symbol) isotherms of COF-5, CCOF-5, and WCCOF-5. (b) Average pore size distributions and (c) Powder X-ray diffraction patterns of each sample, showing pore generation after the removal of B_2O_3 from CCOF-5. (d) Nitrogen adsorption/desorption (filled/empty symbols) isotherms of the three CCOF-5 samples. (e) PSDs of the three WCCOF-5 samples (average pore width is shown on a semilogarithmic scale). (f) Powder X-ray diffraction patterns of CCOF-5 and a commercial B_2O_3 powder.

XPS was conducted to confirm the chemical bonding state of the boron atoms in CCOF-5 and WCCOF-5 (Figure 4.6(a) and (b)). The B 1s spectrum of CCOF-5 could be deconvoluted into two peaks located at 191.0 and 192.0 eV, which are attributed to boron in BC_2O and BCO_2, respectively [4.32, 4.38]. Similarly, the B 1s spectrum of WCCOF-5 also contained two peaks attributable to the same linkages at 190.8 and 192.4 eV [4.32, 4.38]. Based on these results, the BC_2O/BCO_2 molar ratios of CCOF-5 and WCCOF-5 were estimated to be 44/56 and 74/26, respectively. This finding indicates that the amount of boron that was combined with oxygen decreased after the water treatment process.

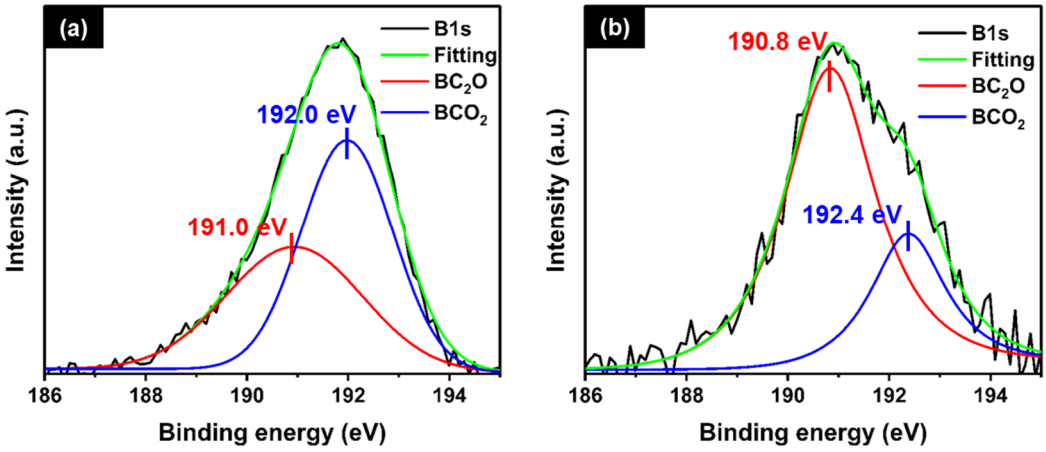

Figure 4.6 XP C1s spectra of (a) CCOF-5 and (b) WCCOF-5, revealing the presence of boron atoms combined with carbon atoms of the resulting carbon structures.

The electrochemical properties of the obtained carbons were evaluated as electrode materials for SCs to demonstrate their potential in energy storage devices. This was accomplished by pulverizing WCCOF-5 to obtain nanoparticles (PCCOF-5) appropriate for producing SC electrode films. In these tests, two types of common activated carbon materials (YP50F and MSP20) were employed as controls. YP50F and MSP20 are produced via physical activation with H_2O-steam and chemical activation with KOH, respectively. Figure 4.7 shows more information on their pore characteristics and electrochemical properties. The CV curves of PCCOF-5 recorded at various sweep rates are shown in Figure 4.8(a); they have approximately rectangular forms, demonstrating excellent capacitive behavior. As shown in Figure 4.8(b), the Nyquist plot of PCCOF-5 exhibits a nearly vertical line in the low-frequency region, indicating EDL capacitive behavior [4.39]. In the high-frequency region, the observed combination of semicircles suggests gaps between the particles, particle/current collector interface, and charge transfer [4.40]. The GCD curves of PCCOF-5 at different current densities in the 0–2.5 V cell voltage range (Figure 4.8(c)) are linear, demonstrating capacitive charging or discharging behavior.

Table 4.2 shows the pore characteristics and specific capacitances (C_g and C_S) of PCCOF-5, YP50F, and MSP20 at a current density of 40 mA g^{-1}. Among the evaluated samples, PCCOF-5 exhibited the lowest specific capacitance (C_g). This is because PCCOF-5 has a lower S_{BET} for all three groups of samples (510, 607, and 689 m^2 g^{-1}) compared to those of YP50F (1670 m^2 g^{-1}) and MSP20 (2318 m^2 g^{-1}) (see Table 4.2). However, the C_g of PCCOF-5 (≈82.9 F g^{-1}) is similar to that of YP50F (~99.6 F g^{-1}) despite its smaller surface area (≈689 m^2 g^{-1}) compared to that of YP50F (1670 m^2 g^{-1}). In comparison to YP50F and MSP20, these findings suggest that PCCOF-5 has a better-optimized pore structure that is only available to electrolyte ions. As a result, PCCOF-5 exhibited the highest double-layer capacitance (C_S) of 15.3 μF cm^{-2} at a current density of 40 mA g^{-1}. This value is more than twice the values reported for the two types of activated carbon (C_S of 6.0 μF cm^{-2} for YP50F and C_S of 6.9 μF cm^{-2} for MSP20) under identical conditions. The presence of a boron atom in PCCOF-5 also resulted in a higher charge density. This is

due to the deficiency of electrons in the boron, which may attract anions to the electrode surface, resulting in a pseudo-capacitive behavior [4.42, 4.43]. Notably, the electrode bulk density of all PCCOF-5 samples was higher than that of other two activated carbons (YP50F and MSP20), as shown in Table 4.2. Figure 4.8(d) and (e) show the C_g and C_s, respectively, of PCCOF-5, YP50F, and MSP20 at different current densities (0.05–10 A g^{-1}), which exhibit similar tendencies of the change in capacitance with the current density. According to these results, the specific capacitance (C_g) can be further enhanced by increasing the S_{BET} and the number of boron atoms in the carbon framework.

Table 4.2 Pore characteristics, electrode bulk density (g cm^{-3}), and capacitances (C_U, C_g and C_s) of PCCOF-5, YP50F, and MSP20, showing the higher charge density (μF cm^{-2}) of PCCOF-5

Carbon	S_{BET} (m^2 g^{-1})	Total pore volume (cm^3 g^{-1})	The bulk density (electrode) (g cm^{-3})	C_U (F cm^{-3})	C_g (F g^{-1})	C_S (μF cm^{-2})
PCCOF-5	607	0.80	0.77	43.8	71.2	11.7
	689	0.65	0.85	56.3	82.9	12.0
	510	0.38	0.71	43.4	78.0	15.3
YP50F	1670	0.79	0.70	52.7	99.6	6.0
MSP20	2318	1.00	0.58	72.9	159.2	6.9

C_U, C_g, and C_s of all the samples were determined at a current density of 40 mA g^{-1}.

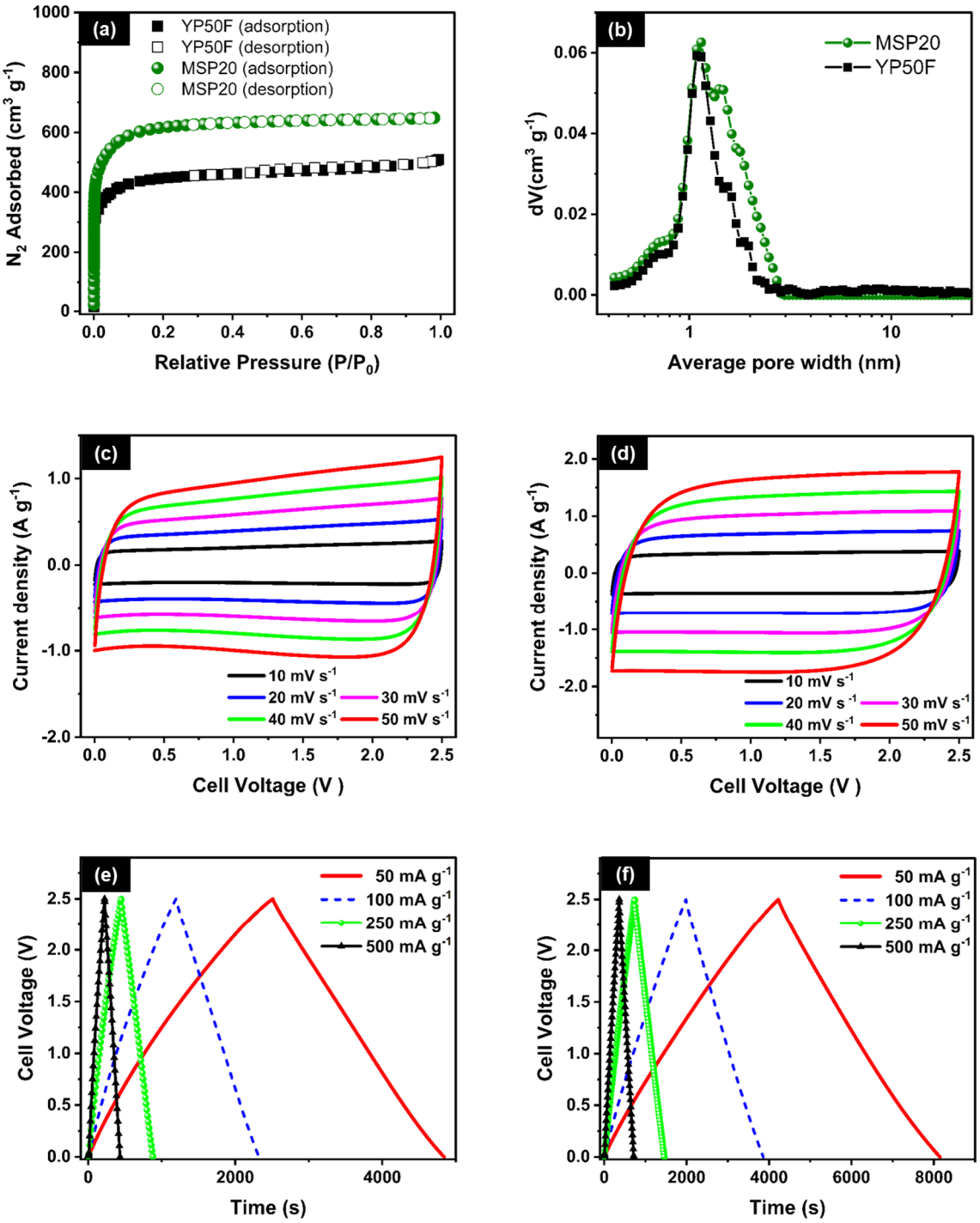

Figure 4.7 (a) Nitrogen adsorption/desorption (filled/empty symbol) isotherms of YP50F (black) and MSP20 (green). (b) Average pore size distribution of each samples. Cyclic voltammograms of (c) YP50F and (d) MSP20 recorded at 10–50 mV s^{-1}. GCD curves of (e) YP50F and (f) MSP20 in 1.0 M $TEABF_4$ in PC at 50–500 mA g^{-1}.

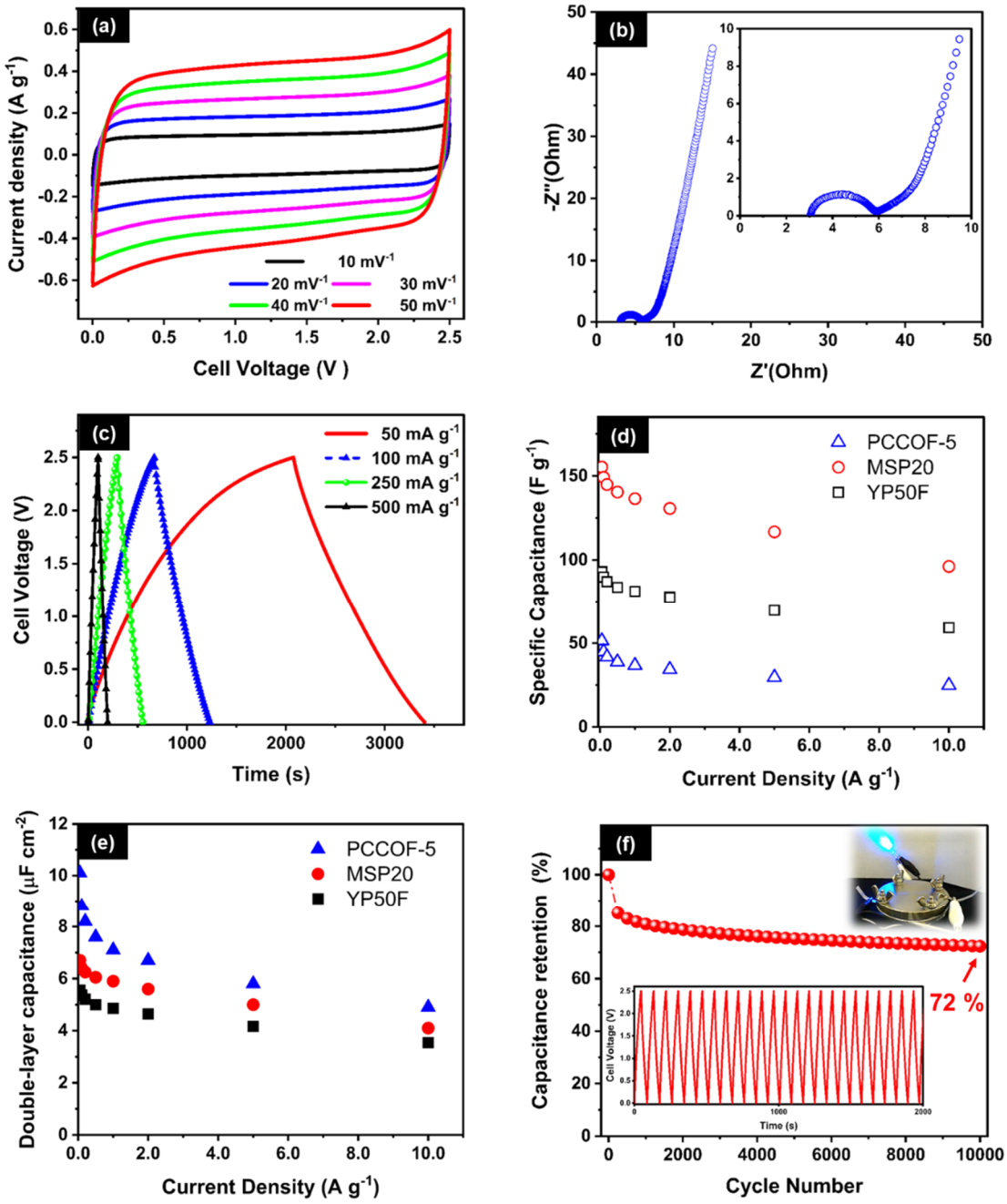

Figure 4.8 (a) Cyclic voltammograms recorded at 10–50 mV^{-1}. (b) Nyquist plots obtained at 0 V and 5.0 mV amplitude in the frequency ranging from 100 mHz to 1.0 MHz. (c) GCD curves of PCCOF-5 in 1.0 M $TEABF_4$ in PC at 50–500 mA g^{-1}. (d) Specific capacitance (C_g) and (e) Double-layer capacitance (C_s) of PCCOF-5, YP50F, and MSP20 recorded at 0.05–10 A g^{-1}. (f) Cycling durability over 10000 GCD cycles. The inset graph shows the GCD curves during the cycling test and the inset photograph at the top (right) shows a blue LED of 2.5 V powered by a supercapacitor based on PCCOF-5 after a few seconds of charging.

The inset of Figure 4.8(f) shows a blue light-emitting diode (LED) powered by an SC based on PCCOF-5, successfully demonstrating the feasibility of applying COF-5 as a SC electrode material. Figure 4.8(f) demonstrates the capacitance retention of 72% after 10000 cycles of GCD at a current density of 1.0 A g^{-1}. A steep decrease in the capacitance retention was observed up to ~250 cycles, which may be attributed to the electrolyte remaining within the pores of the electrode during repeated charge/discharge cycles or the decomposition of the organic electrolyte [4.44]. The pore size tunability is desirable for SC electrodes. Therefore, other boron-based COFs should be designed and synthesized for tuning the pore size of boron-doped porous carbon materials for SC electrodes.

Note that the electrochemical properties, that is, EIS and GCD characteristics of the samples changed dramatically after WCCOF-5 pulverization. Figure 4.9 (a) shows the Raman spectra of WCCOF-5 and PCCOF-5. The intensity ratios of the D (1350 cm^{-1}) and G (1590 cm^{-1}) bands (I_G/I_D) for the two samples are similar at 0.98 (WCCOF-5) and 0.97 (PCCOF-5), suggesting that the degree of graphitization did not significantly change after pulverization. However, as indicated in Table 4.3, the total pore volumes of all PCCOF-5 samples increased after pulverization. After pulverization, the sample's electrochemical characteristics (GCD curves and Nyquist plots) drastically changed. In particular, the specific capacitance (C_g) and double-layer capacitance (C_s) increased after pulverization (Figure 4.9(b),(c), and Table 4.3). This may be attributed to the mesopore volume differences and the reduced contact resistance between the particles. Possibly, WCCOF-5 contained a certain amount of residual B_2O_3 that could not be removed during the initial treatment. As a result of pulverizing the WCCOF-5 particles with water, the remaining B_2O_3 clusters were removed. This resulted in mesoporosity, which is suitable for accommodating electrolytes. Furthermore, the presence of boron atoms in the pulverized carbon sample (PCCOF-5) induced the pseudo-capacitive effect, which was confirmed by XPS (Figure 4.9 (d)).

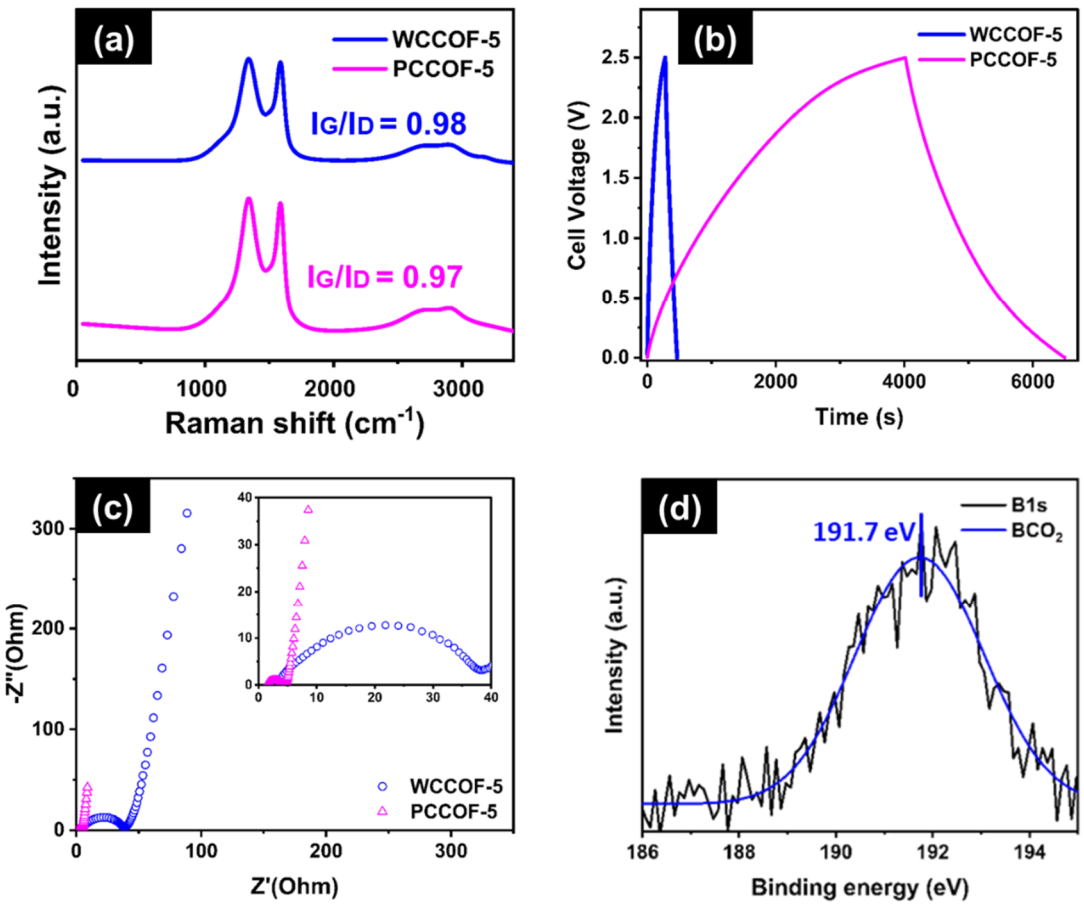

Figure 4.9 (a) Raman spectra, (b) GCD curves, (c) Nyquist plots for WCCOF-5 and PCCOF-5, and (d) XP C1s spectrum of PCCOF-5.

Table 4.3 Pore characteristics and specific capacitance of WCCOF-5 and PCCOF-5

Sample	Carbon	S_{BET} ($m^2\ g^{-1}$)	Mesopore volume ($cm^3\ g^{-1}$)	Total pore volume ($cm^3\ g^{-1}$)	C_g ($F\ g^{-1}$)	C_S ($\mu F\ cm^{-2}$)
1	WCCOF-5	533	0.11	0.30	7.2	1.4
	PCCOF-5	607	0.64	0.80	71.2	11.7
2	WCCOF-5	550	0.31	0.12	26.0	4.7
	PCCOF-5	689	0.47	0.65	82.9	12.0
3	WCCOF-5	525	0.15	0.33	26.0	5.0
	PCCOF-5	510	0.24	0.38	78.0	15.3

The decreased contact resistance was confirmed by the EIS results obtained before and after pulverization (Figure 4.9(c)). The WCCOF-5 aggregates were successfully crushed to PCCOF-5 nanoparticles, as shown by the SEM images in Figure 4.10(a), (b). The SEM images of the electrode films of the two samples (Figure 4.10(c) and (d)) reveal that the PCCOF-5 particles are better linked than the WCCOF-5 particles.

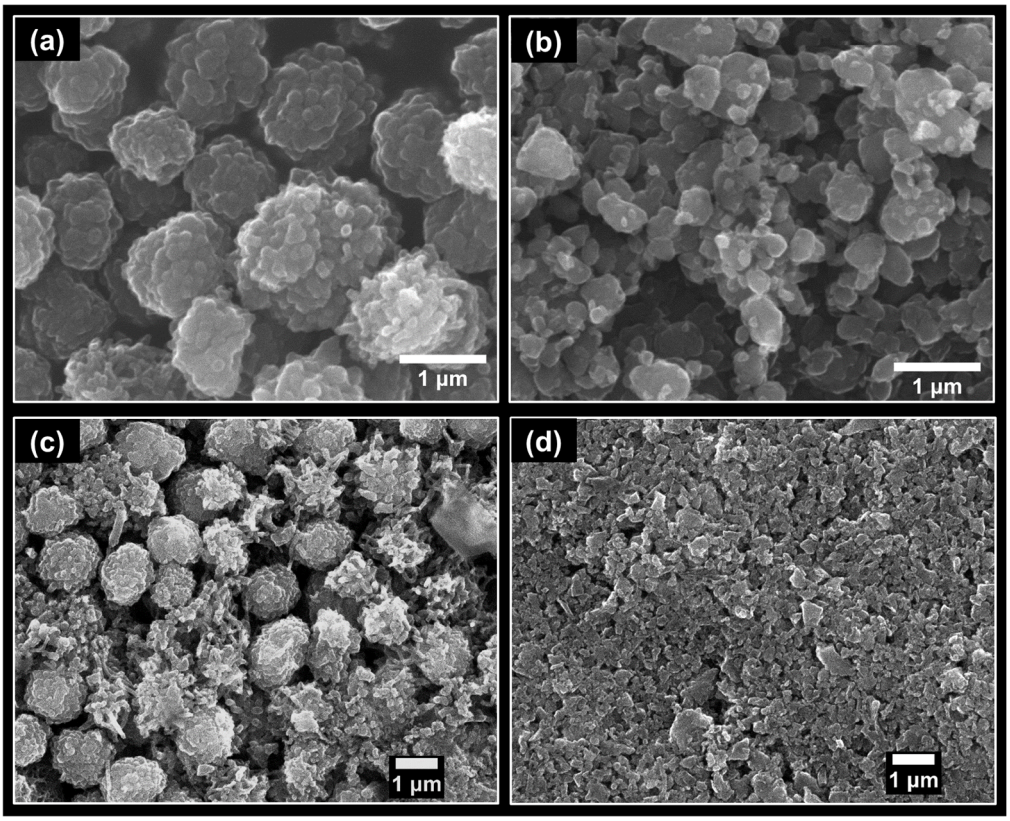

Figure 4.10 SEM images of (a) WCCOF-5 particles and (b) PCCOF-5 particles, confirming that WCCOF-5 aggregates were successfully pulverized to PCCOF-5 nanoparticles. (c) and (d) are SEM images of the electrode films of (a) WCCOF-5 and (b) PCCOF-5, respectively, showing that the PCCOF-5 particles are better connected as compared to those of WCCOF-5.

For comparison, YP50F was also pulverized to obtain YP50F nanoparticles (n-YP50F) using a process identical to that of PCCOF-5. The SEM images obtained before and after pulverization indicate that YP50F was successfully pulverized to nanoparticles by the process (Figure 4.11 (a), (b)). The S_{BET} of n-YP50F (1783 m^2 g^{-1}) slightly increased from that of the precursor YP50F (1670 m^2 g^{-1}), as shown in Figure 4.11 (c) and Table 4.4. Table 4.4 shows that the specific capacitances of YP50F were somewhat greater than those of n-YP50F. This research shows that pulverizing activated carbon (YP50F) has no major impact on the porous structure of the SC electrode.

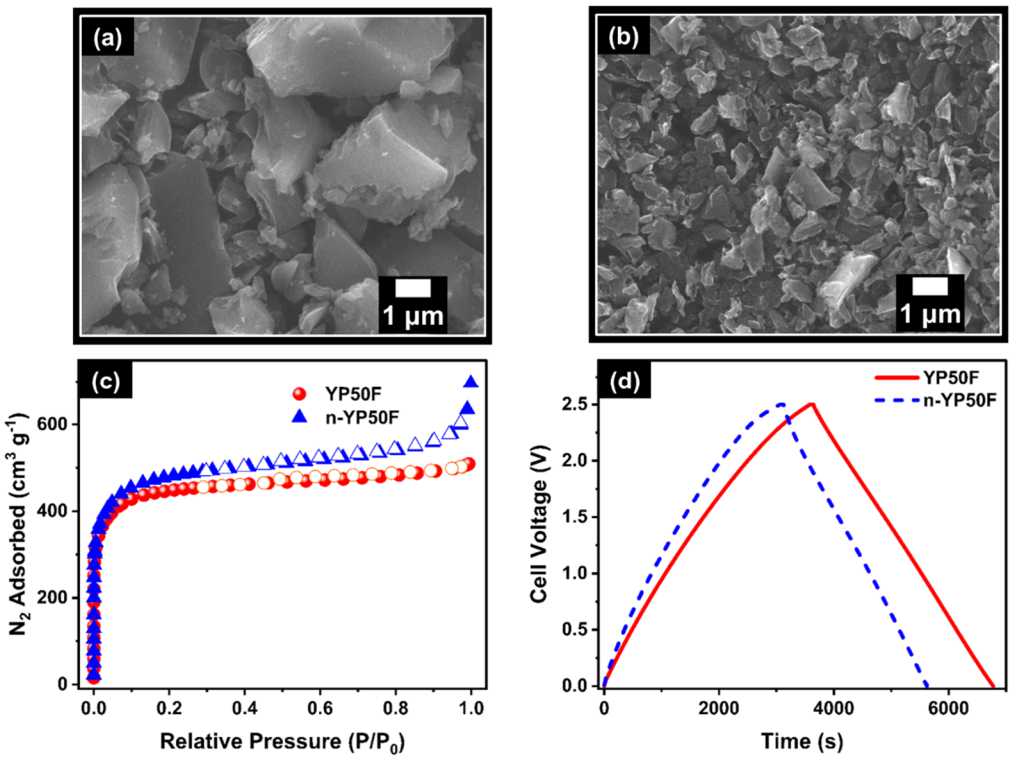

Figure 4.11 SEM images of (a) YP50F and (b) n-YP50F. (c) Nitrogen adsorption/desorption isotherms (filled/empty symbols) and (d) GCD curves of YP50F and n-YP50F.

Table 4.4 Specific surface area and specific capacitance of YP50F and n-YP50F

Carbon	S_{BET} (m^2 g^{-1})	mesopore volume (cm^3 g^{-1})	C_g (F g^{-1})	C_s (μF cm^{-2})
YP50F	1670	0.15	99.6	6.0
n-YP50F	1783	0.33	91.6	5.1

4.4 Conclusion

Porous carbon materials were successfully produced via the water treatment of calcined COF-5 for eliminating B_2O_3 from the resultant carbon. XPS analyses indicated that boron atoms were incorporated into the carbon framework. Using the obtained carbon materials, a higher charge density (15.3 μF cm^{-2} at 40 mA g^{-1}) was achieved, which is twice that of the activated carbon (~6.9 μF cm^{-2} at 40 mA g^{-1}), owing to the pore structure optimized for electrolyte ions as well as the pseudo-capacitive effect induced by the doped boron atoms. Further, capacitance retention of 72% was observed after 10000 cycles of GCD. By increasing the specific surface area of the material and fine-tuning the boron content in the carbon matrix, the C_g of boron-doped carbon can be enhanced even more. Other boron-based COFs could lead to a new type of multifunctional carbon for high-performance energy storage devices if they are further developed.

4.5 References

[4.1] K. Xia, Q. Gao, W. Li, X. Guo, J. Jiang, J. Hu, Hierarchical porous carbons with controlled micropores and mesopores for supercapacitor electrode materials, Carbon **46,** 1718–1726 (2008).

[4.2] H. Liu, X. Liu, W. Li, X. Guo, Y. Wang, G. Wang, D. Zhao, Porous carbon composites for next generation rechargeable lithium batteries, Adv. Energy Mater. **7,** 1700283 (2017).

[4.3] B. Xu, H. Zhang, H. Mei, D. Sun, Recent progress in metal–organic framework-based supercapacitor electrode materials, Coord. Chem. Rev. **420**, 213438 (2020).

[4.4] Z. Yang, H. Nie, X. Chen, X. Chen, S. Huang, Recent progress in doped carbon nanomaterials as effective cathode catalysts for fuel cell oxygen reduction reaction, J. Power Sources **236**, 238–249 (2013).

[4.5] T. Kyotani, Z. Ma, A. Tomita, Template synthesis of novel porous carbons using various types of zeolites, Carbon **41,** 1451–1459 (2003).

[4.6] P. Boonyoung, T. Kasukabe, Y. Hoshikawa, Á. Berenguer-Murcia, D. Cazorla-Amorós, B. Boekfa, H. Nishihara, T. Kyotani, K. Nueangnoraj, A simple "nano-templating" method using zeolite Y toward the formation of carbon schwarzites, Front. Mater. **6**, 1–9 (2019).

[4.7] N.P. Stadie, S. Wang, K.V. Kravchyk, M.V. Kovalenko, Zeolite-templated carbon as an ordered microporous electrode for aluminum batteries, ACS Nano **11**, 1911–1919 (2017).

[4.8] R.J. Dubey, T. Colijn, M. Aebli, E.E. Hanson, R. Widmer, K.V. Kravchyk, M.V. Kovalenko, N.P. Stadie, Zeolite-templated carbon as a stable, high power magnesium-ion cathode material, A.C.S. Appl. Mater. Interfaces **11**, 39902–39909 (2019).

[4.9] T. Morishita, Y. Soneda, T. Tsumura, M. Inagaki, Preparation of porous carbons from thermoplastic precursors and their performance for electric double layer capacitors, Carbon **44**, 2360–2367 (2006).

[4.10] T. Morishita, T. Tsumura, M. Toyoda, J. Przepiórski, A.W. Morawski, H. Konno, M. Inagaki, A review of the control of pore structure in MgO-templated nanoporous carbons, Carbon **48**, 2690–2707 (2010).

[4.11] W. Lin, B. Xu, L. Liu, Hierarchical porous carbon prepared by NaOH activation of nano-

$CaCO_3$ templated carbon for high rate supercapacitors, New J. Chem. **38**, 5509–5514 (2014).

[4.12] Y. Wen, L. Zhang, J. Liu, X. Wen, X. Chen, J. Ma, T. Tang, E. Mijowska, Hierarchical porous carbon sheets derived on a MgO template for high-performance supercapacitor applications, Nanotechnology **30**, 295703 (2019).

[4.13] M. Hu, J. Reboul, S. Furukawa, N.L. Torad, Q. Ji, P. Srinivasu, K. Ariga, S. Kitagawa, Y. Yamauchi, Direct carbonization of Al-based porous coordination polymer for synthesis of nanoporous carbon, J. Am. Chem. Soc. **134**, 2864–2867 (2012).

[4.14] N.L. Torad, R.R. Salunkhe, Y. Li, H. Hamoudi, M. Imura, Y. Sakka, C.-C. Hu, Y. Yamauchi, Electric double-layer capacitors based on highly graphitized nanoporous carbons derived from ZIF-67, Chemistry **20**, 7895–7900 (2014).

[4.15] L. Radhakrishnan, J. Reboul, S. Furukawa, P. Srinivasu, S. Kitagawa, Y. Yamauchi, Preparation of microporous carbon fibers through carbonization of al-based porous coordination polymer (Al-PCP) with furfuryl alcohol, Chem. Mater. **23**, 1225–1231 (2011).

[4.16] A.P. Côté, A.I. Benin, N.W. Ockwig, M. O'Keeffe, A.J. Matzger, O.M. Yaghi, Porous, crystalline, covalent organic frameworks, Science **310**, 1166–1170 (2005).

[4.17] N. Zhang, A. Ishag, Y. Li, H. Wang, H. Guo, P. Mei, Q. Meng, Y. Sun, Recent investigations and progress in environmental remediation by using covalent organic framework-based adsorption method: A review, J. Cleaner Prod. **277**, 123360 (2020).

[4.18] X. Li, C. Yang, B. Sun, S. Cai, Z. Chen, Y. Lv, J. Zhang, Y. Liu, Expeditious synthesis of covalent organic frameworks: A review, J. Mater. Chem. **A 8**, 16045–16060 (2020).

[4.19] H.L. Qian, C.X. Yang, W.L. Wang, C. Yang, X.P. Yan, Advances in covalent organic frameworks in separation science, J. Chromatogr. **A 1542**, 1–18 (2018).

[4.20] J. Kim, J.H. Kim, K. Ariga, Redox-active polymers for energy storage nanoarchitectonics, Joule. **4**, 739–768 (2017).

[4.21] X. Zhang, G. Zhu, M. Wang, J. Li, T. Lu, L. Pan, Covalent-organic-frameworks derived N-doped porous carbon materials as anode for superior long-life cycling lithium and sodium ion batteries, Carbon **116**, 686–694 (2017).

[4.22] Y.-B. Huang, P. Pachfule, J.-K. Sun, Q. Xu, From covalent–organic frameworks to hierarchically porous B-doped carbons: A molten-salt approach, J. Mater. Chem. **A 4**, 4273–4279 (2016).

[4.23] Y. Li, X. Xu, S. Hou, J. Ma, T. Lu, J. Wang, Y. Yao, L. Pan, Facile dual doping strategy via carbonization of covalent organic frameworks to prepare hierarchically porous carbon spheres for membrane capacitive deionization, Chem. Commun. **54**, 14009–14012 (2018).

[4.24] C. Young, R. R. Salunkhe, J. Tang, C.-C. Hu, M. Shahabuddin, E. Yanmaz, M. S. A. Hossain, J. H. Kim, Y. Yamauchi, Zeolitic imidazolate framework (XIF-8) derived nanoporous carbon: the effect of carbonization temperature on the supercapacitor performance in an aqueous electrolyte, Phys. Chem. Chem. Phys **18**, 29308–29315 (2016).

[4.25] P. Liang, C. Zhang, H. Hun, S. Liu, M. Tabe, S. Wang, Photocatalysis of C, N-doped ZnO derived from ZIF-8 for dye degradation and water oxidation, RSC Adv. **6(98)**, 95903–95909 (2016).

[4.26] J. Zou, P. Liu, L. Huang, Q. Zhang, T. Lan, S. Zeng, X. Zeng, L. Yu, S. Liu, H. Wu, W. Tu, Y. Yao, Ultrahigh-content nitrogen-decorated nanoporous carbon derived from metal organic frameworks and its application in supercapacitors, Electrochim. Acta. 271 (2018) 599–608.

[4.27] F. Xu, D. Wu, R. Fu, B. Wei, Design and preparation of porous carbons from conjugated polymer precursors, Mater. Today. **10**, 629–656 (2017).

[4.28] H.M. Lee, K.H. An, S.J. Park, B.J. Kim, Mesopore-rich activated carbons for electrical double-layer capacitors by optimal activation condition. Nanomaterials **9**, 608 (2019).

[4.29] L. Ling, M. Qing-Han, Electrochemical properties of mesoporous carbon aerogel electrodes for electric double layer capacitors, J. Mater. Sci. **40**, 4105–4107 (2005).

[4.30] S. Shiraishi, M. Kibe, T. Yokoyama, H. Kurihara, N. Patel, A. Oya, Y. Kaburagi, Y. Hishiyama, Electric double layer capacitance of multi-walled carbon nanotubes and B-doping effect, Appl. Phys. **A 82**, 585–591 (2005).

[4.31] L.M. Lanni, R.W. Tilford, M. Bharathy, J.J. Lavigne, Enhanced hydrolytic stability of self-assembling alkylated two-dimensional covalent organic frameworks, J. Am. Chem. Soc. **133**, 13975–13983 (2011).

[4.32] S. Wang, X. Jing, Y. Wang, J. Si, High char yield of aryl boron-containing phenolic resins: The effect of phenylboronic acid on the thermal stability and carbonization of phenolic resins, Polym. Degrad. Stab. **99**, 1–11 (2014).

[4.33] L.M. Malard, M.A. Pimenta, G. Dresselhaus, M.S. Dresselhaus, Raman spectroscopy in graphene. Phys. Rep. **473**, 51–87 (2009).

[4.34] K. Sing, The use of nitrogen adsorption for the characterization of porous materials, Colloids Surf. **A 187–188**, 3–9 (2001).

[4.35] S. Mustapha, M.M. Ndamitso, A.S. Abdulkareem, J.O. Tijani, D.T. Shuaib, A.K. Mohammed, A. Sumaila Comparative study of crystallite size using Williamson-Hall and Debye-Scherrer plots for ZnO nanoparticles. Adv. Nat. Sci.: Nanosci. Nanotechnol. **10**, 045013 (2019).

[4.36] A. Ismach, H. Chou, P. Mende, A. Dolocan, R. Addou, S. Aloni, R. Wallace, R. Feenstra, R.S. Ruoff, L. Colombo, Carbon-assisted chemical vapor deposition of hexagonal boron nitride, 2D Mater. **4**, 1–13 (2017).

[4.37] M.D. Johnston, L.T. Khajavi, M. Li, S. Sokhanvaran, M. Barati, High-temperature refining of metallurgical-grade silicon: A review, JOM **64**, 935–945 (2012).

[4.38] T.V. Khai, H.G. Na, D.S. Kwak, Y.J. Kwon, H. Ham, K.B. Shim, H.W. Kim, Comparison study of structural and optical properties of boron-doped and undoped graphene oxide films, Chem. Eng. J. **211–21**2, 369–377 (2012).

[4.39] C. Lei, N. Amini, F. Markoulidis, P. Wilson, S. Tennison, C. Lekakou, Activated carbon from phenolic resin with controlled mesoporosity for an electric double-layer capacitor (EDLC), J. Mater. Chem. A **1**, 6037–6042 (2013).

[4.40] C. Lei, F. Markoulidis, Z. Ashitaka, C. Lekakou, Reduction of porous carbon/Al contact resistance for an electric double-layer capacitor (EDLC), Electrochem. Acta **92**, 183–187 (2013).

[4.41] R. Dubey, V. Guruviah, Review of carbon-based electrode materials for supercapacitor energy storage, Ionics **25**, 1419–1445 (2019).

[4.42] H. Guo, Q. Gao, Boron and nitrogen co-doped porous carbon and its enhanced properties as supercapacitor, J. Power Sources **186**, 551–556 (2009).

[4.43] H. Chen, Y. Xiong, T. Yu, P. Zhu, X. Yan, Z. Wang, S. Guan, Boron and nitrogen co-doped porous carbon with a high concentration of boron and its superior capacitive behavior, Carbon **113**, 266–273 (2017).

[4.44] P. Azais, L. Duclaux, P. Florian, D. Massiot, M. Lillo-Rodenas, A. Linares-Solano, J. Peres, C. Jehoulet, F. Beguin, Causes of supercapacitors ageing in organic electrolyte, J. Power Sources **171**, 1046–1053 (2007).

5 Mechanism underlying pore generations during carbonization of zinc-based metal-organic frameworks

5.1 Introduction

Over the past several decades, MOFs have attracted increasing attention as a new alternative to carbon-based materials for energy storage devices [5.1–5.4]. High-capacity electrodes for LIBs [5.5–5.8] and SCs [5.9–5.14] have been prepared from various MOF-derived carbons. MOFs are porous crystalline structures made up of metal ions/clusters and organic ligands in one, two, or three dimensions [5.15]. Their particle size and porous structures can be tuned to achieve ultrahigh porosity (7140 m^2 g^{-1}) [5.16, 5.17]. The beneficial properties of carbon materials templated by MOFs have been reported. Certain MOFs, for example, can keep their shape and porous architectures following carbonization [5.18, 5.19]. Furthermore, several heteroatom-doped carbons have been prepared by MOF heating [5.20–5.22]. MOFs can be carbonized with metal atoms such as Fe, Co, or Ni, yielding carbons with a certain degree of graphitization [5.23–5.26]. Doping with other metals such as Mg, Al, or Zn obtains amorphous carbons with metal clusters or metal oxides [5.20–5.23, 5.27–5.39], which can then be removed in HF or HCl acid to yield porous carbons [5.24, 5.25, 5.28, 5.29]. Zn-based MOFs (ZMOFs) are particularly interesting among the many MOFs because they make it simple to produce porous carbons and have a large specific surface area [5.30, 5.33–5.35, 5.37–5.39]. In this fabrication, ZnO is reduced to Zn by the surrounding carbon, and the remaining Zn sublimates at relatively low temperature (boiling point: 908 °C) [5.32, 5.33, 5.35, 5.39].

The activation technique achieves high porosity in a single calcination phase, avoiding the use of toxic acids like HF or HCl.

Because of their ease of fabrication and huge surface area, ZMOFs are predicted to be the next-generation carbon precursors for porous carbons. Interestingly, the S_{BET} of ZMOF-derived carbons is linearly related to the Zn/C ratio of the precursors [5.30, 5.31].

The dynamic behavior of ZnO and its effect on both pore formation and reduction with subsequent metal sublimation could be linked to the conversion of Zn compounds. Hence,

the relationship between the dynamic behavior of ZnO and pore formation during carbonization must be clarified by the author.

The present study aims to elucidate the pore-generation mechanism in ZMOFs during carbonization. To this end, the authors synthesized two types of ZMOFs with different Zn/C ratios (denoted as ZMOF1 and ZMOF2). The corresponding ZMOFs were calcined at 1000 °C under a nitrogen flow (Figure 5.1). The resulting carbons (referred to as CZMOFs) from ZMOF1 and ZMOF2 are denoted as CZMOF1 and CZMOF2, respectively.

The influence of the Zn/C ratio and oxygen on pore development was also highlighted by the author. In situ techniques, which allow high-resolution measurements of the bulk characteristics of samples, were used to investigate phase transformation and pore formation during carbonization. Several dynamic approaches, such as in situ PXRD examination, were used to characterize the materials.

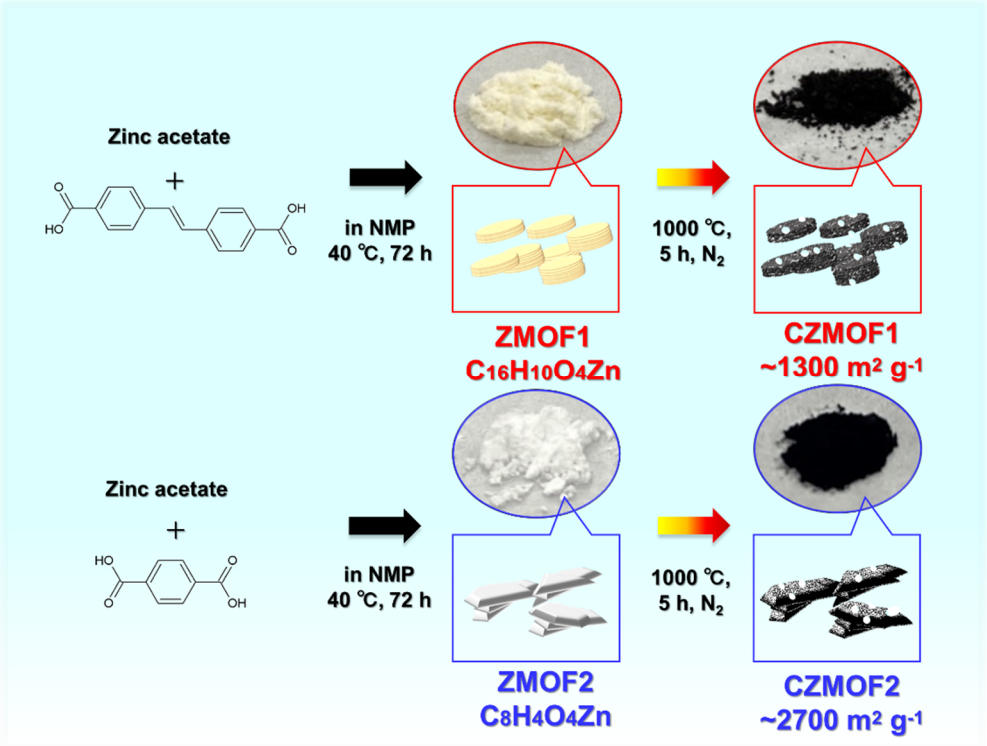

Figure 5.1 Schematic of the synthesis of Zn-based MOF-derived porous CZMOFs

5.2 Experimental procedures

5.2.1. Preparation of ZMOFs

ZMOF1 was synthesized from two types of solutions: (A) zinc acetate (Nacalai Tesque Inc., Japan) (176 mg) dissolved in 30-mL NMP (Nacalai Tesque Inc., Japan), and (B) 4,4-stilbene dicarboxylic acid (Tokyo Chemical Industry Co. Ltd., Japan) (858 mg) dissolved in 400 mL of NMP. Subsequently, solution A was transferred to solution B by a liquid delivery pump (flow speed ~4.0 mL min^{-1}). The mixture was left for 72 h at 40 °C. The formed precipitate was washed with 100 mL of NMP and dried at 120 °C under a vacuum for 12 h, yielding a powdery product (~220 mg). ZMOF2 was similarly synthesized from two types of solutions: (A) as described above and (C) terephthalic acid (Tokyo Chemical Industry Co. Ltd., Japan) (532 mg) dissolved in 80 mL of NMP. Solution A was transferred to solution C by a liquid delivery pump (flow speed ~4.0 mL min^{-1}). The subsequent steps were as described for ZMOF1. The weight of the final powdery product was ~230 mg. Similar MOF synthesis procedures are reported elsewhere [5.40–5.42].

5.2.2 Preparation of CZMOFs and CZIF-8

The ZMOF powder was placed in a ceramic boat made of alumina; the boat was transferred to a quartz furnace tube. The sample was heated under nitrogen, with the purity of 99.99%, at a flow of 200 mL min^{-1} and a heating rate of 10 °C min^{-1} until the temperature reached 1000 °C. This temperature was maintained for 5 h, following which the samples were naturally cooled to room temperature (18–25 °C). CZMOF1 and CZMOF2 are the ZMOF1 and ZMOF2 that were calcined at 1000 °C for 5 h. A bag of black powder was found (CZMOFs). The process was repeated several times, and the mixture of the samples was characterized as follows. Four batches of each of the CZMOFs samples (CZMOF1_b1–b4 and CZMOF2_b1–b4) were prepared for reproducibility. CZMOF1_b3 and CZMOF2_b1 were used for all the characterizations. ZMOF1 and ZMOF2 were calcined at a flow rate of 200 mL min^{-1} and a heating rate of 10 °C min^{-1} to temperatures of 500 °C, 700 °C, 900 °C, and 1000 °C and 300 °C, 500 °C, 700 °C, 900 °C, and 1000 °C, respectively, to investigate

the relationship between the surface area of the calcined ZMOFs and the heating profile. Then, the samples were naturally cooled to room temperature (18–25 °C). Furthermore, under the same conditions as above, ZMOF1 and ZMOF2 were calcined until the temperature reached 1000 °C, and the temperature was maintained for several hours (1, 3, and 5 h). The CZMOF1 and CZMOF2 obtained here, which were calcined at 1000 °C for 5h, are denoted as CZMOF1_b2 and CZMOF2_b3, respectively. The commercial zeolitic imidazolate framework (ZIF-8, Z1200, Sigma-Aldrich, USA) was selected as reference material to compare the pore generation in CZFMOFs with that in other Zn-based MOFs. As with CZMOFs, ZIF-8 was heated at 10 °C min^{-1} under a nitrogen flow of 200 mL min^{-1} until the temperature reached 500 °C, 700 °C, 900 °C, or 1000 °C without holding time. The heated samples were naturally cooled to room temperature (18–25 °C). Besides, ZIF-8 was calcined until the temperature reached 1000 °C under the same conditions described above, and the temperature was maintained for several hours (1, 3, and 5 h). The ZIF-8, which was calcined at 1000 °C for 5 h, is denoted as CZIF-8.

5.2.3 Material characterization

The morphology of each sample was characterized by SEM (JSM-6010LA, JEOL Ltd., Japan) at an accelerating voltage of 15 kV (SE mode) and by TEM (JEM-2100F, JEOL Ltd., Japan) at an accelerating voltage of 200 kV. In preparation for SEM, the powdery sample was set onto a carbon tape on an Al sample holder (10 mm (φ) × 10 mm (H)). For TEM, the sample dispersed in ethanol was poured onto a holey carbon film supported on 3- mm Cu grids, followed by drying at 80 °C for 1 h. The mass and molar ratios of each sample were examined through Energy-dispersive X-ray spectroscopy (EDX) (JEM-2100F, JEOL Ltd., Japan) and determined from the crystallographic information files [5.40, 5.42]. The crystallinities of the resulting products were confirmed in a PXRD analysis (Smart Lab SE, Rigaku, Japan) with Cu $K\alpha_1$ ($\lambda = 0.154$ nm) radiation at a scan rate of 10° min^{-1}. The in situ PXRD patterns of the corresponding ZMOFs were collected during heating to 1100 °C in 50 °C increments under a nitrogen flow of 200 mL min^{-1}. The reference material was

commercial ZnO particles (purity 99.0%; Nacalai Tesque Inc., Japan). The graphitization degree was investigated by Raman spectroscopy (Raman, NRS-4500NMDS, JASCO, Japan) with a 532-nm excitation laser calibrated on Si. The intensity and exposure time were 2 mW and 300 s, respectively. The surface functionalities of the samples were examined by XPS (ESCA5700, ULVAC-PHI Inc., Japan) with Mg $K\alpha_1$ radiation at an accelerating voltage of 15 kV.

The phase-change temperature of each sample was determined by TG–DTA (DTG-60, Shimadzu Corporation, Japan), which was performed at 10 °C min^{-1} under a nitrogen flow of 200 mL min^{-1}. In preparation for TG–DTA, ~5 mg of the powdery sample was placed in the Pt holder. Nitrogen adsorption/desorption (BEL-SORP min, Microtrac-BEL, Japan) isotherms were acquired at 77 K for the S_{BET} measurement, PSD, and information on the pore structure of each sample. Prior to the measurements, the samples were degasified by heating at 300 °C for 24 h in a vacuum. The S_{BET} of each sample was estimated from the isotherms by the BET method (P/P_0 = 0.05–0.10). The S_{meso} was estimated by the BJH method. Total pore (V_{total}), micropore (~2 nm) (V_{micro}), and mesopore (2–50 nm) (V_{meso}) volumes were calculated by the BET, MP, and BJH methods, respectively. The PSD was calculated using the NLDFT.

5.3 Results and discussion

5.3.1 Synthesis of ZMOFs and their characterization

Figure 5.2(a),(b) shows the SEM images of ZMOF1 and ZMOF2, respectively. The ZMOF1 particles exhibited a unique donut-like shape, different from those in previous reports. In a previous study, the same metal species and ligand preferentially yielded nanowires [5.40], whereas the ZMOF2 particles were flake-like. MOF-2 and MOF-5 were originally used to refer to two ZMOFs with the same metal species and ligand as ZMOF2.[5.41] ZMOF1 and ZMOF2 were crystalline (Figure 5.2(c)) and their PXRD patterns resembled those of ZMOFs (simulated) [5.40, 5.42]. The theoretical formulas of ZMOF1 and ZMOF2 were $C_{58}H_{48}N_2O_{14}Zn_3$ ($[Zn_3(SBDC)_3(NMP)_2]$ (4,4-stilbenedicarboxylic acid (=H_2SBDC), N-methyl-2-pyrrolidone (NMP)) and $C_{13}H_{13}NO_5Zn$ ([Zn(BDC)(NMP)] (BDC: benzene-1,4-dicarboxylic acid (=H_2BDC)), respectively [5.40, 5.42]. After removing the guest molecules, the chemical formulas of ZMOF1 and ZMOF2 were re-calculated as $C_{16}H_{10}O_4Zn$ and $C_8H_4O_4Zn$, respectively, excluding the molecular formula of the solvent.

The estimated Zn/C ratios of ZMOF1 and ZMOF2 were 0.0625 and 0.1250, respectively (note that the Zn/C ratio in ZMOF2 was twice that in ZMOF1).

The Zn atoms were spread throughout the particles, as shown in Figure 5.2(d),(e), according to the EDX mappings of ZMOF1 and ZMOF2 (the element ratios in Table 5.1). Figures 5.2 (g),(f) show the unit cell structures of $[Zn_3(SBDC)_3(DMF)_2]$ and [Zn(BDC)(DMA)], respectively. N,N-dimethylacetamide and N,N-dimethylformamide are denoted as DMA and DMF, respectively as abbreviation. In both structures, Zn atoms are located near O atoms, suggesting that ZnO will likely form during carbonization. Note that both $[Zn_3(SBDC)_3(DMF)_2]$ and [Zn(BDC)(DMA)] are non-porous structures. NMP substitutes DMF and DMA in the cell architectures of ZMOF1 and ZMOF2, respectively.

As previously stated, the simulated PXRD patterns of $[Zn(SBDC)_3(DMF)_2]$ and [Zn(BDC)DMA] closely resemble those of ZMOF1 and ZMOF2, respectively (see Figure 5.2 (c)), however ZMOF1 and ZMOF2 morphologies differ from those published in the literature. Guest molecules reportedly serve as ligands during synthesis, as counterions for

charge balance, as pore-filling molecules, or as actual frameworks [5.43]. As a result, the solvent guest (NMP) in the present study might induce the unique donut-like shape of ZMOF1, rather than the nanowires formed when DMF is the solvent. Factors including solvent ratio, synthesis temperature, speed, and pH are also known to influence MOF morphologies [5.44]. The combination of these factors might also produce the unique donut-like shape of ZMOF1. Meanwhile, ZMOF2 and MOF-5 with the same metal species and ligands exhibited different morphologies [5.30, 5.45–5.47]. Whereas ZMOF2 had a flake-like morphology, MOF-5 synthesized in NMP solvent formed cuboid crystals [5.46, 5.47]. MOF-5 was synthesized at above 90 °C by the previous authors, however ZMOF2 was produced at 40 °C. The morphology of the as-prepared ZMOF2 may have been influenced by the temperature differential.

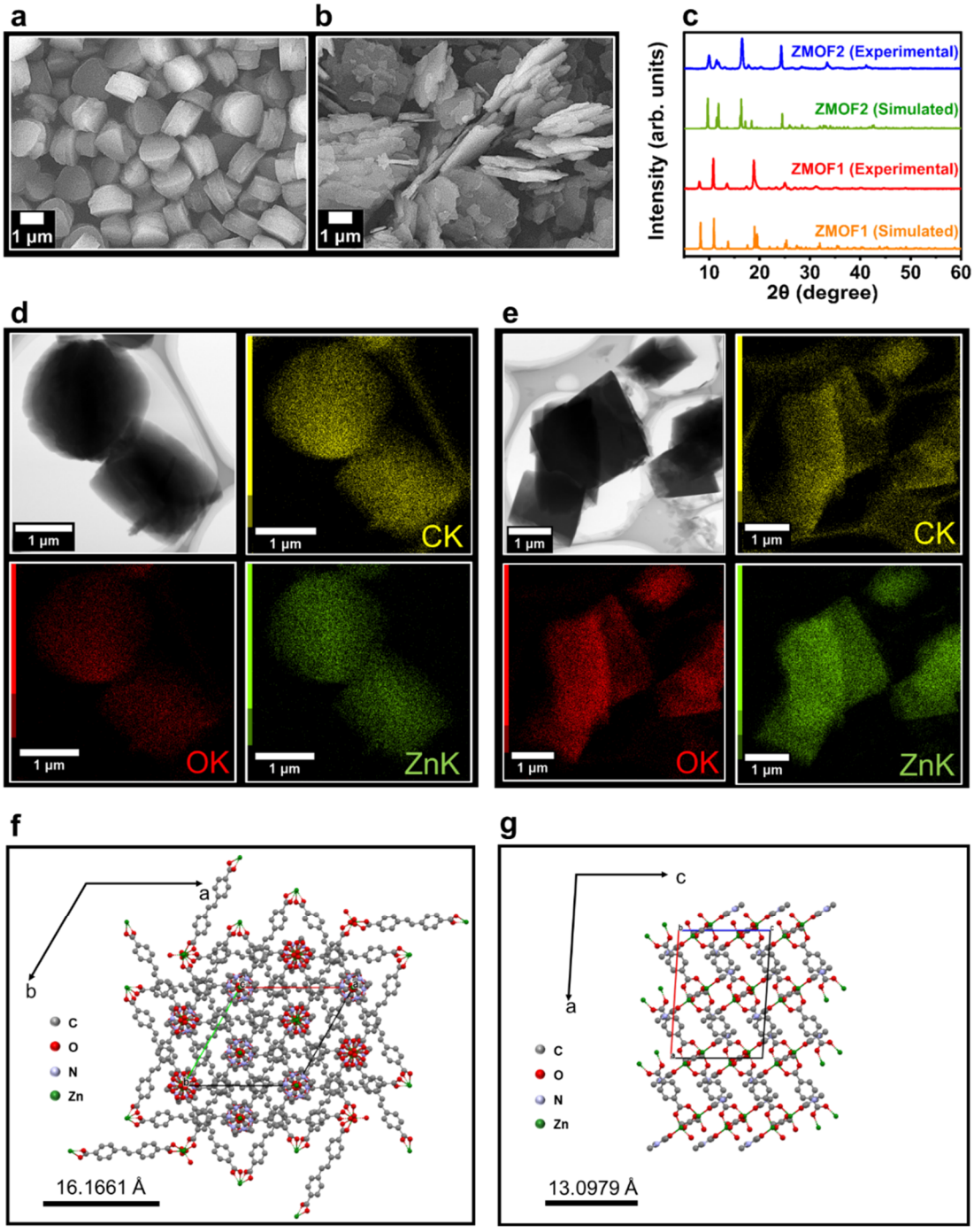

Figure 5.2 SEM (SE mode) images of (a) ZMOF1 and (b) ZMOF2 showing their pellet and flake-like morphologies, respectively; (c) PXRD patterns of ZMOF1 (red) and ZMOF2 (blue), along with the reference patterns of ZMOF1 (orange) and ZMOF2 (green) taken from the literature[40, 42] confirm that ZMOFs are crystalline materials. TEM images and corresponding EDX elemental maps (C (yellow), O (red), and Zn (green)) of (d) ZMOF1 and (e) ZMOF2. (f) Unit cell structure of $[Zn_3(SBDC)_3(DMF)_2]$ taken from the literature [5.40]. SBDC (4,4-stilbenedicarboxylic acid = H_2SBDC) and DMF (N,N- dimethylformamide) (g) Unit cell structure of [Zn(BDC)(DMA)] taken from the literature [5.42]. BDC (benzene-1,4-dicarboxylic acid = H_2BDC) and DMA (N,N-dimethylacetamide).

Table 5.1 Molar ratios of C, O, and Zn atoms in ZMOF1 and ZMOF2

Sample	Carbon atoms (%)	Oxygen atoms (%)	Zinc atoms (%)
ZMOF1	86.3	9.4	4.3
ZMOF2	70.4	21.7	8.0

5.3.2 Pore generation and CZMOF characterization

Figure 5.3 (a),(d) show the SEM images of CZMOF1 and CZMOF2, respectively. Even after calcination at 1000 °C, the particles preserved some of their shape. Images of the CZMOFs obtained using TEM (Figure 5.3(b),(c),(e),(f)) provide additional information on the nanoscale architectures of the particles. Both CZMOF1 and CZMOF2 particles presented a rough surface with micropore (~2 nm) volumes and hierarchical porous structures (see Figure 5.4 (a)–(f) for the additional TEM images acquired at various angles). Micro/mesopores and macropores (≥50 nm) were uniformly distributed on the flake-like surfaces of CZMOF2 (Figure 5.4(g)–(i)). The purity of the CZMOFs was validated by their PXRD patterns, which showed amorphous carbon's typical peaks (Figure 5.3(g)). Meanwhile, the carbon graphitization degree is determined by the Raman spectra of CZMOF1 and CZMOF2 (Figure 5.3 (h)). The intensity ratios of the D (1350 cm^{-1}) and G (1590 cm^{-1}) bands (I_G/I_D) of both samples were 0.98 (CZMOF1) and 1.12 (CZMOF2). The spectrum of CZMOF2 contained a peak corresponding to the 2D band (2600–2800 cm^{-1}), which characterizes a few layers of graphene [5.48]. Therefore, CZMOF2 was more graphitized than CZMOF1.

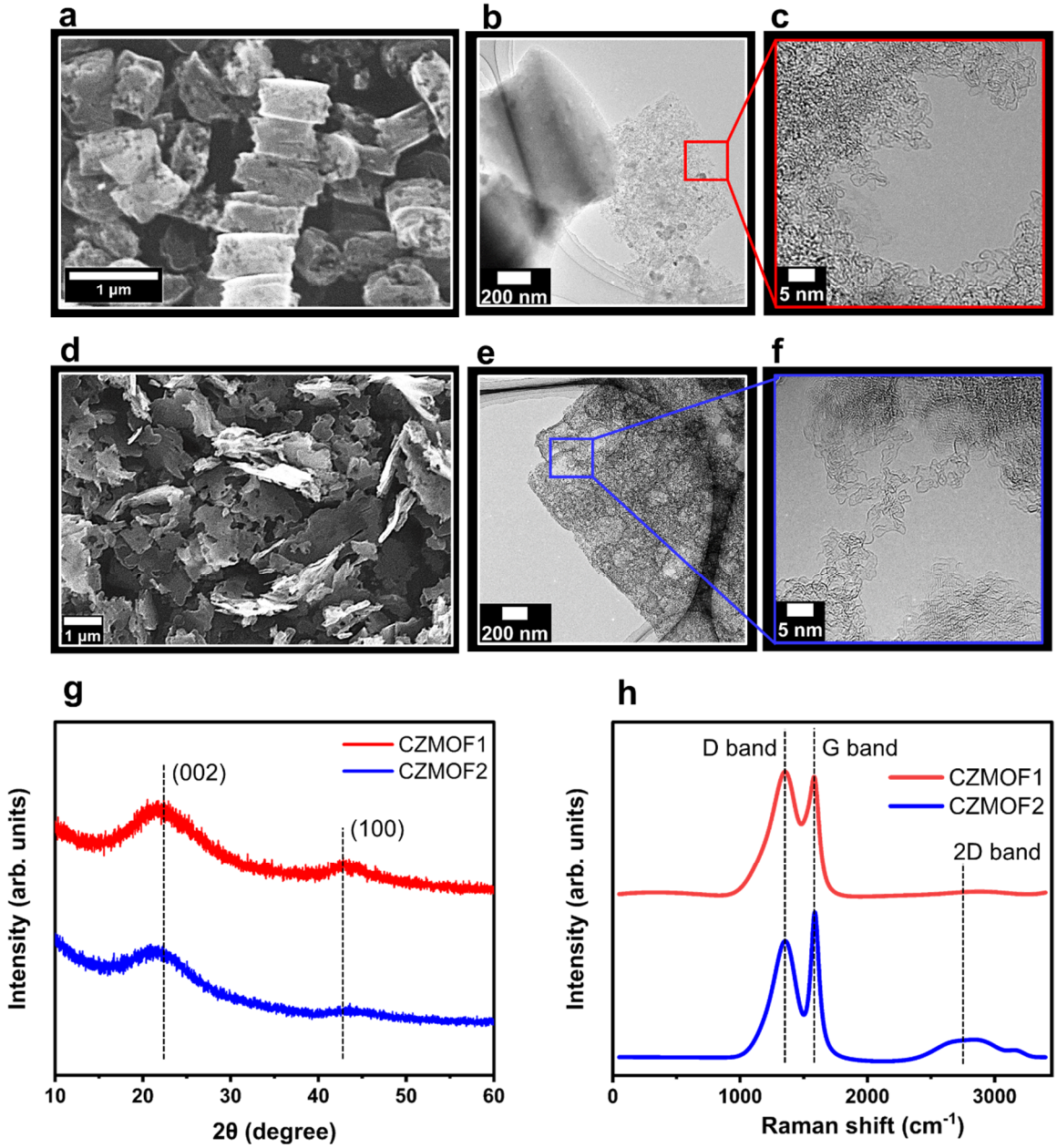

Figure 5.3 SEM images of (a) CZMOF1 and (b) CZMOF2; TEM images of (b),(c) CZMOF1; TEM images of (e),(f) CZMOF2, showing nanosized roughness; (g) PXRD patterns and (h) Raman spectra of CZMOF1 (red) and CZMOF2 (blue), confirming the purity of CZMOF1 and CZMOF2 and increased graphitization in CZMOF2 (I_G/I_D ratio 1.12) compared to CZMOF1 (0.98).

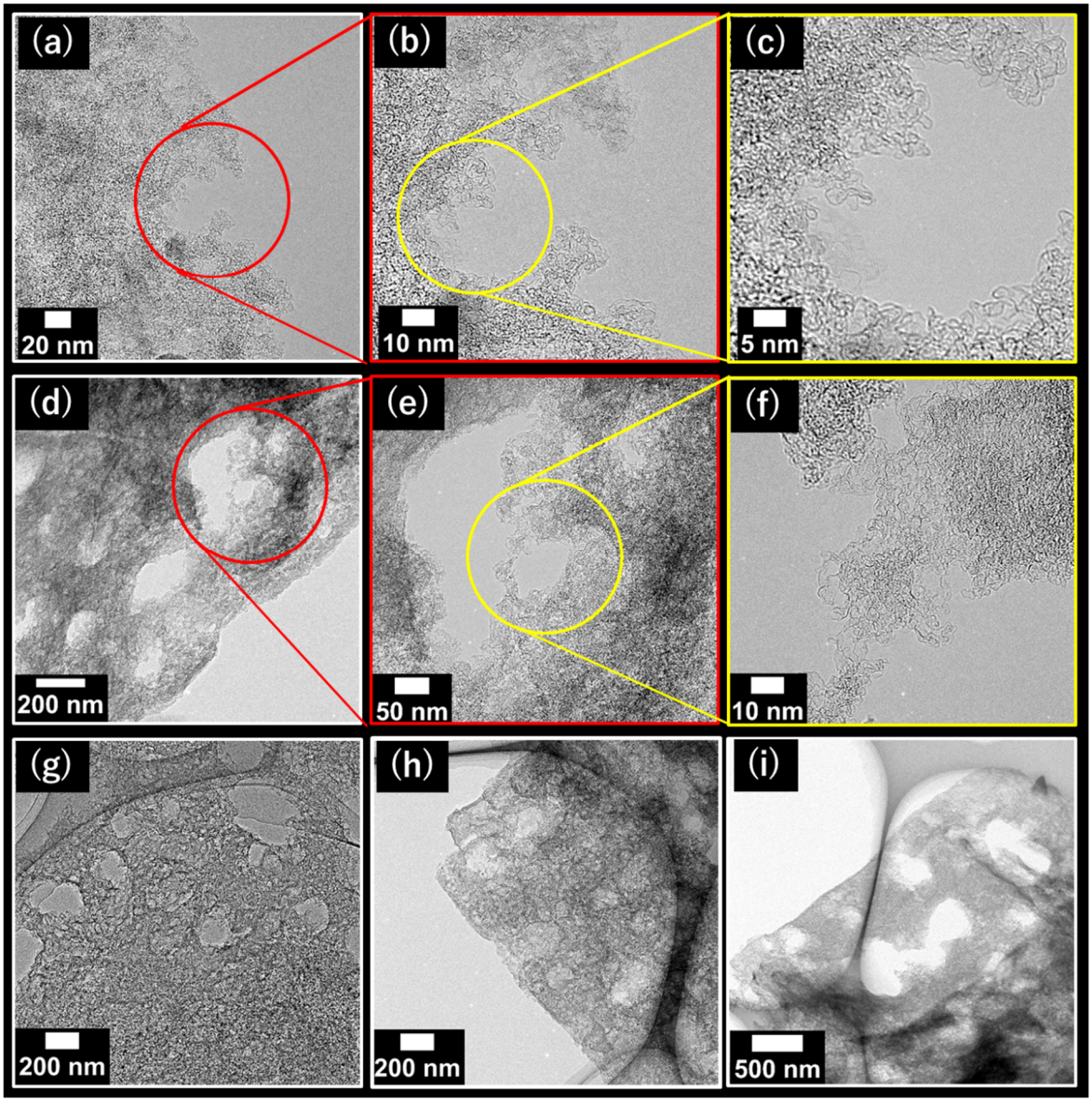

Figure 5.4 Additional TEM images of (a)–(c) CZMOF1, (d)–(f) CZMOF2, and (g)–(i) macropores in CZMOF2 flakes.

5.3.3 Pore characterization of CZMOFs

Figure 5.5(a),(b) show the nitrogen adsorption/desorption isotherms and PSD of CZMOF1 and CZMOF2, respectively. The isotherms of the references (commercial activated carbons YP50F (coconut shell origin, physical activation with H_2O-steam, Kuraray Chemical Co. Ltd., Japan) and MSP20 (phenol resin origin, chemical activation with KOH; Kansai Coke and Chemicals, Japan))[5.49] are also included for comparing the porous structures of the Zn-activated carbons (CZMOF1 and CZMOF2) with those of carbons activated via typical methods. Table 5.2 summarizes the pore characteristics obtained in the above analysis. The S_{BET} values of CZMOF1 and CZMOF2 were 1266 and 2678 $m^2\ g^{-1}$, respectively. The S_{BET} values of the CZMOFs also depended on the Zn/C ratio of the precursor, as reported previously [5.30, 5.31]. The variation in the Zn/C ratios (0.0625 and 0.1250) caused a significant difference in the S_{BET} values of CZMOF1 and CZMOF2 (see Figure 5.5(a) and Table 5.2). The S_{BET} values of other batches of the studied CZMOFs are also provided for reference (Figure 5.5 (c),(d) and Table 5.3). Furthermore, the CZMOFs formed by direct carbonization of ZMOF1 and ZMOF2 were very porous although the original MOFs were non-porous (Table 5.2).

When ZnO was reduced, the carbonized MOFs became porous as carbon atoms were consumed. In our study, the Zn-activation method (which yielded CZMOF1 and CZMOF2) generated significantly more mesopores (size 2–50 nm) than steam (YP50F) or KOH (MSP20) activation (see Figure 5.5(b) and Table 5.2). Moreover, the isotherms of both CZMOF1 and CZMOF2 steeply increased at high relative pressures (> 0.9). According to nitrogen adsorption/desorption theory [5.50], this feature indicates the presence of macropores. Table 5.4 compares the S_{BET} values and total pore volumes of the as-prepared CZMOFs and the ZMOF-derived carbons reported elsewhere. The data in the table are limited to materials with S_{BET} above 2000 $m^2\ g^{-1}$. The maximum S_{BET} of CZMOF2 (2678 $m^2\ g^{-1}$) was comparable to those of the previously reported materials. Moreover, the S_{BET} of CZMOF2 exceeded that of C-MOF-5 with the same metal species and ligand (Table 5.4) [5.30]. The morphology of ZnO reportedly depends on the presence and types of the guest molecules

[5.51]. As mentioned earlier, the guest molecule in ZMOF2 was NMP, whereas DMA [5.42] and DMF [5.30, 5.41] were the guest molecules in MOF-5. Thus, the formation process of ZnO and its reduction behavior might lead to the difference in S_{BET} between the as-prepared ZMOF2 and MOF-5. Moreover, the S_{BET} may depend on factors such as the types of MOFs and gases, heating time, and temperature.

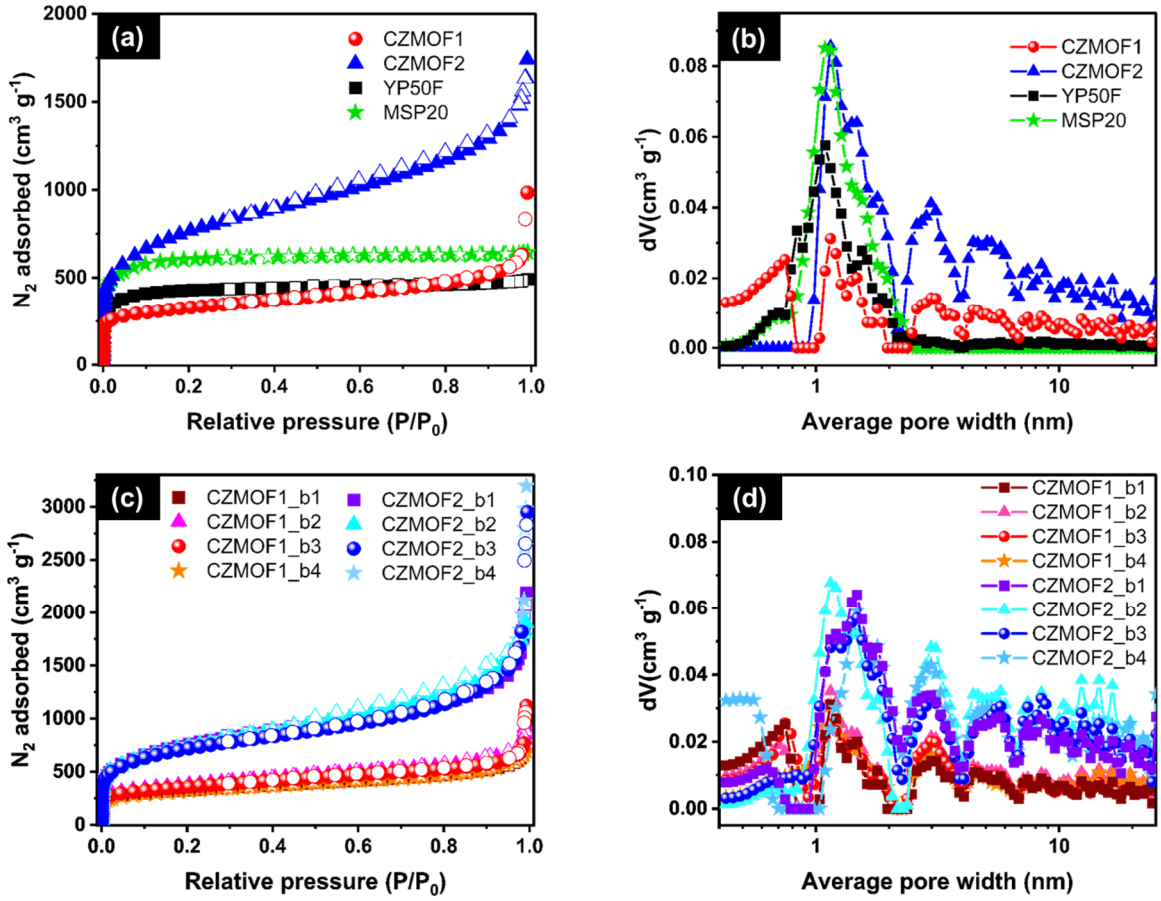

Figure 5.5 (a) Nitrogen adsorption/desorption (solid/empty symbols, respectively) isotherms and (b) Average pore size distributions (average pore width on the semi-logarithmic scale) of CZMOF1 (red), CZMOF2 (blue), and two types of commercial activated carbons (YP50F (black) and MSP20 (green)), showing the generation of 3–10 nm pores unlike those by the standard YP50F and MSP20. (c),(d) shows the pore characterizations of CZMOF1 (b1, b2, b3, and b4) and CZMOF2 (b1, b2, b3, and b4): (c) Nitrogen adsorption/desorption isotherms (solid/empty symbols), and (d) Average pore size distribution (average pore width on the semi-logarithmic scale) of CZMOF1 [b1 (brown), b2 (pink), b3 (red), and b4 (orange)] and CZMOF2 [b1 (purple), b2 (cyan), b3 (blue), and b4 (light-blue)]. The variations in Zn/C ratios caused significant differences in the specific surface areas of CZMOFs.

Table 5.2 Pore characteristics of ZMOFs, CZMOFs, YP50F, and MSP20

Sample	S_{BET} ($m^2\ g^{-1}$)	S_{meso} ($m^2\ g^{-1}$)	V_{total} ($cm^3\ g^{-1}$)	V_{micro} ($cm^3\ g^{-1}$)	V_{meso} ($cm^3\ g^{-1}$)
ZMOF1	4	-	-	-	-
ZMOF2	15	-	-	-	-
CZMOF1	1266	538	1.50	0.58	1.14
CZMOF2	2678	1190	3.09	1.01	2.38
YP50F	1600	133	0.76	0.70	0.15
MSP20	2266	148	1.00	1.02	0.12

Table 5.3 Pore characteristics of CZMOF1 (batches 1–4) and CZMOF2 (batches 1–4)

Sample	S_{BET} ($m^2\ g^{-1}$)	S_{meso} ($m^2\ g^{-1}$)	V_{total} ($cm^3\ g^{-1}$)	V_{micro} ($cm^3\ g^{-1}$)	V_{meso} ($cm^3\ g^{-1}$)
CZMOF1 b1	1179	423	1.48	0.49	1.13
CZMOF1 b2	1103	417	1.08	0.47	0.76
CZMOF1 b3	1266	538	1.50	0.58	1.14
CZMOF1 b4	1135	457	1.05	0.49	0.73
CZMOF2 b1	2678	1190	3.09	1.01	2.38
CZMOF2 b2	2536	1383	2.88	0.94	2.28
CZMOF2 b3	2535	1179	3.92	0.80	3.26
CZMOF2 b4	2649	1383	4.12	1.03	3.49

Table 5.4 Pore characteristics of Zn-based MOF-derived carbons and their heating conditions taken from the literature

Sample	S_{BET} ($m^2\ g^{-1}$)	V_{total} ($cm^3\ g^{-1}$)	Carbon precursors	Gas	Temperature (°C)	Ref.
CZMOF2_b1 (this work)	2678	3.09	[Zn(BDC)(NMP)]	N_2	1000	-
C-MOF-5	2184	-	$[Zn_4O(BDC)_3]$ (=MOF-5)	Ar	1000	5.30
NPC	2872	2.06	FA/MOF-5 composite	Ar	1000	5.33
AS-ZC-800	2972	2.56	$[Zn(MeIM)_2]$(=ZIF-8)	Ar	800	5.34
NPC530	3040	2.79	FA/MOF-5 composite	Ar	530	5.35
C800	2169	1.50	FA/ZIF-8 composite	Ar	800	5.37
C1000	3405	2.58	FA/ZIF-8 composite	Ar	1000	5.37
HPC5b2-1100	2734	5.23	$[Zn_4O(BDC)_3]$ (=MOF-5)	N_2	1100	5.38
HPC5b2-1000	2517	5.53	$[Zn_4O(BDC)_3]$ (=MOF-5)	N_2	1000	5.38
HPC5b2-900	2495	5.41	$[Zn_4O(BDC)_3]$ (=MOF-5)	N_2	900	5.38
MDC-1	3174	4.06	$[Zn_4O(BDC)_3]$ (=MOF-5)	N_2	900	5.39

NMP (N-methylpyrrolidone), BDC (benzene-1,4-dicarboxylic acid, H_2BDC), FA (=furfuryl alcohol), MeIM (=2-methylimidazole)

5.3.4 Phase changes of ZMOFs and ZIF-8 during calcination at 100–650 °C

The transformation of ZMOFs below 500 °C is further detailed in this section. Figure 5.6 schematizes the transformation of the Zn–MOF crystal lattice into a carbon matrix. Solvent molecules evaporate from the pores, breaking the crystal lattice into amorphous MOFs. The weight of Zn–MOF is dramatically reduced as a result of the thermal breakdown of CO, CO_2, or some types of hydrocarbons. Carbonization begins after this weight loss [5.37]. At higher temperatures, carbonization occurs simultaneously with ZnO growth. As carbons are consumed in ZnO reduction, pores form in the residual carbons.

In this section, the author describes the in situ PXRD and TG-DTA results at temperatures below 650 °C. The commercial ZIF-8 ($C_8H_{10}N_4Zn$) was employed as reference material to confirm the effect of oxygen (O) atoms on pore generation.

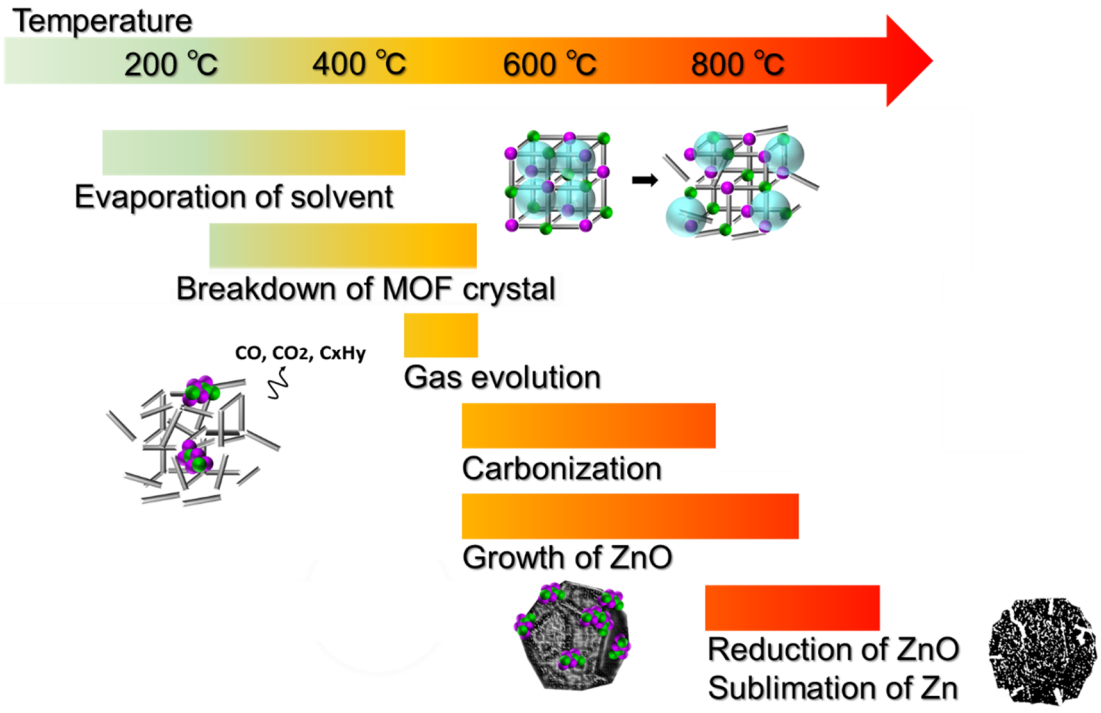

Figure 5.6 Schematic showing the transformation of the Zn–MOF crystal into a carbon matrix as temperature increases

The TG curve of ZMOF1 (Figure 5.7(a)) shows a significant mass drop at 400–450 °C, which can be explained by evaporation of the NMP solvent molecules and the evolution of gases from amorphous MOF. However, the NMP molecules did not escape from the pores even when the temperature approached boiling point (202 °C), because they could not escape through the extremely narrow pores until initial carbonization [5.40]. This result agrees well with the in situ PXRD findings (100–450 °C; see Figure 5.7 (d)). It was inferred that at temperatures above 400 °C, the framework collapsed as the solvent molecules were removed. Simultaneous gas evolution and thermal decomposition resulted in significant weight loss. The first and second significant mass drops in the TG curves of ZMOF2 (Figure 5.7(b)) were attributed to removal of the solvent with framework collapse at ~200 °C and to the gas evolution through thermal decomposition at 420–520 °C, respectively. The first mass drop is supported by the in situ PXRD results (Figure 5.7(e)). From the TG results, the first mass loss was estimated as 30%, which supports the empirical formula of [Zn(BDC)]

(BDC: benzene-1,4-dicarboxylic acid = H_2BDC) after subtracting the molecular formula of NMP from [Zn(BDC)(NMP)]. The second mass drop was similar to that of ZMOF1. Interestingly, the in situ PXRD patterns of ZMOF2 indicate the formation of a transitional intermediate at 400 °C. Meanwhile, the TG curve of ZIF-8 (Figure 5.7 (c)) indicates a small mass drop at 600 °C. The results agree well with in situ PXRD patterns of ZIF-8, showing that the ZIF-8 frameworks completely collapsed after 600 °C (Figure 5.7 (f)). The decomposition temperature was higher than that of ZMOFs, as ZIF-8 does not contain solvent molecules.

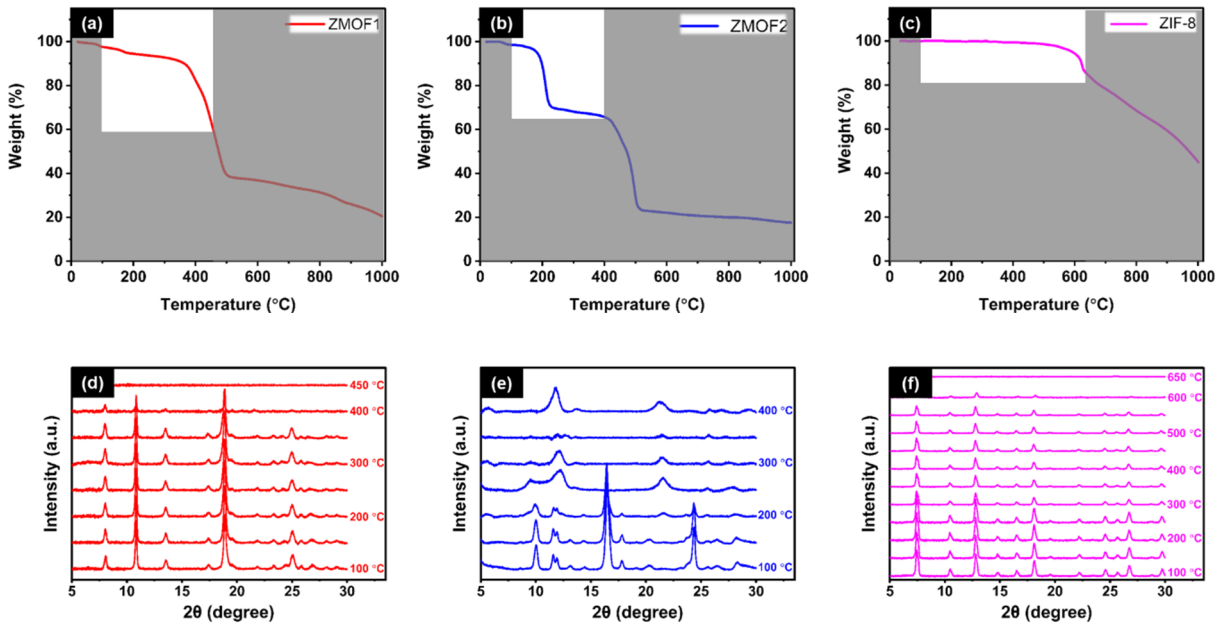

Figure 5.7 Transformation of ZMOF1, ZMOF2, and ZIF-8. TG curves of (a) ZMOF1, (b) ZMOF2, and (c) ZIF-8. In situ PXRD patterns of (d) ZMOF1, (e) ZMOF2, and (f) ZIF-8 at temperatures below 650 °C.

5.3.5 Mechanism underlying pore generation (below 1000 °C)

The author now investigates the effects of Zn and O on pore formation, and hence elucidates the mechanism underlying pore generation in ZMOFs during carbonization.

ZMOFn (n=1 or 2)_X presents ZMOFs that were calcined at X °C without holding time. Based on the TG curves (Figure 5.8 (a)), the S_{BET} values of the ZMOFs calcined at different temperatures were measured to confirm the formation of porous structures through the corresponding transitional processes. The S_{BET} values of the ZMOFs calcined up to 500 °C were similar and ranged from 226 to 244 $m^2\ g^{-1}$ (see Figure 5.8 (a) and Table 5.5). Interestingly, the S_{BET} of ZMOF1_1000 (896 $m^2\ g^{-1}$) was approximately four times that of ZMOF1_500 (226 $m^2\ g^{-1}$), whereas that of ZMOF2_1000 (1497 $m^2\ g^{-1}$) was nearly six times that of ZMOF2_500 (241 $m^2\ g^{-1}$). In both samples, numerous pores were formed at 500–1000 °C. Thus, the author cannot ascribe the porous structure of CZMOFs to the original dense structure of the backbone pristine ZMOFs.

The phase change in calcined ZIF-8 was deduced from the S_{BET} values of ZIF-8 calcined at different temperatures (25 °C, 500 °C, 700 °C, 900 °C, and 1000 °C) as with ZMOFs. Table 5.5 shows the pore characteristics of all ZIF-8-derived carbons. The in situ PXRD patterns of ZIF-8 until 650 °C (Figure 5.7(f)) agreed with the TG curve of ZIF-8. Thermal decomposition might have shrunk the pores above 600 °C, as suggested in the TG curve of ZIF-8 (Figure 5.7(c)). Pore shrinkage caused by decomposition in the ZIF-8 samples may have continued until Zn sublimation. Above 800 °C, the pores were regenerated (Figure 5.8(b) and Table 5.5).

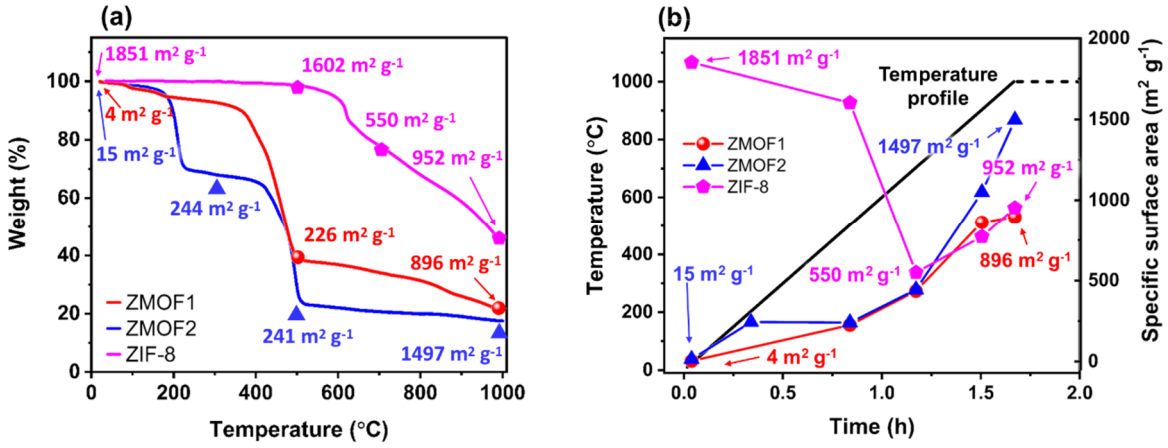

Figure 5.8 (a) TG curves of ZMOF1 (red), ZMOF2 (blue), and ZIF-8 (pink), showing the mass drop points and the S_{BET} at corresponding temperatures. (b) Temperature profile and specific surface area of calcined ZMOF1 (red), ZMOF2 (blue), and ZIF-8 (pink) vs. calcination time indicated that the rate of increase in S_{BET} was different between that up to 1000 °C.

To investigate the effect of the Zn/C ratio and O on pore generation, the author explored the dynamic behavior of Zn atoms in the carbon frameworks at high temperatures (500–1000 °C).

The TG curve of ZMOF1 presented a gradual mass decrease at approximately 850 °C, whereas the mass of ZMOF2 decreased by only a small amount. To clarify the difference between the TG curves and explore the correlation between the Zn/C ratios and S_{BET}, ZMOF1 and ZMOF2 were heated to 1100 °C at 10 °C min^{-1} under a nitrogen flow of 200 mL min^{-1} and analyzed by in situ PXRD (Figure 5.9 (d)), using a commercial ZnO crystal as the reference. Three peaks with Miller indices of (100), (002), and (101) were observed. The peaks shifted toward lower diffraction angles with increasing temperature, reflecting the thermal expansion of the ZnO nanocrystals.

The patterns of both ZMOF1 and ZMOF2 presented the characteristic peaks of ZnO at 500 °C. In the case of ZMOF1, the peaks began to fade around 800 °C and vanished by 950 °C, which is consistent with the TG curve (Figure 5.9 (a)). This suggests that ZnO was reduced to Zn by the surrounding carbons (ZnO + C → Zn (g) + CO) [5.38]. In the case of ZMOF2, the peaks remained until 1050 °C, but disappeared when the temperature was

maintained at 1000 °C for several minutes (Figure 5.10 (a)).

The effect of oxygen (O) on the nucleation of ZnO was explored in an in situ PXRD analysis of ZIF-8 ($C_8H_{10}N_4Zn$) under the same conditions as the ZMOF1 and ZMOF2 analyses. Peaks attributable to ZnO were absent at all temperatures (Figure 5.9 (a)). It was observed that both O and Zn inside the Zn-MOFs were required for ZnO nucleation during carbonization in the inert atmosphere.

In both ZMOF1 and ZMOF2 samples, the (100) peaks were split into two at 800 °C, but the doublet disappeared before 1000 °C (asterisks in Figure 5.9 (d) – (f)). An in situ PXRD investigation of the other samples revealed this fascinating pattern (ZMOF1, ZMOF2, and ZIF-8). When the strength of the characteristic peak of ZnO began to decrease at 800 °C, the intensity of the unidentified peak began to increase (Figure 5.10 (b)). Interestingly, the same phenomenon appeared in the in situ PXRD patterns of ZIF-8 between 800 °C and 900 °C. ZnO was not reduced during the carbonization of ZIF-8 as discussed above. Thus, this phenomenon was possibly attributable to Zn sublimation. A transitional intermediate may have evolved until Zn was sublimed from the carbon matrix, although the mechanism behind this occurrence remains unknown.

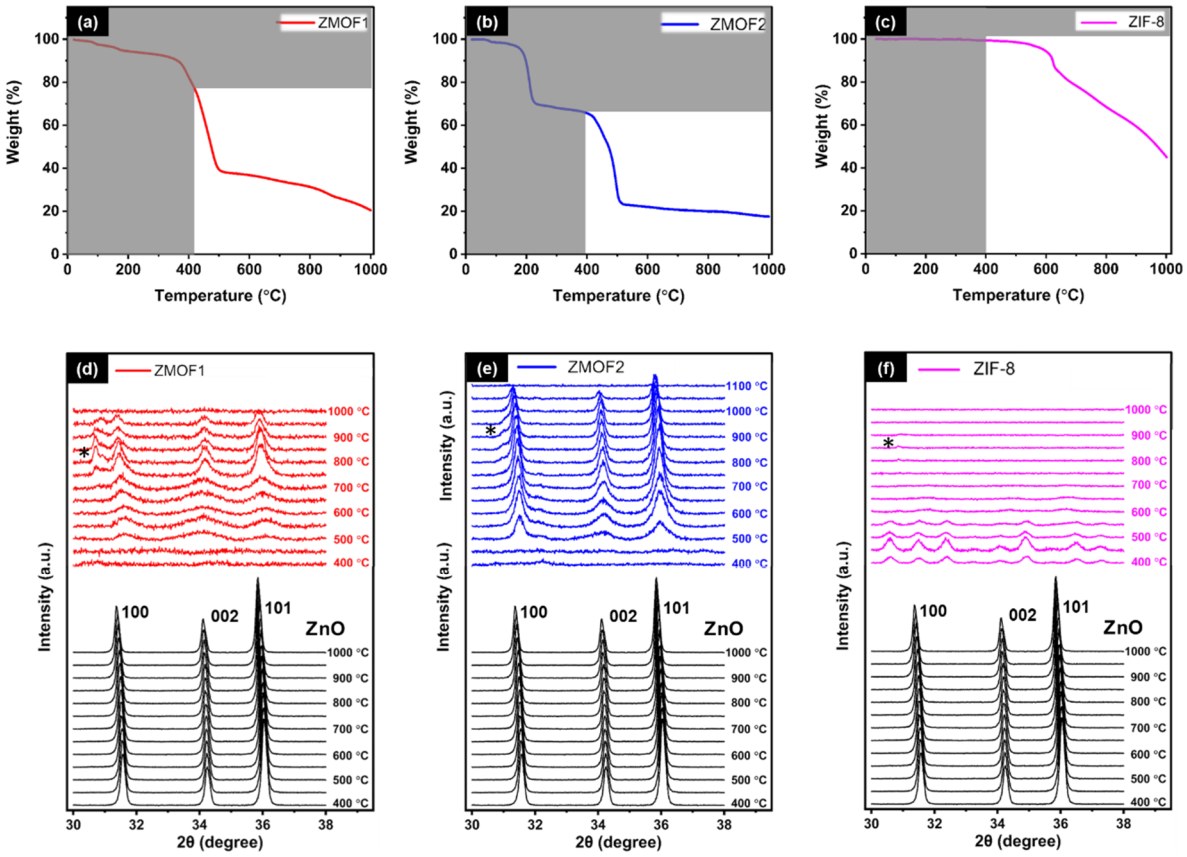

Figure 5.9 TG curves of (a) ZMOF1 (red), (b) ZMOF2 (blue) and (c) ZIF-8 (pink). In situ PXRD patterns (400–1100 °C) of (d) ZMOF1 (red), (e) ZMOF2 (blue), and (f) ZIF-8 (pink), ranging from 30° to 38°, revealing ZnO generation during carbonization in both ZMOF samples. Figures (d) – (f) contains PXRD patterns pure ZnO (black), showing the three typical ZnO peaks.

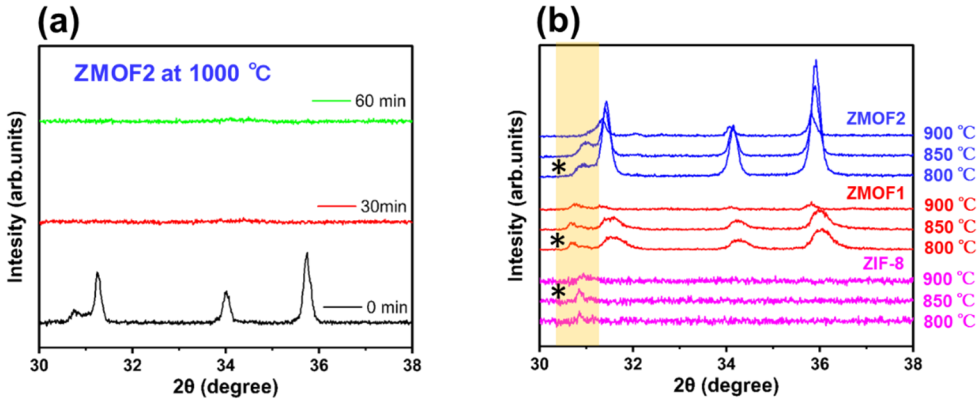

Figure 5.10 (a) In situ PXRD patterns of ZMOF2 at 1000 °C maintained for 0, 30, and 60 min, confirming that at least several tens of minutes were required for the complete reduction of ZnO when maintained at 1000 °C. (b) In situ PXRD patterns of ZMOF1, ZMOF2, and ZIF-8 from 800 °C to 900 °C.

Table 5.5 Pore characteristics of ZMOF1, ZMOF2, and ZIF-8 calcined at different temperatures

Sample	Temperature (°C)	Holding time (h)	S_{BET} ($m^2\ g^{-1}$)	S_{meso} ($m^2\ g^{-1}$)	V_{total} ($cm^3\ g^{-1}$)	V_{micro} ($cm^3\ g^{-1}$)	V_{meso} ($cm^3\ g^{-1}$)
ZMOF1	-	-	4	-	-	-	-
	500	0	226	35	0.14	0.10	0.06
	700	0	435	52	0.21	0.20	0.05
	900	0	862	79	0.41	0.38	0.09
	1000	0	896	143	0.58	0.41	0.26
	1000	1	886	178	0.62	0.39	0.32
	1000	3	988	288	0.82	0.43	0.51
(CZMOF1)	1000	5	1103	417	1.08	0.47	0.76
ZMOF2	-	-	15	-	-	-	-
	300	0	244	44	0.26	0.08	0.17
	500	0	241	67	0.29	0.09	0.22
	700	0	444	142	0.44	0.20	0.31
	900	0	1049	209	0.70	0.49	0.34
	1000	0	1497	478	1.50	0.65	1.04
	1000	1	1779	719	1.81	0.85	1.30
	1000	3	2414	1281	2.73	0.94	2.14
(CZMOF2)	1000	5	2536	1383	2.88	0.94	2.28
ZIF-8	-	-	1851	11	0.69	0.68	0.07
	500	0	1602	41	0.71	0.65	0.11
	700	0	550	38	0.30	0.23	0.09
	900	0	772	59	0.40	0.32	0.12
	1000	0	952	74	0.51	0.40	0.16
	1000	1	N.D.	N.D.	N.D.	N.D.	N.D.
	1000	3	1336	105	0.65	0.57	0.15
(CZIF-8)	1000	5	1369	120	0.74	0.61	0.22

ZIF-8 is the commercial material obtained from Sigma-Aldrich Tokyo, Japan.

Concerning ZMOFs, the Zn/C ratio and the presence of O atoms played a decisive role in the stability of ZnO at high temperatures during carbonization. It appeared that numerous carbons were consumed to complete the reduction of highly stable ZnO, thus forming highly porous carbons. Upon carbonization, the ZnO nanocrystal sizes (~70 nm) for Miller indices of (100), (002), and (101) were calculated using the Debye–Scherrer equation[5.52]:

$$D = (\mathrm{K}\lambda)/\beta cos\theta \tag{5.1}$$

where D, K, β, and θ are the crystallite size, form factor (0.94 for spherical particles), FWHM, and diffraction angle, respectively. The ZnO nanocrystals formed in ZMOF2 (~70 nm) were larger than those formed in ZMOF1 (~50 nm). The Zn/C ratios affected the crystallinity and stability of the ZMOF species during carbonization. The meso/macropore sizes in the respective CZMOFs may have been influenced by the nanocrystal sizes. Thus, the presence of macropores in the carbon matrix may have contributed to the carbon consumption of ZnO reduction and Zn sublimation.

The PSD of CZIF-8 indicated the formation of micropore-rich carbon materials (Figure 5.11 (a), (b)), whereas CZMOFs were dominated by micropores and mesopores. Mesopores may have formed in the CZMOFs as a result of ZnO reduction and subsequent Zn sublimation (Zn has a boiling point of 908 °C). This shows that, as previously noted, ZnO nucleation was linked to the creation of meso-macropores in CZMOF1 and CZMOF2.

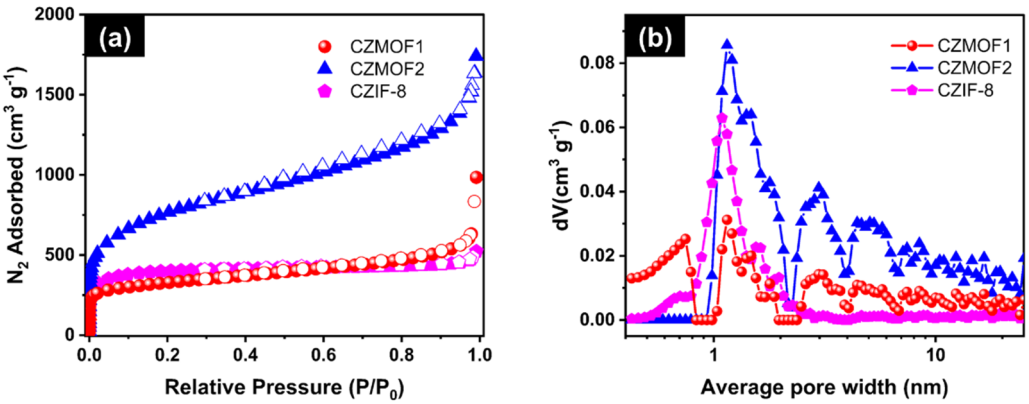

Figure 5.11 (a) Nitrogen adsorption/desorption (solid/empty symbols, respectively) isotherms and (b) Average pore size distributions (average pore width on the semi-logarithmic scale) of CZMOF1 (red), CZMOF2 (blue), and CZIF-8 (pink), showing the generation of 3–10 nm pores unlike those by CZIF-8.

5.3.6 Mechanism underlying pore generation (above 1000 °C)

According to Figure 5.12, pores continued to develop when the temperature was maintained at 1000 °C for 5 h. Figures 5.13(a),(b) show the XP C1s spectra of ZMOF1 and ZMOF2 after calcination at 1000 °C for 0, 3, and 5 h, respectively. The spectra of calcined ZMOF1 showed a diminishing peak corresponding to C–O (286.2–287.5 eV) [5.53], indicating that the amount of oxygen-combining carbon decreased with increasing holding time at 1000 °C. In the spectra of calcined ZMOF2, the peaks corresponding to C–O (286.2–287.5 eV), >C=O (286.5–287.9 eV), and –COO (288.4–289.5 eV)[5.53] disappeared over the holding time, similarly to those in the spectra of calcined ZMOF1. Oxyegn functional groups such as quinone or carbonyl are known to decompose to CO at 900–1000 °C [5.54]. Meanwhile, the S_{BET} values of ZMOF1 and ZMOF2 increased with increasing holding time at 1000 °C (Figure 5.12), because pores could be generated through pyrolysis of the oxygen functional groups at this temperature. Oxygen functional groups such as quinone or carbonyl were degraded from the carbons at 1000 °C with holding, according to the XP C1s spectra of both CZMOFs (see Figures 5.13(a),(b)). Simultaneously, the S_{BET} increased with increasing holding time (Figure 5.12). CO_2 activation formed pores on the carbons at temperatures above 800 °C [5.55]. The reaction is given by

$$C_{(n)} + CO_2 \rightarrow C_{(n-1)} + 2CO \quad (5.2)$$

Initially, the carbon atoms on the active edge sites likely reacted with the oxygen atoms of CO_2. Subsequently, the carbon atoms could be transformed to the transitional intermediates of oxygen functional groups such as quinone or carbonyl, followed by pyrolysis to CO. Pyrolysis of oxygen functional groups can be a step in the CO_2 activation process. As a result, pyrolysis of CZMOF oxygen functional groups is likely to contribute to pore formation and CO_2 activation.

The C1s spectra of the ZIF-8-derived carbons showed almost the same peaks after calcination at 1000 °C for 0, 3, and 5 h (Figure 5.13(c)), suggesting that the oxygen atoms in the ZMOFs formed oxygen functional groups during carbonization. After guest removal, the O/C ratios of ZMOF1 ($C_{16}H_{10}O_4Zn$) and ZMOF2 ($C_8H_4O_4Zn$) were determined to be 0.25 and 0.50, respectively, indicating that the quantity of oxygen functional groups (quinone or carbonyl) in the CZMOFs increased.

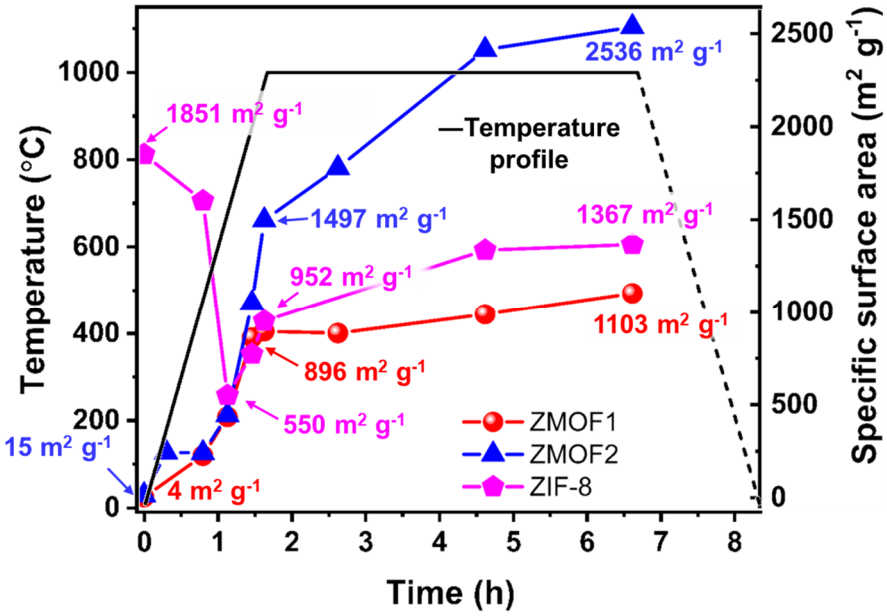

Figure 5.12 Temperature profile and S_{BET} of calcined ZMOF1 (red), ZMOF2 (blue), and ZIF-8 (pink) vs. calcination time indicated that the rate of increase in S_{BET} was different between that up to 1000 °C and that above 1000 °C.

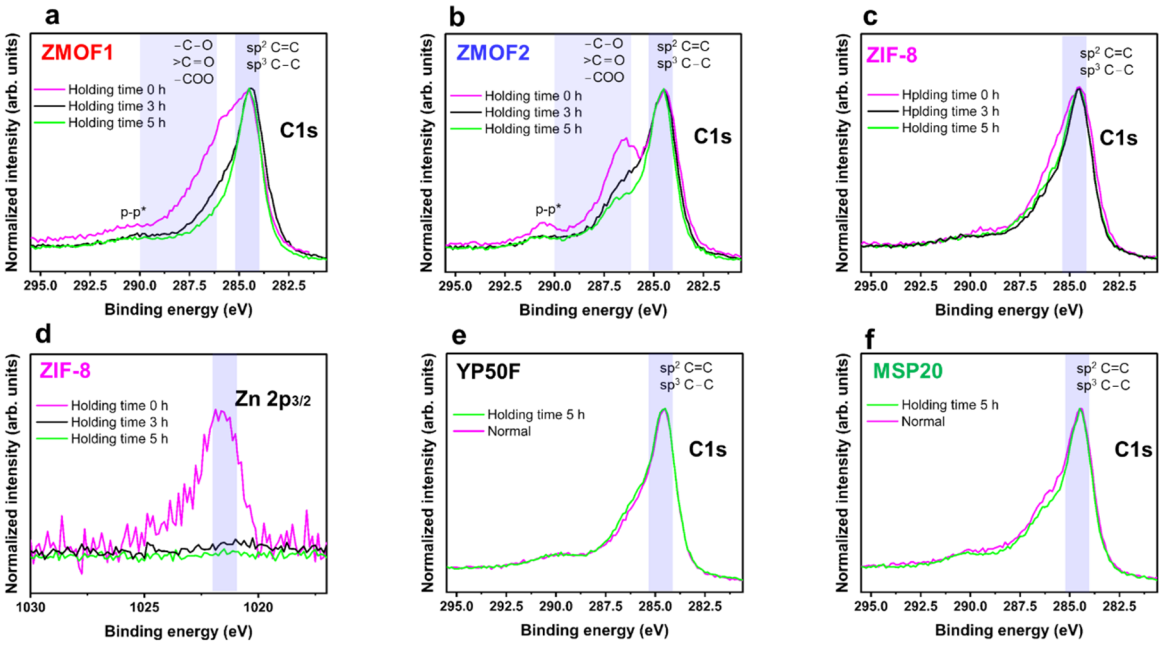

Figure 5.13 (a),(b) XP C1s spectra of ZMOF1 and ZMOF2 calcined at 1000 °C for 0 (purple), 3(black), and 5 h (fluorescent green), normalized at 284.5 eV (C–C and/or C=C) show that the amount of carbon that was combined with oxygen decreased with increasing holding time. (c) XP C1s spectra of ZIF-8 calcined at 1000 °C for 0, 3, and 5 h. (d) XP Zn $2p_{3/2}$ spectra of ZIF-8 calcined at 1000 °C for 0, 3, and 5 h. The Zn peaks disappeared after 3 h of holding. These results elucidate the mechanism of pore generation of ZIF-8 during carbonization. XP C1s spectra (normalized at 284.5 eV (C–C and/or C=C)) of (e) YP50F and (f) MSP20. The corresponding samples were divided into two groups [normal (pink) and calcined at 1000 °C for 5 h (fluorescent green)].

Notably, it was found that in the materials based on ZMOF carbon precursors, the mechanism underlying pore generation at temperatures up to 1000 °C differed from that above 1000 °C. In contrast to the CZMOFs, ZIF-8 samples, which were calcined at 1000 °C for 0, 3, and 5 h, presented no evidence of carbon–oxygen combinations in its XP C1s spectra (Figure 5.13 (c)), suggesting that the oxygen in the ZMOFs formed oxygen functional groups during carbonization. After guest removal, the O/C ratios of ZMOF1 ($C_{16}H_{10}O_4Zn$) and ZMOF2 ($C_8H_4O_4Zn$) were determined to be 0.25 and 0.50, respectively, indicating that the quantity of oxygen functional groups (quinone or carbonyl) in the CZMOFs increased. The amount of oxygen was considered to crucially affect pore generation in the CZMOFs at temperatures above 1000 °C. The pore generation in CZIF-8 above 1000 °C was driven by the sublimation of the remaining Zn. CZIF-8's XP Zn 2p3/2 spectrum revealed that Zn sublimation took a long time at 1000 °C, resulting in high porosity

(Figure 5.11(a) and Figure 5.12). S_{BET} of CZIF-8 did not increase while the temperature was maintained at 1000 °C, as can be seen in Figure 5.12.

Likewise, the XP spectra and S_{BET} values of the two activated carbons (YP50F and MSP20) were unchanged after calcination at 1000 °C for 5 h under identical conditions (Figure 5.13(e),(f) and Figure 5.14). It was discovered that ZMOF-derived carbons have more oxygen atoms than commonly activated carbons (YP50F and MSP20), allowing for the production of highly porous carbons.

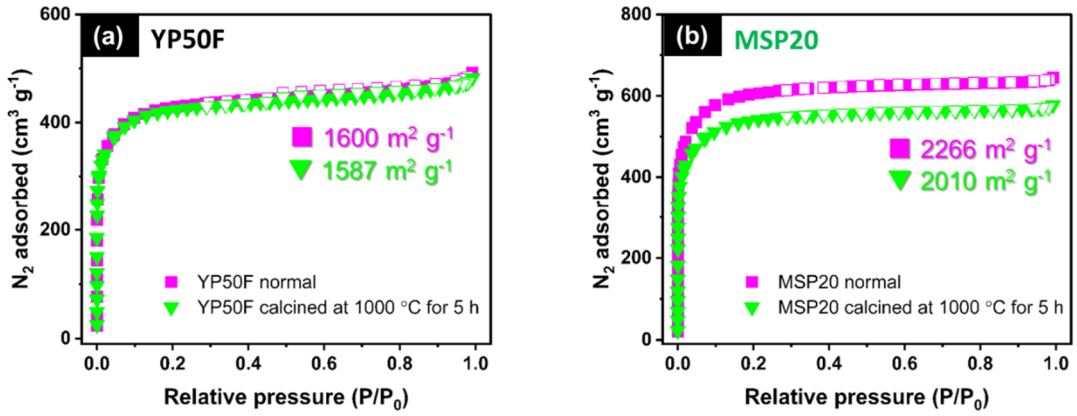

Figure 5.14 Nitrogen adsorption/desorption isotherms of (a) YP50F and (b) MSP20. The corresponding samples were divided into two groups [normal (pink) and calcined at 1000 °C for 5 h (fluorescent green)].

5.4 Conclusion

Two CZMOFs were successfully synthesized by activating ZMOFs with different Zn/C ratios (0.0625 and 0.1250) and O/C ratios (0.25 and 0.50). The Zn/C ratio significantly affected the specific surface areas of the CZMOFs below 1000 °C. The in situ PXRD examination of the carbonized ZMOFs revealed important details about the dynamic behavior of ZnO in the carbonized ZMOFs, demonstrating that the Zn/C ratio influenced the stability of crystalline ZnO at high temperatures. Furthermore, numerous pores were developed during ZnO reduction and Zn sublimation up to 1000 °C. A high O/C ratio was essential for pore generation at >1000 °C because pores were generated by pyrolysis of oxygen functional groups. Whether oxygen atoms are absent or present in the MOF structure, oxide formation and decomposition of oxygen functional groups during the carbonization process play a significant role in pore control. This finding is helpful for the pore control of the carbons derived from other metal-based MOF.

5.5 References

[5.1] Y.-Z. Chen, C. Wang, Z.-Y. Wu, Y. Xiong, Q. Xu, S.-H. Yu and H.-L. Jiang, "From bimetallic metal-organic framework to porous carbon: High surface area and multicomponent active dopants for excellent electrocatalysis." *Adv. Mater.*, 27, 5010–5016 (2015).

[5.2] Q. Yang, C.-C. Yang, C.-H. Lin and H.-L. Jiang, "Metal–organic-framework-derived hollow N-doped porous carbon with ultrahigh concentrations of single Zn atoms for efficient carbon dioxide conversion" *Angew. Chem. Int. Ed.*, **131**, 3549–3533 (2019).

[5.3] V. Shrivastav, S. Sundriyal, P. Goel, H. Kaur, S. K. Tuteja, K. Vikrant, K.-H. Kim, U. K. Tiwari and A. Deep, "Metal-organic frameworks (MOFs) and their composites as electrodes for lithium battery applications: Novel means for alternative energy storage." *Coord. Chem. Rev.*, **393**, 48–78 (2019).

[5.4] B. Xu, H. Zhang, H. Mei and D. Sun, "Recent progress in metal-organic framework-based supercapacitor electrode materials." *Coord. Chem. Rev.*, 420 (2020).

[5.5] X. Lou, Y. Ning, C. Li, M. Shen, B. Hu, X. Hu and B. Hu, "Exploring the capacity limit: A layered hexacarboxylate-based metal-organic framework for advanced lithium storage." *Inorg. Chem.*, **57**, 3126–3132 (2018).

[5.6] P. Wang, X. Lou, C. Li, X. Hu, Q. Yang and B. Hu, " One-pot synthesis of co-based coordination polymer nanowire for Li-Ion batteries with great capacity and stable cycling stability." *Nano-Micro Lett.*, **10**, 19 (2018).

[5.7] X. Hu, X. Lou, C. Li, Y. Ning, Y. Liao, Q. Chen, E. S. Mananga, M. Shen and B. Hu, " Facile synthesis of the basolite F300-like nanoscale Fe-BTC framework and its lithium storage properties." *RSC Adv.*, **6**, 114483–114490 (2016).

[5.8] C. Li, X. Hu, X. Lou, L. Zhang, Y. Wang, J.-P. Amoureux, M. Shen, Q. Chen and B. Hu, "The organic-moiety-dominated Li+ intercalation/deintercalation mechanism of a cobalt-based metal–organic framework." *J. Mater. Chem. A*, 4, 16245–16251 (2016).

[5.9] X. Shi, S. Zhang, X. Chen, T. Tang and E. Mijowska, "Three dimensional graphene/carbonized metal-organic frameworks based high-performance supercapacitor.
" *Carbon*, **157**, 55–63 (2020).

[5.10] R. Ramachandran, C. Zhao, D. Luo, K. Wang and F. Wang, "Morphology-dependent electrochemical properties of cobalt-based metal organic frameworks for supercapacitor electrode materials." *Electrochim. Acta*, **267**, 170–180 (2018).

[5.11] C. Young, J. Kim, Y. V. Kaneti and Y. Yamauchi, "One-step synthetic strategy of hybrid materials from bimetallic metal–organic frameworks for supercapacitor applications." *ACS Appl. Energy Mater.*, **1**, 2007–2015 (2018).

[5.12] Z. Liang, R. Zhao, T. Qiu, R. Zou, and Q. Xu, "Metal-organic framework-derived materials for electrochemical energy applications." *Energy Chem*, **1**, 100001 (2019).

[5.13] K.-B. Wang, Q. Xun, and Q. Zhang,"Recent progress in metal-organic frameworks as active materials for supercapacitors." *Energy Chem*, **2**, 100025 (2020).

[5.14] X. Li, X. Yang, H. Xue, H. Pang, and Q. Xu, "Metal–organic frameworks as a platform for clean energy applications." *Energy Chem*, **2**, 100027 (2020).

[5.15] M. Safaei, M. M. Foroughi, N. Ebrahimpoor, S. Jahani, A. Omidi and M. Khatami, "A review on metal-organic frameworks: Synthesis and applications." *TrAC, Trends Anal. Chem.*, **118**, 401–425 (2019).

[5.16] L. Jiao, J. Y. R. Seow, W. S. Skinner, Z. U. Wang and H.-L. Jiang, " Metal–organic frameworks: Structures and functional applications." *Mater. Today*, **27**, 43-68 (2019).

[5.17] H. Furukawa, K. E. Cordova, M. O'Keeffe and O. M. Yaghi, "The chemistry and applications of metal-organic frameworks." *Science*, **341**, 1230444 (2013).

[5.18] M. Jiang, X. Cao, P. Liu, T. Zhang and J. Zhang, "ZIF-8@Polyvinylpyrrolidone nanocomposites based N-doped porous carbon for highly efficient oxygen reduction reaction in alkaline solution." *J. Electrochem. Soc.,* **163**, H459–H464 (2016).

[5.19] Z. Abbasi, E. Shamsaei, S. K. Leong, B. Ladewig, X. Zhang and H. Wang, "Effect of carbonization temperature on adsorption property of ZIF-8 derived nanoporous carbon for water treatment." *Microporous Mesoporous Mater.*, **236**, 28–37 (2016).

[5.20] P. Liang, C. Zhang, H. Sun, S. Liu, M. Tadé and S. Wang, " Photocatalysis of C, N-doped ZnO derived from ZIF-8 for dye degradation and water oxidation." *RSC Adv.*, **6**, 95903–95909 (2016).

[5.21] C. Young, R. R. Salunkhe, J. Tang, C. C. Hu, M. Shahabuddin, E. Yanmaz, M. S. Hossain, J. H. Kim and Y. Yamauchi, "Zeolitic imidazolate framework (ZIF-8) derived nanoporous carbon: the effect of carbonization temperature on the supercapacitor performance in an aqueous electrolyte." *Phys. Chem. Chem. Phys.*, **18**, 29308–29315 (2016).

[5.22] J. Zou, P. Liu, L. Huang, Q. Zhang, T. Lan, S. Zeng, X. Zeng, L. Yu, S. Liu, H. Wu, W. Tu and Y. Yao, "Ultrahigh-content nitrogen-decorated nanoporous carbon derived from metal organic frameworks and its application in supercapacitors." *Electrochim. Acta*, **271**, 599–607 (2018).

[5.23] L. Wang, Y. Han, X. Feng, J. Zhou, P. Qi and B. Wang, "Metal–organic frameworks for energy storage: Batteries and supercapacitors." *Coord. Chem. Rev.*, **307**, 361–381 (2016).

[5.24] N. L. Torad, R. R. Salunkhe, Y. Li, H. Hamoudi, M. Imura, Y. Sakka, C. C. Hu and Y. Yamauchi, " Electric double-layer capacitors based on highly graphitized nanoporous carbons derived from ZIF-67." *Chem. Eur. J.*, **20**, 7895–7900 (2014).

[5.25] N. L. Torad, M. Hu, S. Ishihara, H. Sukegawa, A. A. Belik, M. Imura, K. Ariga, Y. Sakka and Y. Yamauchi, "Direct synthesis of MOF-derived nanoporous carbon with magnetic Co nanoparticles toward efficient water treatment." *Small*, **10**, 2096–2107 (2014).

[5.26] J. A. Carrasco, J. Romero, G. Abellan, J. Hernandez-Saz, S. I. Molina, C. Marti-Gastaldo and E. Coronado, "Small-pore driven high capacitance in a hierarchical carbon via carbonization of Ni-MOF-74 at low temperatures." *Chem. Commun*, **52**, 9141–9144 (2016).

[5.27] Z. Lv, H. Wang, C. Chen, S. Yang, L. Chen, A. Alsaedi and T. Hayat, "Enhanced removal of uranium(VI) from aqueous solution by a novel Mg-MOF-74-derived porous MgO/carbon adsorbent." *J. Colloid Interface Sci.*, **537**, A1-A10 (2019).

[5.28] M. Hu, J. Reboul, S. Furukawa, N. L. Torad, Q. Ji, P. Srinivasu, K. Ariga, S. Kitagawa and Y. Yamauchi, "Direct carbonization of Al-based porous coordination polymer for synthesis of nanoporous carbon." *J. Am. Chem. Soc.*, **134**, 2864–2867 (2012).

[5.29] L. Radhakrishnan, J. Reboul, S. Furukawa, P. Srinivasu, S. Kitagawa and Y. Yamauchi, "Preparation of microporous carbon fibers through carbonization of Al-based porous coordination polymer (Al-PCP) with furfuryl alcohol." *Chem. Mater.*, **23**, 1225–1231 (2011).

[5.30] H. B. Aiyappa, P. Pachfule, R. Banerjee and S. Kurungot, "Porous carbons from nonporous MOFs: Influence of ligand characteristics on intrinsic properties of end carbon.
" *Cryst. Growth Des.*, **13**, 4195–4199 (2013).

[5.31] S. Lim, K. Suh, Y. Kim, M. Yoon, H. Park, D. N. Dybtsev and K. Kim, "Porous carbon materials with a controllable surface area synthesized from metal–organic frameworks. "*Chem. Commun.*, **48**, 7447–7449 (2012).

[5.32] W. Bao, A. K. Mondal, J. Xu, C. Wang, D. Su and G. Wang, "3D hybrid–porous carbon derived from carbonization of metal organic frameworks for high performance supercapacitors. "*J. Power Sources*, **325**, 286–291 (2016).

[5.33] B. Liu, H. Shioyama, T. Akita and Q. Xu, "Metal-organic framework as a template for porous carbon synthesis." *J. Am. Chem. Soc.*, **130**, 5390–5391 (2007).

[5.34] A. J. Amali, J. K. Sun and Q. Xu, *Chem .Commun.*, "From assembled metal–organic framework nanoparticles to hierarchically porous carbon for electrochemical energy storage. ," **50**, 1519–1522 (2014).

[5.35] B. Liu, H. Shioyama, H. Jiang, X. Zhang and Q. Xu, "Metal–organic framework (MOF) as a template for syntheses of nanoporous carbons as electrode materials for supercapacitor." *Carbon*, **48**, 456–463 (2010).

[5.36] W. Chaikittisilp, M. Hu, H. Wang, H. S. Huang, T. Fujita, K. C. Wu, L. C. Chen, Y. Yamauchi and K. Ariga, "Nanoporous carbons through direct carbonization of a zeolitic imidazolate framework for supercapacitor electrodes." *Chem. Commun.*, **48**, 7259–7261 (2012).

[5.37] H. L. Jiang, B. Liu, Y. Q. Lan, K. Kuratani, T. Akita, H. Shioyama, F. Zong and Q. Xu, " From metal–organic framework to nanoporous carbon: Toward a very high surface area and hydrogen uptake." *J. Am. Chem. Soc.*, **133**, 11854–11857 (2011).

[5.38] G. Srinivas, V. Krungleviciute, Z.-X. Guo and T. Yildirim, "Exceptional CO_2 capture in a hierarchically porous carbon with simultaneous high surface area and pore volume." *Energy Environ. Sci.*, **7**, 335–342 (2014).

[5.39] S. J. Yang, T. Kim, J. H. Im, Y. S. Kim, K. Lee, H. Jung and C. R. Park, "MOF-derived hierarchically porous carbon with exceptional porosity and hydrogen storage capacity. "*Chem. Mater.*, **24**, 464–470 (2012).

[5.40] C. A. Bauer, T. V. Timofeeva, T. B. Settersten, B. D. Patterson, V. H. Liu, B. A. Simmons and M. D. Allendorf, "Influence of connectivity and porosity on ligand-based luminescence in zinc metal−organic frameworks."*J. Am. Chem. Soc.*, **129**, 7136–7144 (2007).

[5.41] J. Xing, L. Schweighauser, S. Okada, K. Harano and E. Nakamura, "Atomistic structures and dynamics of prenucleation clusters in MOF-2 and MOF-5 syntheses. " *Nat. Commun.*, **10**, 3608 (2019).

[5.42] F.-K. Wang, S.-Y. Yang, R.-B. Huang, L.-S. Zheng and S. R. Batten, "Control of the topologies and packing modes of three 2D coordination polymers through variation of the solvent ratio of a binary solvent mixture." *CrystEngComm*, **10** (2008).

[5.43] L. Liu, Y. Yu, K. Li and Z. Zheng, "Wearable energy-dense and power-dense supercapacitor yarns enabled by scalable graphene–metallic textile composite electrodes. " *Nat. Commun.,* **6**, 7260 (2015).

[5.44] N. Stock and S.Biswas, “Synthesis of metal-organic frameworks (MOFs): Routes to various MOF topologies, morphologies, and composites.” *Chem. Rev.,* **112**, 933 (2012).

[5.45] W. Kukulka, K. Cendrowski and E. Mijowska, “Electrochemical performance of MOF-5 derived carbon nanocomposites with 1D, 2D and 3D carbon structures.” *Electrochem. Acta.,* **307**, 582 (2019).

[5.46] J. S. W. Choi, J. Son, J.Kim and W. S. Ahn, “Metal–organic framework MOF-5 prepared by microwave heating: Factors to be considered.” *Microporous Mesoporous Mater.,* **116**, 727 (2008).

[5.47] W. J. Son, J. Kim and W. S. Ahn, “Sonochemical synthesis of MOF-5.” *Chem. Commun.,* 6336 (2008).

[5.48] L. M. Malard, M. A. Pimenta, G. Dresselhaus and M. S. Dresselhaus, "Raman spectroscopy in graphene." *Phys. Rep.*, **473**, 51–87 (2009).

[5.49] H. M. Lee, K. H. An, S. J. Park and B. J. Kim, "Mesopore-rich activated carbons for electrical double-layer capacitors by optimal activation condition." *Nanomaterials*, **9**, 608 (2019).

[5.50] K. Sing, "The use of nitrogen adsorption for the characterisation of porous materials. "*Colloids Surf.*, **187-188**, 3–9 (2001).

[5.51] K. Akhbari and A. Morsali, "Effect of the guest solvent molecules on preparation of different morphologies of ZnO nanomaterials from the $[Zn_2(1,4\text{-bdc})_2(dabco)]$ metal-organic framework." *J. Coord. Chem.*, **64**, 3521–3530 (2011).

[5.52] S. Mustapha, M. M. Ndamitso, A. S. Abdulkareem, J. O. Tijani, D. T. Shuaib, A. K. Mohammed and A. Sumaila, "Comparative study of crystallite size using Williamson-Hall and Debye-Scherrer plots for ZnO nanoparticles." *Adv. Nat. Sci: Nanosci. Nanotechnol*., **10**, 045013

[5.53] T. I. T. Okpalugo, P. Papakonstantinou, H. Murphy, J. McLaughlin and N. M. D. Brown, "High resolution XPS characterization of chemical functionalised MWCNTs and SWCNTs." *Carbon*, **43**, 153–161 (2005).

[5.54] J. L. Figueiredo, M. F. R. Pereira, M. M. A. Freitas and J. J. M. O. rfa˜o, "Modification of the surface chemistry of activated carbons. *Carbon*, **37**, 1379–1389 (1999).

[5.55] S. Roman, J. F. Gonzalez, C. M. Gonzalez-Garcia, and F. Zamora, "Control of pore development during CO_2 and steam activation of olive stones" *Fuel Process. Technol.,* **89**, 715–720, (2008)

6 Feasibility of the electrode materials using zinc-based metal-organic frameworks

6.1 Introduction

Considerable studies on MOFs-based SC electrodes have been reported so far [6.1–6.4]. Most studies on MOF-derived carbons briefly examined the electrochemical properties of SC electrodes through typical measurements, such as GCD tests, EI, and CV. This chapter fully evaluates the electrochemical properties of CZMOFs with aqueous electrolytes (1.0 M H_2SO_4) to provide a more detailed and fundamental discussion. The relationship between the specific voltammetric charge (Q/C g^{-1}) and S_{BET} of the carbon samples was investigated to obtain information on pure EDL behavior. Furthermore, the positive and negative capacitances were calculated individually to precisely estimate the capacitance induced by the adsorption/desorption of the anion/cations.

Non-aqueous electrolytes offer a wider voltage window and higher energy density than aqueous electrolytes [6.5]. Consequently, non-aqueous electrolytes are used in practical SCs. However, to the best of the author's knowledge, there are few reports on the practical applicability of MOF-derived SCs with non-aqueous electrolytes. Moreover, the relationship between pore size and electrolytes should be explored using both aqueous and non-aqueous electrolytes, as discussed in chapter 2. Thus, in this study, SC cells with non-aqueous electrolytes were assembled to demonstrate the practical applicability of the electrode materials based on the CZMOFs. Moreover, 100,000 charge/discharge cycles were conducted to verify the durability of the CZMOFs. The author attempted to confirm the possible extension of the lifetime and the range of applicable temperatures of the ZMOF electrode.

6.2 Experimental procedures

6.2.1 Preparation of ZMOFs

ZMOF1 was synthesized from two types of solutions: (A) zinc acetate (Nacalai Tesque Inc., Japan) (176 mg) dissolved in 30-mL NMP (Nacalai Tesque Inc., Japan), and (B) 4,4-stilbene dicarboxylic acid (Tokyo Chemical Industry Co. Ltd., Japan) (858 mg) dissolved in 400 mL of NMP. Subsequently, solution A was transferred to solution B by a liquid delivery pump (flow speed ~4.0 mL min^{-1}). The mixture was left for 72 h at 40 °C. The formed precipitate was washed with 100 mL of NMP and dried at 120 °C under a vacuum for 12 h, yielding a powdery product (~220 mg). ZMOF2 was similarly synthesized from two types of solutions: (A) as described above and (C) terephthalic acid (Tokyo Chemical Industry Co. Ltd., Japan) (532 mg) dissolved in 80 mL of NMP. Solution A was transferred to solution C by a liquid delivery pump (flow speed ~4.0 mL min^{-1}). The subsequent steps were as described for ZMOF1. The weight of the final powdery product was ~230 mg.

6.2.2 Preparation of CZMOFs

The ZMOF powder was placed in a ceramic boat made of alumina; the boat was transferred to a quartz furnace tube. The sample was heated under nitrogen, with the purity of 99.99%, at a flow of 200 mL min^{-1} and a heating rate of 10 °C min^{-1} until the temperature reached 1000 °C. This temperature was maintained for 5 h, following which the samples were naturally cooled to room temperature (18–25 °C). A black powder was collected (CZMOFs). The process was repeated several times, and the mixture of the samples was characterized as follows. The S_{BET} of CZMOF1 and CZMOF2 obtained here are calculated to be 1266 and 2678 m^2 g^{-1}, respectively.

6.2.3 Fabrication of electrodes (for aqueous electrolytic cells)

The active material (30 mg of CZMOF1 or CZMOF2), a conductive additive (DENKA BLACK, Denka Co. Ltd., Japan) (3.75 mg), and a PTFE binder (6-J, Chemours-Mitsui Fluoroproducts Co. Ltd., Japan) (3.75 mg) were mixed at a mass ratio of 8:1:1 and kneaded with an agate mortar and pestle until a sheet material was formed. Disks of diameter 13 mm were prepared by molding and compressing (60 MPa) the sheet material in a powder-compressed tablet machine (Shimadzu Corporation, Japan). The working electrode was obtained by attaching the disk to a titanium (Ti) mesh current collector, which was not dissolved in H_2SO_4 (see Figure 2.1). The electrochemical properties of the Zn-activated carbons (CZMOF1 and CZMOF2) were compared with those of the reference activated carbons, namely, YP50F (coconut shell origin, physical activation with H_2O-steam, Kuraray Chemical Co. Ltd., Japan) and MSP20 (phenol resin origin, chemical activation with KOH; Kansai Coke and Chemicals, Japan) used for the production of porous carbons and SC electrode materials[6.6]. Besides, the commercial zeolitic imidazolate framework (ZIF-8, Z1200, Sigma-Aldrich, USA) was also selected as reference material to compare the nitrogen (N)-doping effect. As with CZMOFs, ZIF-8 was heated at 10 °C min^{-1} under a nitrogen flow of 200 mL min^{-1} until the temperature reached 1000 °C, and the temperature was maintained for 5 h. The heated samples were naturally cooled to room temperature (18–25 °C). The obtained calcined ZIF-8 is denoted as CZIF-8. The same electrode fabrication process was applied to YP50F, MSP20, and CZIF-8. The mass of the active material in each electrode disk was 37.5 mg. Although mass loading increases the total resistance of the SC electrodes, it is required for avoiding mass error and evaluating the exact capacitance.

6.2.4 Fabrication of electrodes (for supercapacitor cells with non-aqueous electrolytes)

SC cells were prepared from electrode films of the CZMOFs. The films were deliberately thin to reduce the resistance, which increases with film thickness. An active material, carbon black (DENKA BLACK, Denka Company Limited, Japan), and a PVDF binder (W#9300, Kureha Corporation, Japan) were mixed at a mass ratio of 8:1:1. The mixture was stirred in NMP for 10 min. The obtained slurry was pasted onto an etched aluminum foil and was evacuated at 150 °C for 24 h to remove NMP from the carbon. The two activated carbons (YP50F and MSP20) and CZIF-8 were used as the reference electrodes in SC cells with non-aqueous electrolytes.

6.2.5. Material characterization

The electrode surface of each sample was characterized by SEM (JSM-6010LA, JEOL Ltd., Japan) at an accelerating voltage of 15 kV (SE mode) and by TEM (JEM-2100F, JEOL Ltd., Japan) at an accelerating voltage of 200 kV. In preparation for SEM, the electrode film was set onto a carbon tape on an Al sample holder (10 mm (φ) × 10 mm (H)). For TEM, the powdery samples were collected from the electrode materials used after GCD cycle tests. The samples dispersed in ethanol was poured onto a holey carbon film supported on 3- mm Cu grids, followed by drying at 80 °C for 1 h. The graphitization degree was investigated by Raman spectroscopy (Raman, NRS-4500NMDS, JASCO, Japan) with a 532-nm excitation laser calibrated on Si. The intensity and exposure time were 2 mW and 300 s, respectively. The surface functionalities of the electrode films were examined by XPS (ESCA5700, ULVAC-PHI Inc., Japan) with Mg $K\alpha_1$ radiation at an accelerating voltage of 15 kV.

Nitrogen adsorption/desorption (BEL-SORP min, Microtrac-BEL, Japan) isotherms were acquired at 77 K for the S_{BET} measurement, PSD, and information on the pore structure of each sample. Prior to the measurements, the samples were degasified by heating at 300 °C for 24 h in a vacuum. The S_{BET} of each sample was estimated from the isotherms by the BET method (P/P_0 = 0.05–0.10).

6.2.6 Electrochemical measurements (for aqueous electrolytic cells)

The electrochemical properties of the SC electrodes based on porous carbons were measured in a three-electrode system (with reference, counter, and working electrodes of Ag/AgCl, platinum, and a porous carbon, respectively). The electrolyte solution was 1.0 M H_2SO_4 (Nacalai Tesque Inc., Japan). Prior to measurement, the H_2SO_4 in the electrolytic cell was bubbled with N_2 gas for 30 minutes to eliminate any dissolved oxygen. CV, EIS, and GCD experiments were performed on a VSP-300 system (BioLogic, France). CV tests were carried out in the potential window 0.2–0.8 V at several sweep rates (1, 5, 10, 20, and 30 mV s^{-1}). The specific voltammetric charge Q (C g^{-1}) was determined as follows [6.7];

$$Q = (1/v) \int_{V_i}^{V_f} i \, dV \tag{6.1}$$

v, *i*, and *V* are the sweep rate (mV s^{-1}), the current (A), and the potential (V), respectively. *Vi* and *Vf* are the limits of integration interval corresponding to the initial (0.2 V) and the final (0.8 V) potential, respectively. EIS measurements were conducted at 0 V and a sinusoidal 5.0 mV signal over the frequency range 10 mHz to 1.0 MHz. The estimated EIS curves were obtained by applying the equivalent circuit model to the experimental EIS curves of the CZMOF-based electrolytic cell. The solution resistance (R_1), contact resistance (R_2), and diffusion resistance (R_{d3}) were separated from the total cell resistance so as to fit the calculated curves into the experimental ones. GCD tests were performed within the potential window of 0–0.8 V at several current densities (50, 100, 200, 250, 500, 1000, 2000, and 5000 mA g^{-1}). From the GCD curves, the specific capacitance was determined as

$$C_{\mathrm{g(three)}} = (I \times \Delta t)/(m \times \Delta V) \tag{6.2}$$

where $C_{g(three)}$ and m are the gravimetric capacitance (F g^{-1}) and mass of the active material (g), respectively, on a single electrode, I is the discharge current (A), Δt is the discharge time (s), and ΔV is the potential window of the discharge voltage (V) [6.8–6.10]. All electrochemical tests were conducted at 25 °C, and the temperature was maintained in an incubator.

6.2.7 Electrochemical measurements (of supercapacitor cells)

The fabricated electrode was roll-pressed and punched to adjust its dimensions to that of the test cell (HS Flat Cell, Hohsen Corporation, Japan). The electrochemical test cell comprised two symmetrical electrodes divided by a cellulose separator (TF40-50, Nippon Kodoshi Corporation, Japan). The electrolyte was a 1.0-M solution of $TEABF_4$ in PC (LIPASTE-P/EAF 1N, Tomiyama Pure Chemical Industries Ltd., Japan). The test cell was assembled in an argon-filled glove box under oxygen at extremely low concentration, and the moisture was maintained below 1 ppm to prevent oxygen and moisture contamination.

The electrochemical performance was evaluated in GCD tests conducted in a symmetric two-electrode system on a VSP-300 system. The cell capacitance (F g^{-1}) was determined as

$$C_{g(two)} = (I \times \Delta t)/(m \times \Delta V) \tag{6.3}$$

where $C_{g(two)}$ is the gravimetric cell capacitance (F g^{-1}), m is the mass of the active material (g) on the amount of both positive and negative electrodes, and the other variables are as defined above. In the GCD tests, the cell voltage window was 0–2.5 V and the current density was varied (40, 50, 100, 200, 500, 1000, 2000, 5000, and 10000 mA g^{-1}). All electrochemical tests were conducted at 25 °C, and the temperature was maintained in an incubator.

The electrochemical performances of the CZMOF-based electrodes were determined from Ragone plots. The energy density (Wh kg^{-1}) and power density (W kg^{-1}) were respectively calculated as[6.9]

$$E = (1/2) \times (C_{g(two)} \times 1000) \times (\Delta V^2)/3600 \quad (6.4)$$

$$P = (E/\Delta t) \times 3600 \quad (6.5)$$

and $C_{g(three)}$ was computed as[6.11]

$$C_{g(three)} = 4 \times C_{g(two)} \quad (6.6)$$

The volumetric specific capacitance (F cm^{-3}) was calculated as

$$C_{U(three)} = (I \times \Delta t)/(U \times \Delta V) \quad (6.7)$$

where $C_{U(three)}$ and U are the volumetric specific capacitance (F cm^{-3}) and the volume of the electrode material (cm^3), respectively, on a single electrode. $C_{U(three)}$ was computed as

$$C_{U(three)} = 4 \times C_{U(two)} \quad (6.8)$$

The electrode bulk density (ρ, g cm^{-3}) was calculated as

$$\rho = M/U \quad (6.9)$$

where M and U are the mass of the electrode material (g) and the volume of the electrode material (cm^3), respectively on a single electrode.

6.3 Results and discussion

6.3.1 Electrochemical properties of supercapacitor electrodes based on CZMOFs

The electrochemical properties of the CZMOF1 and CZMOF2 SC electrode materials were tested to demonstrate their feasibility in energy storage devices. The CV curves of both CZMOFs, YP50F, and MSP20 exhibited their capacitive behavior (Figure 6.1). Figure 6.2(a) and Table 6.1 show the relationship between the specific voltammetric charge (Q/C g^{-1}) and S_{BET} of the four carbon samples (CZMOF1, CZMOF2, YP50F, and MSP20). Q has a linear relation with S_{BET} at a moderately lower sweep rate (1, 5, and 10 mV s^{-1}). The results mean that S_{BET} can provide a good correlation with the induced Q based on a pure EDL when using aqueous electrolytes (H_2SO_4). This is because S_{BET} was calculated based on the monolayer of the N_2 molecules adsorbed on the outmost surface of a sample [6.12]. The Nyquist plots of both samples exhibited vertical lines in the low-frequency region, confirming their ideal capacitive behavior [6.13], and their frequency range was 10 mHz to 1.0 MHz (Figure 6.2(b)). In the high-frequency region, semicircles were observed in both spectra, indicating that resistances were introduced by the inter-particle gaps, the particle/current collector interfaces, and charge transfer [6.14]. The total resistance of the CZMOF2 electrolytic cell was higher than that of CZMOF1. To provide a conceivable explanation of the difference, an equivalent circuit model (inset of Figure 6.2(b)) was used to separate the individual resistances, such as the solution resistance (R_1), the contact resistance owing to particle gaps or the particle/current collector interface (R_2), and the diffusion resistance (R_3), from the total cell resistance. M_3 indicates the restricted linear diffusion model [6.15]. R_1 and R_2 were not so different for the two CZMOF-based cells, whereas R_{d3} of CZMOF2 was much higher than that of CZMOF1, as shown in Table 6.2. This is owing to the greater thickness of the CZMOF2 electrode material (Table 6.3) or their hierarchical porous structure with a relatively tiny mesopores, as they do not allow electrolyte ions to deeply access pores, increasing the diffusion time (t_{d3}), unlike CNovel with larger mesopores (chapter 2). The greater thickness was attributed to the lower bulk density of CZMOF2 with an extremely high S_{BET} (2678 m^2 g^{-1}), as shown in Table 6.3.

Figure 6.2(c),(d) show the GCD curves of CZMOF1 and CZMOF2, respectively. At current densities of 50, 250, and 1000 mA g^{-1}, the specific capacitances of CZMOF1 were 218, 177, and 142 F g^{-1}, respectively, and those of CZMOF2 were 360, 278, and 221 F g^{-1}, respectively. For comparison, the highest capacitance values of different ZMOF-derived carbons in H_2SO_4 solutions were collected from the literature, and they are presented in Table 6.4 [6.9, 6.16, 6.17–6.21]. CZMOF2 achieved the highest capacitance at all current densities (50, 250, and 1000 mA g^{-1}). Figure 6.2(e) shows the GCD curves of CZMOF1, CZMOF2, YP50F, and MSP20 at a current density of 50 mA g^{-1}, and Figure 6.2(f) shows the specific capacitances of each sample calculated from the GCD curves as functions of current density (50–5000 mA g^{-1}). The specific capacitance of CZMOF2 exceeded those of CZMOF1, YP50F, and MSP20 at all current densities. However, the volumetric capacitance (F cm^{-3}) of CZMOF2 was much smaller than any other carbon samples, as shown in Table 6.3. Porous carbons with an extremely high S_{BET} was found to suffer from the lower volumetric capacitance. On the other hand, the volumetric capacitance (F cm^{-3}) of CZMOF1 was the largest among the four carbon samples (Table 6.3). This is due to the larger bulk density compared with other samples. The result agree well with the case of the CICOFA electrode as discussed in chapter 3 (Table 3.3).

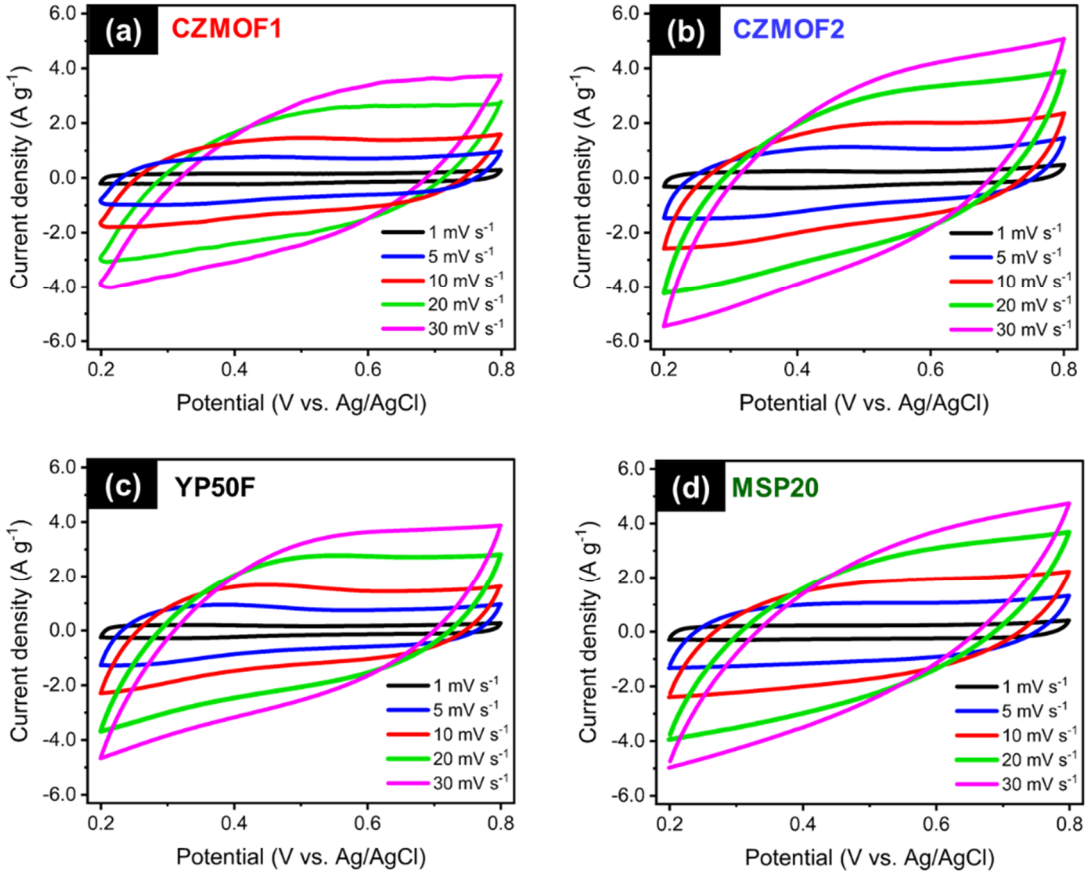

Figure 6.1 Electrochemical properties of CZMOF1, CZMOF2, YP50F, and MSP20 in 1.0 M H_2SO_4: (a), (b), (c), and (d) Cyclic voltammograms of CZMOF1, CZMOF2, YP50F, and MSP20, respectively, at several sweep rates.

Table 6.1 Specific surface area (m^2 g^{-1}) and specific voltammetric charge (Q, C g^{-1}) of CZMOF1, CZMOF2, YP50F, and MSP20 at 1, 5, and 10 mV s^{-1} with an aqueous solution (H_2SO_4).

Sample	S_{BET} (m^2 g^{-1})	Q at 1 mV s^{-1} (C g^{-1})	Q at 5 mV s^{-1} (C g^{-1})	Q at 10 mV s^{-1} (C g^{-1})
CZMOF1 (this work)	1266	98.2	80.6	69.7
CZMOF2 (this work)	2678	159.0	112.5	92.8
YP50F	1600	109.3	89.3	76.5
MSP20	2266	139.6	109.0	88.0

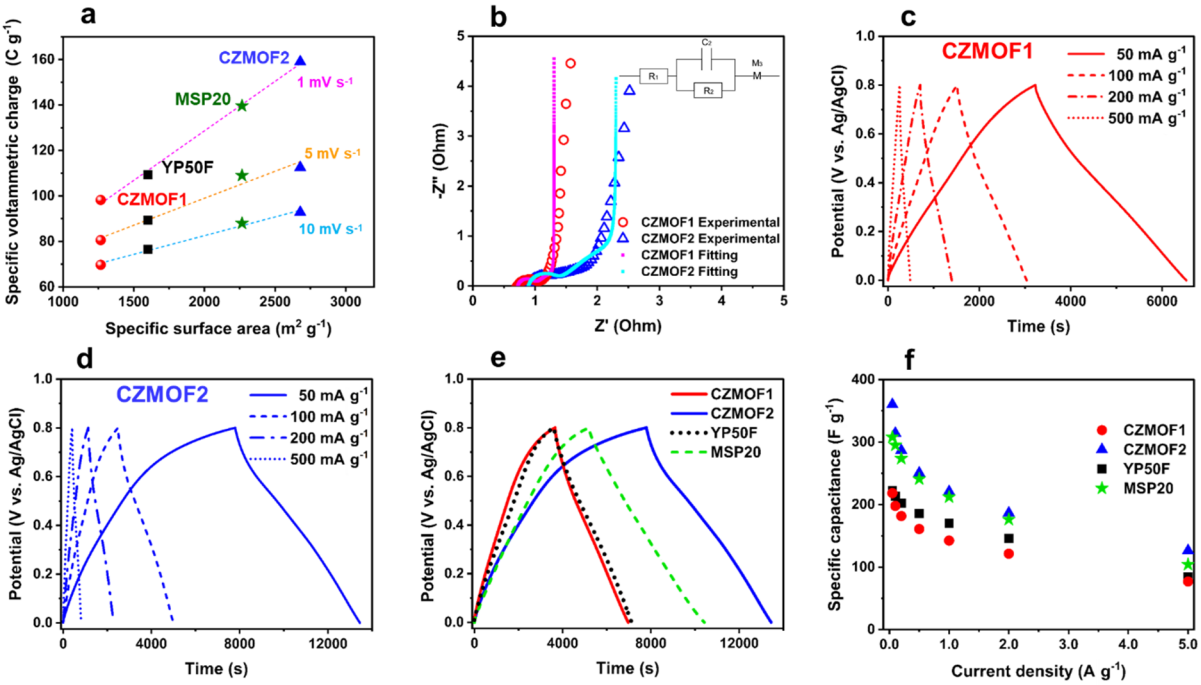

Figure 6.2 (a) The specific voltammetric charge vs. the specific surface area of CZMOF1 (red), CZMOF2 (blue), YP50F (black), and MSP20 (green). (b) Nyquist plots of CZMOF1(red, empty symbols) and CZMOF2 (blue, empty symbols) at 0 V and at an amplitude of 5.0 mV and frequencies ranging from 10 mHz to 1.0 MHz and the fitting curves of CZMOF1 (magenta, solid line) and CZMOF2 (cyan, solid line). (c),(d) GCD curves of CZMOF1 and CZMOF2 in 1-M H_2SO_4 solution at several current densities, confirming their capacitive behavior. (e) GCD curves of CZMOF1 (red), CZMOF2 (blue), YP50F (black), and MSP20 (green) in 1-M H_2SO_4 solution at a current density of 50 mA g^{-1}. (f) Specific capacitances of CZMOF1 (red), CZMOF2 (blue), YP50F (black), and MSP20 (green) in 1 M H_2SO_4 solution versus current density (50–5000 mA g^{-1}), showing that CZMOF2 exhibited the highest capacitance among the four samples.

Table 6.2 Calculated values of the resistance, capacitance, and diffusion time by fitting the equivalent circuit model to the experimental EIS data.

Sample	R_1 (Ohm)	C_2 (F)	R_2 (Ohm)	R_{d3} (Ohm)	t_{d3} (s)
CZMOF1	0.722	0.016	0.239	1.029	3.599
CZMOF2	0.889	0.024	0.384	3.093	13.610

Table 6.3 S_{BET}, volumetric specific capacitance (F cm^{-3}) under H_2SO_4 electrolytic solution, gravimetric specific capacitance (F g^{-1}) under H_2SO_4 electrolytic solution, electrode thickness (μm), and electrode bulk density (g cm^{-3}) of CZMOFs and two commercial activated carbons (YP50F and MSP20).

Sample	S_{BET} (m^2 g^{-1})	Volumetric capacitance (F cm^{-3}) @50 / 250 / 1000 mAg^{-1}	Gravimetric capacitance (F g^{-1}) @50 / 250 / 1000 mAg^{-1}	Electrode thickness (μm)	Bulk density (electrode) (g cm^{-3})
CZMOF1	1266	170 / 139 / 112	218 / 177 / 142	316	0.98
CZMOF2	2678	99 / 77 / 61	360 / 278 / 221	791	0.35
YP50F	1600	122 / 107 / 93	222 / 197 / 170	413	0.68
MSP20	2266	149 / 129 / 103	307 / 267 / 212	449	0.60

Table 6.4 Specific capacitance of CZMOFs, two commercial activated carbons (YP50F and MSP20), and Zn-MOF-derived carbons taken from the literature in H_2SO_4 electrolytic solution.

Sample	S_{BET} (m^2 g^{-1})	Capacitance (F g^{-1})	Current density (mA g^{-1})	Sweep rate (mV s^{-1})	Electrode system	Electrolyte	Ref.
CZMOF1 (this work)	1266	218 / 177 / 142	50 / 250 / 1000	-	3	1.0 M H_2SO_4	-
CZMOF2 (this work)	2678	360 / 278 / 221	50 / 250 / 1000	-	3	1.0 M H_2SO_4	-
YP50F	1600	222 / 197 / 170	50 / 250 / 1000		3	1.0 M H_2SO_4	
MSP20	2266	307 / 267 / 212	50 / 250 / 1000		3	1.0 M H_2SO_4	-
S-900	1823	219	-	5	3	1.0 M H_2SO_4	6.9
C-MOF-2	1378	170	1000	-	2	1.0 M H_2SO_4	6.16
NPC	2872	258	250	-	2	1.0 M H_2SO_4	6.17
AS-ZC-800	2972	251	250	-	2	1.0 M H_2SO_4	6.18
NPC650	1521	222	50	-	2	1.0 M H_2SO_4	6.19
Z-900	1075	214	-	5	3	0.5 M H_2SO_4	6.20
C800	2169	188	-	5	2	1.0 M H_2SO_4	6.21

The maximum values are selected from the corresponding literature. The specific capacitance is calculated for a single electrode.

6.3.2 Electrochemical properties of the anions and cations, and the performance of the positive and negative CZMOF electrodes

The capacitance value was estimated here in the whole potential window of 0–0.8 regardless of the OCP of the CZMOFs-based electrodes. Therefore, the electrochemical

properties of the active material as the positive electrode and negative electrode were individually discussed. The OCP was measured for both the CZMOF1 and CZMOF2 electrodes, and it was found to be approximately 0.3 V and 0.4 V, respectively, as shown in Figure 6.3. CV was conducted at a moderately low sweep rate of 1 mV s^{-1} to exactly analyze each electrochemical property of the anions and cations. Figure 6.4(a),(b) shows the two cyclic voltammograms of the CZMOF1 and CZMOF2 electrodes in the potential windows of 0.0–0.3 V/0.3–0.8 V and 0.0–0.4 V/0.4–0.8 V, respectively. In both samples, the positive/negative current through the adsorption/desorption of the anions was higher than that for the cations. Based on the adsorption/desorption of the anions, the high current may have been probably induced due to the intercalation of SO_4^{2-} into the graphite layers at 0.7 V, and SO_4^{2-} was deintercalated from the graphite layers at 0.5 V [6.22]. This can be explained by the Raman results (Figure 6.5), wherein the Raman spectra of CZMOF1 and CZMOF2 suggest some degrees of graphitization. The positive and negative electrodes were separately estimated based on the following formula [6.22]:

$$C_+ = (I \times \Delta t_+)/(m \times \Delta V_+) \quad (6.10)$$

$$C_- = (I \times \Delta t_-)/(m \times \Delta V_-) \quad (6.11)$$

where C_+ and C_- are the positive and negative capacitances induced by the adsorption of the cations and the desorption of the anions, respectively. $\Delta t_+/\Delta V_+$ and $\Delta t_-/\Delta V_-$ denote the discharge time (s)/ the potential window of the adsorption of the cations and desorption of the anions, respectively. Figure 6.4(c),(d) exhibits the GCD curves of the CZMOF1 and CZMOF2 electrodes, and Table 6.5 shows the positive and negative capacitances (F g^{-1}) in both samples. The positive capacitance was higher for both the CZMOF electrode, similar to the CV results mentioned above.

Figure 6.6 shows the cycling durabilities of both electrodes over 10000 GCD cycles at 1.0 A g^{-1}. At the end of the cycling test, the high capacitance retentions of CZMOF1 (98.9%) and CZMOF2 (97.1%) confirmed their excellent cycling durabilities.

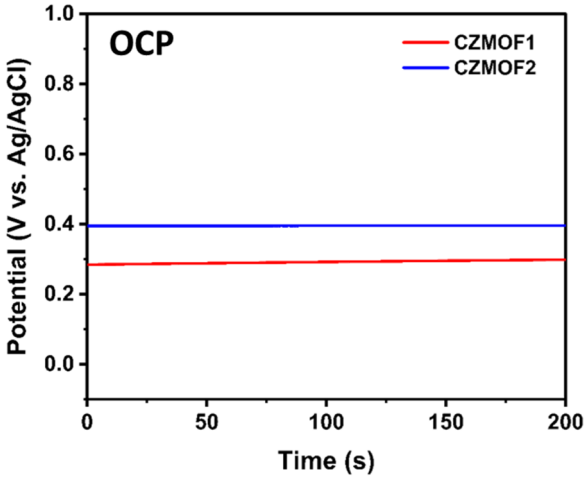

Figure 6.3 Open circuit potential of the CZMOF1 and CZMOF2 electrode materials vs. Ag/AgCl in 1.0 M H_2SO_4.

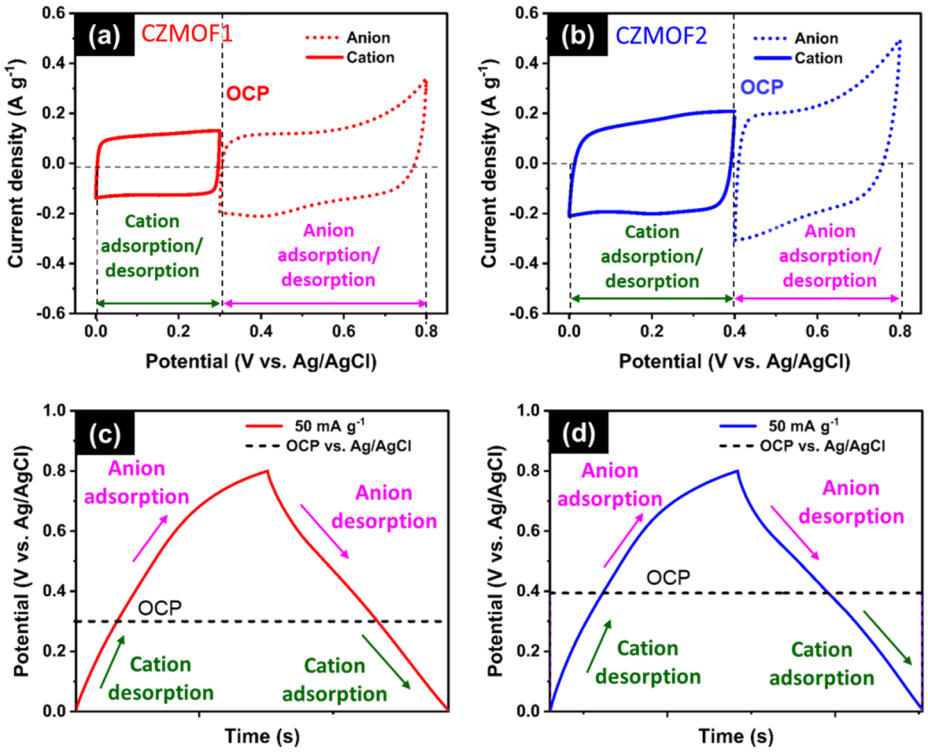

Figure 6.4 Electrochemical properties of the anions and cations, and the performance of the positive and negative electrodes of the CZMOF-based electrodes in aqueous electrolytes (1.0 M H_2SO_4): Cyclic voltammograms of (a) CZMOF1 and (b) CZMOF2. GCD curves of (c) CZMOF1 and (d) CZMOF2.

Table 6.5 Positive (C^+) and negative capacitance (C^-) values estimated by the adsorption/desorption of the anions and cations, respectively, based on GCD tests at 50 mA g^{-1} with an aqueous solution (H_2SO_4).

Sample	C^+ (adsorption of anions) ($F\ g^{-1}$)	C^+ (desorption of anions) ($F\ g^{-1}$)	C^- (adsorption of cations) ($F\ g^{-1}$)	C^- (desorption of cations) ($F\ g^{-1}$)
CZMOF1	257	232	207	127
CZMOF2	721	361	345	248

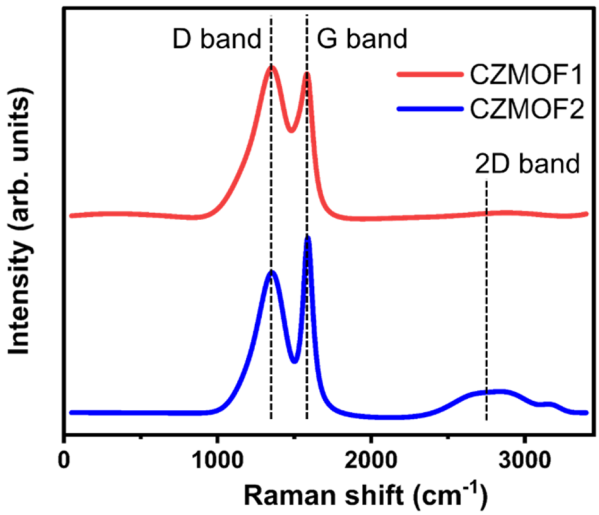

Figure 6.5 Raman spectra of CZMOF1 (red) and CZMOF2 (blue), confirming the purity of CZMOF1 and CZMOF2 and increased graphitization in CZMOF2 (I_G/I_D ratio 1.12) compared to CZMOF1 (0.98).

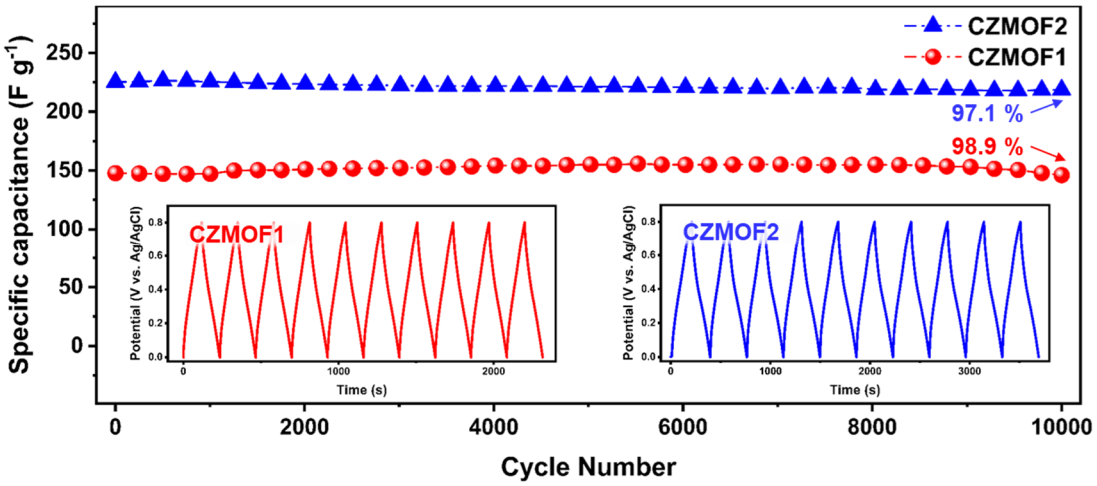

Figure 6.6 cycling durabilities of CZMOF1 (red) and CZMOF2 (blue) over 10000 GCD cycles in 1-M H_2SO_4 solution, confirming the applicability of CZMOF1 and CZMOF2 as supercapacitor electrode materials. Insets are typical GCD curves, representing capacitive behavior.

6.3.3 The practical applicability of CZMOF electrodes in supercapacitor cells

Non-aqueous electrolytes are used in practical SCs because they offer a wider voltage window and provide higher energy density than aqueous electrolytes [6.23]. A 1.0 M solution of $TEABF_4$ in PC can withstand a higher voltage (~2.7 V) [6.24] compared to H_2SO_4 (~1.2 V). Thus, to demonstrate the practical feasibility of the CZMOF-based SCs, the author constructed SC cells containing the CZMOF electrodes in $TEABF_4$/PC electrolytes. A two-electrode setup was used for the tests. The GCD curves of the CZMOF1 and CZMOF2 samples at various current densities (0.5, 1.0, 2.0, and 5.0 A g^{-1}) are shown in Figure 6.7(a),(b). The behavior of both samples was typical of capacitive behavior. The specific capacitances of CZMOFs, YP50F, and MSP20 are compared in Figure 6.7(c),(d), and Table 6.6. The specific capacitance was lower in $TEABF_4$ than in H_2SO_4 for all samples (Table 6.6). This difference was attributable to the different sizes of the electrolytes. The estimated diameters of solvated H^+ and SO_4^{2-} were 0.56 and 0.76 nm, respectively [6.23], whereas those of TEA^+ and BF_4^- were reported as 1.36 and 1.40 nm, respectively [6.23].

The electrode bulk density of the four carbon samples was listed in table 6.7. Interestingly, the bulk density of CZMOF1 differs extremely between the pellet electrode and the slurry

electrode. In the process of producing the slurry electrode, the dispersity of the powdery carbon samples in NMP may be related to the resultant bulk density.

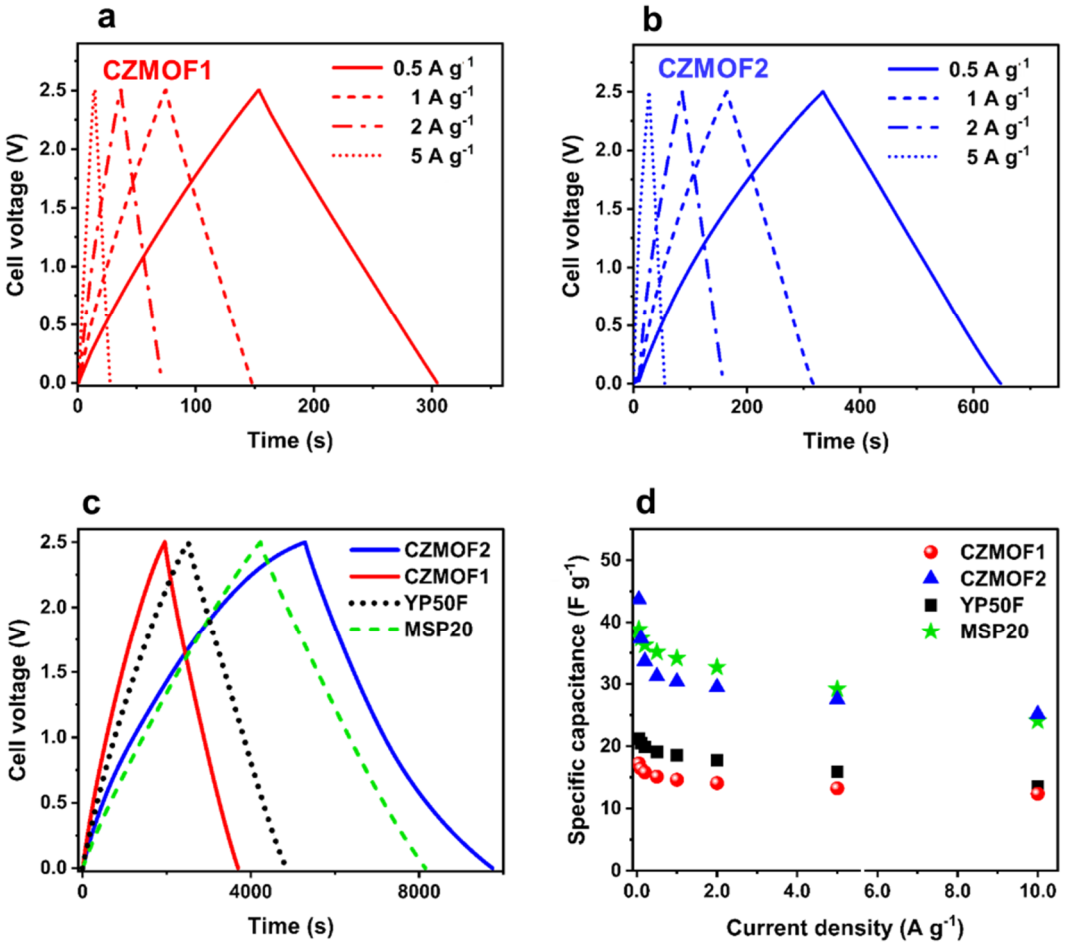

Figure 6.7 (a) and (b) GCD curves of CZMOF1 and CZMOF2, respectively, in $TEABF_4$/1.0 M PC solution at several current densities, indicating their capacitive behavior. (c) GCD curves of CZMOF1, CZMOF2, YP50F, and MSP20 in $TEABF_4$/1.0 M PC solution at a current density of 50 mA g^{-1}, and (d) Specific capacitances of CZMOF1, CZMOF2, YP50F, and MSP20 in $TEABF_4$/1.0 M PC solution at several current densities (50–10000 mA g^{-1})

As shown in the Ragone plots of CZMOF1 and CZMOF2 (Figure 6.8), the energy density (Wh kg^{-1}) was higher in $TEABF_4$/PC than in H_2SO_4, because the withstanding voltage was higher in the organic electrolyte $TEABF_4$/PC than in inorganic H_2SO_4. The conductivity is reportedly lowered in non-aqueous solutions because the solvated anions and cations are larger and the viscosity is higher than in aqueous solutions [6.5]. In the present test, the energy densities of CZMOF1 and CZMOF2 were lower in H_2SO_4 than in $TEABF_4$ at high power densities (over 5 kW kg^{-1}). This result can be explained by the greater thickness (and hence resistance) of the pellet electrode than the thin film electrode (~800 μm vs. ~50 μm) (see Figure 2.12).

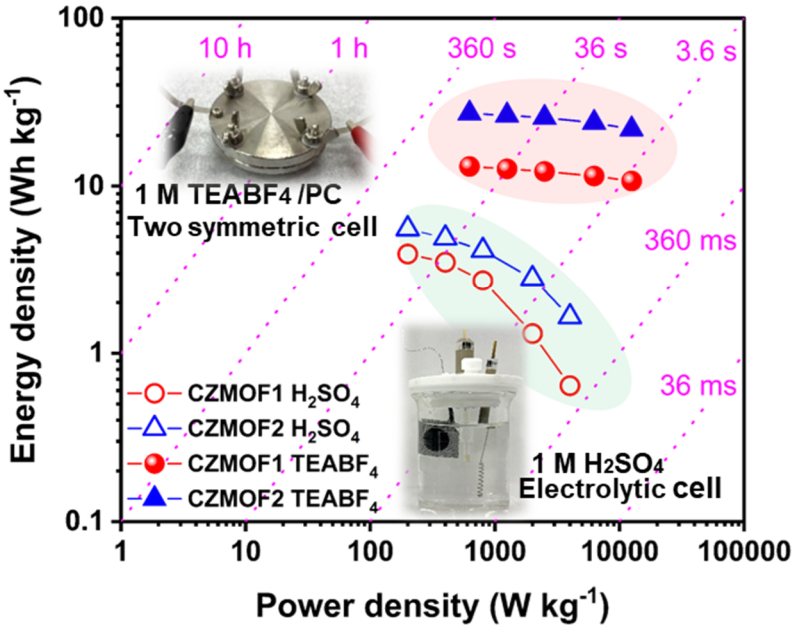

Figure 6.8 Ragone plots of the supercapacitors based on CZMOF1 (red solid symbols) and CZMOF2 (blue solid symbols) with $TEABF_4$/PC showing higher energy densities than those based on CZMOF1 (red, empty symbols) and CZMOF2 (blue, empty symbols) with H_2SO_4. Insets show the electrolytic cells with aqueous electrolytes and the symmetric test cell for non-aqueous electrolytes.

Table 6.6 Specific capacitances of CZMOF1, CZMOF2, YP50F, and MSP20 at 50 mA g^{-1} with an aqueous solution (H_2SO_4) and a non-aqueous solution ($TEABF_4$)

Sample	S_{BET} (m^2 g^{-1})	Capacitance (H_2SO_4) (F g^{-1}) *	Capacitance ($TEABF_4$) (F g^{-1}) *	Capacitance ($TEABF_4$) (F g^{-1}) **
CZMOF1 (this work)	1266	218	68.8	17.2
CZMOF2 (this work)	2678	360	174.8	43.7
YP50F	1600	222	85.2	21.3
MSP20	2266	307	155.2	38.8

*Specific capacitance on a single electrode.
**Specific capacitance on a two-electrode cell.

Table 6.7 Electrode bulk density of CZMOF1, CZMOF2, YP50F, and MSP20

Sample	Pellet electrode (g cm^{-3})	Slurry electrode (g cm^{-3})
CZMOF1 (this work)	0.98	0.25
CZMOF2 (this work)	0.35	0.36
YP50F	0.68	0.78
MSP20	0.60	0.58

6.3.4 Electrochemical properties of ZIF-8-derived porous carbons

Figure 6.9(a) and (b) show the CV and GCD curves of the CZIF-8-based electrode material with H_2SO_4, respectively. Based on the GCD curves, the specific capacitance was calculated as 298 F g^{-1}. The capacitance value is larger for the S_{BET} of CZIF-8 (1360 m^2 g^{-1}) than the specific capacitance of CZMOFs, YP50F, and MSP20 for their S_{BET}. Double-layer capacitance, $C_{S(three)}$ (μF cm^{-2}) [3.12, 3.13] was calculated as follows:

$$C_{g(two)} = (I \times \Delta t)/(m \times \Delta V) \quad (6.12)$$

$$C_{S(three)} = C_{g(three)}/S_{BET} \quad (6.13)$$

The $C_{s(three)}$ of CZIF-8 was estimated to be 21.8 μF cm^{-2}, which is much higher than those of the other carbon samples (CZMOF1, CZMOF2, YP50F, and MSP20), as shown in Table 6.8. This could be attributed to the pseudo-capacitive effect, which can be induced by N-doped carbons, as discussed in chapter 3. N-doped porous carbons can be obtained by

carbonizing N atoms-containing ZIF-8 ($C_8H_{10}N_4Zn$). Two peaks corresponding to the pyridinic N (~398.4 eV) and graphitic (quaternary) N (~400.6 eV) were observed in the XP N 1s spectrum of CZIF-8 (Figure 6.9 (c)). Thus, the capacitance was enhanced by both the high S_{BET} (1367 $m^2\ g^{-1}$) and the pseudo-capacitive effect.

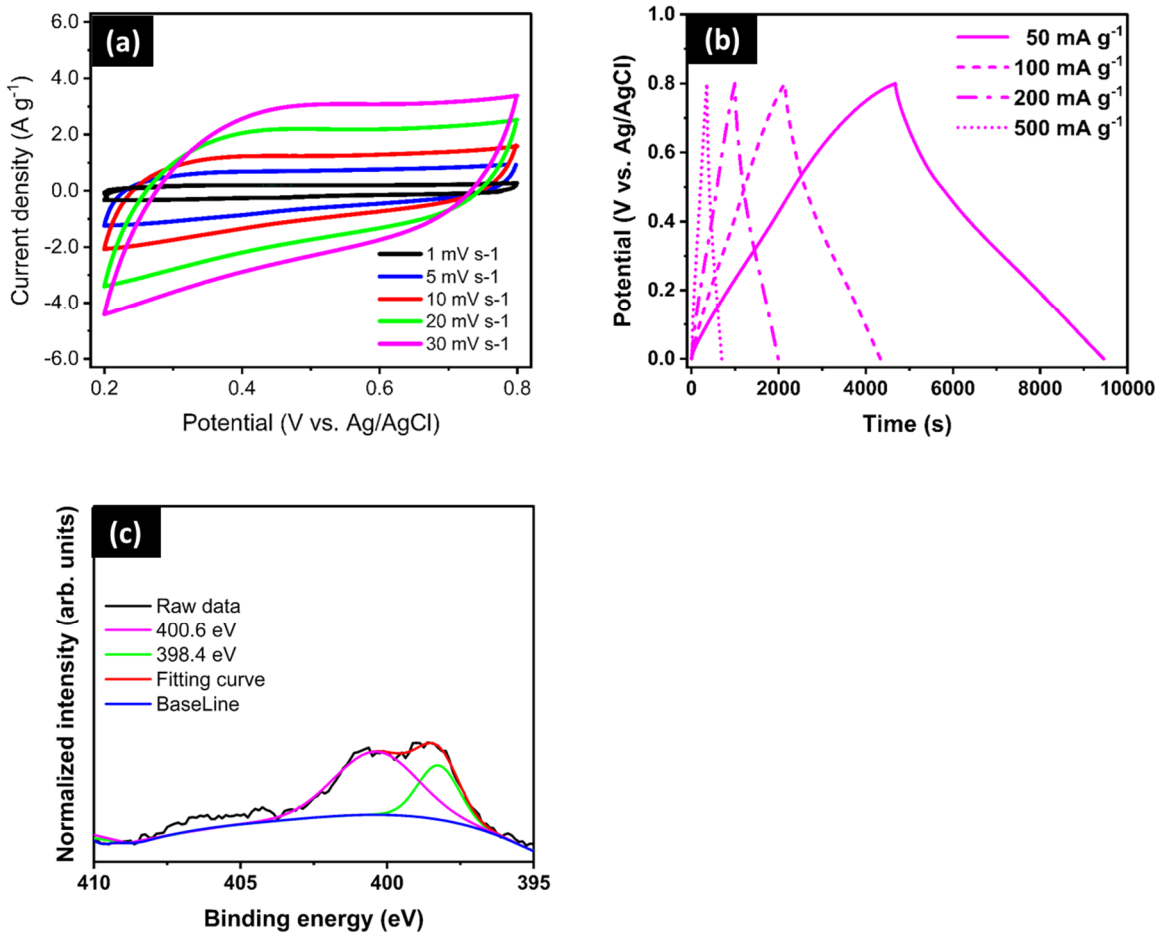

Figure 6.9 Electrochemical properties of CZIF-8 with 1.0 M H_2SO_4 (a) Cyclic voltammograms of CZIF-8 recorded at 1–30 mV s^{-1}. (b) GCD curves of CZIF-8 in 1.0 M H_2SO_4 at 50–500 mA g^{-1}. (c) XP N1s spectrum of CZIF-8.

Table 6.8 S_{BET}, specific capacitance (C_g), and double-layer capacitance (C_s) of CZMOF1, CZMOF2, CZIF-8, YP50F, and MSP20 with H_2SO_4 at 50 mA g^{-1}.

Sample	S_{BET} (m^2 g^{-1})	C_g (F g^{-1})	C_s (μF cm^{-2})
CZMOF1	1266	218	17.2
CZMOF2	2678	360	13.4
CZIF-8	1369	298	21.7
YP50F	1600	222	13.9
MSP20	2266	307	13.5

The electrochemical properties based on CZIF-8 were examined using non-aqueous electrolytes ($TEABF_4$). Figures 6.10(a) and (b) show the CV and GCD curves, respectively. Based on the GCD curves, the specific capacitance was calculated as 16. 3 F g^{-1}. Unlike the specific capacitances estimated under H_2SO_4, those under $TEABF_4$ have a linear relation with S_{BET}, as shown in Figure 6.10(c). The results suggest that the specific capacitance was induced based on pure EDL capacitive behavior when using $TEABF_4$. This can be explained by the similar C_s of the five-carbon electrodes, as shown in Table 6.9.

Table 6.9 S_{BET}, specific capacitance (C_g), and double-layer capacitance (C_s) of CZMOF1, CZMOF2, YP50F, MSP20, and CZIF-8 with $TEABF_4$ at 50 mA g^{-1}.

Sample	S_{BET} (m^2 g^{-1})	C_g (F g^{-1})	C_s (μF cm^{-2})
CZMOF1	1266	68.8	5.3
CZMOF2	2678	174.8	6.5
CZIF-8	1369	65.2	4.8
YP50F	1600	85.2	5.3
MSP20	2266	155.2	6.8

*Specific capacitance (C_g) was calculated based on a single electrode.

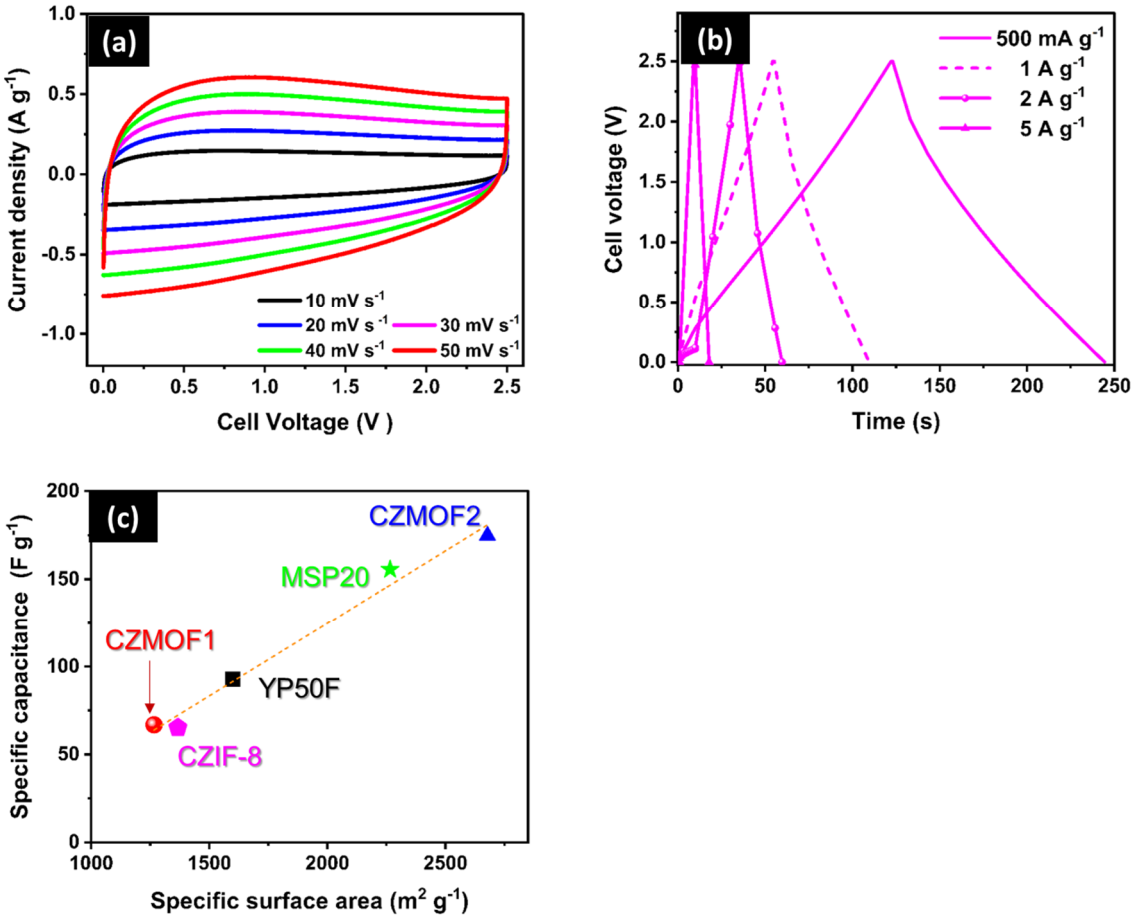

Figure 6.10 Electrochemical properties of CZIF-8 with $TEABF_4$ (a) Cyclic voltammograms of CZIF-8 recorded at 10–50 mV s^{-1}. (b) GCD curves of CZIF-8 in 1.0 M $TEABF_4$ in PC at 500 mA g^{-1}–5 A g^{-1}. The specific capacitance vs. the specific surface area of CZMOF1 (red), CZMOF2 (blue), YP50F (black), MSP20 (fluorescent green), and CZIF-8 (pink).

6.3.5 Cycle and thermal durability of supercapacitor cells based on CZMOFs after GCD cycles

Figure 6.11 shows the results of GCD tests conducted over 300 cycles at 25, 50, and 75 °C during 1–100, 101–200, and 201–300 cycles, respectively, for the two CZMOFs. The corresponding capacitances are shown in Table 6.10. Because high temperatures result in low viscosity and high conductivity, capacitance increased with temperature in both samples [6.23]. However, the capacitance retention of CZMOF2 decreased considerably at 75 °C. The huge specific surface area of CZMOF2 (as previously indicated) shows that the carbon

structure of CZMOF2 has a significant number of active edge sites, which may aid breakdown at high temperatures. More importantly, after 100000 GCD cycles, the capacitance retentions of CZMOF1 and CZMOF2 remained high at 74.7% and 77.5%, respectively (Figure 6.12). In CZMOF2, the capacitance retention exceeded 100% from 237 to 25362 cycles, possibly due to electrochemical activation [6.25]. CZMOF1 displayed a steep decrease in capacitance retention at approximately 46600 cycles (see Figure 6.13). Electrolytes entering the pores of the electrode during repeated charge/discharge cycles or degradation of the organic electrolyte may be to blame for the steady decline in capacitance retention in both samples [6.26]. The insets of Figure 6.12 show a blue or red LED powered by an SC containing the CZMOF2 electrode after 100,000 GCD cycles. The blue and red LEDs were illuminated for approximately 40 s and 60 s, respectively (Figure 6.12). In a similar test, an SC cell with the CZMOF1 electrode delivered the same level of performance. The usefulness of CZMOFs as SC electrode materials was proven in these studies.

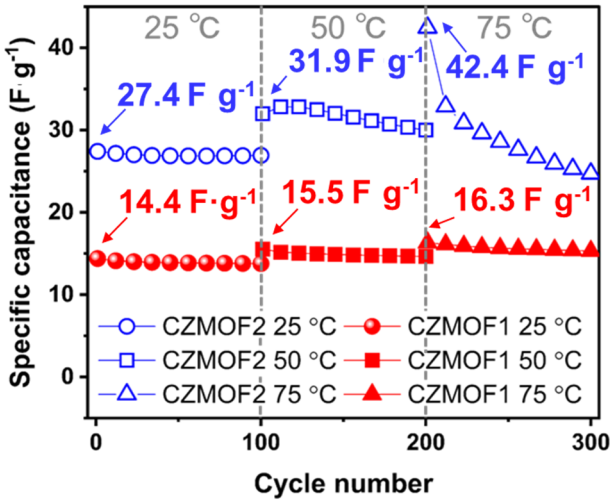

Figure 6.11 Capacitance retentions of CZMOF1 (red) and CZMOF2 (blue) at several temperatures, suggesting that the electrode based on CZMOF1 is more stable at high temperatures compared to that based on CZMOF2.

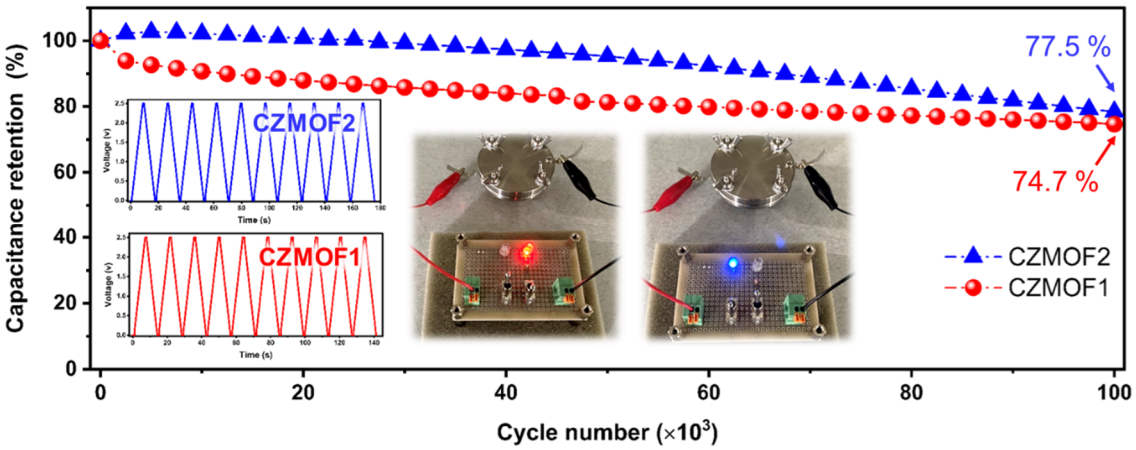

Figure 6.12 Cycling durability of GCD tests showed that the supercapacitors successfully operated for up to 100000 cycles. Insets show typical GCD curves indicating the capacitive behavior and blue and red light-emitting diodes (LED) powered by the CZMOF2-based supercapacitor cell after 100000 GCD cycles.

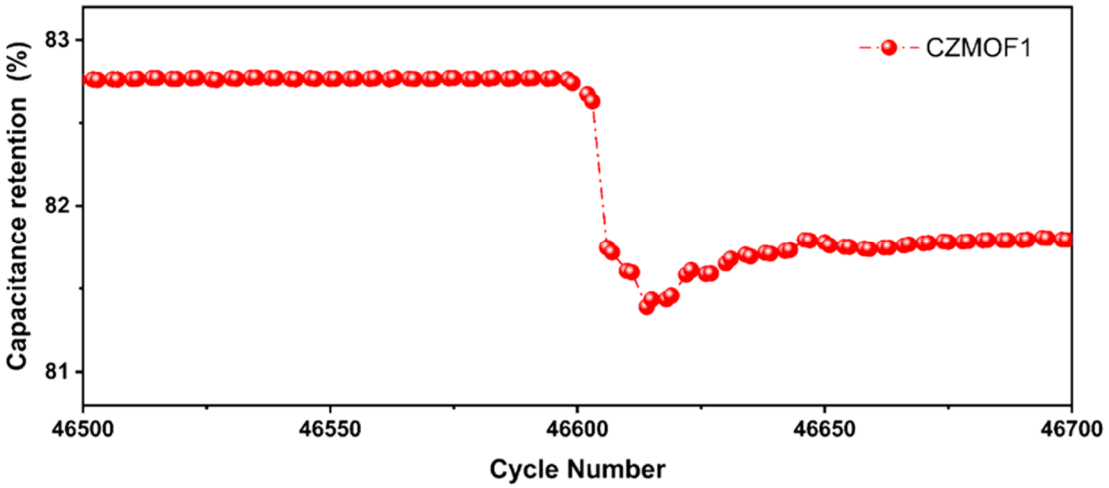

Figure 6.13 Specific capacitance of CZMOF1 during the GCD cycling test. The cycling durability of the CZMOF1 electrode dropped sharply at the 46474th cycle.

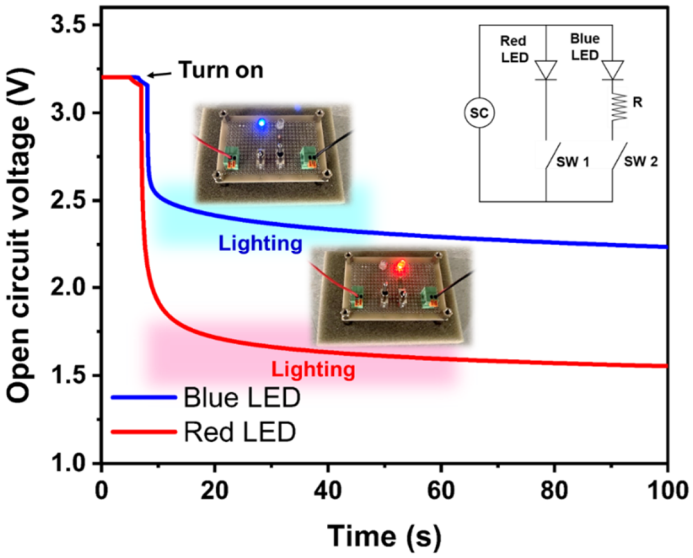

Figure 6.14 Open circuit voltage measured while lighting a blue or red LED by the supercapacitor cell based on CZMOF2. Upper right inset is a circuit diagram of the experiment.

Table 6.10 Specific capacitances of CZMOFs at 1.0 A g^{-1} at different temperatures, showing the higher thermal durability of CZMOF1 than of CZMOF2

Sample	Temperature (°C)	Cycle number	Capacitance (F g^{-1})
CZMOF1	25	1	14.4
		100	13.8
	50	101	15.5
		200	14.6
	75	201	16.3
		300	15.3
CZMOF2	25	1	27.4
		100	26.9
	50	101	31.9
		200	29.9
	75	201	42.4
		300	24.7

6.3.6 Degradation of electrode surfaces of CZMOF1 and CZMOF2 after GCD cycles

To investigate whether CZMOF electrodes can extend the lifetime of a cell, the author investigated the electrode surfaces before and after the GCD cycles. The test cells were run through 100000 cycles and the thermal durability tests (Figure 6.12) were re-assembled to examine the state of the electrode surfaces after cycling.

A steep drop in the capacitance retention appeared at approximately 46600 cycles (Figure 6.13). Moreover, after cycling, the surfaces of both the positive and negative electrodes of CZMOF1 were covered with precipitates (Figure 6.15(a)–(c) and Figure 6.16(a)–(c)), but no structural change appeared on the electrode surfaces of CZMOF2 (Figure 6.15(d)–(f) and Figure 6.16(d)–(f)). Nevertheless, the durability over the charge/discharge cycles appeared to be higher in CZMOF1 than in CZMOF2 (Figure 6.12). The capacitance retention curve of CZMOF1 was almost flat, whereas that of CZMOF2 gradually decreased (Figure 6.12). Furthermore, CZMOF1 was more thermally stable than CZMOF2, as evidenced by the steep decrease in the capacitance of CZMOF2 during the cycling test at 75 °C. The precipitates on the CZMOF1 electrode surfaces might have protected the interaction between the electrolytic ions and the carbon surface, thus shielding the pores from higher voltages and temperatures.

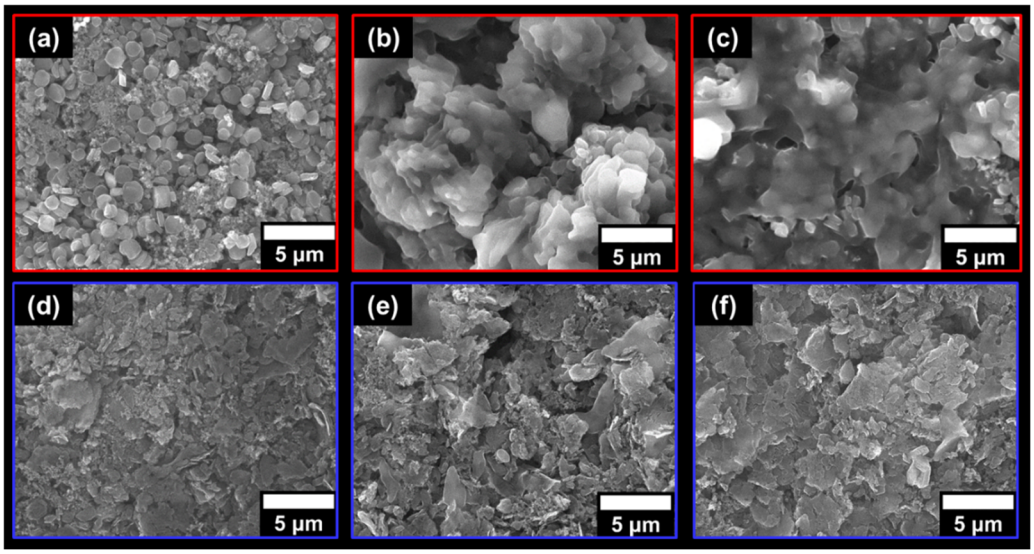

Figure 6.15 Degradation of electrode materials after 100,000 GCD cycles. SEM images of the (a)–(c) CZMOF1 and (d)–(f) CZMOF2 electrode surfaces. (a) and (d) show the fresh electrode surfaces. (b), (e) and (c), (f) show the positive and negative electrode surfaces, respectively, after 100,000 GCD cycles in $TEABF_4$ at 25 °C.

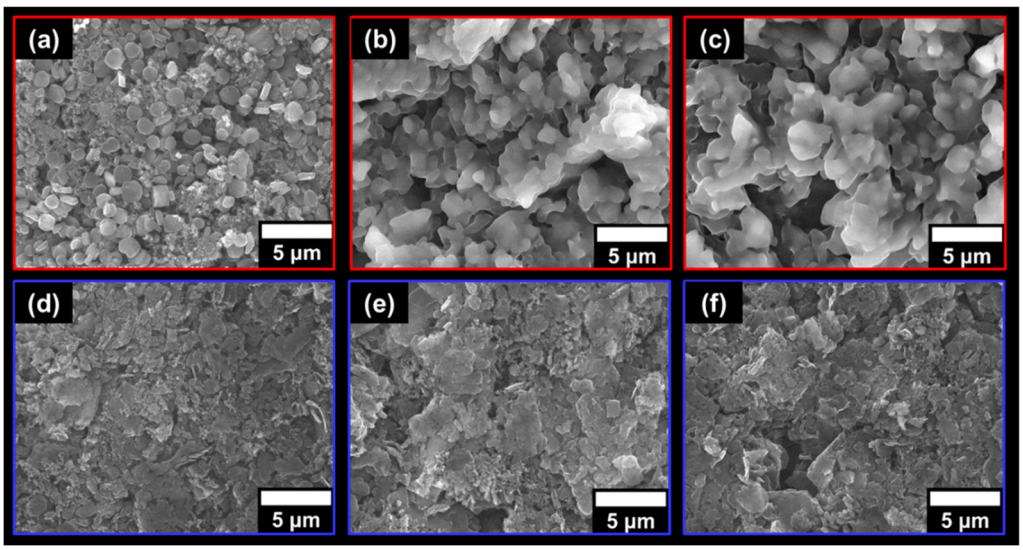

Figure 6.16 Degradation of electrode materials after the thermal durability tests. SEM images of the electrode surfaces based on (a)–(c) CZMOF1 and (d)–(f) CZMOF2. (a) and (d) show the fresh electrode surfaces. (b), (e) and (c), (f) show the positive and negative electrode surfaces, respectively, after 300 GCD cycles in $TEABF_4$ at 25 °C (1–100 cycles), 50 °C (101–200 cycles), and 75 °C (201–300 cycles).

To investigate the CZMOF electrode surface after the 100000 cycling charge/discharge cycles in more detail, the nanostructure was examined through TEM, and the electrode surfaces were investigated using XPS. No noticeable changes in the nanostructure were observed from the TEM images of the samples after the cycle tests (Figure 6.18(d)–(f), (j)–(l)). The precipitates, which can be observed in the SEM images mentioned above, could not be observed in the TEM images. This is probably because the TEM sample was dispersed in ethanol before the measurement. The XP spectra of the sample, however, acquired after the cycle test, revealed some peak sifts or extra peaks. Figure 6.17(a) shows the XP survey spectra of the CZMOF-based electrode surfaces, confirming the peaks attributable to B1s, C1s, N1s, O1s, and F1s. From the wide spectra, narrow spectra were obtained on the respective binding energy (Figure 6.17(b)–(f)). No significant changes were seen in the O1s spectra in all the samples. In contrast, the other B1s, C1s, N1s, and F1s spectra of the fresh electrode surfaces obviously differed from those after the cycle tests. Particularly among them, the XP C1s and F1s peaks were found to have several components. To analyze the spectra in more detail, the XP C1s and F1s peaks were separated into several ones (Figure 6.18(a)–(c), (g)–(i) and Figure 6.19(a)–(f)). The XP C1s peaks in both the CZMOF1 and CZMOF2 fresh electrode surfaces could be separated into those derived from the C-F bonding (286 eV) [6.27] and C–C and/or C=C bonding (284.5 eV)[6.28], which are attributable to the constituents of the binder used for electrode materials and CZMOFs carbons, respectively, as shown in Figures 6.20(a) and (g). In both the CZMOF electrode surfaces, the peaks at 286 eV became more prominent after the cycle tests. The peaks were derived from the C-N bonding attributable to the TEA^+ used for the cations, simply because the N1s spectra also indicated that corresponding peaks appeared after the cycle tests (Figure 6.17(d)). The peak at 688.1 eV was observed in the F1s spectra of both the CZMOF fresh electrodes and is attributed to the F-C bonding [6.29], which was probably derived from the binder constituent. After the cycle tests, the F1s spectra were found to contain several components (Figure 6.19), which can be separated into two peaks at 688.31–688.8 eV and 686.9–687 eV. The former peaks were also attributable to the F-C bonding from the binder,

whereas the latter peaks to semi-ionically bound to SP^2 carbons [6.30]. This may be due to the BF_4^- used for the anions. These findings suggest that the carbon dangling bonds may have reacted with the nitrogen from TEA^+ and the fluorine from BF_4^- during the cycle test, incurring pore blockages.

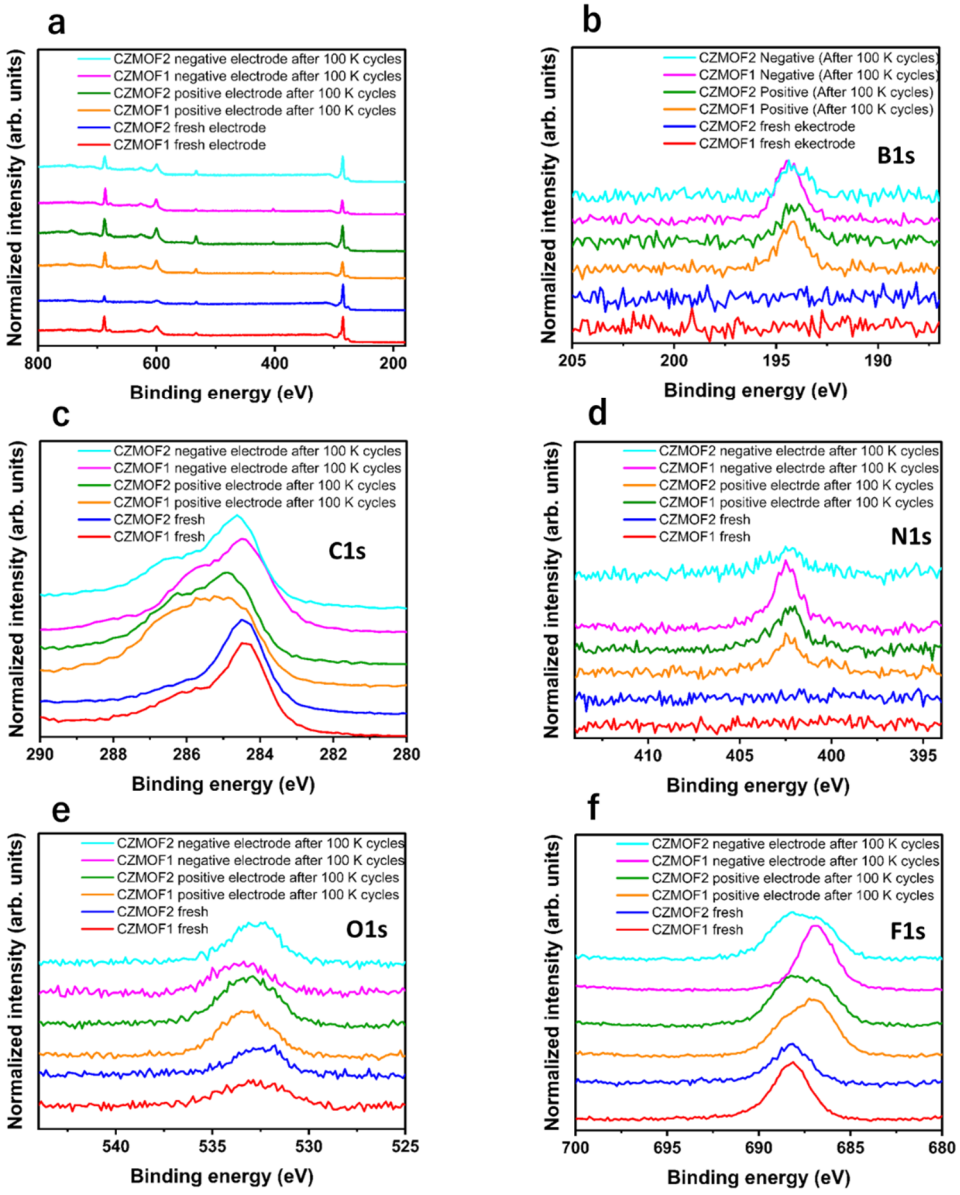

Figure 6.17 XP spectra of the CZMOF-based electrode materials before and after 100,000 GCD cycling tests in non-aqueous electrolytes ($TEABF_4$ in PC): (a) XP survey spectra of the CZMOF-based electrodes; (b), (c), (d), (e), and (f) are XP B1s, C1s, N1s, O1s, and F1s narrow spectra of the CZMOF-based electrodes, respectively.

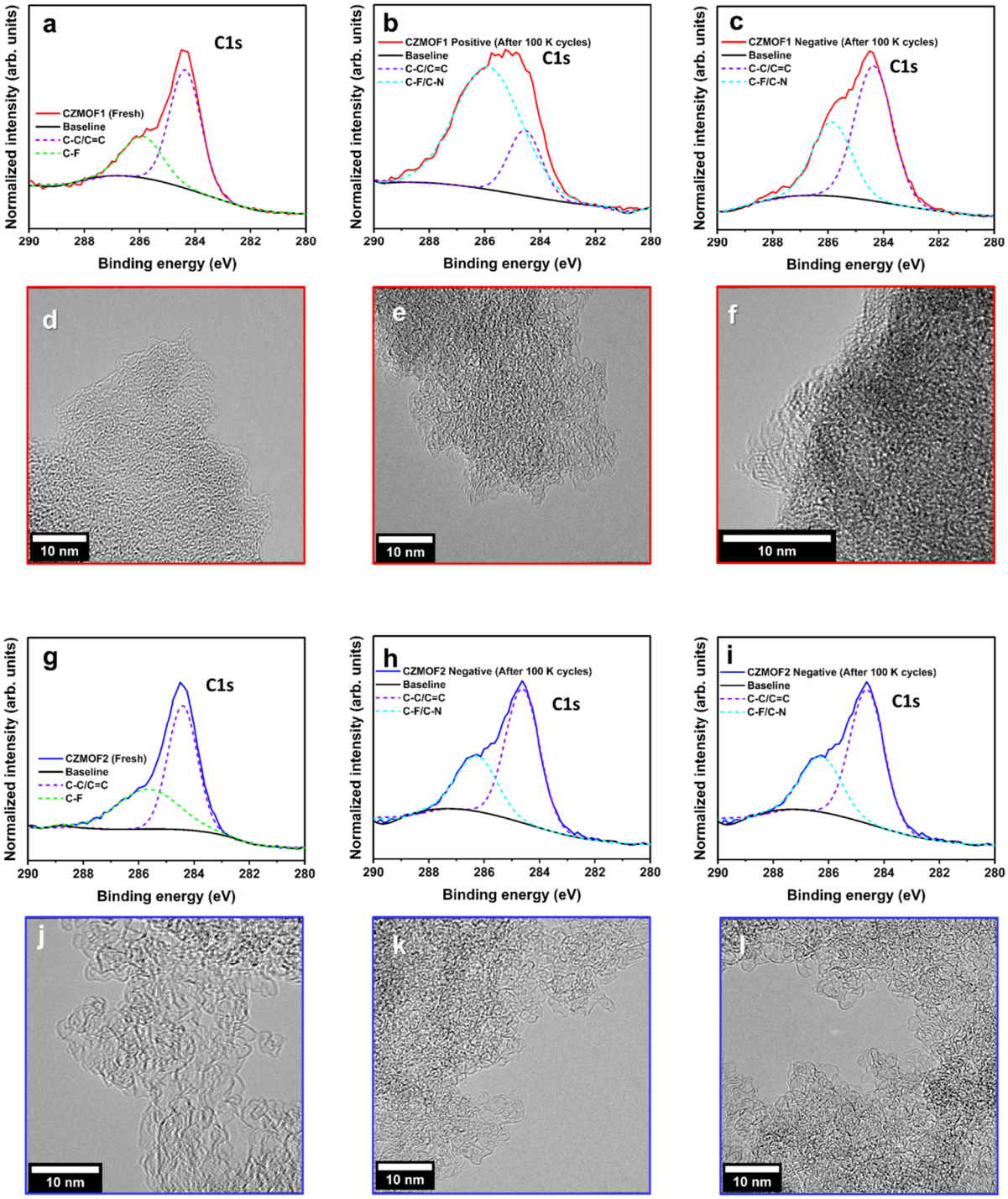

Figure 6.18 XP C1s spectra (normalized at 284.5 eV (C–C and/or C=C)) of the CZMOF-based electrode surfaces based on (a)–(c) CZMOF1 and (g)–(i) CZMOF2. (a) and (g) show the XP C1s spectra of the fresh electrode surfaces. (b), (h) and (c), (i) show the XP C1s spectra of the positive and negative electrode surfaces, respectively, after 100,000 GCD cycles in $TEABF_4$. TEM images of the electrode surfaces based on (d)–(f) CZMOF1 and (j)–(l) CZMOF2. (d) and (j) show TEM images of the fresh electrode surfaces. (e), (k) and (f), (l) show TEM images of the positive and negative electrode surfaces, respectively, after 100,000 GCD cycles in $TEABF_4$.

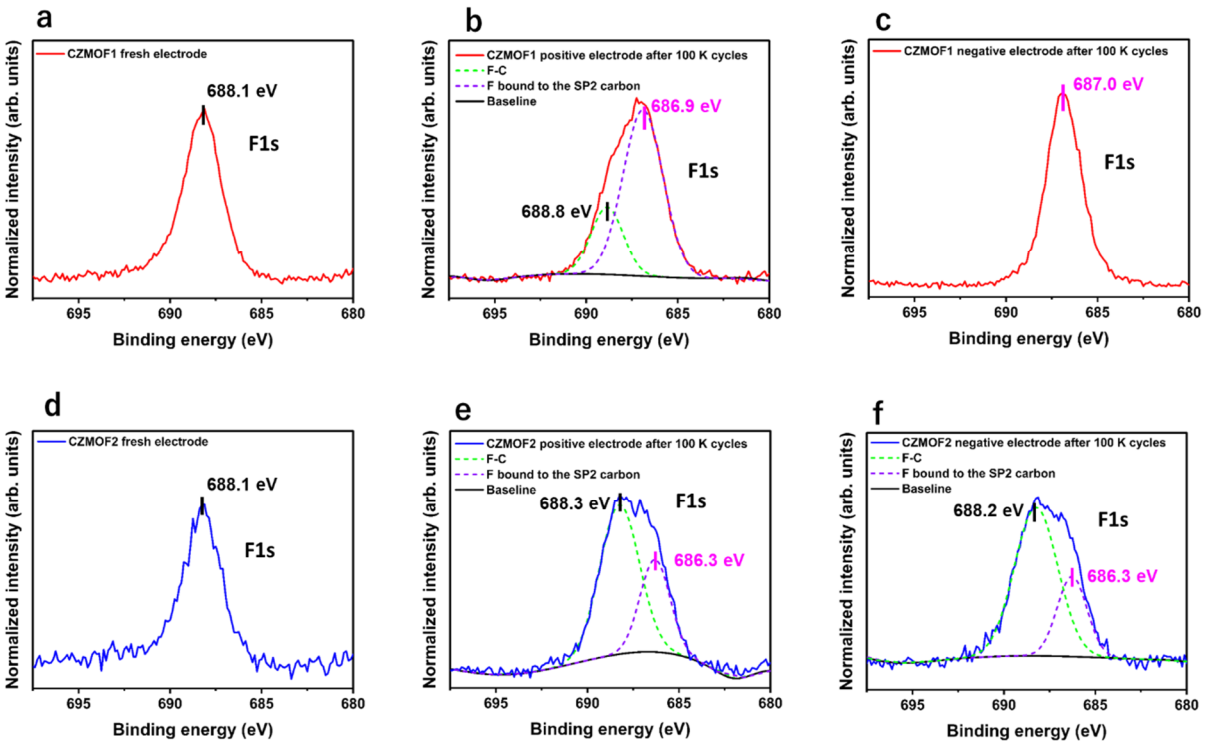

Figure 6.19 XP F1s spectra of the CZMOF-based electrode surfaces based on (a)–(c) CZMOF1 and (d)–(f) CZMOF2. (a) and (d) show XP F1s spectra of the fresh electrode surfaces. (b), (e) and (c), (f) show XP F1s spectra of the positive and negative electrode surfaces, respectively, after 100,000 GCD cycles in $TEABF_4$.

6.4 Conclusion

The electrochemical properties of CZMOFs were evaluated in detail using aqueous electrolytes (1.0 M H_2SO_4). Notably, CZMOF2 with an S_{BET} of 2678 $m^2\ g^{-1}$ exhibited specific capacitances of 360, 278, and 221 F g^{-1} at current densities of 50, 250, and 1000 mA g^{-1}, respectively. To date, these capacitances are the highest reported values in SCs with Zn-based MOF-derived electrodes and H_2SO_4 electrolytes. However, CZMOF2 with an extremely high S_{BET} was found to suffer from the lower volumetric capacitance (lower bulk density). Therefore, the electrode materials with high charge density (C_s) are desired earnestly as the next step. In both CZMOF1 and CZMOF2, above 98% capacitance retention was notably maintained even after 10000 GCD cycling tests at 1.0 A g^{-1}. Furthermore, the electrochemical properties of CZMOFs with non-aqueous electrolytes ($TEABF_4$) were investigated to confirm the feasibility of CZMOF-based SCs. As with H_2SO_4, the specific capacitance of CZMOF2 also exceeded that of the two activated carbons. The degradation of the electrode surfaces was analyzed through SEM, TEM, and XPS, confirming that electrolytes deteriorated the electrode surfaces while charging/discharging. Remarkably, the two symmetric SC cells based on CZMOFs with $TEABF_4$ electrolytes exhibited excellent performance, indicating their applicability as SC electrode materials.

6.5 References

[6.1] B. Xu, H. Zhang, H. Mei and D. Sun, "Recent progress in metal-organic framework-based supercapacitor electrode materials." *Coord. Chem. Rev.*, 420 (2020).

[6.2] Z. Liang, R. Zhao, T. Qiu, R. Zou, and Q. Xu, "Metal- organic framework- derived materials for electrochemical energy applications." *Energy Chem*, **1**, 100001 (2019).

[6.3] K.-B. Wang, Q. Xun, and Q. Zhang,"Recent progress in metal-organic frameworks as active materials for supercapacitors." *Energy Chem*, **2**, 100025 (2020).

[6.4] X. Li, X. Yang, H. Xue, H. Pang, and Q. Xu, "Metal–organic frameworks as a platform for clean energy applications." *Energy Chem*, **2**, 100027 (2020).

[6.5] E. Frackowiak, "Carbon materials for supercapacitor application."*Phys. Chem. Chem. Phys.*, **9**, 1774–1785 (2007).

[6.6] H. M. Lee, K. H. An, S. J. Park and B. J. Kim, "Mesopore-Rich Activated Carbons for Electrical Double-Layer Capacitors by Optimal Activation Condition." *Nanomaterials*, **9**, 608 (2019).

[6.7] W. G. Pell, B. E. Conway, "Voltammetry at a de Levie brush electrode as a model for electrochemical supercapacitor behavior." *J. Electroanal. Chem*., **500**, 121–133 (2001).

[6.8] R. Ramachandran, C. Zhao, D. Luo, K. Wang and F. Wang, "Morphology-dependent electrochemical properties of cobalt-based metal organic frameworks for supercapacitor electrode materials." *Electrochim. Acta*, **267**, 170–180 (2018).

[6.9] C. Young, R. R. Salunkhe, J. Tang, C. C. Hu, M. Shahabuddin, E. Yanmaz, M. S. Hossain, J. H. Kim and Y. Yamauchi," Zeolitic imidazolate framework (ZIF-8) derived nanoporous carbon: the effect of carbonization temperature on the supercapacitor performance in an aqueous electrolyte." *Phys. Chem. Chem. Phys.*, **18**, 29308–29315 (2016).

[6.10] N. L. Torad, R. R. Salunkhe, Y. Li, H. Hamoudi, M. Imura, Y. Sakka, C. C. Hu and Y. Yamauchi, " Electric Double-Layer Capacitors Based on Highly Graphitized Nanoporous Carbons Derived from ZIF-67." *Chem. Eur. J.*, **20**, 7895–7900 (2014).

[6.11] D. Qu, H. Shi, “Studies of activated carbons used in double-layer capacitors.
” *J. Power Sources*, **74**, 99–107 (1998).

[6.12] K. Sing, "The use of nitrogen adsorption for the characterisation of porous materials. "*Colloids Surf.*, **187-188**, 3–9 (2001).

[6.13] C. Lei, N. Amini, F. Markoulidis, P. Wilson, S. Tennison and C. Lekakou, "Activated carbon from phenolic resin with controlled mesoporosity for an electric double-layer capacitor (EDLC). " *J. Mater. Chem. A*, **1** (2013).

[6.14] C. Lei, F. Markoulidis, Z. Ashitaka and C. Lekakou, "Reduction of porous carbon/Al contact resistance for an electric double-layer capacitor (EDLC). " *Electrochim. Acta*, **92**, 183–187

[6.15] L. M. D. Silva, R. Cesar, C. M. R. Moreira, J. H. M. Santos, L. G. D. Souza, B. M. Pires, R. Vicentini, W. Nunes, and H. Zanin, " Reviewing the fundamentals of supercapacitors and the difficulties involving the analysis of the electrochemical findings obtained for porous electrode materials." *Energy Stor. Mater*., **27**, 555–590 (2020).

[6.16] H. B. Aiyappa, P. Pachfule, R. Banerjee and S. Kurungot, "Porous Carbons from Nonporous MOFs: Influence of Ligand Characteristics on Intrinsic Properties of End Carbon.
" *Cryst. Growth Des.*, **13**, 4195–4199 (2013).

[6.17] B. Liu, H. Shioyama, T. Akita and Q. Xu, "Metal-Organic Framework as a Template for Porous Carbon Synthesis." *J. Am. Chem. Soc.*, **130**, 5390–5391 (2007).

[6.18] A. J. Amali, J. K. Sun and Q. Xu, *Chem .Commun.*, "From assembled metal–organic framework nanoparticles to hierarchically porous carbon for electrochemical energy storage. ,” **50**, 1519–1522 (2014).

[6.19] B. Liu, H. Shioyama, H. Jiang, X. Zhang and Q. Xu, "Metal–organic framework (MOF) as a template for syntheses of nanoporous carbons as electrode materials for supercapacitor." *Carbon*, **48**, 456–463 (2010).

[6.20] W. Chaikittisilp, M. Hu, H. Wang, H. S. Huang, T. Fujita, K. C. Wu, L. C. Chen, Y. Yamauchi and K. Ariga, "Nanoporous carbons through direct carbonization of a zeolitic imidazolate framework for supercapacitor electrodes." *Chem. Commun.*, **48**, 7259–7261 (2012).

[6.21] H. L. Jiang, B. Liu, Y. Q. Lan, K. Kuratani, T. Akita, H. Shioyama, F. Zong and Q. Xu, "

From Metal–Organic Framework to Nanoporous Carbon: Toward a Very High Surface Area and Hydrogen Uptake." *J. Am. Chem. Soc.*, **133**, 11854–11857 (2011).

[6.22] D. Hulicova-JuracovaJ, M. Seredych, Y. Jin, G. Qing Lu, T. J. Bandosz, "Specific anion and cation capacitance in porous carbon blacks." *Carbon*, **48**, 1767–1778 (2010).

[6.23] L. Pilon, H. Wang and A. d'Entremont, " Recent Advances in Continuum Modeling of Interfacial and Transport Phenomena in Electric Double Layer Capacitors." *J. Electrochem. Soc.*, **162**, A5158–A5178 (2015).

[6.24] S. Ishimoto, Y. Asakawa, M. Shinya and K. Naoi, *J. Electrochem. Soc.*, "Degradation Responses of Activated-Carbon-Based EDLCs for Higher Voltage Operation and Their Factors.," **156**, A563–A571 (2009).

[6.25] B. H. Ka and S. M. Oh, "Electrochemical Activation of Expanded Graphite Electrode for Electrochemical Capacitor." *J. Electrochem. Soc.*, **155**, A685–A692 (2008).

[6.26] P. Azaïs, L. Duclaux, P. Florian, D. Massiot, M.-A. Lillo-Rodenas, A. Linares-Solano, J.-P. Peres, C. Jehoulet and F. Béguin, "Causes of supercapacitors ageing in organic electrolyte. " *J. Power Sources*, **171**, 1046–1053 (2007).

[6.27] D.-G. Wang, N. Li, Y. Hu, S. Wan, M. Song, G. Yu, Y. Jin, W. Wei, K. Han, G.-C. Kuang, and W. Zhang, "Highly Fluoro-Substituted Covalent Organic Framework and Its Application in Lithium–Sulfur Batteries." *ACS Appl. Mater. Interfaces*, **10**, 42233–42240 (2018).

[6.28] T.I.T. Okpalugo, P. Papakonstantinou, H. Murphy, J. McLaughlin, N.M.D. Brown, "High resolution XPS characterization of chemical functionalised MWCNTs and SWCNTs." *Carbon*, **43**, 153–161 (2005).

[6.29] L. Sygellou, S. Kakogianni, A. K. Andreopoulou, K. Theodosiou, G. Leftheriotis, J. K. Kallitsis, and A. Siokou, "Evaluation of the electronic properties of perfluorophenyl functionalized quinolines and their hybrids with carbon nanostructures." *Phys. Chem. Chem. Phys*, **18**, 4154–4165 (2016)

[6.30] J.-M. Lee, S. J. Kim, J. W. Kim, P.-H. Kang, Y. C. Nho, Y.-S. Lee, "A high resolution XPS study of sidewall functionalized MWCNTs by fluorination." *J Ind Eng Chem*, **15**, 66–71 (2009)

7 Conclusions and perspectives

This doctoral thesis summarizes the studies on multi-functional carbons for SC electrodes.

Chapter 1 briefly noted the recent environmental and energy issues in the opening sentence, where the author emphasized the more use of renewable energy resources. Multi-functional carbons are expected to provide some environmental contributions owing to their excellent physical, chemical, and electrochemical properties. Therefore, the latter part focused on the overview of SCs among several kinds of energy storage devices that contribute to environmental issues and confirmed the significance of the development of SCs.

Chapter 2 provided a basic understanding of the electrochemical properties of SCs both experimentally and analytically. The pore characteristics and electrochemical properties of the three kinds of commercial porous carbons were discussed in the first part. The relationship between electrolytes and the specific capacitance was revealed by evaluating the electrochemical properties with H_2SO_4 and $TEABF_4$ individually. A simulation model was introduced in the second part to promote a greater understanding of the experimental data. The relationship between the waveforms and the electrochemical parameters was successfully clarified by calculating analytical GCD and EIS curves.

Chapter 3 discussed the nitrogen doping effects using two types of ICOFs as carbon precursors. The direct carbonization of ICOFs successfully produced nitrogen-doped porous carbons (CICOFs). Particle size was successfully controlled by adjusting synthetic conditions. Most importantly, N-doped CICOFA achieved higher charge density (37.4 μFcm^{-2}) than other porous carbons, owing to the N-doping effect. These results verified that the direct carbonization of COFs produces heteroatom-doped carbons and that they have high prospects as carbon precursors for multi-functional carbon materials.

Chapter 4 reported B-doped porous carbons for SC electrodes. B-doped porous carbons were prepared by carbonizing B-based COFs (COF-5). Through several steps for preparing B-doped porous carbons, the author discovered a unique and simplistic process of producing B-doped porous carbons. The gentle water treatment of the calcined COF-5 (CCO-5) successfully produced B-doped porous carbons. As with nitrogen-doped carbons introduced

in chapter 3, the obtained B-doped porous carbons exhibited high charge density (15.3 μF cm^{-2}) under $TEABF_4$, which exceeded that of other commercial activated carbons (~7 μF cm^{-2}).

Chapter 5 elucidated the mechanism underlying pore generation using Zinc-based MOFs (ZMOFs) as carbon precursors. Two kinds of porous carbons (CZMOF1 and CZMOF2) were successfully prepared by activating ZMOFs with different Zn/C ratios (0.0625 and 0.1250) and O/C ratios (0.25 and 0.50). An extremely high S_{BET}, ~2700 m^2 g^{-1}, was achieved for CZMOF2. The Zn/C ratio significantly affected the specific surface areas of the CZMOFs below 1000 °C. The in situ PXRD analysis of the ZMOFs provided insightful information on the dynamic behavior of ZnO in the carbonized ZMOFs, revealing that the Zn/C ratio also affected the stability of crystalline ZnO at high temperatures. Notably, numerous pores were developed during ZnO reduction and Zn sublimation up to 1000 °C. Furthermore, a high O/C ratio was observed to be essential for pore generation at >1000 °C because pores were generated by pyrolysis of oxygen functional groups. Whether oxygen atoms are absent or present in the MOF structure, oxide formation and decomposition of oxygen functional groups during the carbonization process play a significant role in pore control. This finding is helpful for the pore control of the carbons derived from other metal-based MOFs.

Chapter 6 reported the detailed evaluation of the electrochemical properties of SC electrodes based on CZMOFs, which were introduced in chapter 5. CZMOF2 with an S_{BET} of 2678 m^2 g^{-1} exhibited specific capacitances of 360, 278, 221 Fg^{-1} at current densities of 50, 250, and 1000 mA g^{-1}, respectively. To date, these capacitances are the highest reported values in SCs with Zn-based MOF-derived electrodes and H_2SO_4 electrolytes. However, porous carbons with an extremely high S_{BET} was confirmed to suffer from the lower volumetric capacitance (lower bulk density). Therefore, the electrode materials with high charge density (C_s) will be desired, as discussed in chapter 3 and 4. The electrochemical properties of CZMOFs with non-aqueous electrolytes ($TEABF_4$) were evaluated to confirm the feasibility of CZMOFs-based SCs. As with H_2SO_4, the specific capacitance of CZMOF2

also exceeded that of the two activated carbons. The degradation of the electrode surfaces was analyzed through SEM, TEM, and XPS, confirming that electrolytes deteriorated the electrode surfaces while charging/discharging. Significantly, the two symmetric SC cells based on CZMOFs with $TEABF_4$ exhibited excellent performance, indicating their applicability as SC electrode materials.

All the findings are expected to apply to future works on multi-functional carbons for SC electrodes. MOFs or COFs still face difficulties in realizing MOF or COF-derived SC electrodes in terms of cost. The author thinks that the insightful findings obtained in this study will play crucial roles when using biomass-based carbon precursors for SC electrodes.

Acknowledgments

This doctoral thesis summarizes my studies on multi-functional carbons for supercapacitor electrodes. After graduating from Graduate School of Engineering and Faculty of Engineering at Kyoto University, I joined the R & D department of SEIWA ELECTRIC MFG. CO., LTD. since 2012. The company allowed me to study supercapacitor electrode materials from 2013 to 2019. During this period, I successfully developed several unique processes for producing multi-functional carbon materials. To consolidate the studies, I collaborated with Prof. Yasuhiko Hayashi from the Graduate School of Natural Science and Technology at Okayama University since 2013 and Prof. Daisuke Tanaka from the Department of Chemistry, School of Science at Kuwansei Gakuin University since 2016. In 2019, Prof. Yasuhiko Hayashi offered me the opportunity to obtain a doctoral degree and submit some peer-reviewed papers.

I acknowledge Prof. Yasuhiko Hayashi for his comprehensive support for obtaining the doctoral degree. He guided me and provided much helpful advice; his encouragement contributed to the success of the doctoral program. Two manuscripts were accepted in famous journals, Carbon (IF = 9.594) and Energy & Environmental Materials (IF = 15.122), due to his efficient instruction.

I acknowledge Associate Prof. Kazuma Gotoh from the Graduate School of Natural Science and Technology at Okayama University. He checked the manuscript elaborately before submissions and made vital suggestions that greatly improved the manuscripts.

I acknowledge Yoshifumi Yamashita, an Associate Professor in the Graduate School of Natural Science and Technology at Okayama University. He checked and judged the doctoral thesis.

I acknowledge Prof. Daisuke Tanaka for his comprehensive instruction regarding MOFs and COFs. He always promptly responded to my several questions, no matter how busy he was. Notably, his instruction helped me to successfully submit the manuscript accepted for publication in both Carbon and Energy & Environmental Materials.

I acknowledge Prof. Soushi Shiraishi from Gunma University for his comprehensive support. Since 2014, I received the experimental instructions for assembling a supercapacitor cell and evaluating its electrochemical properties from him. Besides, he kindly answered my questions about electrochemistry and carbon materials.

I acknowledge Prof. S. Ravi P. Silva, a distinguished professor and the director of the Advanced Technology Institute at the University of Surrey. He provided much insightful information on the mechanism underlying pore generation during the carbonization of MOFs. My English skills were improved while discussing with him many times by email and online meetings.

I acknowledge Dr. Vlad Stolojan, a Senior Lecturer in Nanomaterials Characterization, working in the Advanced Technology Institute as part of the Nano-Electronics Centre. He also checked the manuscript elaborately. I was impressed by his knowledgeable advice.

I acknowledge Dr. Mika Yoneda, currently a Technical Expert Staff, Faculty of Engineering, Okayama University. Owing to her skills in TEM observation, I successfully observed the nanostructure of carbon samples.

I acknowledge Hiroo Suzuki, an Assistant Professor in the Graduate School of Natural Science and Technology at Okayama University. He kindly offered much valuable advice on paper submission and presentations.

I acknowledge Dr. Hirotaka Inoue, who graduated from YASUHIKO HAYASHI LAB in the Graduate School of Natural Science and Technology at Okayama University. He was one of my colleagues in the LAB. When I was unfamiliar with writing papers, he introduced me to much useful software that helped me edit efficiently. He still responds to my questions by e-mail even after his graduation.

I acknowledge Mr. Kohei Komatsubara for experimental support and literature review. He is a member of YASUHIKO HAYASHI LAB in the Graduate School of Natural Science and Technology at Okayama University. Furthermore, his papers on Highly Oriented Carbon Nanotube Supercapacitors helped in the study.

I acknowledge Mr. Koji Yoshikawa, a supervisor who organized the R & D department to enhance the technological capabilities of SEIWA ELECTRIC MFG. CO., LTD. He provided much helpful advice on my studies and encouraged me to obtain a doctoral degree. Moreover, he has changed my view of life. He and Prof. Yasuhiko Hayashi arranged the opportunity to embark on a doctoral degree.

I acknowledge Mr. Takashi Douura, my senior coworker in the R & D department of SEIWA ELECTRIC MFG. CO., LTD. I have cooperated with him for ten years to progress the study. He kindly offered many unique ideas, which successfully produced several multi-functional carbon materials. Without his continued support, this study wouldn’t have come this far.

I acknowledge SEIWA ELECTRIC MFG. CO., LTD., who endorsed my admission into the Graduate School of Natural Science and Technology at Okayama University.

I gratefully acknowledge my parents and sisters, who have supported my life since my childhood. Notably, due to my parents' strong support, I successfully got admitted and completed a program at Kyoto University, opening my research career.

I gratefully acknowledge my wife and son for supporting my life. I could not spare private time sufficiently. Nevertheless, she allowed me to write or edit manuscripts even on holidays. Owing to her devoted support, I was able to continue the doctoral program to my heart's content.

Research achievements

【Publications】

1. **S. Umezawa**, T. Douura, Y. Yoshikawa, Y. Takashima, M. Yoneda, K. Gotoh, V. Stolojan, S. R. P. Silva, Y. Hayashi, D. Tanaka, "Supercapacitor electrode with high charge density based on boron-doped carbon derived from covalent organic frameworks." Carbon **184**, 418–425 (2021). https://doi.org/10.1016/j.carbon.2021.08.022

2. **S. Umezawa**, T. Douura, K. Yoshikawa, D. Tanaka, V. Stolojan, S. R. P. Silva, M. Yoneda, K. Gotoh, Y. Hayashi, "Zinc-based metal-organic frameworks for high-performance supercapacitor electrodes: Mechanism underlying pore generation. Energy Environ. Mater, in press. https://doi.org/10.1002/eem2.12320

3. K. Komatsubara, H. Suzuki, H. Inoue, M. Kishibuchi, S. Takahashi, T. Marui, **S. Umezawa**, T. Nakagawa, K. Nasu, M. Maetani, Y. Tanaka, M. Yamada, T. Nishikawa, Y. Yamashita, M. Hada, Y. Hayashi, Highly Oriented Carbon Nanotube Supercapacitors, ACS Applied Nano Materials, in press. https://doi.org/10.1021/acsanm.1c04236

【Presentations】

International conference

1. Supercapacitor Electrode with High Charge Density using Boron-based Covalent Organic Frameworks-derived Porous Carbon (Poster only)

   Shigeyuki Umezawa, Takashi Douura, Koji Yoshikawa, Daisuke Tanaka, Yasuhiko Hayashi

   Twenty-First International Conference on the Science and Application of Nanotubes and Low-Dimensional Materials (NT21) (Rice University, Houston, USA, 7-11 June 2021), Online.

2. Facile synthesis of boron-doped porous carbons for supercapacitor electrode toward high charge density (Presentation only)

   Shigeyuki Umezawa, Takashi Douura, Koji Yoshikawa, Daisuke Tanaka, Yasuhiko Hayashi

   31st International Conference on Diamond and Carbon Materials (6-9 September 2021), ONLINE: Live and on-demand

Domestic conference

1. Carbons derived from covalent organic frameworks and their electrochemical properties of electric double layer capacitor" (Presentation)

   Shigeyuki Umezawa, Takashi Douura, Koji Yoshikawa, Daisuke Tanaka, Yasuhiko Hayashi,

   46 th Annual meeting of The Carbon Society of Japan, 2C07 (Okayama University, Okayama, Japan, 28-30, June 2019).

【Professional membership】

1. The Electrochemical Society of Japan

   October 2013-present

2. The Carbon Society of Japan

   July 2019-present

【Awards and honors】

N/A

【Grants and scholarships】

This research did not receive any specific grant from funding agencies in the public, commercial, or not-for-profit sectors.